Transverse-Target Single-Spin Azimuthal Asymmetry in Hard Exclusive Electroproduction of Single Pions at HERMES

DISSERTATION

zur Erlangung des akademischen Grades
doctor rerum naturalium
(Dr. rer. nat.)
im Fach Physik

eingereicht an der
Mathematisch-Naturwissenschaftlichen Fakultät I
Humboldt-Universität zu Berlin

von
Frau Magister Ivana Hristova

Präsident der Humboldt-Universität zu Berlin:
Prof. Dr. Christoph Markschies

Dekan der Mathematisch-Naturwissenschaftlichen Fakultät I:
Prof. Dr. Christian Limberg

Gutachter:

1. Prof. Dr. Hermann Kolanoski
2. Prof. Dr. Dirk Ryckbosch
3. Dr. Marek Kowalski

eingereicht am:	22. August 2007
Tag der mündlichen Prüfung:	13. Dezember 2007

Abstract

We present the analysis of data taken in the years 2002-2004 with the 27.56 GeV positron beam of the HERA storage ring at DESY and the internal transversely polarised hydrogen fixed target of the HERMES experiment. Events with a scattered positron and a produced pion are selected. Exclusive production of single pions, $e^+p \to e^{+\prime} n \pi^+$, is ensured by requiring the missing mass in the event to be equal to the mass of the neutron, which is not detected. The cross section for this process depends on the Bjorken scaling variable, the four-momentum transfer, and the transverse four-momentum transfer, whose average values for our sample are $\langle x \rangle = 0.12$, $\langle Q^2 \rangle = 2.3\,\mathrm{GeV}^2$, $\langle t' \rangle = -0.18\,\mathrm{GeV}^2$, respectively, and two azimuthal angles: the angle ϕ between the scattering and production planes (their common line contains the virtual photon), and the angle ϕ_S between the scattering plane and the target polarisation vector. The hard scattering is selected by requiring $Q^2 > 1\,\mathrm{GeV}^2$.

The asymmetry, also called transverse-target single-spin azimuthal asymmetry, is defined as the ratio of the difference to the sum of the cross sections for positive and negative target polarisation. It is characterised by six azimuthal sine modulations, whose amplitudes can vary from -1 to 1. We measure the asymmetry from a sample of 2093 events with a signal-to-background ratio of $1:1$. At average kinematics, the values of the amplitudes are found to be small or consistent with zero, except for the amplitude $A_{UT,meas}^{\sin\phi_S} = 0.38 \pm 0.06(stat)^{+0.12}_{-0.06}(syst)$. The amplitude of main interest for comparison with theory, $A_{UT,meas}^{\sin(\phi-\phi_S)} = 0.09 \pm 0.05(stat)^{+0.10}_{-0.03}(syst)$, after correction for the background contribution becomes $A_{UT,bg.cor}^{\sin(\phi-\phi_S)} = 0.22 \pm 0.13(stat)^{+0.10}_{-0.04}(syst)$. As a function of t', the measured values of this amplitude increase as $\sqrt{-t'}$ and at larger $|t'|$ the corrected ones approach the prediction, however, within their large statistical uncertainties.

The phenomenology of hard exclusive electroproduction of pions is explained at present in terms of the so called QCD factorisation theorem: the amplitude for the cross section is given as a convolution of a hard scattering part calculable in perturbative quantum chromodynamics, a distribution amplitude describing the pion, and generalised parton distributions that parameterise the complex structure of the proton. Using QCD factorisation and models for the particles' structure, the value of the leading amplitude $A_{UT}^{\sin(\phi-\phi_S)}$ is predicted to be of order unity. Although our results appear to support this prediction, a direct and more precise data-to-theory comparison requires larger statistics and improved detector capabilities than available for the present measurement.

Keywords:
QCD, exclusive, proton structure, asymmetry

Zusammenfassung

Wir präsentieren die Analyse der Daten, die in den Jahren 2002-2004 mit dem 27.56 GeV Positronenstrahl des HERA Speicherrings am DESY und dem internen transversal polarisierten Wasserstofftarget ('fixed target') des HERMES Experiments aufgenommen wurden. Ereignisse mit einem gestreuten Positron und einem erzeugter Pion wurden selektiert. Die ausschließliche Erzeugung eines einzelnen Pions, $e^+p \rightarrow e^{+\prime}n\pi^+$, wird durch die Anforderung gewährleistet, daß die fehlende Masse des Ereignisses der Masse des Neutrons, das nicht gemessen wird, entspricht. Der Streuquerschnitt für diesen Prozess hängt von der Bjorken-Skalenvariable, den Vierer-Impulsübertrag und den Transversalimpulsübertrag, deren durchschnittliche Werte für unsere Datensätze bei $\langle x\rangle = 0.12$, $\langle Q^2\rangle = 2.3\,\mathrm{GeV}^2$, $\langle t'\rangle = -0.18\,\mathrm{GeV}^2$ liegen, sowie zwei azimuthale Winkel: der Winkel ϕ zwischen den Streu- und Produktionsebene (die Schnittlinie der Ebenen enthält das virtuelle Photon), und der Winkel ϕ_S zwischen der Streuebene und dem Polarisationsvector des Targets. Die harte Streuung wird durch die Bedingung von $Q^2 > 1\,\mathrm{GeV}^2$ bestimmt.

Die Asymmetrie, auch Transversal-Target-Einzelspin-Azimuthalasymmetrie genannt, wird als das Verhältnis der Differenz zur Summe der Streuquerschnitte für die positive und negative Targetpolarisation definiert. Es wird durch sechs azimuthale Sinus-Modulationen charakterisiert, deren Amplituden von -1 bis 1 varieren können. Wir messen die Asymmetrie eines Datensatzes von 2093 Ereignissen mit einem Signal-Rausch-Verhältnis von $1:1$. Im Durchschnitt wurden geringe oder mit Null übereinstimmende Amplitudenwerte gefunden, abgesehen von der Amplitude $A_{UT,meas}^{\sin\phi_S} = 0.38 \pm 0.06(stat)^{+0.12}_{-0.06}(syst)$. Die Amplitude mit größten Bedeutung für den Vergleich mit der Theorie, $A_{UT,meas}^{\sin(\phi-\phi_S)} = 0.09 \pm 0.05(stat)^{+0.10}_{-0.03}(syst)$, wird nach einer Korrektur für den Untergrundbeitrag $A_{UT,bg.cor}^{\sin(\phi-\phi_S)} = 0.22 \pm 0.13(stat)^{+0.10}_{-0.04}(syst)$. Als Funktion von t' steigen die gemessenen Werte dieser Amplitude mit $\sqrt{-t'}$ an und für höhere $|t'|$-Werte entsprechen die korrigierten Amplituden den Vorhersagen, allerdings innerhalb der großen exprimentellen Unsicherheiten.

Die Phänomenologie von harter exklusiver Electroproduktion von Pionen wird zurzeit in Form des sogenannten QCD-Faktorisierungstheorems erklärt: die Amplitude des Streuquerschnitts ist die Faltung eines harten Teils der Streuung, aus der perturbativen Quantenchromodynamik berechenbar, mit einer Verteilungsfunktion, die das Pion beschreibt, und verallgemeinerte Parton-Verteilungen, die die komplexe Struktur des Protons parametrisiert. Mit Hilfe der QCD-Faktorisierung und den Modellen der Teilchenstruktur wird der maximale Wert der Hauptamplitude $A_{UT}^{\sin(\phi-\phi_S)}$ zu 1 vorausgesagt. Obwohl unsere Ergebnisse die Voraussage zu bestätigen scheinen, ein direkter und genauerer Vergleich der Daten mit der Theorie verlangt größere Statistik und verbesserte Fähigkeiten des Detektors als für die vorliegende Messung vorhanden waren.

Schlagwörter:
Quantenchromodynamik, exklusiv, Protonstruktur, Asymmetrie

Contents

List of Figures

List of Tables

Chapter 1

Introduction

The proton p (with radius $r_p \approx 10^{-15}\,\mathrm{m}$) represents the nucleus of the hydrogen atom H ($r_H \approx 10^{-10}\,\mathrm{m}$). The ground states of the hydrogen spectrum (which is similar to atomic and nuclear spectra) are correctly described by postulating the existence of spin-$\frac{1}{2}$ pointlike (having no internal structure of their own) particles, called quarks q ($r_q < 10^{-18}\,\mathrm{m}$), which compose the proton, i.e., $p = (uud)$, with $e_u = \frac{2}{3}$ and $e_d = -\frac{1}{3}$ the charges of the up u and down d quarks, respectively. In this quark model, e.g., the pion $\pi^+ = (u\bar{d})$ is a bound state of u and an antiquark $\bar{d}$ with $e_{\bar{d}} = \frac{1}{3}$.

Further information about the structure of the proton is obtained, e.g., from the scattering of high-energy pointlike electrons e^- ($r_{e^-} \approx 10^{-18}\,\mathrm{m}$) off protons. In the proton's rest frame the constituent particles of the proton interact with each other on a time scale of order r_p/c, where c is the speed of light. However, in the centre-of-mass frame of the scattering the proton appears to be boosted (moves very fast) and Lorentz-contracted, i.e., $r_{p,||} \to 0$ (but keeping its transverse extension, i.e., $r_{p,\perp} \neq 0$) in the planes parallel (transverse) to the boost direction. The rapidly moving proton can be treated as a jet of quasi-free particles moving almost collinear. Before a next interaction between the particles inside the proton takes place, time-dilation implies that the one before occurred a long distance ($\approx 100\, r_p$) upstream, which is much larger than the short scale of the scattering. The scattering distance scale is $\frac{r_p}{Q}$, where Q is the four-momentum transferred from the electron to the proton, so that with $Q \gg 1\,\mathrm{GeV}$ the corresponding distance is $\ll r_p$. Thus the electron–proton scattering takes place on a much shorter-distance, shorter-time scale compared with the long-distance slow interaction between the constituents. This suggests that only a single almost-free constituent, called a parton, participates in any instant of the scattering. By this simple parton model, invented in 1969 [11, 32], a large variety of hard ($Q \gg 1\,\mathrm{GeV}$) scattering processes are successfully described. The partons can be identified with the quarks. The quark-parton picture is still at present a valuable model.

The fundamental theory of the interactions between quarks, established in 1972 [37, 36] and called Quantum Chromodynamics (QCD), incorporates all properties of the quark-parton model and also solves other puzzles. By analogy with the electric charge in Quantum Electrodynamics (QED), 'colour' is the charge of strong interactions in QCD. It follows from the theory that in the regime of short-distance, short-time scales the partons (quarks and gluons in QCD) become quasi-free, a phenomenon called asymptotic freedom. This key feature, which allows one to use the powerful technical tool of perturbation theory, is responsible for the enormous success of perturbative QCD (pQCD) in high-energy physics, in particular, in the phenomenology of (semi-)inclusive processes.

QCD is supposed to describe also long-distance, long-time effects like the binding of the proton. A hypothesis suggested by the structure of QCD is that of confinement, meaning that the observed in the scattering particles—called hadrons—are bound states of quarks, yet quarks never appear alone. In this low-energy domain non-perturbative techniques and effective theories are developed, which incorporate the main features of QCD. Lattice theory [4] is one of the essential tools for calculating hadronic properties from first principles. However, many problems remain still unsolved and currently there is no exact explanation (analytical expression) for the way quarks are bound by strong interactions to form hadrons. Thus, on one hand, the quark and gluon fields are the elementary objects that are described by the theory, and on the other hand, the hadrons are the only real physical objects that are observed in any experiment, and the link is still missing to describe within QCD the transition between these two scales of the strong interaction.

In attempts towards unified understanding of all phenomena of strong interactions, the basic ideas of the parton model are presently applied also in the description of, e.g., hard (at very high squared four-momentum transfer Q^2) exclusive reactions. Under the name of factorisation (into a 'hard' and a 'soft' part of the scattering process), these ideas are the basis of the following physical picture [48]: The description of hard processes involving hadrons in the initial or final states is divided into the partonic subprocess taking place at short distances/times and the long-distance binding effects contained in the hadronic matrix elements of parton field operators between hadron states. In this picture partonic subprocesses and binding effects decouple and do not influence each other. The former are calculable within pQCD and the latter are parameterised in the form of a priori unknown functions like the form factors (FFs) in case of elastic processes, the parton distribution functions (PDFs) appearing in deep inelastic scattering (DIS), or the generalised parton distributions (GPDs) accessible in exclusive measurements.

The possibility to study GPDs in suitable exclusive scattering processes rests on factorisation theorems, as does the method to extract usual parton distributions from inclusive and semi-inclusive measurements. The proofs of these theorems are based on properties of Feynman diagrams and are very similar to the factorisation proofs for inclusive DIS or Drell-Yan pair production [20]. GPDs can be represented in terms of the wave functions [14] of the target , thus offering a further way to explicitly reveal which kind of information on hadron structure is contained in these quantities. In this scheme a hadron state is expanded in terms of the partonic Fock states created from the vacuum by the operators which appear in the decomposition of the components of quark and gluon fields. However, a discussion on the attempts to compute the form factors and parton distributions from a fundamental dynamical scheme is beyond our scope.

The discussion of hard processes is greatly simplified in terms of the light-cone quantisation [15], whose concepts and notions follow closely the basic ideas of the parton model, to which in fact they provide the formal theoretical justification. In distinction to canonical quantisation, where the theory is quantised at equal time, e.g., $z^0 = 0$, the light-cone quantisation is performed at equal 'light-cone time', e.g., $z^+ = \frac{z^0+z^3}{2} = 0$, where z is a four-vector. Introduced by Dirac in 1949 [28] as another parameterisation of space-time, the light-cone coordinates were rediscovered in the form of the infinite-momentum frame, which appeared in 1965 [38] in connection with current algebra as the limit of a reference frame moving very fast with almost the speed of light.

* * *

A QCD factorisation theorem for hard exclusive electroproduction of mesons was proved in 1997 [19] thus providing a new probe to study the dynamics of exclusive scattering in QCD and to test our understanding of the proton structure. The theorem was applied for the first time in 1999 [33] to the theoretical study of hard exclusive production of single pions from transversely polarised protons by longitudinal virtual photons, and a prediction was made for an observable, called the transverse-target single-spin azimuthal asymmetry. The asymmetry is characterised by six azimuthal sine modulations, whose amplitudes can vary from -1 to 1. The measurement of the amplitudes of the azimuthal asymmetry is the subject of this thesis.

In this work the analysis is presented of exclusive production of single pions in hard scattering of 27.56 GeV positrons off an internal transversely polarised hydrogen fixed target of the HERMES experiment in the HERA storage ring at DESY. The process is denoted as $e^+p \rightarrow e^{+\prime}n\pi^+$. A brief introduction to the formalism for describing scattering processes in terms of parton distributions is given in Chapter 2. The generalised parton distributions appear in the description of exclusive processes at the amplitude level. In order to access certain (combinations of) GPDs a polarised target is required. Chapter 3 outlines the theoretical description of hard exclusive pion electroproduction and the GPD model used to obtain a numerical prediction for the transverse-target single-spin azimuthal asymmetry. Chapter 4 describes the experimental setup with emphasis on those parts which are essential to this analysis, including trigger, data acquisition, and processing systems. In Chapter 5 the Monte Carlo generators used for description of the data are introduced. Chapter 6 presents the data sample, the methods of data treatment, and an estimate of the measured yield of exclusive pions using data only. Using Monte Carlo simulation further separation of signal from background is achieved and the contributions from different processes to the data sample are estimated. In Chapter 7 the extraction of the amplitudes of the azimuthal asymmetry from data is described and smearing effects are studied. A method for correction of the measured amplitudes for the background contribution is applied. Chapter 8 presents the final results for the measured and the corrected amplitudes, and a comparison of the latter with theoretical predictions. The thesis concludes with Summary and Conclusion.

Chapter 2

Introduction to Parton Distributions

We give a crude presentation of some of the main formulas that are used in the description of scattering processes in terms of parton distributions. The aim is to outline the steps leading to the definition of the generalised parton distributions in Section 2.6 in analogy with the form factors and parton distribution functions. See [8, 40, 48] for detailed discussions.

We introduce in Section 2.1 the electromagnetic current, which is used in Section 2.2 to define the elastic Dirac and Pauli form factors. In a similar way, the axial and pseudoscalar form factors, g_A and g_P, respectively, are defined using the axial current. The hadronic tensor is defined in Section 2.3 for elastic scattering and in Section 2.4 its expression is given for the case of inclusive scattering in terms of the matrix elements of quark-field operators. We turn to the light-cone representation of the hadronic tensor in Section 2.5.1. In Section 2.5.2 the form factors are expressed via non-diagonal matrix elements of local operators, while in Section 2.5.3 the parton distributions, in particular, the helicity distribution Δq, are defined through diagonal matrix elements of bilocal quark-field operators. Finally, in Section 2.6 the generalised parton distributions $\widetilde{H}$ and $\widetilde{E}$ are introduced as the form factors of non-diagonal matrix elements of bilocal quark-field operators at light-like separation. The quantities $\widetilde{H}$ and $\widetilde{E}$, as well as g_A, g_P, and Δq are the relevant ones for describing the process studied in this thesis (see Chapter 3).

In order to learn about the internal structure of nucleons, we must consider the scattering of particles as pointlike as possible, such as the scattering of high-energy electrons off protons. Since electrons do not posses a resolvable internal structure and at high energies they have a very small wavelength ($\lambda_e \approx \frac{1}{E_e} < 0.2 \cdot 10^{-15}\,\mathrm{m}$), the cross sections of these reactions depend only on the internal structure of the proton. By comparing the results of different scattering processes, we thus obtain an almost complete description of the proton structure.

2.1 Interaction of Particles

From the relativistic Dirac equations for a free four-spinor field Ψ (e.g., an electron e^-) and for an interaction of the field with an electromagnetic potential A_μ [40],

$$(i\gamma^\mu \partial_\mu - m)\Psi = 0 \quad \text{and} \quad [i\gamma^\mu(\partial_\mu - ieA_\mu) - m]\,\Psi = 0, \tag{2.1}$$

the interaction can be extracted in the form $\gamma^0 \hat{V} = (-e)\gamma^\mu A_\mu$, where $(-e)$ is the electron charge. This representation of $\hat{V}$, which preserves gauge invariance, corresponds to an exchange of a single photon in the interaction (one-photon approximation).

The transition amplitude (S-matrix element) of the particle (field) from an initial state Ψ_i

into a final state Ψ_f is in first-order perturbation theory given by [40]

$$S_{fi} \sim i\int d^4x\, \Psi_f^\dagger \hat{V}\Psi_i = i\int d^4x\, (\Psi_f^\dagger\gamma^0)(\gamma^0\hat{V})\Psi_i = i\int d^4x\, \bar{\Psi}_f(-e\gamma^\mu A_\mu)\Psi_i = i\int d^4x\, J^\mu A_\mu, \tag{2.2}$$

where $\bar{\Psi} = \Psi^\dagger\gamma^0$ and $J^\mu = (-e)\bar{\Psi}_f\gamma^\mu\Psi_i$ is the particle electromagnetic current. Using the particle plane wave representation [40], $\Psi_i(x) = \psi_i(l)\, e^{-il\cdot x}$ and $\Psi_f(x) = \psi_f(l')\, e^{-il'\cdot x}$, i.e., $\Psi_i(x)$ and $\Psi_f(x)$ are solutions to the free Dirac equation, the current becomes explicitly

$$J_\mu(x) = (-e)\bar{\psi}_f(l')\gamma_\mu\psi_i(l)\, e^{-i(l-l')\cdot x}, \tag{2.3}$$

where ψ_i and ψ_f are four-component spinors, x is a space-time four-vector, l and l' are four-momenta, and γ_μ ($\mu = 0, 1, 2, 3$) are Dirac matrices.

We now consider the current (2.3) as a matrix element of an electromagnetic current operator (Heisenberg operator) $\hat{J}_\mu(x)$, e.g., between electron states

$$J_\mu(x) = \langle e^-(l')|\hat{J}_\mu(x)|e^-(l)\rangle, \tag{2.4}$$

where $|e^-(l)\rangle$ and $\langle e^-(l')|$ denote the initial and the final electron state, respectively. Thus, using (2.3) and (2.4), we can write

$$\langle e^-(l')|\hat{J}_\mu(x)|e^-(l)\rangle = (-e)\bar{\psi}_f(l')\gamma_\mu\psi_i(l)\, e^{-i(l-l')\cdot x}, \tag{2.5}$$

$$\langle e^-(l')|\hat{J}_\mu(0)|e^-(l)\rangle = (-e)\bar{\psi}_f(l')\gamma_\mu\psi_i(l). \tag{2.6}$$

The matrix element (2.6) is taken with plane electron waves so that its space-time x dependence is given by the exponential factor in (2.5). The matrix element (2.6) describes the transition of interacting pointlike electrons from the initial state with momentum l to the final state with momentum l'. We note that the left-hand side of (2.6), by definition, is related to the physics observables of the interaction process, while its right-hand side is a calculable quantity. In this way theoretical calculations/predictions can be confronted with experimental measurements.

From (2.5) and (2.6) we can derive the relation

$$\langle e^-(l')|\hat{J}_\mu(x)|e^-(l)\rangle = \langle e^-(l')|\hat{J}_\mu(0)|e^-(l)\rangle\, e^{-i(l-l')\cdot x}. \tag{2.7}$$

2.2 Elastic Form Factors

We turn now to a particle with internal structure (e.g., the proton p). The left-hand side of (2.6) holds essentially unmodified, but we expect that the strong interaction modifies the right-hand side of (2.6), so that the proton matrix element is written by analogy with (2.6) as [40]

$$\langle p(P')|\hat{J}_\mu(0)|p(P)\rangle = (+e)\bar{\psi}_f(P')\Gamma_\mu\psi_i(P), \tag{2.8}$$

where $(+e)$ is the proton charge, P and P' are four-momenta. We cannot calculate (2.8) from theory, but we can proceed by parameterising the four-current, or Γ_μ, on the right-hand side of (2.8). The subscripts i and f, as well as $(+e)$ and ˆ are omitted in the following.

Lorentz covariance of the theory imposes that the four-current $\bar{\psi}(P')\Gamma_\mu\psi(P)$ must be a Lorentz vector. The most general structure of Γ_μ is thus [40]

$$\Gamma_\mu = A\gamma_\mu + BP'_\mu + CP_\mu + iD\sigma_{\mu\nu}P'^\nu + iE\sigma_{\mu\nu}P^\nu, \quad \sigma_{\mu\nu} = \frac{1}{2}i\,[\gamma_\mu, \gamma_\nu] = \frac{1}{2}i(\gamma_\mu\gamma_\nu - \gamma_\nu\gamma_\mu), \tag{2.9}$$

where the quantities $A, B, .., E$ depend only on Lorentz-invariant quantities. All these invariants can be expressed in terms of the proton mass M_p and the squared four-momentum transfer

$t = \Delta^2 = (P' - P)^2$, therefore $A = A(t)$, $B = B(t)$, etc. holds. Gauge invariance (or current conservation) $\partial^\mu J_\mu = 0$ imposes that

$$0 = \langle p(P')|\partial^\mu J_\mu(0)|p(P)\rangle = i(P'-P)^\mu \langle p(P')|J_\mu(0)|p(P)\rangle \quad :\Delta^\mu \bar{\psi}(P')\Gamma_\mu \psi(P) = 0. \tag{2.10}$$

Inserting Γ_μ from (2.9) into (2.10) gives $E = -D$ and $C = B$. Hence the four-current becomes

$$\bar{\psi}(P')\Gamma_\mu(P',P)\psi(P) = \bar{\psi}(P')\left[A(t)\gamma_\mu + B(t)(P'+P)_\mu + iD(t)\sigma_{\mu\nu}(P'-P)^\nu\right]\psi(P). \tag{2.11}$$

In order to connect the transition current (operator) to physics observables we must demand that it is Hermitian. For (2.11) to be invariant under the transformation $(...)^\dagger|_{P_\mu \to P'_\mu}$, i.e., (2.11) to be equal to its own conjugate transpose, then A, B, and D must be real. Finally, using the Gordon decomposition identity $\bar{\psi}(P')\gamma_\mu\psi(P) = \bar{\psi}(P')\left[\frac{(P'+P)_\mu}{2M_p} + \frac{i\sigma_{\mu\nu}(P'-P)^\nu}{2M_p}\right]\psi(P)$, the transition current is usually written as [40]

$$\bar{\psi}(P')\Gamma_\mu(P',P)\psi(P) = \bar{\psi}(P')\left[F_1(t)\gamma_\mu + F_2(t)\frac{i\sigma_{\mu\nu}\Delta^\nu}{2M_p}\right]\psi(P). \tag{2.12}$$

The quantities $F_1(t)$ and $F_2(t)$ are combinations of $A(t)$, $B(t)$, and $D(t)$ and are called the Dirac and Pauli form factors of the proton, respectively.

The pseudovector (axial) and pseudoscalar form factors, $g_A(t)$ and $g_P(t)$, respectively, are defined analogously, starting from (2.1), by inserting γ_5 in the interaction potential, i.e., $\gamma^\mu A_\mu \to \gamma^\mu\gamma_5 A_\mu$, or replacing the four-vector with the axial four-vector (pseudovector) current in (2.6), i.e., $J^\mu \to J^{\mu 5} = (+e)\bar{\Psi}_f\gamma^\mu\gamma_5\Psi_i$ (with $(+e)$ for the proton). The resulting four-current (or matrix element) is parameterised in the following way

$$\bar{\psi}(P')\Gamma_{\mu 5}(P',P)\psi(P) = \bar{\psi}(P')\left[g_A(t)\gamma_\mu\gamma_5 + g_P(t)\frac{\gamma_5\Delta_\mu}{2M_p}\right]\psi(P). \tag{2.13}$$

2.3 Scattering Amplitude and Cross Section

Elastic electron–proton scattering can be described by assuming that the electric charge of the electron creates a potential by which the proton is scattered. The particles interact via exchange of a virtual photon (in the one-photon-exchange approximation). The electron four-vector potential has the form $A^\mu(x) = -\frac{1}{t}\langle e^-(l')|J^\mu(x)|e^-(l)\rangle$. Inserting the latter into (2.2), replacing J_μ in (2.2) with the proton current $\langle p(P')|J_\mu(x)|p(P)\rangle$, and using the relation (2.7), we get for the S-matrix element of the scattering process [40]

$$\begin{aligned} S &\sim i\int d^4x\, \langle p(P')|J_\mu(x)|p(P)\rangle \left(-\frac{1}{t}\right) \langle e^-(l')|J^\mu(x)|e^-(l)\rangle \\ &\sim i\int d^4x\, \langle p(P')|J_\mu(0)|p(P)\rangle\, e^{-i(P-P')\cdot x} \left(-\frac{1}{t}\right) \langle e^-(l')|J^\mu(0)|e^-(l)\rangle\, e^{-i(l-l')\cdot x} \\ &\sim i(2\pi)^4\delta^{(4)}(l+P-l'-P')\mathcal{A}, \end{aligned} \tag{2.14}$$

where $\left(-\frac{1}{t}\right)$ with $t = (l'-l)^2 = (P'-P)^2$ corresponds to the virtual-photon propagator, the scattering amplitude $\mathcal{A}$ is given by the current-current coupling connected with the virtual-photon propagator

$$\mathcal{A} = \langle e^-(l')|J^\mu(x)|e^-(l)\rangle \left(-\frac{1}{t}\right) \langle p(P')|J_\mu(x)|p(P)\rangle, \tag{2.15}$$

and the Dirac delta function (in its Fourier-transform representation),

$$\delta^{(4)}(l+P-l'-P') = \int \frac{d^4x}{(2\pi)^4}\, e^{-i(l+P-l'-P')\cdot x}, \tag{2.16}$$

accounts for four-momentum conservation in the process.

The cross section for the electron-proton scattering process is defined as [40]

$$d\sigma \sim (2\pi)^4\delta^{(4)}(l+P-l'-P')\frac{d^3l'}{(2\pi)^3 2l'_0}\frac{d^3P'}{(2\pi)^3 2P'_0}\,|\mathcal{A}|^2, \quad |\mathcal{A}|^2 = \mathcal{A}^*\mathcal{A} = L^{\mu\nu}W_{\mu\nu}, \tag{2.17}$$

where the leptonic and hadronic tensors, $L^{\mu\nu}$ and $W_{\mu\nu}$, respectively, are given by (see (2.14))

$$L^{\mu\nu} = \langle e^-(l')|J^\mu(0)|e^-(l)\rangle^*\langle e^-(l')|J^\mu(0)|e^-(l)\rangle, \tag{2.18}$$

$$W_{\mu\nu} = \langle p(P')|J_\mu(0)|p(P)\rangle^*\langle p(P')|J_\mu(0)|p(P)\rangle. \tag{2.19}$$

The leptonic tensor contains all the information about the electron probe, which can be described in perturbative QED. It is given by [40]

$$L^{\mu\nu} = 2[l^\mu l'^\nu + l^\nu l'^\mu + (m_e^2 - l\cdot l')g^{\mu\nu}], \tag{2.20}$$

where m_e is the electron mass and $g^{\mu\nu}$ is the metric tensor.

2.4 Hadronic Tensor

We focus on the hadronic tensor $W_{\mu\nu}$ (2.19), which contains the information on the proton target. For the case of an electron–proton reaction in which the proton undergoes transition into a final state χ with four-momentum P_χ, the hadronic tensor can be written as [8]

$$\begin{aligned} 2M_pW_{\mu\nu} =& \frac{1}{2\pi}\sum_\chi \int \frac{d^3P_\chi}{(2\pi)^3 2P^0_\chi}(2\pi)^4\delta^{(4)}(q+P-P_\chi) \\ & \times \langle p(P)|J_\mu(0)|\chi(P_\chi)\rangle\,\langle\chi(P_\chi)|J_\nu(0)|p(P)\rangle, \end{aligned} \tag{2.21}$$

where $q = l - l'$ is here the four-momentum of the virtual photon. Notice that in (2.21) the state χ is integrated over since, e.g., in inclusive processes χ can be any final state which remains undetected. By Fourier transforming the delta function (see, e.g., (2.16)), translating one of the current operators (see, e.g., (2.7)), and using the completeness relation

$$\sum_\chi |\chi(P_\chi)\rangle\langle\chi(P_\chi)| = 1, \tag{2.22}$$

we can write the hadronic tensor (2.21) as

$$\begin{aligned} 2M_pW_{\mu\nu} &= \frac{1}{2\pi}\int d^4x\, e^{iq\cdot x}\langle p(P)|J_\mu(x)J_\nu(0)|p(P)\rangle \\ &= \frac{1}{2\pi}\int d^4x\, e^{iq\cdot x}\langle p(P)|[J_\mu(x), J_\nu(0)]|p(P)\rangle, \end{aligned} \tag{2.23}$$

where the commutator gives $[J_\mu(x), J_\nu(0)] = J_\mu(x)J_\nu(0) - J_\nu(0)J_\mu(x)$. The contribution from the second term of the commutator vanishes because four-momentum conservation requires $E_\chi < M_p$, however, such a state χ does not exist since the proton is the state of lowest energy.

Now we apply the concepts of the quark-parton model, which assumes that at sufficiently high energies ($Q^2 = -q^2 \to \infty$) the scattering of the electron takes place off a quark of mass m inside the proton. Hence the final state χ can be split in a quark ψ plus a state X with momentum P_X. Then J_μ in (2.21) is the quark current, which by analogy with (2.3), is given by

$$J_\mu(x) = (e_q)\bar{\psi}(k')\gamma_\mu\psi(k)\, e^{-i(k-k')\cdot x}, \quad \psi(k)\bar{\psi}(k) = (\not{k} + m),\ \not{k} = \gamma \cdot k = \gamma^\mu k_\mu, \tag{2.24}$$

where (e_q) is the quark fractional charge. Considering the electron-quark interaction at tree level and omitting the antiquark contribution, the hadronic tensor can be written as [8]

$$\begin{aligned} 2M_pW_{\mu\nu} =& \frac{1}{2\pi}\sum_q e_q^2 \sum_X \int \frac{d^3P_X}{(2\pi)^3 2P_X^0} \int \frac{d^3k}{(2\pi)^3 2k^0}(2\pi)^4\delta^{(4)}(P + q - k - P_X) \\ & \times \langle p(P)|\bar{\psi}^j(0)|X(P_X)\rangle\langle X(P_X)|\psi^i(0)|p(P)\rangle\gamma_\mu^{jn}(\not{k} + m)^{nl}\gamma_\nu^{li}, \end{aligned} \tag{2.25}$$

where k is the momentum of the struck quark. The integration over the phase-space of the final-state quark can be replaced by a four-dimensional integral with an on-shell condition

$$\frac{d^3k}{2k^0} \to d^4k\,\delta(k^2 - m^2)\,\theta(k^0 - m), \tag{2.26}$$

where θ is the Heaviside step function. We introduce the momentum $p = k - q$ and Fourier transform the delta function in (2.25) (see, e.g., (2.16) with the space-variable x replaced with z). The $e^{-i(P-P_X)\cdot z}$ part of the exponential is then used to perform a translation of one of the field operators (see, e.g., (2.7)), and finally the completeness relation (see, e.g., (2.22)) is used to eliminate the unobserved X states, so that the hadronic tensor (2.25) can be rewritten as

$$\begin{aligned} 2M_pW_{\mu\nu} =& \sum_q e_q^2 \int d^4p\,\delta((p + q)^2 - m^2)\theta(p^0 + q^0 - m) \\ & \times \int \frac{d^4z}{(2\pi)^4}\, e^{-ip\cdot z}\langle p(P)|\bar{\psi}^j(z)\psi^i(0)|p(P)\rangle\gamma_\mu^{jn}(\not{p} + \not{q} + m)^{nl}\gamma_\nu^{li}. \end{aligned} \tag{2.27}$$

The part of the hadronic tensor in (2.27), denoted as [8, 48]

$$\Phi^{ij}(p, P) = \int \frac{d^4z}{(2\pi)^4} e^{-ip\cdot z}\langle p(P)|\bar{\psi}^j(z)\psi^i(0)|p(P)\rangle, \tag{2.28}$$

is the so called quark-quark correlation function, which describes the non-perturbative correlation between quarks inside the proton. We replace the implicit sum over the repeated indices i, l, n, j in (2.27) with the trace Tr to obtain

$$2M_pW_{\mu\nu} = \sum_q e_q^2 \int d^4p\,\delta((p + q)^2 - m^2)\theta(p^0 + q^0 - m)\,\mathrm{Tr}[\Phi(p, P)\gamma_\mu(\not{p} + \not{q} + m)\gamma_\nu]. \tag{2.29}$$

2.5 Light-Cone Representation

Now we use the light-cone coordinates of the four-vectors P, p, and q in (2.29) as defined, e.g., in the right-hand side of (2.30) for any four-vector a,

$$a^\mu(a^0, a^1, a^2, a^3) \to a^\mu = [a^-, a^+, a_\perp] = [\frac{a^0 - a^3}{\sqrt{2}}, \frac{a^0 + a^3}{\sqrt{2}}, a^1, a^2], \tag{2.30}$$

where a^+, a^-, and $a_\perp = (a^1, a^2)$ are referred to as the plus, minus, and transverse components of a^μ. The product of a with a four-vector b, and with a Dirac matrix γ is given by

$$a \cdot b = a^+ b^- + a^- b^+ - a_\perp \cdot b_\perp, \quad \not{a} = \gamma \cdot a = \gamma^+ a^- + \gamma^- a^+ - \gamma_\perp \cdot a_\perp. \tag{2.31}$$

The light-cone components of the proton four-momentum P, the virtual photon four-momentum q, and the quark four-momentum p are parameterised [8, 48] here as

$$P^\mu = [\frac{M_p^2}{2P^+}, P^+, 0_\perp], \quad q^\mu = [\frac{Q^2}{2x_B P^+}, -x_B P^+, 0_\perp], \quad p^\mu = [\frac{p^2 + |p_\perp|^2}{2xP^+}, xP^+, p_\perp], \tag{2.32}$$

$$\text{where} \quad x = \frac{p^+}{P^+}, \quad x_B = \frac{p}{P} = \frac{Q^2}{2P \cdot q}. \tag{2.33}$$

It is also assumed that the quark virtuality, p^2, and its squared transverse momentum, $|p_\perp|^2$, are small compared with the hard scale Q^2. In this case the relevant component of the quark momentum is p^+, which is given as a fraction xP^+ of the momentum P^+ of the fast-moving proton.

2.5.1 Hadronic Tensor

Inserting the approximate expression for the delta function (where $\frac{1}{Q}$-suppressed terms are neglected)

$$\delta((p+q)^2 - m^2) \approx \frac{1}{2P \cdot q}\,\delta(x - x_B), \tag{2.34}$$

and replacing d^4p with

$$d^4p = d^2p_\perp dp^- dp^+ = d^2p_\perp dp^- dx\, P^+ \tag{2.35}$$

in (2.29) for the the hadronic tensor, we get

$$\begin{aligned} 2M_p W_{\mu\nu} &\approx \sum_q e_q^2 \int d^2p_\perp dp^- dx\, \frac{P^+}{2P \cdot q}\,\delta(x - x_B)\,\mathrm{Tr}[\Phi(p,P)\gamma_\mu(\not{p} + \not{q} + m)\gamma_\nu] \\ &= \sum_q e_q^2 \frac{1}{2}\,\mathrm{Tr}[\Phi(x_B)\gamma_\mu \frac{P^+}{P \cdot q}(\not{p} + \not{q} + m)\gamma_\nu], \end{aligned} \tag{2.36}$$

where x_B is the Bjorken scaling variable defined in (2.33). The second line in (2.36) is obtained by integrating the delta function and introducing the integrated correlation function [8]

$$\Phi^{ij}(x) = \int d^2p_\perp dp^-\, \Phi^{ij}(p,P)|_{p^+ = xP^+} = \int \frac{dz^-}{2\pi}\, e^{-ip\cdot z}\langle p(P)|\bar{\psi}^j(z)\psi^i(0)|p(P)\rangle|_{z^+=0, z_\perp=0}. \tag{2.37}$$

Finally, from the outgoing quark momentum, $p + q$, only the minus component can be selected to obtain from (2.36) the final form for the hadronic tensor [8]

$$2M_p W_{\mu\nu} \approx \sum_q e_q^2 \frac{1}{2}\,\mathrm{Tr}[\Phi(x_B)\gamma_\mu \gamma^+ \gamma_\nu]. \tag{2.38}$$

The following relations are used that lead from (2.36) to (2.38)

$$\frac{P^+}{P \cdot q}(\not{p} + \not{q} + m) \approx \frac{P^+}{P \cdot q}\gamma^+ (p+q)^- \approx \frac{P^+}{P \cdot q}\gamma^+ \frac{Q^2}{2xP^+} = \gamma^+. \tag{2.39}$$

The minus component is the dominant one in the so-called infinite momentum frame, where $p^- + q^-$ is of the order of $Q = \sqrt{-q^2}$, while $p^+ + q^+$, and $p_\perp$ and m are of the order of 1. Moreover, it can be checked that in any collinear frame the dominant terms in the hadronic tensor arise only from the combination of plus component in the correlation function and minus components in the outgoing quark momentum.

A graphical representation of the hadronic tensor (2.29), (2.38) (i.e., a bilocal forward matrix element) is given by the so-called handbag diagram in Fig. 2.1.

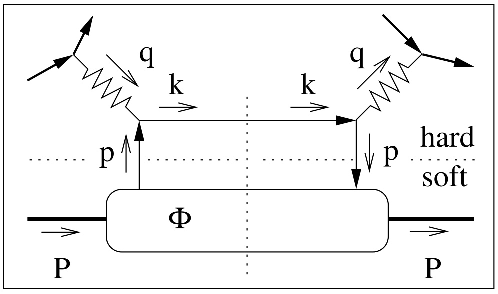

Figure 2.1: PDFs: $P^+ \int \frac{dz^-}{2\pi} e^{ip^+z^-} \langle p(P)|\bar{\psi}(\frac{-z}{2}\gamma^+\psi(\frac{z}{2}))|p(P) = \bar{\psi}(P)\gamma^+\psi(P)f_1(x)$

2.5.2 Elastic Form Factors

We can replace the proton four-momenta P and P' with their light-cone plus components also for the case of exclusive processes, in which the final state is detected. By analogy with (2.9) for the vertex function Γ_μ, we get for the light-cone representation

$$\Gamma^+ = A\gamma^+ + BP'^+ + CP^+ + iD\sigma^{+i}P_i + iE\sigma^{+i}P_i, \quad \sigma^{+i} = \frac{1}{2}i[\gamma^+, \gamma^i] = \frac{1}{2}i(\gamma^+\gamma^i - \gamma^i\gamma^+), \tag{2.40}$$

where $i = 1, 2$ is the transverse index of the light-cone four-vectors. With the parameterisation (2.40), the matrix elements of the light-cone four-vector and axial four-vector currents, $J^+(0) = \bar{\psi}(0)\gamma^+\psi(0)$ and $J^{+5}(0) = \bar{\psi}(0)\gamma^+\gamma_5\psi(0)$, respectively, are written as

$$\begin{aligned} \langle p(P')|\bar{\psi}(0)\gamma^+\psi(0)|p(P)\rangle &= \bar{\psi}(P')\left[\gamma^+ F_1(t) + \frac{i\sigma^{+i}\Delta_i}{2M_p} F_2(t)\right]\psi(P), && (2.41)\\ \langle p(P')|\bar{\psi}(0)\gamma^+\gamma_5\psi(0)|p(P)\rangle &= \bar{\psi}(P')\left[\gamma^+\gamma_5\, g_A(t) + \frac{\gamma_5\Delta^+}{2M_p} g_P(t)\right]\psi(P). && (2.42) \end{aligned}$$

These are the analogs of (2.12) and (2.13), respectively. A graphical representation of the (local non-forward) matrix element (2.41) is given in Fig. 2.2.

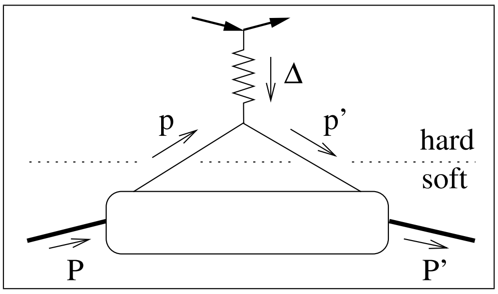

Figure 2.2: FFs: $\langle p(P')|\bar{\psi}(0)\gamma^+\psi(0)|p(P)\rangle = \bar{\psi}(P')[\gamma^+F_1(t) + \frac{i\sigma^{+i}\Delta_i}{2M_p}F_2(t)]\psi(P)$

2.5.3 Parton Distribution Functions

We take a closer look at the bilocal ($z_1 \neq z_2$) quark-field operator

$$\bar{\psi}(z_2)G\psi(z_1) = \psi^\dagger(z_2)(\gamma^0 G)\psi(z_1), \tag{2.43}$$

which occurs in the definitions of the hadronic tensor (2.38) and, in its localised form with $z_1 = z_2$, of the electromagnetic form factors (2.41), (2.42). The matrix G can be $G = \gamma^+$ (see (2.38), (2.41)), $\gamma^+\gamma_5$ (see (2.42)), $i\sigma^{+i}\gamma_5$ (see (2.49) below), or another combination of Dirac matrices. In the chiral (Weyl) representation defined by the 4×4 matrices [48]

$$\gamma^0 = \begin{pmatrix} 0 & 1 \\ 1 & 0 \end{pmatrix}, \quad \gamma^j = \begin{pmatrix} 0 & -\sigma^j \\ \sigma^j & 0 \end{pmatrix}, \quad \gamma_5 = \begin{pmatrix} 1 & 0 \\ 0 & -1 \end{pmatrix}, \tag{2.44}$$

where σ^j ($j = 1, 2, 3$) are the Pauli matrices, the quark four-spinor fields ψ and their product $\psi^\dagger\psi$ take the explicit form [48]

$$\psi = \begin{pmatrix} \phi_R \\ \chi_R \\ \chi_L \\ \phi_L \end{pmatrix}, \quad \psi^\dagger\psi = \begin{pmatrix} \phi_R^\dagger\phi_R & \chi_R^\dagger\phi_R & \chi_L^\dagger\phi_R & \phi_L^\dagger\phi_R \\ \phi_R^\dagger\chi_R & \chi_R^\dagger\chi_R & \chi_L^\dagger\chi_R & \phi_L^\dagger\chi_R \\ \phi_R^\dagger\chi_L & \chi_R^\dagger\chi_L & \chi_L^\dagger\chi_L & \phi_L^\dagger\chi_L \\ \phi_R^\dagger\phi_L & \chi_R^\dagger\phi_L & \chi_L^\dagger\phi_L & \phi_L^\dagger\phi_L \end{pmatrix}, \tag{2.45}$$

where the (chirality) subscripts R and L denote the right- and left-handed 'good' ϕ and 'bad' χ light-cone components of the fields. At given light-cone time, e.g., $z^+ = 0$, ϕ are the independent dynamical fields of QCD, while χ are given in terms of ϕ and the potential $A_\perp$. The 'effective twist' of a matrix element in (2.45) depends on whether it consists of 'good', or 'bad', or both components of the quark fields. The elements $\phi^\dagger\phi$, $\phi^\dagger\chi$ or $\chi^\dagger\phi$, and $\chi^\dagger\chi$ give rise to twist-2 (leading twist), twist-3, and twist-4 operators, respectively.

Using (2.45) and the matrices [48]

$$\gamma^0\gamma^+ \sim \begin{pmatrix} 1 & 0 & 0 & 0 \\ 0 & 0 & 0 & 0 \\ 0 & 0 & 0 & 0 \\ 0 & 0 & 0 & 1 \end{pmatrix}, \gamma^0\gamma^+\gamma_5 \sim \begin{pmatrix} 1 & 0 & 0 & 0 \\ 0 & 0 & 0 & 0 \\ 0 & 0 & 0 & 0 \\ 0 & 0 & 0 & -1 \end{pmatrix}, \gamma^0 i\sigma^{+1(2)}\gamma_5 \sim (i)\begin{pmatrix} 0 & 0 & 0 & (-)1 \\ 0 & 0 & 0 & 0 \\ 0 & 0 & 0 & 0 \\ 1 & 0 & 0 & 0 \end{pmatrix}, \tag{2.46}$$

we obtain the following expressions for the leading-twist bilocal quark-field operators (2.43) (see also [8, 48])

$$\begin{aligned} \mathrm{Tr}(\Phi\gamma^+) \sim \bar{\psi}(z_1)\gamma^+\psi(z_2) \quad &\sim \quad \phi_R^\dagger(z_1)\phi_R(z_2) + \phi_L^\dagger(z_1)\phi_L(z_2) \sim f_1(x) \equiv q(x), & (2.47) \\ \mathrm{Tr}(\Phi\gamma^+\gamma_5) \sim \bar{\psi}(z_1)\gamma^+\gamma_5\psi(z_2) \quad &\sim \quad \phi_R^\dagger(z_1)\phi_R(z_2) - \phi_L^\dagger(z_1)\phi_L(z_2) \sim g_1(x) \equiv \Delta q(x), & (2.48) \\ \mathrm{Tr}(\Phi i\sigma^{+i}\gamma_5) \sim \bar{\psi}(z_1)i\sigma^{+i}\gamma_5\psi(z_2) \quad &\overset{i=1,2}{\sim} \quad \phi_R^\dagger(z_1)\phi_L(z_2) - \phi_L^\dagger(z_1)\phi_R(z_2) \sim h_1(x) \equiv \delta q(x), & (2.49) \end{aligned}$$

where, according to the the chiral structure of the expressions with quark fields ϕ, the function $f_1(x)$ is the unpolarised parton distribution, $g_1(x)$ is the (chiral-even) parton helicity distribution, and $h_1(x)$ is the (chiral-odd) transversity distribution; the latter is interpreted in the transverse-spin representation of the γ matrices (i.e., if one changes basis from states of definite helicity to states of definite transversity).

2.6 Generalised Parton Distributions

The diagonal ($P' = P$) bilocal ($z_1 = 0$, $z_2 = z$) quark-quark correlation function (2.28) of quark fields, and the non-diagonal ($P' \neq P$) local ($z_1 = z_2 = 0$) matrix elements (2.41) and (2.42) of electromagnetic currents can be generalised to define the following non-diagonal bilocal quark-quark correlation function [48]

$$\Phi'_{ij}(p,P,\Delta) = \int \frac{d^4z}{(2\pi)^4} e^{-i\bar{p}\cdot z} \langle p(P')|\bar{\psi}_j(\frac{-z}{2})\psi_i(\frac{z}{2})|p(P)\rangle, \tag{2.50}$$

where $\bar{p} = \frac{p+p'}{2}$. This function describes probes which are absent in nature, e.g., a quark with momentum p being taken out from the initial proton state $|p(P)\rangle$ and reinserted with a different momentum p' to form the final proton $\langle p(P')|$. In (2.50) the initial and final proton states are not identical ($P' \neq P$). Notice that $\Phi'_{ij}(p,P,\Delta)$ is defined on the level of the amplitude of the process, unlike $\Phi^{ij}(p,P)$ (see (2.28)) which is defined on the cross section level.

From the quark-quark correlation (2.50) the generalised parton distributions (GPDs) are defined as the Dirac projections, $\mathrm{Tr}(\Phi' G)$, integrated over the light-like momentum components, $d\bar{p}^-$ and $d^2\bar{p}_\perp$, thus constraining the bilocality of the quark-field operators to a light-like distance in minus direction. The leading-twist projection with γ^+ defines two functions, $H(x,\xi,t)$ and $E(x,\xi,t)$, corresponding to proton helicity non-flip and helicity-flip, respectively, [48],

$$\begin{aligned}\bar{P}^+ \int d\bar{p}^- d^2\bar{p}_\perp \mathrm{Tr}(\Phi'\gamma^+)|_{\bar{p}^+=x\bar{P}^+} &= \bar{P}^+ \int \frac{dz^-}{2\pi}\, e^{-i\bar{p}^+z^-} \langle p(P')|\bar{\psi}(\frac{-\bar{z}}{2})\gamma^+\psi(\frac{\bar{z}}{2})|p(P)\rangle|_{z^+=0,z_\perp=0} \\ &= \bar{\psi}(P')\left[\gamma^+ H(x,\xi,t) + \frac{i\sigma^{+i}\Delta_i}{2M_p}E(x,\xi,t)\right]\psi(P),\end{aligned} \tag{2.51}$$

where $\bar{P} = \frac{P'+P}{2}$ and $\bar{z} = [0, z^-, 0_\perp]$. The projection with $\gamma^+\gamma_5$ defines two more functions, $\widetilde{H}(x,\xi,t)$ and $\widetilde{E}(x,\xi,t)$, corresponding to quark helicity non-flip and helicity flip, respectively, [48],

$$\begin{aligned}\bar{P}^+ \int d\bar{p}^- d^2\bar{p}_\perp \mathrm{Tr}(\Phi'\gamma^+\gamma_5)|_{\bar{p}^+=x\bar{P}^+} &= \bar{P}^+ \int \frac{dz^-}{2\pi}\, e^{-i\bar{p}^+z^-} \langle p(P')|\bar{\psi}(\frac{-\bar{z}}{2})\gamma^+\gamma_5\psi(\frac{\bar{z}}{2})|p(P)\rangle|_{z^+=0,z_\perp=0} \\ &= \bar{\psi}(P')\left[\gamma^+\gamma_5 \widetilde{H}(x,\xi,t) + \frac{\gamma_5\Delta^+}{2M_p}\widetilde{E}(x,\xi,t)\right]\psi(P).\end{aligned} \tag{2.52}$$

The GPDs H, E, $\widetilde{H}$, and $\widetilde{E}$ depend on the (average) momentum fraction $x = \frac{(p+p')^+}{(P+P')^+} = \frac{\bar{p}^+}{\bar{P}^+}$, the skewness $\xi = \frac{(P-P')^+}{(P+P')^+}$ characterising the change of momentum fraction between initial and final quark, and the squared momentum transfer $t = \Delta^2 = (P'-P)^2$. These GPDs are hybrid objects, which combine properties of the parton distributions (PDFs), $f_1(x)$ and $g_1(x)$, and the elastic form factors (FFs), $F_1(t)$, $F_2(t)$, $g_A(t)$, and $g_P(t)$. A graphical representation of the bilocal non-forward matrix element (2.51) is given in Fig. 2.3.

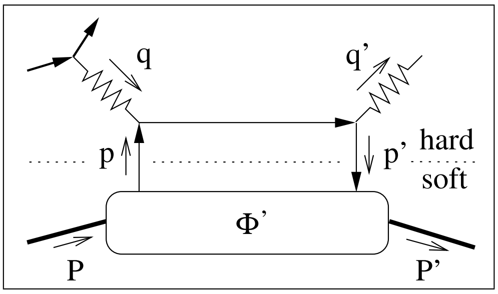

Figure 2.3: GPDs: $\bar{P}^+ \int \frac{dz^-}{2\pi}\, e^{i\bar{p}^+z^-} \langle p(P')|\bar{\psi}(\frac{-\bar{z}}{2})\gamma^+\psi(\frac{\bar{z}}{2})|p(P)\rangle = \bar{\psi}(P')[\gamma^+ H(x,\xi,t) + \frac{i\sigma^{+i}\Delta_i}{2M_p}E(x,\xi,t)]\psi(P)$

Chapter 3

Exclusive Pion Production

The theoretical description of hard exclusive electroproduction of a single pion in the process $e^+p \rightarrow e^{+\prime}n\pi^+$ is outlined in this chapter. The basic steps and formulas are given, concerning the kinematics of the process, the factorisation theorem, the generalised parton distributions, and the transverse-target single-spin azimuthal asymmetry. The equations throughout the sections are consistent up to certain numerical factors or up to a particular definition of the kinematic variables which may vary in the literature [10, 23, 26, 27, 33, 39], on which this presentation is based.

3.1 Quantities of Physical Interest

3.1.1 Kinematics

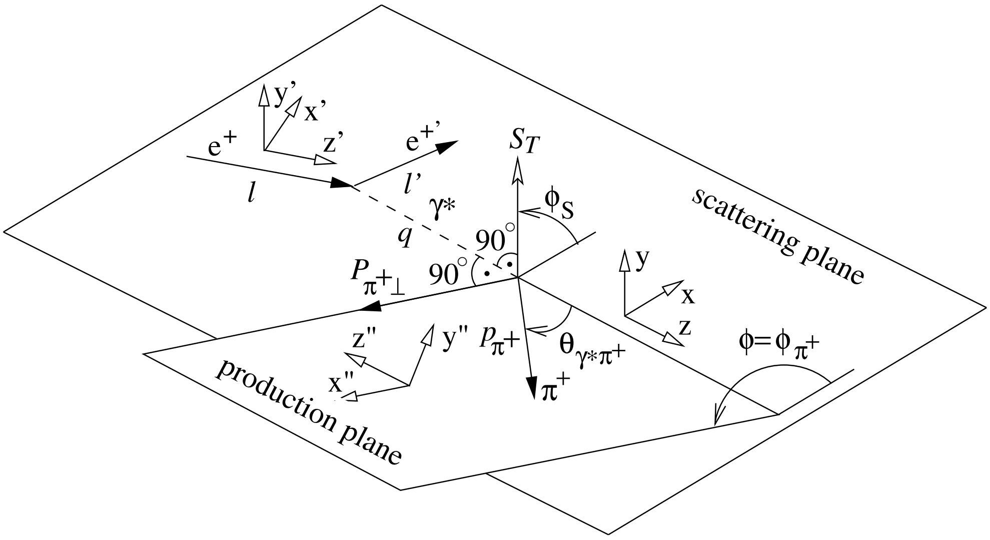

Figure 3.1: Kinematics of the exclusive pion electroproduction process (3.1) in the proton-target rest frame (see also Table 3.1). $P_{\pi^+\perp}$ and S_T, respectively, are the components of p_{π^+} and of the target polarisation vector S (not shown) perpendicular, i.e. at 90° angle, to q. Denoted by ϕ_{π^+} and ϕ_S, respectively, are the azimuthal angles of p_{π^+} and S in the coordinate system with axes x, y, z, in accordance with the Trento conventions [9]. A detailed discussion of this process is given in [27].

We consider exclusive production of a single pion in positron-proton scattering [27] (Fig. 3.1)

$$e^+(l) + p(P) \rightarrow e^{+\prime}(l') + n(P') + \pi^+(p_{\pi^+}) \tag{3.1}$$

kinematic variable	numeric value ’≈’ if $m_{e^+} = m_e \approx 0$ ’*lab*’ = proton rest frame	explanation
M_p	$938.272029 \pm 0.000080\,\mathrm{MeV}$ [70]	proton mass
M_n	$939.565360 \pm 0.000081\,\mathrm{MeV}$ [70]	neutron mass
m_{π^+}	$139.57018 \pm 0.00035\,\mathrm{MeV}$ [70]	π^+ mass
m_e	$510.998918 \pm 0.000044\,\mathrm{keV}$ [70]	electron mass
E	$E_{e^+} = 27.5699997\,\mathrm{GeV}$	beam energy
l	$\overset{lab}{=} q_{e^+} = (E, 0, 0, l_z) \approx (E, 0, 0, E)$	beam positron four-momentum
l'	$\overset{lab}{=} q_{e^{+\prime}} = (E', l'_x, l'_y, l'_z)$	scattered positron four-momentum
P	$\overset{lab}{=} q_p = (M_p, 0, 0, 0)$	target proton four-momentum
P'	$\overset{lab}{=} q_n = (E'_n, P'_x, P'_y, P'_z)$	recoiling neutron four-momentum
p_{π^+}	$\overset{lab}{=} q_{\pi^+} = (E_{\pi^+}, p_x, p_y, p_z)$	produced π^+ four-momentum
$\Theta_{e^{+\prime}}$	angle between l and l'	positron polar scattering angle
S-axis	$\overset{lab}{=} (0, 0, -1, 0)$	target polarisation axis
$q = l - l'$	$\overset{lab}{=} q_{e^+} - q_{e^{+\prime}} = q_{\gamma^*} = (E_{\gamma^*}, q_x, q_y, q_z)$	virtual photon four-momentum, four-momentum transfer
$Q^2 \equiv -q^2 = -(l - l')^2$	$\overset{lab}{\approx} 4EE' \sin^2 (\frac{\Theta_{e^{+\prime}}}{2})$	squared virtual photon four-momentum
$s = (l + P)^2$	$\overset{lab}{=} (q_{e^+} + q_p)^2 \approx M_p^2 + 2M_pE$	invariant centre-of-mass energy
$t = (q - p_{\pi^+})^2 = (P - P')^2$	$\overset{lab}{=} (q_{\gamma^*} - q_{\pi^+})^2$ $\overset{lab}{=} (q_p - q_n)^2 = M_p^2 + M_n^2 - 2M_pE'_n$	invariant transverse four-momentum transfer, squared four-momentum exchanged between the virtual photon and the proton
$\nu = \frac{P\cdot q}{M_p}$	$\overset{lab}{=} E - E' = E_{\gamma^*}$	positron energy loss, energy transfer
$y = \frac{P\cdot q}{P\cdot l}$	$\overset{lab}{=} \frac{\nu}{E}$	inelasticity, normalised/relative energy transfer of the virtual photon, fraction of the positron energy taken by the virtual photon
$x = x_B = \frac{Q^2}{2P\cdot q}$	$\overset{lab}{=} \frac{Q^2}{2M_p\nu}$	Bjorken scaling variable, fraction of the proton momentum carried by the struck quark
$W^2 = (q + P)^2$	$\overset{lab}{=} (q_{\gamma^*} + q_p)^2 = M_p^2 + 2M_p\nu - Q^2 = M_p^2 + \frac{1-x}{x}Q^2$	invariant photon-nucleon centre-of-mass energy, squared mass of the hadronic final state
$z = \frac{P\cdot p_{\pi^+}}{P\cdot q}$	$\overset{lab}{=} \frac{E_{\pi^+}}{\nu}$	fraction of energy carried by π^+
$M_n^2 = P'^2 = (q + P - p_{\pi^+})^2$	$\overset{lab}{=} (q_{\gamma^*} + q_p - q_{\pi^+})^2$	invariant squared missing mass

Table 3.1: Standard kinematic variables for deep inelastic scattering. The corresponding four-vectors and/or the expression in the laboratory frame for exclusive pion production are given, as well as the name of each variable. The description of the exclusive process requires three independent variables, e.g., x, Q^2, and t.

with four-momenta given in parentheses. The symbols e^+ and $e^{+\prime}$ denote the incoming and the scattered beam positron, respectively, p the target proton, n the recoiling neutron, and π^+ the produced positively charged pion. The process can be described by the standard kinematic variables for deep inelastic scattering, e.g., Q^2, x, and y, where only two of them are independent, plus an additional variable t appearing in the description of elastic scattering (Section 2.2). The kinematic variables are defined in Table 3.1. The symbol x often appears in the following either as the Bjorken variable x_B or as the parameter of the GPDs $x \in (-1, 1)$ (see (2.33)). We note that the discussion in this section applies also to the case of semi-inclusive deep inelastic scattering, i.e., if $n(P')$ in (3.1) is replaced by an inclusive system of hadrons $X(P')$. No kinematic approximations are made before Section 3.1.3 except for neglecting the positron mass, $m_{e^+} \approx 0$.

The hard positron-proton interaction proceeds predominantly via the exchange of one virtual photon γ^*, so the physics process considered is $\gamma^* p \to n\pi^+$. When π^+ is measured, an additional relevant parameter is the angle between the plane defined by e^+ and $e^{+\prime}$ (scattering plane) and the one defined by γ^* and π^+ (production plane), namely, the azimuthal angle $\phi \equiv \phi_{\pi^+}$. In addition, the azimuthal angle ϕ_S between the scattering plane and the target polarisation vector can be defined for a transversely polarised target. The angles ϕ and ϕ_S are computed in this work from the expressions

$$\phi = \arccos\left(\frac{(\vec{q}\times\vec{l})\cdot(\vec{q}\times\vec{p}_{\pi^+})}{|(\vec{q}\times\vec{l})\cdot(\vec{q}\times\vec{p}_{\pi^+})|}\right)\frac{(\vec{q}\times\vec{l})\cdot\vec{p}_{\pi^+}}{|(\vec{q}\times\vec{l})\cdot\vec{p}_{\pi^+}|}, \tag{3.2}$$

$$\phi_S = \arccos\left(\frac{(\vec{q}\times\vec{l})\cdot(\vec{q}\times\vec{S})}{|(\vec{q}\times\vec{l})\cdot(\vec{q}\times\vec{S})|}\right)\frac{(\vec{q}\times\vec{l})\cdot\vec{S}}{|(\vec{q}\times\vec{l})\cdot\vec{S}|}, \tag{3.3}$$

where the target polarisation axis $\vec{S} = (0, -1, 0)$ is fixed in the proton rest frame, while the target polarisation vector is flipped parallel and antiparallel to this axis. The polar angle between the virtual photon and the produced pion, $\theta_{\gamma^*\pi^+}$, is given as

$$\theta_{\gamma^*\pi^+} = \arccos\left(\frac{\vec{q}\cdot\vec{p}_{\pi^+}}{|\vec{q}||\vec{p}_{\pi^+}|}\right). \tag{3.4}$$

In the rest frame, in which the proton is at rest, one can define three right-handed coordinate systems $C(x, y, z)$ and $C'(x', y', z')$, whose vertical axes are normal to the scattering plane, and $C''(x'', y'', z'')$, whose vertical axis is normal to the production plane, as shown in Fig. 3.1. The z' axis points along the e^+ direction, whereas z (z'') is parallel (anti-parallel) to the γ^* direction with x (x'') in the scattering (production) plane. C is defined in accordance with the Trento conventions [9]. C' coincides with the HERMES coordinate system (Section 4.3) where measurements are performed relative to the beam direction, whereas theoretical calculations are more conveniently carried out in C or C'' relative to the virtual-photon direction. The two coordinate systems C and C' are related via a rotation about the y axis by the polar angle $\theta \equiv \theta_{\gamma^*}$ between q and l given by

$$\sin\theta = \gamma\sqrt{\frac{1 - y - \frac{1}{4}y^2\gamma^2}{1+\gamma^2}}, \quad \gamma = \frac{2xM_p}{Q}. \tag{3.5}$$

Further we consider that the proton target in (3.1) is transversely polarised with respect to the positron beam, with P_T and $P_L \ll P_T$ the components of the target polarisation vector P perpendicular and parallel to the beam direction (z' in Fig. 3.1), respectively. The target polarisation vector with respect to the virtual photon in the C'' frame is given by

$$S \overset{C''}{=} \begin{pmatrix} S_T\cos(\phi-\phi_S) \\ S_T\sin(\phi-\phi_S) \\ S_L \end{pmatrix}, \qquad \begin{aligned} S_T &= \frac{\cos\theta}{\sqrt{1-\sin^2\theta\sin^2\phi_S}}P_T, \\ S_L &= \frac{\sin\theta\cos\phi_S}{\sqrt{1-\sin^2\theta\sin^2\phi_S}}P_T, \end{aligned} \tag{3.6}$$

where $\phi \equiv \phi_{\pi^+}$ and ϕ_S are the azimuthal angles in the C frame (Fig. 3.1). The coordinate system C'' is favoured in theoretical calculations for describing the $\gamma^* p$ process. In this coordinate system the spin density matrix of the proton target can be written as

$$\rho_{ji} = \frac{1}{2}(\delta_{ji} + \vec{S}\cdot\vec{\sigma}_{ji}) \overset{C''}{=} \frac{1}{2}\begin{pmatrix} 1+S_L & S_T e^{-i(\phi-\phi_S)} \\ S_T e^{i(\phi-\phi_S)} & 1-S_L \end{pmatrix}, \quad \chi_{+\frac{1}{2}} = \begin{pmatrix}1\\0\end{pmatrix}, \quad \chi_{-\frac{1}{2}} = \begin{pmatrix}0\\1\end{pmatrix}, \tag{3.7}$$

where the two-component spinors $\chi_{+\frac{1}{2}}$ and $\chi_{-\frac{1}{2}}$ (the eigenstates to $\vec{\sigma}^2$ and σ_z) specify the basis of the proton polarisation states in the $\gamma^* p$ centre-of-mass frame, the indices i, j denote the corresponding eigenvalues, i.e., the definite spin projections $+\frac{1}{2}$ and $-\frac{1}{2}$ along the z'' axis, and the right- and left-handed proton helicity in the $\gamma^* p$ centre-of-mass frame. The components of $\vec{\sigma}$ are the Pauli matrices.

3.1.2 Cross Section

The cross section for the process (3.1) can be written as

$$d\sigma^{e^+p\to e^{+\prime}n\pi^+} \sim L^{\nu\mu}W_{\mu\nu}\frac{d^3l'}{2E'}\frac{d^3p_{\pi^+}}{2E_{\pi^+}}\frac{d^3P'}{2E'_n}, \tag{3.8}$$

with a proportionality factor depending on the kinematic variables x, y, and Q^2. The leptonic tensor $L^{\nu\mu}$ is precisely calculable, while the hadronic tensor $W_{\mu\nu}$ reads

$$W_{\mu\nu} = \sum_{ij} \rho_{ji}\, \delta^{(4)}(P' + p_{\pi^+} - P - q) \sum_{spins} \langle p(i)|J_\mu(0)|n\pi^+\rangle\langle n\pi^+|J_\nu(0)|p(j)\rangle, \tag{3.9}$$

where J_μ is the hadronic part of the electromagnetic current. The sum $\sum_{ij}$ is over the target spin states $i, j = +\frac{1}{2}, -\frac{1}{2}$ and $\sum_{spins}$ is the sum over all polarisations in the final hadronic state, i.e., $n\pi^+$.

The polarisation vector ϵ_m for definite helicity $m = 0, +1, -1$ of the virtual photon is introduced as

$$\epsilon_0^\mu = \frac{1}{Q\sqrt{1+\gamma^2}}(q^\mu + \frac{Q^2}{P\cdot q}P^\mu), \quad \epsilon_{+1} = \frac{1}{\sqrt{2}}(0,-1,i,0), \quad \epsilon_{-1} = \frac{1}{\sqrt{2}}(0,1,i,0), \tag{3.10}$$

where γ is defined in (3.5) and the components of $\epsilon_{\pm 1}$ are given in coordinate system C'' (Fig. 3.1). Then the leptonic tensor $L^{\nu\mu}$ can be expanded as a linear combination of terms $\epsilon_n^\nu \epsilon_m^{\mu *}$ with coefficients forming the spin density matrix of the virtual photon. The coefficients depend on Q^2, on the beam polarisation P_{e^+}, on the azimuthal angle ϕ, and on the ratio of longitudinal to transverse virtual-photon fluxes ε. The flux of transverse virtual photons Γ_T and the ratio $\varepsilon = \frac{\Gamma_L}{\Gamma_T}$ [51] with Hand's convention [44] for the virtual-photon flux are given by

$$\Gamma_T(x(y), Q^2) = \Gamma_T(y, Q^2) = \frac{\alpha_{\mathrm{em}}}{2\pi}\frac{y^2}{1-\varepsilon}\frac{1-x}{x}\frac{1}{Q^2} = \frac{\alpha_{\mathrm{em}}y^2(2M_pEy - Q^2)}{2\pi Q^4}\frac{1}{1-\varepsilon}, \tag{3.11}$$

$$\varepsilon(x(y), Q^2) = \varepsilon(y, Q^2) = \frac{1}{1 + 2\frac{\nu^2+Q^2}{4EE'-Q^2}} = \frac{4E^2 - 4E^2y - Q^2}{4E^2 - 4E^2y + 2E^2y^2 + Q^2}, \tag{3.12}$$

where α_{em} is the electromagnetic fine structure constant and Γ_L is the flux of longitudinal virtual photons.

The contraction $L^{\nu\mu}W_{\mu\nu}$ can then be written as

$$\sigma_{mn} = \sum_{ij} \rho_{ji}\sigma_{mn}^{ij} \sim \int dM_n^2\, (\epsilon_m^{\mu *} W_{\mu\nu} \epsilon_n^\nu), \tag{3.13}$$

where σ_{mn} is the $\gamma^* p$ cross section for photon helicity n (m) in the initial (final) state, and the integration in (3.13) is over M_n^2 (Table 3.1). The σ_{mn}^{ij} are the polarised photoabsorption cross sections and interference terms, given by

$$\sigma_{mn}^{ij}(x, Q^2, t) \sim \int dM_n^2\, \delta^{(4)}(P' + p_{\pi^+} - P - q) \sum_{spins} (\mathcal{A}_m^i)^* \mathcal{A}_n^j, \tag{3.14}$$

in terms of the amplitudes $\mathcal{A}_m^i$ (see (2.17)) for the process $\gamma^* p \to n\pi^+$ with proton polarisation i and photon polarisation m. The indices $m, n = 0, +1, -1$ refer to the proton and $i, j = +\frac{1}{2}, -\frac{1}{2}$ to the photon polarisation states.

With the polarisation states for protons and photons defined in the coordinate system C'', the electroproduction cross section for the process (3.1) for transverse target polarisation with respect to the lepton beam is given by [27]

$$\left[\frac{\cos\theta}{1 - \sin^2\theta \sin^2\phi_S}\right]^{-1} \left[\frac{1}{4\pi^2}\Gamma_T(x, Q^2)\right]^{-1} \frac{d\sigma(x, Q^2, t, \phi, \phi_S)}{dx\, dQ^2\, dt\, d\phi\, d\phi_S} \equiv d\sigma = d\sigma_{UU} + d\sigma_{UT} \tag{3.15}$$

$$\begin{aligned} d\sigma_{UU} = {} & \frac{1}{2}(\sigma_{++}^{++} + \sigma_{++}^{--}) + \varepsilon\sigma_{00}^{++} \\ & - \varepsilon\cos(2\phi)\,\mathrm{Re}\,\sigma_{+-}^{++} - \sqrt{\varepsilon(1+\varepsilon)}\cos\phi\ \mathrm{Re}\,(\sigma_{+0}^{++} + \sigma_{+0}^{--}) \end{aligned} \tag{3.16}$$

$$d\sigma_{UT} \quad = \quad -\frac{P_T}{\sqrt{1 - \sin^2\theta\sin^2\phi_S}} \sum_{k=1}^{6} \sin(\mu\phi + \lambda\phi_S)_k\ \Sigma_k, \tag{3.17}$$

where $k = 1, \ldots, 6$; $\mu = \mu(k) = 0, 1, 2, 3$; $\lambda = \lambda(k) = -1, 1$, and

k	$\sin(\mu\phi + \lambda\phi_S)_k$ azimuthal modulation	Σ_k polarised photoabsorption cross section/interference term
1	$\sin(\phi - \phi_S)$	$\cos\theta\,\mathrm{Im}\,(\sigma_{++}^{+-} + \varepsilon\sigma_{00}^{+-}) + \frac{1}{2}\sin\theta\sqrt{\varepsilon(1+\varepsilon)}\,\mathrm{Im}\,(\sigma_{+0}^{++} - \sigma_{+0}^{--})$
2	$\sin(\phi + \phi_S)$	$\frac{1}{2}\cos\theta\,\varepsilon\,\mathrm{Im}\,\sigma_{+-}^{+-} + \frac{1}{2}\sin\theta\sqrt{\varepsilon(1+\varepsilon)}\,\mathrm{Im}\,(\sigma_{+0}^{++} - \sigma_{+0}^{--})$
3	$\sin\phi_S$	$\cos\theta\sqrt{\varepsilon(1+\varepsilon)}\,\mathrm{Im}\,\sigma_{+0}^{+-}$
4	$\sin(2\phi - \phi_S)$	$\cos\theta\sqrt{\varepsilon(1+\varepsilon)}\,\mathrm{Im}\,\sigma_{+0}^{-+} + \frac{1}{2}\sin\theta\,\varepsilon\,\mathrm{Im}\,\sigma_{+-}^{++}$
5	$\sin(3\phi - \phi_S)$	$\frac{1}{2}\cos\theta\,\varepsilon\,\mathrm{Im}\,\sigma_{+-}^{-+}$
6	$\sin(2\phi + \phi_S)$	$\frac{1}{2}\sin\theta\,\varepsilon\,\mathrm{Im}\,\sigma_{+-}^{++}$

In the notation for the electroproduction cross sections the first (second) index denotes the beam (target) polarisation, e.g., $d\sigma_{UT}$ refers to unpolarised beam (U) and transversely polarised target (T). In a more common but less explicit notation $\sigma_T = \frac{1}{2}(\sigma_{++}^{++} + \sigma_{++}^{--})$ and $\sigma_L = \sigma_{00}^{++}$ are the unpolarised transverse (T) and longitudinal (L) $\gamma^* p$ photoabsorption cross sections, and $\sigma_{TT} = \mathrm{Re}\,\sigma_{+-}^{++}$ and $\sigma_{TL} = \mathrm{Re}\,(\sigma_{+0}^{++} + \sigma_{+0}^{--})$ are the interference terms in the unpolarised pion electroproduction cross section. In (3.15), (3.16), (3.17) the cross sections $d\sigma$, $d\sigma_{UU}$, $d\sigma_{UT}$, and σ_{mn}^{ij} are differential with respect to x, Q^2, t, ϕ, and ϕ_S, e.g., $\sigma_{00}^{+-} \equiv \frac{d\sigma_{00}^{+-}(x,Q^2,t,\phi,\phi_S)}{dx\,dQ^2\,dt\,d\phi\,d\phi_S}$.

The following factors appearing in (3.15) and (3.17) are set to unity in the following, i.e.,

$$\Gamma \equiv \frac{\cos\theta}{1 - \sin^2\theta\sin^2\phi_S} \approx 1, \quad f(\sin^2\phi_S) \equiv \frac{1}{\sqrt{1 - \sin^2\theta\sin^2\phi_S}} \approx 1. \tag{3.18}$$

This approximation is valid for HERMES kinematics (Section 7.1).

3.1.3 Azimuthal Asymmetry

The cross section (3.15), integrated over the kinematic variables x, Q^2, and t while keeping the dependence on the azimuthal angles ϕ and ϕ_S (Fig. 3.1), can be written as

$$\left[\frac{\Gamma_T}{4\pi^2}\right]^{-1}\frac{d\sigma(\phi,\phi_S)}{d\phi\, d\phi_S} \equiv d\sigma(\phi,\phi_S) = [d\sigma_{UU}(\phi) + d\sigma_{UT}(\phi,\phi_S)], \tag{3.19}$$

where the differential variables are denoted in parentheses. The target transverse polarisation P_T (3.6) is a degree of freedom that allows one to construct an asymmetry, which is given by the difference between the cross sections for the two target polarisation states, $P_T > 0$ (positive) and $P_T < 0$ (negative), corresponding to azimuthal angles ϕ_S ('spin up') and $\phi_S + \pi$ ('spin down'), respectively. According to the Trento conventions [9], the asymmetry is defined as

$$A(\phi,\phi_S) = \frac{1}{|P_T|}\frac{d\sigma(\phi,\phi_S) - d\sigma(\phi,\phi_S+\pi)}{d\sigma(\phi,\phi_S) + d\sigma(\phi,\phi_S+\pi)} = \frac{d\sigma_{UT}(\phi,\phi_S)}{d\sigma_{UU}(\phi)}. \tag{3.20}$$

Note that with the choice of normalisation, given by the denominators in (3.20), the asymmetry can vary in the range $-\frac{1}{|P_T|} \leq A(\phi,\phi_S) \leq \frac{1}{|P_T|}$, which for $|P_T| = 1$ gives values from -1 to 1. $A(\phi,\phi_S)$ is called the transverse-target single-spin (polarised target, unpolarised beam) azimuthal (ϕ, ϕ_S dependent) asymmetry, abbreviated as TTSSAA or briefly TSA.

3.1.4 Asymmetry Amplitudes

Inserting (3.17) in (3.19) and the latter in (3.20), with the approximation (3.18) being applied, we get for the asymmetry (3.20)

$$A(\phi,\phi_S) \;=\; -\frac{\sum_{k=1}^{6}\sin(\mu\phi+\lambda\phi_S)_k\Sigma_k}{d\sigma_{UU}(\phi)} = -\sum_{k=1}^{6} A_{UT}^{\sin(\mu\phi+\lambda\phi_S)_k}\sin(\mu\phi+\lambda\phi_S)_k, \tag{3.21}$$

where we define

$$A_{UT}^{\sin(\mu\phi+\lambda\phi_S)_k} \;\equiv\; \frac{\Sigma_k}{d\sigma_{UU}(\phi)} \overset{>}{\underset{<}{=}} 0. \tag{3.22}$$

The quantities $A_{UT}^{\sin(\mu\phi+\lambda\phi_S)_k}$ multiplying the sine modulations $\sin(\mu\phi+\lambda\phi_S)_k$ of the asymmetry in (3.21) are called the asymmetry amplitudes. The notation $\overset{>}{\underset{<}{=}} 0$ in (3.22) expresses the fact that the sign of the asymmetry amplitudes is not predicted by theory. The sign of a given amplitude k in (3.22) is determined by the sign of the polarised photoabsorption cross sections/interference terms σ_{mn}^{ij} in Σ_k (see table following (3.17)) which can be positive, zero, or negative depending on the dynamics of the process. Predictions for the sign (and the size) of the amplitudes can be obtained presently from models of σ_{mn}^{ij} (Section 3.4).

Substitution in (3.21) of the μ, λ values for a given k (see table following 3.17) gives the six azimuthal modulations and the respective amplitudes of the asymmetry in the form

$$\begin{aligned} A(\phi,\phi_S) = &- A_{UT}^{\sin(\phi-\phi_S)}\sin(\phi-\phi_S) - A_{UT}^{\sin(\phi+\phi_S)}\sin(\phi+\phi_S) - A_{UT}^{\sin\phi_S}\sin\phi_S \\ &- A_{UT}^{\sin(2\phi-\phi_S)}\sin(2\phi-\phi_S) - A_{UT}^{\sin(3\phi-\phi_S)}\sin(3\phi-\phi_S) \\ &- A_{UT}^{\sin(2\phi+\phi_S)}\sin(2\phi+\phi_S). \end{aligned} \tag{3.23}$$

The extraction of all six amplitudes in (3.23) from data is performed in Chapter 7. In the following discussion only longitudinal virtual photons are considered and a prediction of $A_{UT}^{\sin(\phi-\phi_S)}$ is made using a model for σ_{00}^{+-} and σ_{00}^{++}.

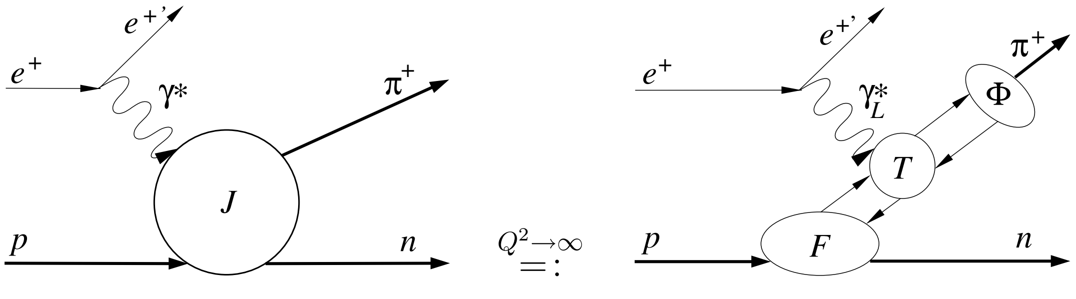

Figure 3.2: Factorisation theorem for exclusive pion production (3.1). The amplitude for the process (the matrix element for the electromagnetic current J) factorises into the generalised parton distribution for the proton (the non-diagonal matrix element F), the hard scattering amplitude T, and the pion distribution amplitude Φ.

3.2 Factorisation Theorem

The possibility to study the exclusive process (3.1) and to calculate the cross section (3.15) in QCD relies on factorisation of the scattering process in 'hard' and 'soft' parts. Theoretical studies of exclusive pion production are presented in [10, 26, 27, 33, 39]. A detailed proof of the QCD factorisation theorem for hard exclusive electroproduction of mesons is given in [19]. At present factorisation applies only for longitudinal virtual photons γ^*_L (helicity $m = 0$). Applied to pion production, the theorem states that the amplitude for the process $\gamma^*_L p \to n\pi^+$ factorises into a transition operator for the hard process T_{ud} convoluted with the distribution function (i.e., the non-diagonal matrix element denoted by F_{ud}) for the $p \to n$ transition and with the distribution amplitude of the pion Φ_{π^+} [10, 27, 33]

$$\begin{aligned}\mathcal{A}^{\gamma^*_L p\to n\pi^+}(\xi,t) &\equiv \langle \pi^+(p_{\pi^+}) n(P')|J_{\mathrm{em}}\cdot\epsilon_0|p(P)\rangle \\ &= \frac{1}{Q}\int_{-1}^{1} dx \int_0^1 dz\, T_{ud}(x,\xi,z)\, F_{ud}(x,\xi,t)\, \Phi_{\pi^+}(z),\end{aligned} \tag{3.24}$$

up to power corrections in $\frac{1}{Q}$. The factorisation (3.24) is valid in the limit $Q^2 \to \infty$ at fixed $\frac{Q^2}{W^2}$ and t. The parton types u and d connect the hard scattering part of the process to the proton and to the pion bound states. J_{em} is the electromagnetic current, ϵ_0 is the polarisation vector for longitudinal virtual photons, and ξ is introduced in Section 2.6. The factorisation theorem (3.24) is illustrated in Fig. 3.2.

The factorisation theorem also states that all other helicity transitions, e.g., $\gamma^*_T p \to n\pi^+$ for transversely polarised photons (helicity $m = +1, -1$), are of order $\frac{1}{Q^2}$ or higher, hence suppressed compared with $\gamma^*_L p \to n\pi^+$. The following hierarchy for the photoabsorption cross sections and interference terms in (3.16) and (3.17) is found to hold:

- the only leading-twist observables are σ^{++}_{00} and σ^{+-}_{00},
- σ^{ij}_{+0} are at least one power of $\frac{1}{Q}$ down compared with σ^{++}_{00},
- σ^{ij}_{++} and σ^{ij}_{+-} are suppressed by at least $\frac{1}{Q^2}$ compared with σ^{++}_{00}.

We denote by $\widetilde{H}$ and $\widetilde{E}$ the functions that parameterise F_{ud} in (3.24) and introduce the scattering amplitudes $\widetilde{\mathcal{H}}$ and $\widetilde{\mathcal{E}}$ as [10]

$$\left\{\begin{matrix}\widetilde{\mathcal{H}}\\ \widetilde{\mathcal{E}}\end{matrix}\right\}(x,\xi,t) = \int_{-1}^{1} dx \int_0^1 dz\, T_{ud}(x,\xi,z) \left\{\begin{matrix}\widetilde{H}\\ \widetilde{E}\end{matrix}\right\}(x,\xi,t)\, \Phi_{\pi^+}(z). \tag{3.25}$$

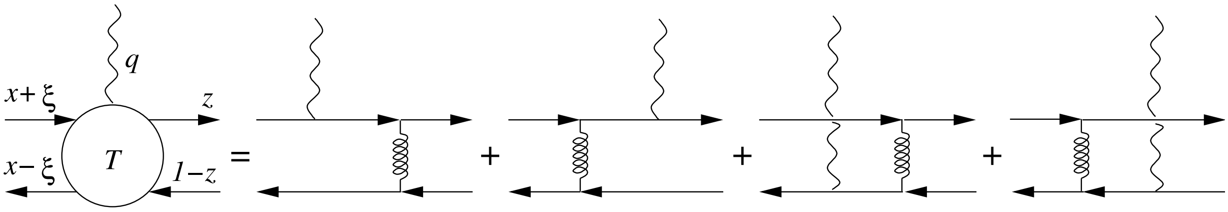

Figure 3.3: Hard scattering coefficient functions to leading order [10].

From the squared amplitude $\mathcal{A}^*\mathcal{A}$, the leading-twist results for the t-differential longitudinal photoabsorption cross section and the interference term can be derived in the form [27]

$$\left[\frac{\alpha_{\rm em}}{Q^6}\frac{x^2}{1-x}\right]^{-1}\frac{d\sigma_{00}^{++}}{dt} = (1-\xi)|\widetilde{\mathcal{H}}|^2 - \xi^2\frac{t}{4M_p^2}|\widetilde{\mathcal{E}}|^2 - 2\xi^2\,\mathrm{Re}\,(\widetilde{\mathcal{E}}^*\widetilde{\mathcal{H}}) \tag{3.26}$$

$$\left[\frac{\alpha_{\rm em}}{Q^6}\frac{x^2}{1-x}\right]^{-1}\frac{d\sigma_{00}^{+-}}{dt} = \sqrt{1-\xi^2}\frac{\sqrt{t_0-t}}{M_p}\xi\,\mathrm{Im}\,(\widetilde{\mathcal{E}}^*\widetilde{\mathcal{H}}), \tag{3.27}$$

where the scaling variable (skewness) ξ and the smallest kinematically allowed momentum transfer t_0 are given by [27]

$$\xi = \frac{x}{2-x}, \quad -t_0 = \frac{4\xi^2M_p^2}{1-\xi^2} = \frac{x^2M_p^2}{1-x}, \tag{3.28}$$

up to correction factors of order $\frac{xM_p^2}{Q^2}$, $\frac{xt}{Q^2}$, and $\frac{m_{\pi^+}^2}{Q^2}$.

3.3 Pion Electroproduction Amplitude

The calculation of the hard scattering amplitude $\mathcal{A}$ (3.24) in QCD in the leading-twist approximation and at leading order in the strong coupling α_S is outlined below.

The hard subprocess, denoted by T in Figs. 3.2, 3.3 and T_{ud} in (3.24), encodes the short distance dynamics of parton scattering and is the only factorisation term that can be consistently calculated in QCD perturbation theory as a series in the strong coupling α_S. Evaluation of the tree diagrams in Fig. 3.3 gives for the hard amplitude T_{ud} to leading order in α_S the following result [33]

$$T_{ud}(x,\xi,z) \sim \frac{e_u}{z\left(x+\frac{\xi}{2}\right)-i0} + \frac{e_d}{(1-z)\left(x-\frac{\xi}{2}\right)+i0} + \mathcal{O}(\alpha_S^2), \tag{3.29}$$

where $e_u = \frac{2}{3}$ and $e_d = -\frac{1}{3}$ are the quark charges.

The other blocks of the factorisation theorem, F_{ud} and Φ_{π^+}, which carry the long-distance (soft) physics information for the process, cannot be calculated from first principles in QCD. However, they are universal, i.e., process independent. The 'truly' non-diagonal matrix element F_{ud} has the form [23]

$$\begin{aligned} F_{ud}(x,\xi,t) &= \bar{P}^+\int\frac{dz^-}{2\pi}\,e^{ix\bar{P}^+z^-}\langle n(P')|\bar{d}(\frac{-\bar{z}}{2})\gamma^+\gamma_5 u(\frac{\bar{z}}{2})|p(P)\rangle|_{z^+=0,z_\perp=0} \\ &= \bar{u}_n(P')\left[\gamma^+\gamma_5\widetilde{H}(x,\xi,t) + \frac{\gamma_5\Delta^+}{2M_p}\widetilde{E}(x,\xi,t)\right]u_p(P), \end{aligned} \tag{3.30}$$

where $\Delta = P'-P$, $\bar{P} = \frac{P'+P}{2}$, and $\bar{z} = [0, z^-, 0_\perp]$ is a shorthand notation for the light-cone four-vector. 'Truly' refers to the fact that the production of π^+ is described by a 'new' transition matrix element between proton and neutron ($p \to n$). Using the isospin relations [33]

$$\langle n|\bar{d}u|p\rangle = \langle p|\bar{u}u|p\rangle - \langle n|\bar{u}u|n\rangle = \langle p|\bar{u}u|p\rangle - \langle p|\bar{d}d|p\rangle, \tag{3.31}$$

one can relate (at fixed x) the 'new' matrix elements to the usual ones that describe a proton–proton transition ($p \to p$)

$$F_{ud}^{p\to n}(x) = F_{uu}^{p\to p}(x) - F_{dd}^{p\to p}(x). \tag{3.32}$$

Therefore, $\widetilde{H}$ and $\widetilde{E}$ in (3.30) are in fact isovector functions given by the difference of the GPDs for u and d quarks [33]

$$\widetilde{H}(x,\xi,t) = \widetilde{H}_u(x,\xi,t) - \widetilde{H}_d(x,\xi,t), \quad \widetilde{E}(x,\xi,t) = \widetilde{E}_u(x,\xi,t) - \widetilde{E}_d(x,\xi,t) \tag{3.33}$$

The leading-twist distribution amplitude for the pion is given by [23]

$$\Phi_{\pi^+}(z) = \frac{1}{f_{\pi^+}} \int \frac{dx^-}{2\pi}\, e^{i(2z-1)p^+_{\pi^+}x^-/2} \langle \pi^+(p_{\pi^+})|\bar{d}(\frac{-\bar{x}}{2})\gamma^+\gamma_5 u(\frac{\bar{x}}{2})|0\rangle|_{x^+=0,x_\perp=0}, \tag{3.34}$$

where $\bar{x} = [0, x^-, 0_\perp]$ denotes the light-cone four-vector. The pion decay (structure) constant is $f_{\pi^+} \approx 93\,\mathrm{MeV}$.

Thus in the leading-twist approximation and at leading order in the strong coupling α_S the amplitude for exclusive π^+ production is given by the expression [33]

$$\begin{aligned} \mathcal{A}(\xi,t) &= -\frac{4ie\pi\alpha_S f_{\pi^+}}{27Q} \int_0^1 dz \frac{\Phi_{\pi^+}(z)}{z} && (3.35) \\ &\times\ \bar{u}(P')\left\{\int_{-1}^1 dx\alpha(x)\left[\gamma^+\gamma_5\widetilde{H}(x,\xi,t) + \frac{\gamma_5\Delta^+}{2M_p}\widetilde{E}(x,\xi,t)\right]\right\}u(P), && (3.36) \end{aligned}$$

where

$$\alpha(x) = 3\alpha^-(x) - \alpha^+(x), \quad \alpha^\pm(x) = \frac{1}{x+\frac{\xi}{2}-i0} \pm \frac{1}{x-\frac{\xi}{2}+i0}. \tag{3.37}$$

3.4 Proton Generalised Parton Distributions

In analogy to the usual parton distributions (PDFs) the generalised parton distributions (GPDs) are defined as the form factors parameterising matrix elements of (twist-two bilocal) quark-field operators at a light-like separation, as shown in (3.30) for the 'polarised' GPDs $\widetilde{H}$ and $\widetilde{E}$. 'Polarised' here refers to the spin of the partons (not the target) so that $\widetilde{H}$ and $\widetilde{E}$ correspond to the difference over parton helicities in the target nucleon.

We notice that the non-diagonal matrix elements in (3.30) are taken between states of unequal momenta $P' \neq P$, which is in distinction to the definition of PDFs for $P' = P$ (Chapter 2). Because of Lorentz invariance the GPDs can only depend on the kinematic variable x, the transverse four-momentum transfer t, and the skewness parameter ξ, which is the projection of t on the (light-cone) direction in which the nucleon is rapidly moving within the picture of the parton model.

In the forward limit ($t \to 0$, $P' = P$) and for equal helicities of the initial and final state nucleons $p(P)$ and $n(P')$, respectively, the matrix element in (3.30) reduces to the usual spin dependent parton density $\Delta q(x)$ for the quark q [23, 39]

$$\widetilde{H}^q(x,0,0) = \Delta q(x), \tag{3.38}$$

where $\Delta q(x)$ is defined through the diagonal matrix element (see also 2.48) [23]

$$P^+ \int \frac{dz^-}{2\pi}\, e^{ixP^+z^-} \langle n(P)|\bar{d}(\frac{-\bar{z}}{2})\gamma^+\gamma_5 u(\frac{\bar{z}}{2})|p(P)\rangle|_{x^+=0,x_\perp=0} = \bar{u}_n(P)\gamma^+\gamma_5 u_p(P)\Delta q(x). \quad (3.39)$$

Since in (3.30) $\widetilde{E}$ is multiplied with factors proportional to $\Delta = P' - P$, no relation analogous to (3.38) exists for $\widetilde{E}$ and therefore this GPD decouples in the forward limit.

Integration of (3.30) over x gives a matrix element of a local quark-antiquark operator, so that the x-integral of the GPDs $\widetilde{H}$ and $\widetilde{E}$ is related to the form factors (FFs) of these local currents [23, 39]

$$\int_{-1}^{1} dx\, \widetilde{H}^q(x,\xi,t) = g_A^q(t), \qquad \int_{-1}^{1} dx\, \widetilde{E}^q(x,\xi,t) = g_P^q(t), \quad (3.40)$$

where the axial (pseudovector) and pseudoscalar form factors, $g_A^q(t)$ and $g_P^q(t)$, are defined for a quark flavour q through (see also (2.42)) [23]

$$\langle p(P')|\bar{q}(0)\gamma^+\gamma_5 q(0)|p(P)\rangle = \bar{u}(P')\left[\gamma^+\gamma_5\, g_A^q(t) + \frac{\gamma_5\Delta^+}{2M_p}\, g_P^q(t)\right] u(P). \quad (3.41)$$

Note that the integrals in (3.40) are independent of ξ due to Lorentz invariance: integrating the matrix element (3.30) over x removes any reference to the particular light-cone direction with respect to which ξ is defined, thus the result must be ξ-independent.

Although the GPDs $\widetilde{H}$ and $\widetilde{E}$ can be reduced in certain limiting cases to quantities already known from measurements, i.e., the parton distribution in (3.38) and the form factors in (3.40), unlike the latter three, even the quantitative behaviour of the former is largely unknown. Like PDFs and FFs, GPDs cannot be calculated from first principles in QCD. That is why model calculations (see [10, 26, 39, 73] and references therein) of these quantities are of big importance.

3.4.1 Model for $\widetilde{H}(x,\xi,t)$

To provide numerical estimates for the physics observables, the model for $\widetilde{H}$ assumes a factorised ansatz for the (x,ξ) and t dependence, which is valid at small t [26]

$$\widetilde{H}^q(x,\xi,t) = \widetilde{H}^q(x,\xi)\frac{g_A^q(t)}{g_A^q(0)}, \quad (3.42)$$

where the following dipole parameterisation is taken for the form factor [26]

$$\frac{g_A^q(t)}{g_A^q(0)} = \frac{1}{[1 - t/(1.05\,\mathrm{GeV}^2)]^2}. \quad (3.43)$$

For the t-independent function $\widetilde{H}(x,\xi)$ in (3.42) a double-distribution based ansatz [53] is used, whose ingredients are the usual parton distributions at a given factorisation scale μ and a so-called profile parameter b, where μ and b are considered as free parameters of the model. The model gives [26]

$$\widetilde{H}^q(x,\xi) = \int_{-1}^{1} d\beta \int_{-1+|\beta|}^{1-|\beta|} d\alpha\, \delta(x-\beta-\xi\alpha) h(\beta,\alpha)[\theta(\beta)\Delta q(\beta) + \theta(-\beta)\Delta\bar{q}(-\beta)], \quad (3.44)$$

where θ denotes the step function, and Δq and $\Delta\bar{q}$ are the polarised quark and antiquark distributions, respectively. The profile function [10, 26]

$$h(\beta,\alpha) = \frac{\Gamma(2b+2)}{2^{2b+1}\Gamma^2(b+1)}\frac{[(1-|\beta|)^2-\alpha^2]^b}{(1-|\beta|)^{2b+1}} \quad \overset{b=1}{:} \quad h(\beta,\alpha) = \frac{3}{4}\frac{(1-|\beta|)^2-\alpha^2}{(1-|\beta|)^3}, \quad (3.45)$$

with the parameter $b = 1$ is used. Assuming an $SU(2)$ symmetric sea, i.e., $\Delta\bar{q}(\beta) = \Delta\bar{u}(\beta) - \Delta\bar{d}(\beta) = 0$, one has only the contribution from the valence quarks $\Delta q(\beta) = \Delta u(\beta) - \Delta d(\beta)$. The known forward parton densities Δu and Δd at $Q^2 = 4\,\mathrm{GeV}^2$ are used for the numerical evaluation of the asymmetry (Section 3.5). Note that the simple ansatz (3.42) for $\widetilde{H}$ is chosen such that constraints arising from the reduction to the forward limit (3.38) and the sum rule for the lowest moment (3.40) are satisfied.

3.4.2 Model for $\widetilde{E}(x, \xi, t)$

An important role in determining the size of $\widetilde{E}$ plays the spontaneously broken chiral symmetry of QCD. We remind that the GPD $\widetilde{E}$ satisfies the sum rule of (3.40) in terms of the pseudoscalar form factor g_P^q. It is known that due to the spontaneously broken chiral symmetry this form factor at small four-momentum transfer t is dominated by the contribution of the chiral singularity (pion pole) of the form [39]

$$\lim_{t \to m^2_{\pi^+}} g_P^q(t) = \frac{1}{2}\tau^3_{qq}\frac{4g_A^q(0)M_p^2}{m^2_{\pi^+} - t}, \tag{3.46}$$

where $g_A^q(0) \approx 1.267$ is the nucleon isovector axial charge and τ^3_{qq} is the Pauli matrix in flavour space. The presence of the pion pole on the right-hand side of the sum rule (3.40) for $\widetilde{E}$ implies that one should also expect the presence of the pion pole in the the GPD $\widetilde{E}$ itself at small t. The form of this singularity is specified to be [39]

$$\lim_{t \to m^2_{\pi^+}} \widetilde{E}^q(x, \xi, t) = \frac{1}{2}\tau^3_{qq}\frac{4g_A^q(0)M_p^2}{m^2_{\pi^+} - t}\frac{\theta(|x| \leq \xi)}{2\xi}\Phi_{\pi^+}(\frac{x+\xi}{2\xi}), \tag{3.47}$$

where Φ_{π^+} is the (universal) pion distribution amplitude entering, e.g., the description of the pion electromagnetic form factor at large momentum transfer and the hard reaction $\gamma^*\gamma \to \pi^0$. The pion-pole term (3.47) and the deviations from it are computed in the framework of the chiral quark-soliton model [21, 22]. It is found in this model that the pion-pole part to $\widetilde{E}$ dominates over a wide range of t and ξ values.

Next a phenomenological and physically motivated parameterisation of $\widetilde{E}$ is needed in order to connect this GPD to observables. The contribution to $\widetilde{E}$ is obtained by evaluating $\widetilde{E}$ under the assumption that it is entirely due to the pion pole. Since the pion exchange is isovector, one has [39]

$$\widetilde{E}^u = -\widetilde{E}^d = \frac{1}{2}\widetilde{E}_{\pi\,pole}, \tag{3.48}$$

where the t-dependence of $\widetilde{E}_{\pi\,pole}(x, \xi, t)$ is fixed by the sum rule (3.40) in terms of $g_P^q(t)$.

In the region $-\xi \leq x \leq \xi$, the quark and antiquark couple to the pion field of the nucleon. Therefore this coupling should be proportional to the pion distribution amplitude, for which the asymptotic form is adopted. With the quark's longitudinal momentum fraction z in the pion taken in the symmetric range $-1 \leq z \leq 1$, the asymptotic distribution amplitude is given by $\Phi_{\pi^+,as}(z) = \frac{3}{4}(1-z^2)$, and is normalised as $\int_{-1}^{+1} dz\, \Phi_{\pi^+,as}(z) = 1$. The light-cone momentum fractions of the quark and antiquark in the pion are given by $\frac{x+\xi}{2\xi}$ and $\frac{x-\xi}{2\xi}$, respectively, so that $\widetilde{E}_{\pi\,pole}$ is finally modelled in the estimates as [39]

$$\widetilde{E}_{\pi\,pole} = \frac{\theta(|x| \leq \xi)}{\xi}g_P^q(t)\Phi_{\pi^+,as}(\frac{x}{\xi}), \quad \text{where } g_P^q(t \to m^2_{\pi^+}) = \frac{4g_A^q(0)M_p^2}{m^2_{\pi^+} - t}. \tag{3.49}$$

Note that the parameterisation (3.49) satisfies the sum rule (3.40) for $\widetilde{E}$.

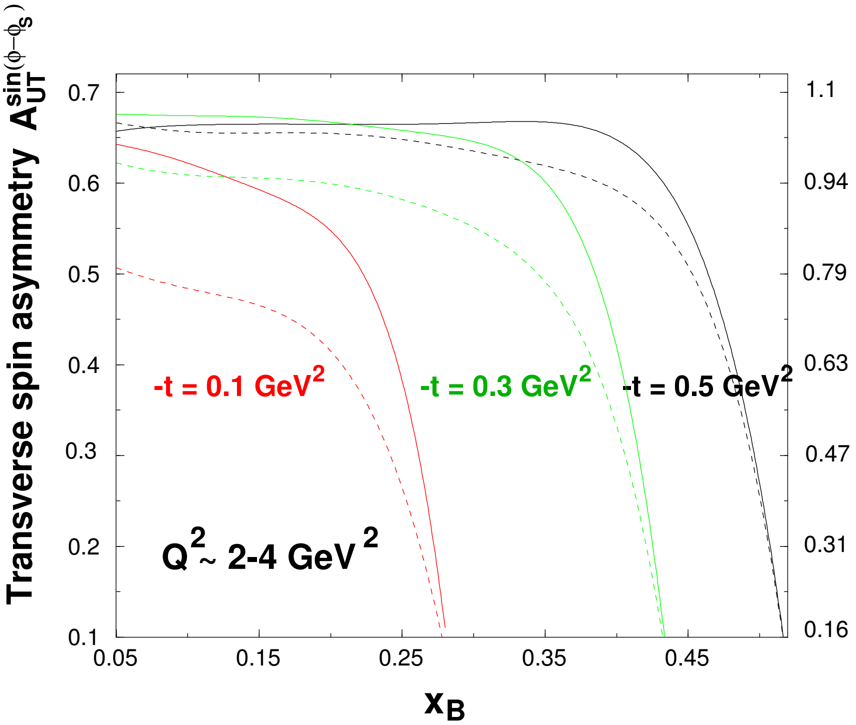

Figure 3.4: The transverse-target single-spin azimuthal asymmetry as a function of Bjorken x at $t = -0.1$, -0.3, and $-0.5\,\mathrm{GeV}^2$. Solid lines: with asymptotic pion distribution amplitude $\eta = 1$. Dashed lines: with Chernyak-Zhitnitsky pion distribution amplitude $\eta = \frac{5}{3}$. Figure taken from [33]. The right-hand-side vertical axis indicates the size of the amplitude after it has been scaled by a factor $\frac{\pi}{2}$ (see (3.53)) in accordance with the Trento conventions [9] used in this work.

3.5 Transverse-Target Single-Spin Azimuthal Asymmetry

According to the definition in [10, 33] the transverse-target single-spin azimuthal asymmetry is given by

$$A = \frac{1}{|P_T|} \frac{\int_{-\pi}^{0} d(\phi - \phi_S) d\sigma(\phi, \phi_S) - \int_{0}^{\pi} d(\phi - \phi_S) d\sigma(\phi, \phi_S)}{\int_{-\pi}^{\pi} d(\phi - \phi_S)\, d\sigma(\phi, \phi_S)} = \frac{2}{\pi} \frac{d\sigma_{UT}(\phi, \phi_S)}{d\sigma_{UU}(\phi)}, \tag{3.50}$$

where the integration is over $\phi-\phi_S$ which varies between $-\pi$ and π. The pion electroproduction cross sections $d\sigma$, $d\sigma_{UU}$, $d\sigma_{UT}$ are related as given in (3.19).

Considering only the leading-twist contribution $d\sigma_{00}^{+-}$ (3.27) to the cross section for the process $\gamma_L^* p \to n\pi^+$ and using the parameterisations of the GPDs $\widetilde{H}$, $\widetilde{E}$ and of the pion distribution amplitude Φ_{π^+} as outlined above, the asymmetry is obtained in the form [33]

$$A \approx \frac{\sqrt{t_0 - t}}{\pi M_p} \frac{2\sqrt{1-x}}{2-x} \frac{18\,\eta\, g_P^q(t)\,\mathrm{Im}H}{|H|^2(1-\frac{\xi^2}{4}) - \frac{81\,\eta^2\, t}{4M_p^2} g_P^q(t)^2 - 9\,\xi\, g_P^q(t)\,\mathrm{Re}H}, \tag{3.51}$$

where $H = \int_{-1}^{1} dx\, \widetilde{H}(x, \xi, t)\alpha(x)$ with $\alpha(x)$ from (3.37), $\eta = \frac{2}{3}\int_{-1}^{1} dz\, \frac{\Phi_{\pi^+}(z)}{(1-z^2)}$ ($\eta = 1$ for the asymptotic pion distribution amplitude $\Phi_{\pi^+,as}(z)$), and $g_P^q(t)$ from (3.49).

The calculated asymmetry (3.51) is shown in Fig. 3.4 at several values of t as a function of Bjorken x. It is plotted for $\eta = 1$ (corresponding to the asymptotic Φ_{π^+}, solid lines), and for $\eta = \frac{5}{3}$ (corresponding to the Chernyak-Zhitnitsky model for Φ_{π^+}, dashed lines) in order to illustrate the sensitivity of the asymmetry to the shape of the pion distribution amplitude.

We note that because of different conventions, the predicted asymmetry defined in [10, 33] (see (3.50)) and the one to be measured here (see (3.20)) are related to each other by a factor $\frac{2}{\pi} \approx 0.64$, namely,

$$A_{UT}^{\sin(\phi-\phi_S)}(\text{theory [10, 33]}) = \frac{2}{\pi}\, A_{UT}^{\sin(\phi-\phi_S)}(\text{this analysis}). \tag{3.52}$$

The relation (3.52) holds for the other amplitudes in (3.23) as well. For data-to-theory comparison the prediction for the leading amplitude, whose maximal value is $A_{UT}^{\sin(\phi-\phi_S)} = 0.64$ in Fig. 3.4, should be scaled by the inverse factor $\frac{\pi}{2} \approx 1.57$, i.e.,

$$max.A_{UT}^{\sin(\phi-\phi_S)}(\text{theory, scaled}) = \frac{\pi}{2}\, max.A_{UT}^{\sin(\phi-\phi_S)}(\text{theory}) \approx 1.57 \cdot 0.64 = 1.00. \tag{3.53}$$

Thus the maximal possible value of 1.0 for this amplitude is predicted by theory. The right-hand-side vertical axis in Fig 3.4 indicates the size of the amplitude after it has been scaled (as in (3.53)) in accordance with the Trento conventions [9] used in this work.

One can see from Fig 3.4 that the amplitude $A_{UT}^{\sin(\phi-\phi_S)}$ in the production of charged pions from a transversely polarised proton target is expected to be very large, which makes it interesting to measure this asymmetry at current experiments like HERMES. Also it is seen that the sensitivity to the form of the pion distribution amplitude is maximal at small transverse momentum transfer t.

The asymmetry amplitude $A_{UT}^{\sin(\phi-\phi_S)}$ is proportional to the interference term of two GPDs via $\text{Im}(\widetilde{\mathcal{E}}^*\widetilde{\mathcal{H}})$ (3.27), whose phase may appear to be zero for our measurement. We also note [24] that both calculations [10, 33] are leading-twist predictions, which are likely to be insufficient to reproduce the absolute cross section in our kinematics. In addition, this may also be the case where higher-twist 'corrections' [26] do not cancel in the azimuthal asymmetry. One-pion exchange in the t-channel (i.e., the 'pion-pole contribution') only contributes to $\widetilde{\mathcal{E}}$ (because of spin structure), and it has a large positive higher-twist correction as far as known from phenomenology [24]. That is not the case for $\widetilde{\mathcal{H}}$, where higher-twist corrections are expected to rather decrease than increase the leading-twist result. In a region where $\widetilde{\mathcal{E}} \gg \widetilde{\mathcal{H}}$, $A_{UT}^{\sin(\phi-\phi_S)}$ is given at leading twist by the ratio of the (polarised) interference term $\frac{d\sigma_{00}^{+-}}{dt} \sim \text{Im}(\widetilde{\mathcal{E}}^*\widetilde{\mathcal{H}})$ (3.27) and the (unpolarised) longitudinal photoabsorption cross section $\frac{d\sigma_{00}^{++}}{dt} \sim |\widetilde{\mathcal{E}}|^2$ (3.26). Thus one obtains

$$A_{UT}^{\sin(\phi-\phi_S)} \sim \frac{d\sigma_{00}^{+-}}{d\sigma_{00}^{++}} \sim \frac{\text{Im}\,(\widetilde{\mathcal{E}}^*\widetilde{\mathcal{H}})}{|\widetilde{\mathcal{E}}|^2}, \tag{3.54}$$

so that the above type of power corrections does not cancel. Such effects reduce the value of the asymmetry computed in the leading-twist approximation. In Chapter 8 an attempt is made to compare our results with the leading-twist prediction in Fig. 3.4.

Chapter 4

Experimental Setup

The experiment HERMES (**HERA** **ME**asurement of **S**pin) is located on the HERA electron/positron storage ring at DESY in Hamburg. We describe in some detail the construction and principle of operation of those parts of the setup, which are most relevant for the present work. Therefore, beam polarisation and related issues (spin rotators, polarimeters) [17, 64, 65, 66, 68] are omitted in the following discussion.

4.1 The HERA Electron Storage Ring

HERA [74] is the first and still (in 2007) the only operating lepton-hadron collider with high-energy superconducting (proton) storage ring and longitudinally polarised (in the interaction regions) high-energy electron/positron storage ring, used for precise studies of the nucleon structure.

The HERA tunnel has a circumference of 6.3 km and is located 15-30 m below surface. It consists of four 90° arcs with 797 m radius of curvature joined by 360 m-long straight sections. In the tunnel, the counter-rotating 920 GeV proton and 27.56 GeV electron (positron) beams are accelerated and stored in independent vacuum pipes, which cross each other only in the middle of two of the straight sections (North and South Halls). There, the particles produced in the head-on collisions at $\sqrt{s} = 318\,\text{GeV}$ centre-of-mass energy are detected by the H1 and ZEUS experiments in the years 1992-2007. Only the proton beam is scattered off an internal fixed target at $\sqrt{s} = 42\,\text{GeV}$ to study heavy quark production in proton–nucleus reactions by the HERA-B experiment (West Hall), in the period 2002-2003. Only the electron beam is used by the HERMES experiment (East Hall) in 1995-2007 for scattering off fixed gas targets at $\sqrt{s} = 7.3\,\text{GeV}$.

All magnets of the storage ring (dipoles, quadrupoles, sextupoles and steering coils) are normal conducting. Typical magnetic fields of the bending dipoles are 0.3 T. The accelerating field of $\sim 500\,\text{kV/m}$ is produced by a total of 50 5-cell and 32 7-cell normal copper cavities, and 16 superconducting cavities. The radio-frequency system operates at 499.668 MHz. Positrons are accelerated to 27.56 GeV energy in maximum of 220 number of bunches spaced by 96 ns (i.e., 10.4 MHz rate).

4.2 The Internal Gas Target

The use of a polarised gas target internal to the storage ring is a valuable tool to study nucleon properties via the measurement of polarisation observables. At HERMES the polarisation of the gas is based on the atomic beam source (ABS) technique [43]. During 1996-1997 (1998-2000) hydrogen (deuterium) was used in a longitudinal magnetic holding field, which in 2001 was turned to transverse for operation with hydrogen only. In this section the principles of gas polarisation [58] relevant for hydrogen and ABS are discussed in detail, followed by a description of the target setup and the measurement of the polarisation. Unlike for the spectrometer, here z is the vertical axis.

The HERMES target holds the record for the longest operating time for production of polarised hydrogen and deuterium atoms, and also for quality in terms of reliability and suppression of systematic errors. Various optimisation studies at the design stage and during the operation of the target have led to improvements of its parameters, in particular, the values for the gas flow and the target thickness, which are the best published results for ABS that use a storage cell [61]. The best figure-of-merit achieved for an internal nuclear polarised hydrogen gas target is reported in [62], where the laser-driven target (LDT) technique is employed.

4.2.1 Treatment of Hydrogen Atoms in the ABS

A hydrogen atom in an external static magnetic field, B, is found in any of four possible states with energies $E_1 > E_2 > E_3 > E_4$. With increasing field strength $E_{1,2}$ increase, whereas $E_{3,4}$ decrease. B is called a guide or holding field because it 'holds' the atom on a given energy level (state). This so called hyperfine splitting of the states (Table 4.1) is due to the interaction of B with the magnetic moments of the electron and the proton inside the hydrogen atom (see [59] and Appendix A). The direction of B is, likewise, conveniently taken as the quantisation axis for the electron spin, S, and the proton spin, I. The components of S and I along the field axis can take two values each, $m_S = \pm\frac{1}{2}$ and $m_I = \pm\frac{1}{2}$, respectively. The sign $+$ $(-)$ denotes the spin component parallel (antiparallel) to the magnetic field direction.

In a weak field ($B \ll B_C$, where B_C is some critical field) S and I are coupled to each other, i.e., $F = S + I$ and m_F is a good quantum number. The four states with different electron and proton spin orientations form a basis of eigenstates $|m_S, m_I\rangle$. In the strong field limit ($B \gg B_C$) the new eigenstates $|i\rangle$ are pure states, $|i\rangle \equiv |m_S, m_I\rangle$ for $i = 1, 3$, while each of the states $|2\rangle$ and $|3\rangle$ is a mixture of $|+\frac{1}{2}, -\frac{1}{2}\rangle$ and $|-\frac{1}{2}, -\frac{1}{2}\rangle$ with $|B|$-dependent coefficients. S and I decouple in a strong field.

	state	weak field			state	strong field			
energy	$\lvert m_S, m_I\rangle$	m_F	P_e	P_z		m_S	m_I	P_e	P_z
$E_1 > 0$	$\lvert +\frac{1}{2}, +\frac{1}{2}\rangle$	$+1$	1	1	$\lvert 1\rangle$	$+\frac{1}{2}$	$+\frac{1}{2}$	1	1
$E_2 > 0$	$\lvert +\frac{1}{2}, -\frac{1}{2}\rangle$	0	0	0	$\lvert 2\rangle$	$+\frac{1}{2}$	$-\frac{1}{2}$	1	-1
$E_3 < 0$	$\lvert -\frac{1}{2}, -\frac{1}{2}\rangle$	-1	-1	-1	$\lvert 3\rangle$	$-\frac{1}{2}$	$-\frac{1}{2}$	-1	-1
$E_4 < 0$	$\lvert -\frac{1}{2}, +\frac{1}{2}\rangle$	0	0	0	$\lvert 4\rangle$	$-\frac{1}{2}$	$+\frac{1}{2}$	-1	1

Table 4.1: Hyperfine states of the hydrogen atom.

The polarisation P is a characteristic of a sample of particles (P_e for electrons and P_z for protons) giving the average 'fictitious spin' of the whole sample. But instead of summing spins of individual particles in atoms, one counts atoms in different states—spins and states being strictly related (Table 4.1). The normalisation of states is done such that the polarisation is positive (negative) and maximal, $P = 1$ ($P = -1$), when the spins of all particles are directed parallel (antiparallel) to some axis, e.g., z. Of course $P = n_+ - n_-$ can take any value between $-1 < P < 1$ depending on the fractions of particles, n_+ and n_-, with spins parallel and antiparallel to z, respectively. The sample (target) is said to be polarised if $P \neq 0$. Note that polarisation has a different meaning here than in 'photon polarisation', therefore the use of 'proton/electron polarisation' or 'target spin' is avoided in the following.

Unless further measures are taken, a hydrogen sample located in an external static magnetic field is unpolarised ($P = 0$) because atoms occupy with equal probability any of the four states

(Table 4.1). The principle of creating a polarisation rests on the possibility of preparing atoms in such a way that the four states are not equally populated. Because the energy difference between states with electron spin $m_S = +\frac{1}{2}$ and $m_S = -\frac{1}{2}$ is large, it is relatively easy to separate them from one another (using the Stern-Gerlach principle). The separation is accomplished by deflection in a strong ($B \gg B_C$) inhomogeneous ($B \neq const$) magnetic field of a sextupole magnet. The radial dependence of the field strength is given by $B(r) = B_m(\frac{r}{r_m})^2$, where B_m is the magnitude of the field at the pole tips and r_m is the distance of the pole tips from the axis (at $r = 0$). The energy of an atom becomes a function of position via the interaction of the magnetic moment with the field ($E(r) = -\mu \cdot B(r)$), and the atom experiences a radial force $f(r) = -\frac{\partial E(r)}{\partial r}$. For the electron spin, $E(r) = -\mu_S \cdot B(r) = -q_e g_S \mu_B m_S |B(r)| = g_S \mu_B m_S |B(r)|$, where μ_S is the magnetic moment and $q_e = -e$ the charge of the electron. Since the electron carries a negative charge ($q_e = -e$) its magnetic moment is (in a right-handed coordinate system) anti-parallel to S. Because $|B(r)|$ increases with r, the force is pointing oppositely (minus sign) towards the axis for states whose energy $E(r)$ increases with $|B(r)|$ (states with $m_S = +\frac{1}{2}$, $E(r) > 0$, $f(r) < 0$) and away from the axis for states whose energy decreases with $|B(r)|$ (states with $m_S = -\frac{1}{2}$, $E(r) < 0$, $f(r) > 0$). Thus, if a beam of hydrogen atoms is directed along the axis of the magnet, atoms in states $|1\rangle$ and $|2\rangle$ are deflected towards the axis of the magnet, while atoms in states $|3\rangle$ and $|4\rangle$ are rejected for a strong field (Table 4.1). For a weak field most of the accepted atoms are in state $|1\rangle$. Note that the spin rejection acts on the electron spin of the hydrogen atoms, not the nuclear spin.

Unless even further measures are taken, a non-degenerate hydrogen sample emerging from the exit of a sextupole magnet (in the Stern-Gerlach selected electron states $|1\rangle$ and $|2\rangle$) is polarised in electron spin only ($P_e = 1$) but no nuclear polarisation is present ($P_z = 0$) in a strong magnetic field as the nuclear states $|1\rangle$ and $|2\rangle$ are equally occupied (Table 4.1; in a weak field nuclear polarisation, $P_z = 1$, is however present). Nuclear polarisation is obtained once it is possible to cause a transition $|1\rangle \rightarrow |3\rangle$ ($|2\rangle \rightarrow |4\rangle$) of one of the selected states, so that in combination with the other state $|2\rangle$ ($|1\rangle$), i.e., $|3\rangle + |2\rangle$ ($|4\rangle + |1\rangle$) the desired value $P = -1$ ($P = 1$) is obtained.

Radiofrequency (rf) transitions [5, 12] (in nuclear or electron spin) are used to change the population of the hydrogen atomic states. The required frequency for a transition between states $|i\rangle$ and $|j\rangle$ is determined from the energy difference between the states, $\omega_{ij} = \frac{E_i - E_j}{\hbar}$. The static holding field is applied in the vertical z direction with strength $B = const$ and the rf-field with circular frequency ω and amplitude $2B^{rf}$ in the x-direction, so that the total external field vector B^{ext} has components [13]

$$B_x^{ext} = 2B^{rf} \cos \omega t, \quad B_y^{ext} = 0, \quad B_z^{ext} = B. \tag{4.1}$$

The variation of the magnetic moment μ_I with time (due to the precession) is given by (Table 4.2)

$$\frac{d\mu_I}{dt} = q_p g_I \mu_N (\mu_I \times B). \tag{4.2}$$

Consider the case $B^{rf} \ll B$ with both fields positive and constant. Further assume that ω is close to the nuclear Larmor frequency $\omega_0 = q_p g_I \mu_N B$, i.e, $|\omega - \omega_0| \ll \omega_0$. Then the actual oscillating field in the x-direction can be effectively replaced by a field with components

$$B_x^{ext} = B^{rf} \cos \omega t, \quad B_y^{ext} = \mp B^{rf} \sin \omega t, \tag{4.3}$$

rotating around the z-direction with the sign of B_y^{ext}, the rotation being negative or positive, depending on whether $q_p g_I \mu_N$ is positive or negative. Defining the polar angle $\theta = \angle(\mu, B)$, the expression (4.2) is satisfied by the following components of the magnetic moment

$$\mu_{I,x} = \mu_I \sin\theta \cos \omega t, \quad \mu_{I,y} = \mp \mu_I \sin\theta \sin \omega t, \quad \mu_{I,z} = \mu_I \cos\theta, \tag{4.4}$$

variable	numeric value	explanation
f	$= ma$	linear force
i	-	moment of inertia
ω	$= \frac{d\phi}{dt}$	angular velocity, circular frequency
α	$= \frac{d\omega}{dt}$	angular acceleration
$L = i\omega$	$= mrv$	angular momentum
μ	$= \binom{closedloop}{current}\binom{enclosed}{area} = (q\frac{v}{2\pi r})(\pi r^2) = \frac{qL}{2m}$	magnetic moment (classic)
$\tau = i\alpha$	$= i\frac{d\omega}{dt} = \frac{dL}{dt} = \frac{L\sin\theta d\phi}{dt} = L\sin\theta\omega = L \times \omega$	torque
$E = -\mu_I \cdot B$	$= -g_I\mu_N m_I B$	magnetic interaction energy
$f = -\frac{dE}{dr}$	$= \frac{d(\mu_I \cdot B)}{dr}$	linear force
$\tau = dr \times f$	$= dr \times \frac{\mu_I \cdot B}{dr} = \frac{dr}{dr} \times \mu_I \cdot B = 1 \cdot (\mu_I \times B) = \mu_I \times B$	torque
τ	$= I \times \omega_0$	torque
$\omega_0 = q_p g_I \mu_N B$	$I \times \omega_0 = \mu_I \times B \rightarrow I \times \omega_0 = q_p g_I \mu_N I \times B$	nuclear Larmor frequency
$\frac{dI}{dt} = \mu_I \times B$	$\rightarrow \frac{d\mu_I}{dt} = q_p g_I \mu_N (\mu_I \times B)$	time variation of μ_I
e	$= +1$	elementary charge
q_p	$= +e$	nuclear charge
I	-	nuclear spin
m_I	$= \pm\frac{1}{2}$	nuclear spin quantum number
g_I	$= 5.5857$	nuclear gyromagnetic factor
μ_N	$= \frac{e\hbar}{2M_p}$	nuclear magneton
$\mu_I = q_p g_I \mu_N I$	$= q_p g_I \mu_N m_I$	nuclear magnetic moment

Table 4.2: Derivation of the time dependence of the magnetic moment (known as precession) and related quantities.

provided $\theta = const$ and chosen such that

$$\tan\theta = \frac{q_p g_I \mu_N B^{rf}}{q_p g_I \mu_N B \mp \omega_0}, \tag{4.5}$$

with the minus or plus sign depending on whether $q_p g_I \mu_N$ is positive or negative. Denoting $B^* = \frac{\omega}{|q_p g_I \mu_N|}$ the 'resonance field at frequency ω', i.e., the field B^{ext} for which the Larmor frequency $\omega_* = q_p g_I \mu_N B^{ext}$ is equal to the frequency of the oscillating field, $\omega_* = \omega$, then

$$\tan\theta = \frac{B^{rf}}{B - B^*}. \tag{4.6}$$

The expression (4.4) is interpreted as a rotation of the magnetic moment around the z-direction, i.e., around the strong field B and in such a way that it lies at any instant in the common plane of this field and the effective rotating field (4.3). The angle θ between the magnetic moment μ_I and the static magnetic field B follows from (4.6) to depend on the relative strengths of the static and rf-field (note that $B^{rf} \ll B$ is assumed)

- $\theta \approx 0 \Leftrightarrow B - B^* \gg B^{rf}$: μ_I is almost parallel to the direction of $B \| z$.
- $\theta = \frac{\pi}{4} \Leftrightarrow B - B^* = B^{rf}$: μ_I starts to deviate significantly from the z-direction but its projection is still parallel to B.

- $\theta = \frac{\pi}{2} \Leftrightarrow B = B^*$: μ_I is perpendicular to the z-direction, and thus to B.

- $\theta = -\frac{\pi}{4} \Leftrightarrow B^* - B = B^{rf}$: μ_I turns opposite to B but with half its magnitude (z-projection).

- $\theta \approx -\pi \Leftrightarrow B^* - B \ll B^{rf}$. Finally μ_I points completely in a direction opposite to B.

The magnetic moment of the proton is related to its spin via $\mu_I = q_p g_I \mu_B I$ (Table 4.2). Since the proton carries a positive charge ($q_p = +e$) its magnetic moment is (in a right-handed coordinate system) parallel to I. Therefore the change of μ_I's direction, from parallel to anti-parallel with respect to B, implies that the nuclear spin is flipped from $m_I = \pm\frac{1}{2}$ to $m_I = \mp\frac{1}{2}$, with the sign + to − or − to + depending on whether $q_p g_I \mu_B$ is positive or negative. The spin flip can also be visualised quantum mechanically in terms of the quantum energy of transition between the two possible spin states of the proton (Appendix A). But the expectation value of the vector operator representing the magnetic moment (or the spin) necessarily follows the same time dependence as obtained from the classical equation of motion for μ_I used above.

Since states are determined by the spin, by flipping the spin of the protons the atoms undergo transitions between pairs of states, thus changing the relative populations of the four hydrogen hyperfine states.

4.2.2 Target Setup

The HERMES polarised target setup is shown schematically in Fig. 4.1. Any parameter values occurring below refer to the target operation with hydrogen.

ABS The Atomic Beam Source injects a polarised beam of hydrogen atoms, H, into the storage cell. Hydrogen molecules, H_2, are dissociated by radiofrequency discharge with a frequency of 13.56 MHz in a pyrex tube, producing a degree of dissociation up to 80% at a flow of about $1\,\mathrm{mbl\,s^{-1}}$ and radiofrequency power of 300 W. The atomic gas flows through a conical nozzle with an opening diameter of 2 mm. The water produced in the discharge freezes on the 100 K cold walls of the tube, however, the ice layer is found to reduce surface recombination. The gas then expands into a chamber evacuated by a powerful pumping system with a total nominal pumping speed of more than $15000\,\mathrm{l\,s^{-1}}$, thus ensuring that the scattering of the atomic beam is suppressed. The magnet system consists of a total of five Halbach type segmented permanent sextupole magnets with a maximum poletip field of about 1.5 T. Four high-frequency transition units are available: two between the sextupole magnets (Strong and Medium Field Transition) and two after the last magnet (Medium and Weak Field Transition). The system provides enough flexibility that many different combinations of hyperfine states can be injected into the cell. Fluxes of $\sim 6.5 \times 10^{16}\,\mathrm{atoms\,s^{-1}}$ (states $|1\rangle$ and $|2\rangle$) are achieved.

Storage Cell The storage cell increases the areal target density up to $1.4 \times 10^{14}\,\mathrm{nucleons\,cm^{-2}}$, i.e., by about two orders of magnitude compared to a free jet atomic beam. The cell is made of two $75\,\mu\mathrm{m}$ thin pure aluminium sheets, which are tightly spot-welded together. It is 400 mm long and has an elliptical shape with a cross section of 21 mm × 8.9 mm. All the inner aluminium parts are coated with Drifilm (radiation hard hydrophobic silicon based polymer) to minimise gas depolarisation and recombination caused by the wall collisions. The operating temperature is about 100 K, where recombination and depolarisation effects are low, and, due to the lower conductance the target thickness is higher by a factor $\sqrt{3}$ compared to room temperature.

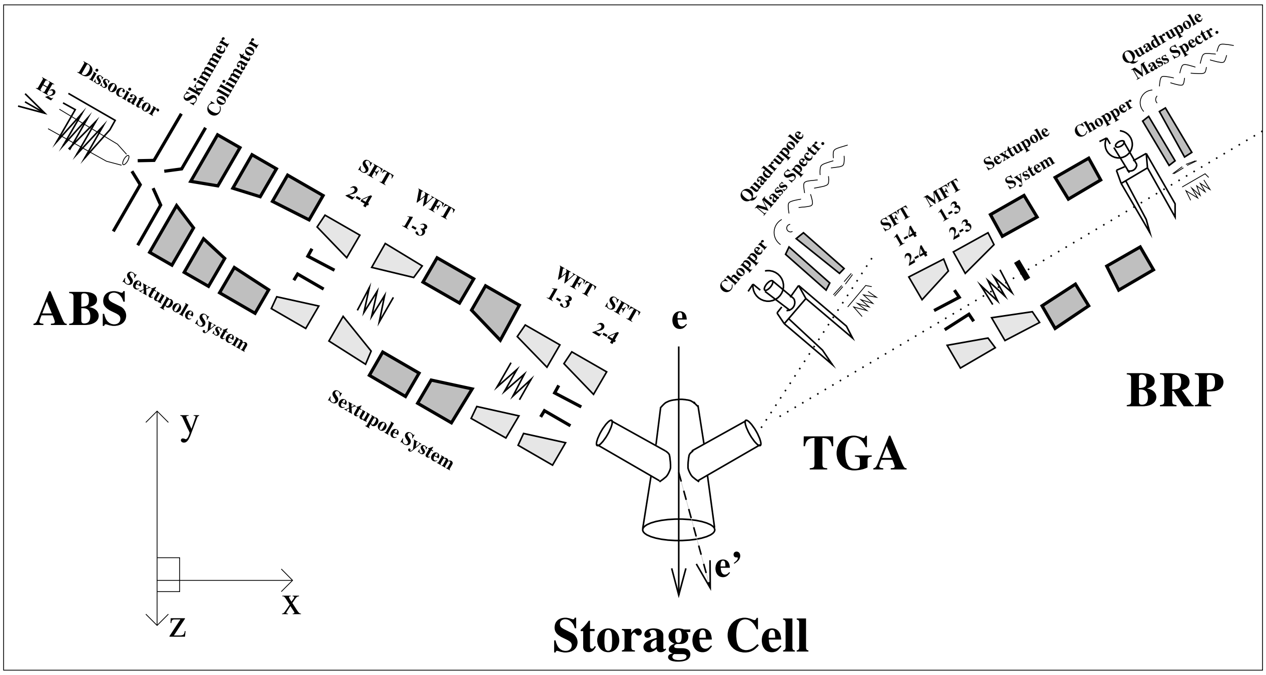

Figure 4.1: A schematic view of the polarised target setup.

TGA The Target Gas Analyser measures the relative atomic and molecular content of a sample of gas, extracted from the target cell through a sample tube. The particles entering an ionising volume are ionised by 70 eV electrons emitted from a filament and extracted. The ionised atoms (H^+) and molecules (H_2^+) are separated from each other on the basis of their mass in the magnetic field of a quadrupole mass spectrometer (Balzers QMA 430). The ions are detected by a channel electron multiplier (DeTech 401A), which converts the single-ion signals into electrically measurable pulses, counted by a multichannel time resolving counter.

BRP The Breit-Rabi Polarimeter determines the atomic polarisations of a sample of gas from the target centre by measuring the relative populations of the hydrogen hyperfine states. The absolute atomic polarisation can be calculated by applying the knowledge of the magnetic field strength. The sample beam passes through two transition units (Strong Field Transition for π, σ transitions and Medium Field Transition for π transitions) and a sextupole magnet system with $m_S = +\frac{1}{2}$ selection. The detector stage is identical to the one used for the target gas analyser but only hydrogen atoms (no molecules) are analysed by the BRP.

Transverse Magnet The magnet surrounding the storage cell provides a holding field, defines the polarisation axis, and prevents spin relaxation by decoupling the magnetic moments of electrons and protons. The field is homogeneous (within 0.05%) and vertical, (i.e., along y in the HERMES coordinate system (Section 4.3)) with a field strength of $B = 297\,\mathrm{mT}$, limited by the amount of synchrotron radiation power generated by the deflection of the beam by the magnet (5 kW maximum).

4.2.3 Target Polarisation Measurement

The total flux, ϕ_{tot}, of hydrogen gas that flows into the target can be presented as the sum of the fluxes of (i) polarised H-atoms, ϕ_a, (ii) molecules from recombined polarised H-atoms, ϕ_r, and, (iii) unpolarised molecules from a) ballistic flow from the ABS, ϕ_{ball}, and, b) residual gas in the target chamber, ϕ_{rg} [63]. Thus $\phi_a + \phi_r$ is the total number of atoms if recombination were absent. The fraction of atoms in the absence of recombination is

$$\alpha_0 = \frac{\phi_a + \phi_r}{\phi_{tot}}. \tag{4.7}$$

Out of all atoms in the storage cell, the fraction of atoms surviving recombination is given by

$$\alpha_r = \frac{\phi_a}{\phi_a + \phi_r}, \tag{4.8}$$

and, the fraction of atoms undergoing recombination in the cell is equal to

$$\frac{\phi_r}{\phi_a + \phi_r} = \frac{\phi_a + \phi_r - \phi_a}{\phi_a + \phi_r} = 1 - \alpha_r. \tag{4.9}$$

In this way one is able to represent the total fraction of polarised protons as a sum of (i) the fraction of polarised protons inside H-atoms, $\alpha_0\alpha_r = \frac{\phi_a}{\phi_{tot}}$, and, (ii) the fraction of polarised protons inside H_2-molecules due to recombination, $\alpha_0(1-\alpha_r) = \frac{\phi_r}{\phi_{tot}}$. This differentiation between atoms and molecules is necessary because the protons inside atoms and molecules contribute differently to the average nuclear polarisation of the target gas. Denoting the polarisation coming from atoms and molecules by P_a and P_m, respectively, the target proton polarisation, P_T, as seen by the electron beam is given by

$$P_T = \alpha_0\alpha_r P_a + \alpha_0(1-\alpha_r)P_m. \tag{4.10}$$

The values for α_0, α_r, and P_a are calculated using the TGA and BRP combined with various calibrations, accounting for the differences between the sample measurement and the actual conditions of the whole target (e.g., differences in the number of wall collisions, depolarisation mechanisms, non-uniform surface in the cell and sample tube). The sample and target values are related via the sampling corrections

$$c_\alpha \equiv \frac{\alpha_r}{\alpha_r^{TGA}}, \quad c_P \equiv \frac{P_a}{P_a^{BRP}}, \tag{4.11}$$

which depend on the geometry of the storage cell, its surface properties and the detectors' acceptances. They are calculated by means of a Monte Carlo simulation of the stochastic motion of particles in the storage cell.

A direct precise measurement of the proton polarisation contained in the molecules, P_m, is not possible at HERMES as it requires the use of cells of various materials and/or with various coatings and/or at various temperatures [61]. Without any such information one has to allow a conservative limit $0 \leq \beta \leq 1$ for the ratio $\beta = \frac{P_m}{P_a}$. However, an upper limit for $\beta_{high}^{100\,\mathrm{K}} \leq 0.83$ is found from a measurement at a higher cell temperature (260 K instead of the nominal 100 K), $\beta^{260\,\mathrm{K}} = 0.68$ (supposing the recombination mechanism is the same but the recombination probability (residence time on the surface) at 100 K is smaller (greater) than at 260 K). The lower limit on $\beta^{100\,\mathrm{K}} \geq 0.45$ follows from a simple argument that surface recombination involves target atoms ($P_a \approx 1.0$) and totally depolarised surface atoms, plus accounting for depolarisation of molecules while colliding with the walls. Thus, taking the range $0.45 \leq \beta^{100}\,\mathrm{K} \leq 0.83$, reduces the contribution of β to the total systematic uncertainty of the target polarisation.

Example values measured during the 2002 target operation are $\alpha_0 = 0.92 \pm 0.03$, $\alpha_r = 0.98 \pm 0.02$ [61]. Although the injected proton polarisation can be large, e.g., $P_{z+} = +0.9726$

and $P_{z-} = 0.9738$, there are various processes occurring inside the cell—recombination, spin relaxation, wall relaxation, spin exchange depolarisation, bunch field induced depolarisation—all of which lead to a decrease of $P_a < 1$. The transverse target proton polarisation values (4.10) are $P_T = 0.783 \pm 0.041$ during 2002, $P_T = 0.795 \pm 0.033$ for 2003, $P_T = 0.777 \pm 0.039$ for 2004 and in the second part of the 2004 data taking period due to unstable performance values between 0.648 ± 0.090 and 0.775 ± 0.044 are measured, giving an average proton polarisation of $\langle P_T \rangle = 0.754 \pm 0.050$ for the whole sample analysed in this work.

4.3 The Spectrometer

The particles originating from the target are scattered in the forward direction along the beam. The ordering of the detectors along the particle track is as follows: drift vertex chambers (DVCs), trigger hodoscope (H0), a pair of 'front' drift chambers (FC 1/2), three proportional chambers (MC 1-3) embedded in the gap of the spectrometer magnet, a pair of 'back' drift chambers (BC 1/2), a Cherenkov detector, another pair of drift chambers (BC 3/4), trigger hodoscope (H1), transition radiation detector (TRD), a preshower detector (H2) and a calorimeter.

The HERMES coordinate system has its origin at the centre of the target. The positive z-axis coincides with the lepton beam direction, the y-axis points vertically upwards and (in this orthogonal right-handed coordinate system) the x-axis is oriented horizontally towards the outside of the ring.

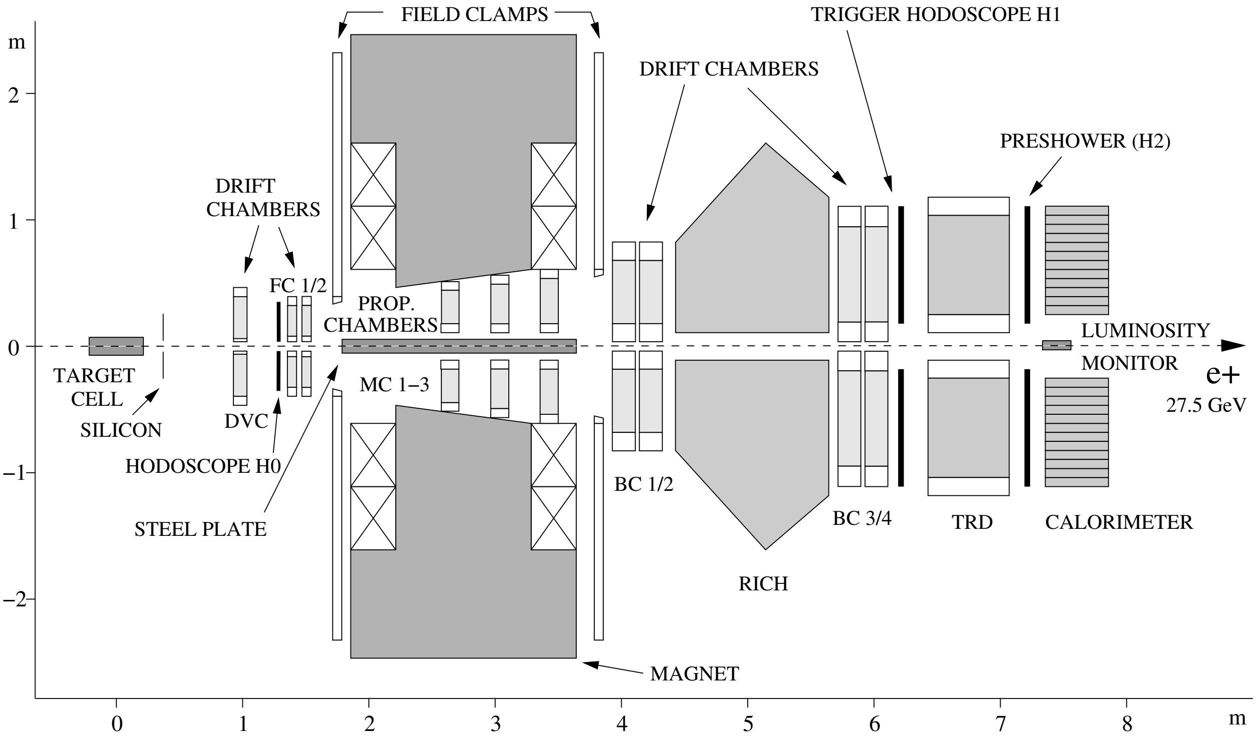

Figure 4.2: A schematic view of the HERMES spectrometer.

The HERMES forward spectrometer [67] consists of two halves of virtually identical modules placed above and below the beam pipe. The magnet creates a vertical magnetic dipole field with an integrated field strength of maximum 1.5 T m. A septum plate in the (x, z)-plane at $y = 0$ (in the septum of the magnet) is used to shield the beam from the strong magnetic field. The field clamps in front of and behind the magnet coils reduce the outer fringe fields.

Inside the magnet the particle tracks are bent horizontally such that only small deviations are expected in y, larger ones in x. The bending radius is proportional to the particle's momentum. Outside the magnet the particle tracks are straight lines.

4.3.1 Tracking Detectors

The purpose of the tracking system is the precise determination of the particle trajectories and momenta using a magnet and a set of drift chambers. The reconstruction program makes use of two methods: the tree-search algorithm for fast track finding and a look-up table for fast momentum determination of the tracks.

Charged particles passing through a gas lose energy by ionisation of the atoms and molecules. E.g., for a pion moving in argon gas, in the ionisation process $\pi\, Ar \rightarrow \pi\, Ar^+\, e^-$, positively charged argon ions Ar^+ and free electrons e^- are produced along the pion path. In the presence of static electric field the electrons e^- (the Ar^+ ions) drift to the anode (cathode) creating a detectable electric signal. By measuring the drift time of the electrons and knowing their drift velocity, the distance from the anode to the place of origin of the electrons (ions), and thus spatial information, is obtained.

The drift chambers DVC, FC 1/2, BC 1/2 and BC 3/4 (Fig. 4.2) are of conventional horizontal-drift type. The basic unit, a layer of drift cells, consists of a plane of alternating anode and cathode wires between a pair of cathode foils. The cathode wires and foils are at negative high voltage of a few thousand volts with the anode sense wires at ground potential. The cells are filled with a gas mixture of $Ar(90\%)/CO_2(5\%)/CF_4(5\%)$, which is both fast and non-flammable. The drift velocity is, e.g., $> 7\,\frac{\mathrm{cm}}{\mu\mathrm{sec}}$ at $E = 800\,\frac{\mathrm{V}}{\mathrm{cm}}$. The DC-readout system consists of Amplifier/Shaper/Discriminator (ASD) cards mounted onboard the drift chambers, driving ECL signals on 30 m long flat cables to LeCroy 1877 Multihit FastBus TDCs in an external electronics trailer.

Each drift chamber module is capable of measuring a space point (hit) with (x, y, z)-coordinates. The z-coordinate is directly given by the position of the module along the longitudinal z-axis. Since wires with at least three different orientations are needed to reconstruct unambiguously an unique point in the vertical (x, y)-plane, each modules consists of three vertical layers with wires arranged in three coordinate doublets, UU', XX', and VV'. The wires are vertical for the X layer and at an angle of $\pm 30°$ to the vertical for the U and V layers. The X', U', and V' layers are staggered with respect to their partners by half the cell size in order to resolve the remaining left-right ambiguities. The average efficiency of a layer is typically above 99% for lepton tracks, whereas it drops to 97% when all tracks (mainly hadrons) are considered, due to the smaller energy deposited in the chambers by hadrons. The spatial resolution per layer is about 220 μm for the DVC, 225 μm for the FC 1/2, and 275 μm (300 μm) for the BC 1-2 (3-4).

The track finding is based on pattern recognition using the tree-search algorithm. This is possible because the particle track can be well approximated with an unique pattern of drift chamber hits. All allowed patterns (about 10^8 in total but in fact 50000 after symmetry considerations) are generated and stored in a database. The pattern recognition algorithm consists in looking at the whole pattern of actual hits in the drift chambers with increasing resolution and comparing at each step the measured pattern with the data base of allowed tracks. Only the patterns consistent with an allowed track are retained (tree-search). The search continues until the full detector resolution is reached (typically in 14 steps). Since no calculation of track parameters is done during processing, the tree-search algorithm is very fast. By using hits from the DVC and FCs, and separately from the BCs, 'partial' front and back tracks are reconstructed uniquely in space. In those regions the tracks are approximately straight lines. All combinations of front and back tracks are tested to see if they match spatially within a specified tolerance at the (x, y)-plane in the centre of the magnet (Fig. 4.2). For each associated pair, the front-track is forced to agree with the magnet mid-point of the back track, and then the front track is recomputed accordingly. This procedure improves the resolution of the front-tracking system (DVC and FCs).

The momentum measurement, similarly to the track finding procedure, avoids the time consuming computations on a track by track basis. Instead, 520000 tracks with different momenta are generated and their trajectories in the inhomogeneous field of the magnet are computed once and stored in a look-up table. The table contains the momentum of a given track as a function of the track parameters in front of and behind the magnet. For the actual momentum measurement the track parameters of a measured track are compared to the table values. The number of stored tracks in the table is chosen such that the actual track momentum is determined with a resolution of better than $\frac{\Delta p}{p} = 0.5\%$, using interpolation methods.

4.3.2 Particle Identification

A charged particle passing through matter causes the emission of so called Cherenkov radiation whenever the velocity of the particle, v, is greater than the velocity of light in the traversed medium, v_t,

$$v(= \beta c) > v_t(= c/n), \tag{4.12}$$

where n is the refractive index of the medium, c is the velocity of light in vacuum, v_t denotes the sought threshold velocity, and $\beta = v/c$. The photons from the Cherenkov radiation are emitted under a constant angle, θ_c, with respect to the direction of the moving particle

$$\theta_c = \arccos{(v_t/v)} = \arccos{(1/\beta n)}, \tag{4.13}$$

so that the faster the particle, the larger the angle. The Cherenkov photons thus lie on a cone which projects to a circle in a plane perpendicular to the direction of the moving particle. The fastest particles (of a given type) with $\beta = 1$ produce the maximum emission angle $\theta_c = \arccos{(1/n)}$ provided their exact value of β (γ) exceeds the threshold given by

$$\beta_t = 1/n = v_t/c \quad (\gamma_t = n/\sqrt{n^2 - 1}), \tag{4.14}$$

where $\gamma = 1/\sqrt{1 - \beta^2}$ is the Lorentz factor.

The above set of relations and the particle kinematics ($E^2 - |p|^2 = m^2$, $\beta = p/E$) give

$$p_t/\sqrt{p_t^2 + m^2} = 1/n \quad \rightarrow \quad p_t = m/\sqrt{n^2 - 1}, \tag{4.15}$$

$$\theta_c = \arccos{(pn/\sqrt{p^2 + m^2})}. \tag{4.16}$$

This allows one to find the threshold momentum, p_t, which a particle with mass m must possess to produce Cherenkov radiation in the detector material with a known index of refraction n. For the same material, different particles (pions, kaons, protons) have different threshold momenta because $m_\pi < m_K < m_p$. Reversely, by measuring the momentum of an unknown particle in the experiment and just by counting the presence or absence of Cherenkov radiation, some information about the particle mass, and thus its type, can be inferred. The unambiguous separation of particles requires the Cherenkov angle θ_c to be measured in addition to the momentum, and that is the basic principle of particle identification with the ring imaging Cherenkov detector.

Cherenkov Counter

The HERMES single-gas radiator threshold Cherenkov counter [67] provides only pion identification. The radiator is a gas mixture of 70% nitrogen, N_2, and 30% perfluorobutane, C_4F_{10}, with a refractive index of $n = 1.000629$. The Cherenkov threshold momenta for leptons, pions, kaons, and protons are 0.014, 3.8, 13.6, and 25.8 GeV, respectively. Thus the passage of all leptons results in an emission of Cherenkov radiation. The momentum range over which pions can be distinguished from other hadrons spans from 3.8 to 13.6 GeV. Even below 13.6 GeV kaons cannot be cleanly identified because of contamination from pions whose Cherenkov radiation is not detected due to the few percent inefficiency of the counter. The counter was operational in 1995-1997 and was upgraded to a RICH in 1998.

Ring Imaging Cherenkov Detector

The HERMES dual-radiator ring imaging Cherenkov (RICH) [69] detector provides particle identification for pions, kaons, and protons in the momentum range from 2 to 15 GeV, covering most of the kinematic acceptance of the experiment. This difficult range was inaccessible to conventional techniques until 1998 when new technology became available. It relies on the development of new clear silica aerogel with a low index of refraction and excellent optical properties. The first successful use of clear silica aerogel in a combination with a heavy gas, C_4F_{10}, in a RICH detector was realised at HERMES. This dual-radiator configuration was first proposed for the LHCb experiment.

A particle passes through the 5.5 cm aerogel wall at the entrance of the detector and then through the rest of the volume filled with gas. A spherical mirror array located at the rear of the radiator box images the Cherenkov radiation cones onto a focal surface located above (below) the active volume of the upper (lower) half. This surface is instrumented with an array of photomultiplier tubes (PMTs) which detect the photons from the Cherenkov rings. The Cherenkov angle θ_c is reconstructed from the PMT hit pattern. The angle versus the hadron momentum for the two radiators and the three hadron types is plotted in Fig. 4.3. The indices of refraction for the two radiators, the threshold momenta for positrons, pions, kaons, and protons and the maximum separation momenta can be found in Table 4.3. The latter is defined as the maximum momentum for which the angle θ_c for two particle types is separated by 4.65 standard deviations of the reconstructed photon angle distribution σ_θ. A value of $\sigma_\theta \approx 7$ mrad—also called the single photon resolution—was measured for aerogel and gas.

Pion identification with the RICH is essential for the following analysis. The lower limit of the momentum range in which a detected hadron track can be identified as a pion is given by the pion threshold momentum $p_t = 0.6$ GeV for the aerogel radiator. The upper limit is restricted to the pion/kaon maximum separation momentum $p_{max} = 15$ GeV for the C_4F_{10} radiator. Above this value the Cherenkov rings produced by pions and kaons become indistinguishable in the detector.

Particle Identification with the RICH Detector

The particle identification scheme is described and the 'quality' of the identification within this scheme is explained below.

The analysis of the PMT-matrix hit pattern is complex due to background hits, sparse number of signal hits on the ring, and distortions from a simple ring structure. To find the Cherenkov angle θ_c corresponding to a ring, the inverse ray tracing method (IRT) is used, see references 8-9 in [69]. This algorithm reconstructs two θ_c angles for each hit, assuming that the hit is coming from a photon emitted in the aerogel and in the gas, respectively. The

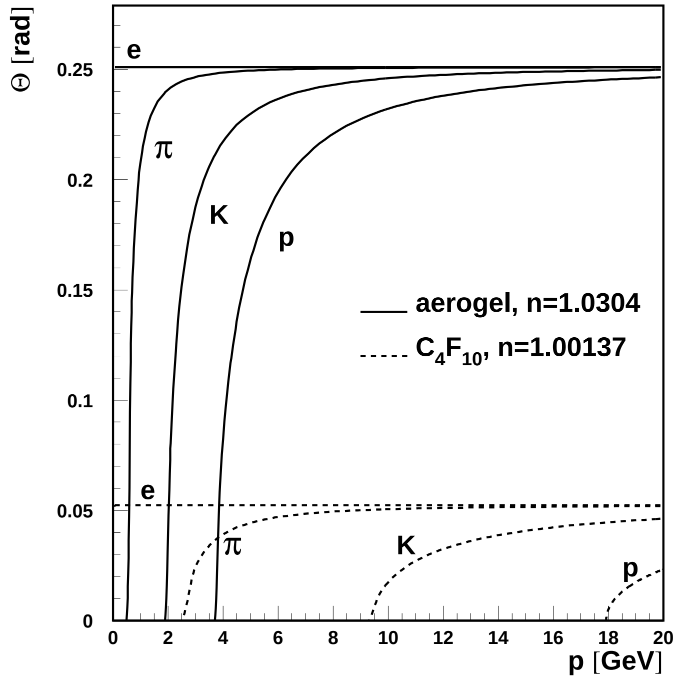

Figure 4.3: The Cherenkov angle $\theta \equiv \theta_c$ versus hadron momentum for the aerogel and C_4F_{10} radiators. Figure taken from [69].

	Aerogel	C_4F_{10}
n	1.0304	1.00137
$\beta_t\gamma_t$	4.03	19.10
$p_t(e)$	2.06 MeV	9.76 MeV
$p_t(\pi)$	0.6 GeV	2.7 GeV
$p_t(K)$	2.0 GeV	9.4 GeV
$p_t(p)$	3.8 GeV	17.9 GeV
$p_{max}(\pi/K)$	6.7 GeV	15.0 GeV
$p_{max}(K/p)$	11.2 GeV	25.3 GeV

Table 4.3: Cherenkov radiation threshold momenta (p_t) and maximum separation momenta (p_{max}) for pions, kaons, and protons. The index of refraction n is given at 633 nm.

theoretically expected angles θ_c^{th} (4.16) for aerogel and gas are calculated for each particle type hypothesis (m_π, m_K, m_p) from the measured track momenta. For each radiator and for each particle hypothesis, an average Cherenkov angle $\langle\theta_c\rangle$ is then calculated including only the reconstructed angles θ_c within $\pm 4\sigma_\theta$ of the theoretically expected angle. Here σ_θ is the single photon resolution of the RICH detector.

The distributions of reconstructed average angles are normalised such as to form a probability (density function, p.d.f.) and this probability is used to form a likelihood. Assuming that the average angle distribution has Gaussian shape and its resolution is independent of the particle type, the normalisation of the probability distribution is chosen so that the maximum value of the likelihood is unity, namely,

$$L(\langle\theta_c\rangle) = \exp[-\frac{(\theta_c^{th} - \langle\theta_c\rangle)^2}{2\sigma^2_{\langle\theta_c\rangle}}], \tag{4.17}$$

where $\langle\theta_c\rangle = \sigma_\theta/\sqrt{N}$ is the average angle resolution for N hits.

The likelihoods for the two radiators are multiplied to give an overall likelihood for each particle hypothesis $h = \pi, K, p$, that is $L_h = L_h^{aerogel} \cdot L_h^{gas}$. The particle is assigned the type with the highest likelihood. To avoid the cases when two hypotheses are equally likely, a quality parameter is introduced as the logarithmic ratio of the two most probable particle hypotheses, $rQp = \log_{10} \frac{L_{h_1}}{L_{h_2}}$. In the analysis, the rQp parameter is required to be larger than zero. Recall the maximum value L_{h_1} and L_{h_2} can take is unity.

4.3.3 Lepton-Hadron Separation

While the RICH detector provides particle identification for hadrons (pions, kaons, and protons), the discrimination between hadrons and leptons (e.g., scattered beam positrons) requires information from other detectors. The lepton-hadron separation detectors can be characterised by a pion rejection factor (PRF), defined as the ratio of the total number of incident hadrons (most hadrons being pions) to the number of hadrons that are misidentified as leptons.

In certain kinematic regions the hadron production can exceed the rate of positrons by a factor 400 : 1. In an offline analysis, by combining the data from up to four detectors, a pion rejection factor (PRF) of at least 10^4 is reached, thus keeping the contamination of the positron sample by hadrons below 1% for the whole kinematic range.

Transition Radiation Detector

The transition radiation detector (TRD) provides a pion rejection factor (PRF) of at least 130 for 90% positron efficiency at 5 GeV and above.

When a charged particle with velocity $\beta = v/c \approx 1$ traverses the boundary between two materials, it produces so called transition radiation. The (X-ray) photons from the radiation are emitted at an angle $\theta = 1/\gamma$ ($\gamma = 1/\sqrt{1-\beta^2}$), so that they almost coincide with the direction of the moving particle. The intensity of the photon flux is proportional to $m\gamma$, where m is the particle's mass. These properties of the radiation determine the TRD design.

The HERMES TRD consists of six contiguous fibre radiator modules. A module is 6.35 cm thick and consists of (VILEDON C 1900/034) fibres of 17...20 μm diameter put in a material with a density of 0.059 g/cm^3. The fibres are interspersed pseudo-randomly but predominantly in a two dimensional matrix, thus forming an average of 267 transition layers. Such a configuration is found to give an optimal photon flux. Adjacent to the rear side of each radiator is a 2.54 cm thick multi-wire proportional chamber (MWPC) filled with a gas mixture of 90% xenon, Xe, and 10% methan, CH_4. This gas is an efficient X-ray absorber. Positrons, hadrons, and transition radiation photons deposit energy by creating electrons and ions in the gas. These charges drift in the +3100 V electric field and are collected on the electrodes of the chamber. The signal is proportional to the deposited energy, while the deposited energy, E, depends on the particle momentum.

Due to the transition radiation and the relativistic rise in in the energy loss, $\frac{dE}{dx} \sim \frac{1}{\beta^2}$, positrons deposit on average approximately twice the amount of energy deposited by hadrons.

Preshower

The lead-scintillator preshower counter (H2) provides trigger signals and lepton-hadron separation information. A pion rejection factor (PRF) of ~ 10 is possible with 95% efficiency for positron detection.

The particles/photons in the experiment carry enough energy to ionise an atom by removing an electron from its orbit. This happens when they pass through the 1 cm thick plastic material (BC-412 from Bircon Co.) of the H2 counter. The de-excitation of the displaced electrons results in scintillation—emission of short light pulses. The light from each 9.3 cm-wide 91 cm-long scintillator strip of H2 is detected by a photomultiplier tube (Thorn EMI 9954).

A passive radiator consisting of 11 mm (two radiation lengths) of lead, Pb, sandwiched between two 1.3 mm stainless steel sheets, is placed in front of the scintillator. The traversing particles initiate electromagnetic showers in the radiator. Part of the shower energy is deposited in the scintillator. Typically positrons produce a broad distribution of deposited energies (with a mean of 20...40 MeV), while hadrons give a narrow peak at lower energies (only about 2 MeV for pions).

Calorimeter

The calorimeter provides a first level trigger for scattered positrons based on energy deposition ($\geq 3.5\,\mathrm{GeV}$ or $\geq 1.4\,\mathrm{GeV}$) in a localised spatial region. It also provides a hadron rejection exceeding 10 at the trigger level and a further off-line pion rejection factor (PRF) of about 100.

The calorimeter consists of radiation resistant F101 lead-glass blocks with a face area of $9\,\mathrm{cm} \times 9\,\mathrm{cm}$ and a length of 50 cm (about 18 radiation lengths) along the beam. This block size meets the requirement that about 90% of the shower is contained in the block for an axially-incident positron. Each block is coupled to a photomultiplier tube (Philips XP3461). The sum of the signals in the hit block and in the eight surrounding blocks accounts for more than 99% of the signal created by the electromagnetic shower. This 3×3 array is called a cluster in the following. The performance of a 3×3 array of counters in a test beam gives the following parameters, (i) an energy response to electrons linear within 1% over the energy range 1...30 GeV, (ii) an energy resolution that can be parameterised as $\frac{\sigma(E)}{E}[\%] = \frac{5.1\pm1.1}{\sqrt{E[\,\mathrm{GeV}]}} + (1.5 \pm 0.5)$, similar to that obtained for other large lead-glass calorimeters, and (iii) a spatial resolution of the impact point of about 0.7 cm.

Separation Algorithm

The algorithm to discriminate between lepton and hadron tracks is based on Bayesian statistics. The Bayes' theorem gives for each track the conditional probabilities $P(H_l|E,p,\theta)$ and $P(H_h|E,p,\theta)$ for the hypotheses H that a track is a lepton l and a hadron h, respectively, given the track momentum p, its polar angle θ, and an energy deposition E in the detector

$$P(H_{l(h)}|E,p,\theta) = \frac{P(H_{l(h)}|p,\theta)\ P(E|H_{l(h)},p)}{\sum_{i=l,h} P(H_i|p,\theta)\ P(E|H_i,p)}. \tag{4.18}$$

Hence the sought lepton (hadron) probability can be computed from the probability (the parent distribution) $P(E|H_{l(h)},p)$ that a lepton (hadron) with momentum p will deposit an energy E in the detector and the prior probability (the particle flux) $P(H_{l(h)}|p,\theta)$ that a track with momentum p and polar angle θ is a lepton (hadron). The denominator acts as a normalising constant resulting from the requirement that the sum of the probabilities for the two hypotheses should be 1. The detector responses are assumed to be uniform within the detector's acceptance and therefore independent of θ.

For convenience, the conditional probabilities $P(H_l|E,p,\theta)$ and $P(H_h|E,p,\theta)$ are converted into a logarithmic likelihood ratio

$$L = \log_{10}\frac{P(H_l|E,p,\theta)}{P(H_h|E,p,\theta)} = \log_{10}\frac{P(E|H_l,p)\ P(H_l|p,\theta)}{P(E|H_h,p)\ P(H_h|p,\theta)} = PID - \log_{10}\Phi, \tag{4.19}$$

where

$$PID \equiv \log_{10}\frac{P(E|H_l,p)}{P(E|H_h,p)} \quad \text{and} \quad \Phi \equiv \frac{\phi_h}{\phi_l} \equiv \frac{P(H_h|p,\theta)}{P(H_l|p,\theta)}. \tag{4.20}$$

This scheme allows one to combine the responses of several detectors in order to achieve a better lepton-hadron separation compared to the capabilities provided by each detector separately. The information of all detectors is taken into account in the sum of the PID-values for each detector

$$PID = PID_{cal} + PID_{pre} + PID_{rich} + PID_{trd}, \tag{4.21}$$

where $PID_{rich} = PID_{aerogel} + PID_{gas}$ is the sum of the probability ratios for the aerogel and gas response, and $PID_{trd} = \sum_{i=1}^{6} PID_{trd,i}$ is the sum over the six TRD modules. PID values commonly defined are

$$\begin{aligned} PID2 &\equiv PID_{cal} + PID_{pre}, && (4.22)\\ PID3 &\equiv PID_{cal} + PID_{pre} + PID_{rich}, && (4.23)\\ PID5 &\equiv PID_{trd}. && (4.24)\end{aligned}$$

The lepton-hadron separation is based on the following requirements

$$\begin{aligned} L &= PID3 + PID5 - \log_{10}\Phi > 0 \Leftrightarrow \text{lepton}, && (4.25)\\ L &= PID3 + PID5 - \log_{10}\Phi < 0 \Leftrightarrow \text{hadron}. && (4.26)\end{aligned}$$

The parent distributions $P(E|H_{l(h)}, p)$ for a given detector are extracted from data recorded during normal running of the experiment. For this purpose clean lepton (hadron) samples are selected by imposing stringent cuts on the responses of the other lepton-hadron identification detectors. For the determination of the flux value Φ the PID value is a necessary input which in turn depends on Φ, therefore Φ is calculated in an iterative procedure from the same data. More details on the lepton-hadron separation algorithm are given in references Wen99 and Wen01 in [45].

4.4 The Luminosity Monitor

The luminosity monitor [71] is a stand-alone detector system with high live-time for precise measurement of the luminosity. The luminosity $\mathcal{L} = \frac{\rho I}{e}$ is the product of the target density ρ and beam current I, normalised to the elementary beam charge e. Although each of these components can be measured separately, the product can be determined much more accurately using the luminosity monitor (LUMI).

The luminosity measurement with LUMI is based on the observation of elastic scattering rates R of beam positrons off target gas electrons $e^+e^- \rightarrow e^+e^-$ (Bhabha scattering) or of positron–electron annihilation into photon pairs $e^+e^- \rightarrow \gamma\gamma$, or, with an electron beam, on elastic electron-electron scattering $e^-e^- \rightarrow e^-e^-$ (Møller scattering). The cross sections σ for these processes are known precisely from theory. Thus the luminosity is obtained from

$$\mathcal{L} = \frac{R}{\sigma_{\Delta\Omega}}, \quad \sigma_{\Delta\Omega} = \int_{\Delta\Omega} d\Omega\, \varepsilon \left(\frac{d\sigma}{d\Omega}\right), \tag{4.27}$$

where $\sigma_{\Delta\Omega}$ is the integral of the differential cross section for the process over the acceptance $\Delta\Omega$ of the luminosity detector, taking into account the detector efficiency ε. The integrated luminosity

$$L = \int_{\Delta t} dt\, \mathcal{L} \tag{4.28}$$

is the measured luminosity $\mathcal{L}$ integrated over the time of measurement Δt corrected for dead-time effects.

For a beam energy of 27.56 GeV the symmetric scattering angle is 6.1 mrad, both scattered particles have half of the beam energy, and their tracks lie in a plane. These particles leave the beam pipe at 7.2 m after the centre of the target cell and are detected in coincidence by two small calorimeters (with a horizontal acceptance of 4.6-8.9 mrad). Upon impact on the calorimeter faces the scattered particles initiate an electromagnetic shower and deposit their energy. Most of the background events have a high energy deposition in only one of the detectors, while Bhabha events have a high energy deposition (reduced by lateral shower leakage) in both detectors. The latter type of events are separated from background by triggering on a coincident signal with energy above 4.5 GeV in both the left and right calorimeter. This coincidence rate is the high statistics LUMI rate R. The cross section $\sigma_{\Delta\Omega}$ is calculated from a Monte Carlo simulation, which requires knowledge of the four beam parameters ((x, y)-positions and slopes) at the HERMES interaction point. Given that the measurements of the beam position monitors are not always reliable, the parameters are extracted from the LUMI data at the position of the LUMI detector. The systematic uncertainty for absolute (relative) luminosity measurements is 6.3-6.4% (0.9-1.5%).

4.5 Data Collection

4.5.1 Trigger

The trigger hodoscope H1 is identical in construction to H2 in the preshower detector described above. Each half (top and bottom) of H0 consists of one 3.2 mm (0.7% of a radiation length) thick scintillator paddle coupled to two photomultiplier tubes.

The beam intersects the target once every 96 ns, i.e., at a rate of 10 MHz. As the produced particles pass through the sensitive components of the detectors, the effects from the passage are converted into electronic signals kept in buffers of the electronic modules. The signals are further saved upon a trigger occurring within $\sim$ 400 ns of the interaction, otherwise they are lost. This first-level trigger is formed from the hit information in the fastest detectors. Also higher-level triggers, which require further signal processing and occur on time scales of 50 μs, few-100 μs, and $\leq$ 1 ms, are implemented in the trigger logic, however they are found to be unnecessary in practice and are not used in the experiment.

The main physics trigger (numbered 21) used to select the events in this analysis requires the coincidence of

- hits in the three scintillator hodoscopes H0, H1, and H2,
- deposited energy in two adjacent columns of the calorimeter above 3.5 GeV

in the top or in the bottom half of the detector, and in coincidence with the HERA clock signal. These conditions are fulfilled by a single particle traversing one full detector half. The signal in the preshower H2, required to exceed the minimum ionising signal, and the calorimeter threshold increase the probability that the particle is a positron from the deep inelastic scattering (DIS) process, rather than a hadron (Section 4.3.3). The trigger-21 rate varies between 50...100 Hz depending on the beam current, the target density, and the beam background conditions (e.g., Bremsstrahlung, influence from the proton beam) during data taking. However, not all particles that pass the trigger-21 requirements belong to a DIS process. It turns out later that 4...6% of these triggers are identified as DIS interactions in the analysis.

4.5.2 Data Acquisition

The data acquisition system is able to cope with rates up to 500 Hz with dead times below 10%. A measure of the dead time is the ratio of the number of generated ($N_{generated}$) and the number of accepted ($N_{accepted}$) triggers. The dead (live) time τ_{dead} (τ_{live}) is defined as

$$\tau_{dead} = 1 - \tau_{live} = 1 - \frac{N_{accepted}}{N_{generated}} = \frac{N_{generated} - N_{accepted}}{N_{accepted}} = \frac{N_{rejected(or\ missing)}}{N_{generated}}. \qquad (4.29)$$

While the DAQ is busy processing the event from a previous trigger, no new triggers can be accepted.

Physics Event

The trigger initiates the digitisation by the readout electronics of the signals in all detectors. The drift chamber signals are digitised using LeCroy 1877 TDCs (Time to Digital Converters), while the TRD chambers and the charges from the various photomultiplier tubes are digitised by LeCroy 1881M ADCs (Analog to Digital Converters). The magnet chamber and RICH readout is instrumented with VME based PCOS4 system, consisting of LeCroy 2749 and LeCroy 2748 modules. The vertex chamber signals are handled by a Struck ECL interface. The electronic modules are located either in the vicinity of the detectors or in an electronics trailer separated at an effective distance of $\sim 30\,\mathrm{m}$ cable length from the experiment.

The output data (in the form of bit words) from the electronic modules (TDCs, ADCs, etc.) are handled by 10 Fastbus crates—the backbone of the data acquisition (DAQ) system. The (set of) Fastbus crate(s), corresponding to each detector, is read out by a single dedicated CERN Host Interface (CHI) (STR330) Fastbus master. Pairs of detector Fastbus crates are connected via Cluster Interconnects. To enhance the readout performance of the CHIs (e.g., for a second-level triggering), the (TRD and calorimeter) CHIs are equipped with Struck Fastbus Readout Engines (STR330/FRE), featuring one or two Motorola 96002 Digital Signal Processors (DSPs). The CHIs (or the DSPs in case of second-level triggering) receive the physics event trigger and read the ADC and TDC information into their memory (or FIFO in case of the DSPs). Most of the programs running on the CHIs and DSPs are in assembly language, however high-level code (in Fortran and C) is ported as well to allow an easy modification of the setup, e.g., the addition of new digitising modules.

The detector CHIs send their data to the CHI of an Event Collector Fastbus crate via Segment Interconnects. Upon reading data from all detectors, the Event Collector's CPU executes a routine which converts the data in EPIO (Experimental Physics Input Output Package) format [1] in the memory of the Event Collector.

Slow Control

The trigger and flow of data described above are driven by the beam-target interactions. Asynchronously to the physics trigger, data generated by 'user' triggers and various scalers are also collected over the course of the data taking. These scaler and 'user' events are handled in parallel and independently from the physics events.

Scaler data are taken over a 10 s period called a burst. Scaler modules (counters), coupled to a detector, produce just counts. Scaler counts are, e.g., the luminosity monitor trigger rate (exceeding 5 kHz) and the number of generated and accepted physics triggers during a burst. Slow-control data come from the readout of detector parameters that change on a slow ($\sim$ minutes) time scale. Examples are the high voltage settings and the beam current. Scaler, slow-control, and other calibration tasks are handled by a suite of programs running continuously on the computers in the control room, using Fastbus, Camac, VME, or RS232 interface to the respective detectors. Depending on the task, the data are either collected directly by the Event Collector Fastbus crate during idle time between physics events, or by dedicated additional Fastbus crates and then 'injected' as so called user events into the DAQ data stream. For example the data from the longitudinal polarimeter (LPOL) [68] form an user event.

Raw Data

The event is the smallest unit within the EPIO data structure. The different type of events,

- physics event (trigger-21),

- scaler event (data obtained from Fastbus scalers every 10 s),
- user event (slow-control and calibration data injected at the start of each run),

are sent from the Event Collector via Fibre Optical Link (STR330/FOL) to the CHI of the Event Receiver Fastbus crate (in the control room). There the accumulated events are packed into chunks called runs. Each run corresponds to one file of data. The file volume, 450 MB (or typically 10 min of data taking), is limited by the EPIO structure. The Event Receiver is connected via SCSI interface to a computer (Alpha OSF station, a Linux machine since 2002), where the raw data files are buffered on local disk. At the end of each fill the data are transferred to a taping robot at the DESY main site via an FDDI (Fibre Distributed Data Interface) link. In addition, they are backed up locally onto DLT magnetic tapes.

4.5.3 Data Organisation and Event Reconstruction

Main Production

The layout of the offline software is shown in Fig. 4.4. Any sensitive detector component (e.g., wire, scintillator paddle, PMT) holds a channel number. The channels' number and reading for each detector are the actual data stored in the EPIO files. The raw data are passed to a HERMES DeCoder package (HDC) that converts the numbers into physics quantities (hit coordinates and deposited energies) via mapping (of a readout channel to a physical detector component), calibration (of the reading to an energy), and geometry (of the component in the HERMES coordinate system (Section 4.3)). The program filters the physics events from the slow-control and user events, and stores the output in separate files in ADAMO format [2]. The physics event data are passed to the HERMES ReConstruction package (HRC) that uses the wire chamber hits to assemble tracks in the detector and to compute the tracks' momenta (Section 4.3.1). For each track the package also provides a link between the track and the amount of deposited energy in the particle identification detectors. During the Main Production chain the data are passed through intermediate programs (in addition to HDC and HRC) which perform specific tasks, e.g., correction of the PMT gains with input from the Gain Monitoring System (GMS), target magnet correction, computation of tracking plane efficiencies.

Slow-Control Production

The slow-control in combination with the tracking efficiency data serve as input both to the Slow-Control Production and to the Quality Control package. In addition, this production receives as an input external (non-physics event) data provided by the subdetector experts (after some analysis of the raw data) and so called fill-files with data collected by the online monitoring server-client software during the fills (one file per fill). For example, the beam polarisation (LPOL [68], TPOL [64]) information is provided externally. The purpose of the Slow-Control Production is to collect data from the three (four, including the mapping-calibration-geometry) different sources and to merge them in a specific way so that initially one file per run is produced, and finally the slow-control data for all runs contained in a fill are kept in one single file. The data quality information, when ready, is incorporated into the Slow-Control Production as well, resulting in enhanced final slow-control data files.

The main concern of the slow-control production is the time synchronisation (on the millisecond level) of the collected data. The data coming from different sources are merged into a time ordered fill-file by using their time stamps.

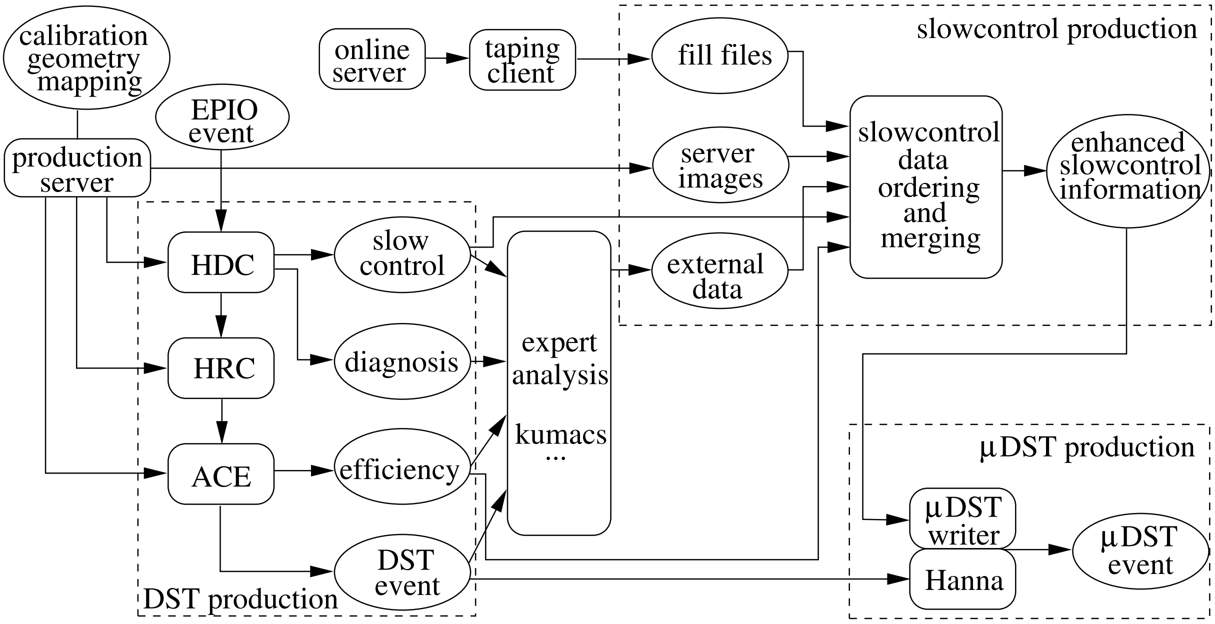

Figure 4.4: Layout of the data processing and production chain.

μDST Production

The μDST production produces a single data file for each run which contains the tracking data from the Main Production (HRC) for selected events only, the relevant slow-control data from the slow-control production, and the data quality information. The HRC and slow-control files are two data streams that contain data collected on different time scales. The time stamps of the data are used to associate events from HRC files with the calibrations and other measurements recorded in the slow-control files. The μDST production also reads subdetector expert files containing offline calibrations related to data quality (run or burst is thrown away if a detector experienced a fault). Example expert files are the parent distributions for the PID, and calibrated polarisation information from the target group. The PID and other calculations are performed as well.

These very final files, called μDSTs, can be reliably used for physics analysis by the analysers to produce physics results without considering the details of the data collection. There is one file per data taking run. The μDST files are much smaller than the HRC files because only the information needed for physics analysis is being written, e.g., events that do not originate from trigger-21 and events with one track only are discarded. The μDST files are organised at burst, event, and track level. However the fundamental organisation is at the burst level, i.e., each burst corresponds to one ADAMO record in the μDST file. Within each burst there may be many events, each of which may contain many tracks. A utility library is available, which navigates the analyser through the track-event-burst structure during the analysis.

Data Quality

At the last stage of the offline data production, each μDST production is carefully checked by the data quality group, which prepares plots of all important detector quantities versus the run number and goes through them looking carefully for regions where there is a problem. After the source has been identified, e.g., missing input file from subdetector expert or runs failed the production for some reason, the μDST production is repeated.

The data quality information is encoded in a burstlist, prepared by the data quality group and made available to the analysers. It happens that during some bursts or entire runs, part of the experiment is malfunctioning (due to a failure of some device). Such periods are marked as 'bad' and later the analysers must exclude these data to avoid biasing the physics results. There are up to 32 data quality conditions (one 8-digit hexadecimal number) predefined for each μDST production. A Data Quality program tests each burst in the μDST production against each condition. The condition can be either fulfilled or not, thus the corresponding bit is set either to 0 or 1. In Section 6.1 the quality of the data used in this analysis is checked and 'bad' data are removed.

Chapter 5

Monte Carlo Simulation

5.1 Monte Carlo Generators

The physics aspects of the two Monte Carlo (MC) event generators used in the studies are described. Since no single generator is available that can reproduce the event distributions of the data, one generator is used to simulate the signal and the other generator serves to describe the background.

5.1.1 Generator for Exclusive Pion Production

The Monte Carlo generator gmc_exclpion (called 'exclusive MC' in the following) for exclusive π^+ events is developed and maintained by HERMES authors [42]. In this generator the production of single pions in hard exclusive positron–proton scattering is modelled according to

$$\frac{d\sigma_{UU}^{e^+p\rightarrow e^{+\prime}n\pi^+}(x,Q^2,t,\phi)}{dx\,dQ^2\,dt\,d\phi} \approx \frac{1}{2\pi}\,\Gamma_T(x,Q^2)\,\varepsilon(x,Q^2)\,\frac{d\sigma_{00}^{++}(x,Q^2,t,\phi)}{dt\,d\phi}, \tag{5.1}$$

where $\Gamma_T(x,Q^2)$ (3.11) is the flux of transverse virtual photons, $\varepsilon(x,Q^2)=\frac{\Gamma_L}{\Gamma_T}$ (3.12) is the ratio of transverse to longitudinal virtual-photon fluxes, and σ_{00}^{++} is the unpolarised photoabsorption cross section for longitudinal virtual photons (3.26). Note that here the azimuthal angle ϕ_S is integrated over, therefore one has the factor $\frac{1}{2\pi}$ in (5.1) instead of $\frac{1}{4\pi^2}$ in (3.15).

Several reasonable assumptions are made to obtain (5.1) from the exact theoretical expression for the unpolarised cross section (3.16), [27]. The approximation (3.18) is applied as well. We remind (Section 3.2) that $\sigma_T=\frac{1}{2}(\sigma_{++}^{++}+\sigma_{++}^{--})$ and $\sigma_{TT}=\,\mathrm{Re}\,\sigma_{+-}^{++}$ ($\sigma_{TL}=\,\mathrm{Re}\,(\sigma_{+0}^{++}+\sigma_{+0}^{--})$) are expected to be suppressed by at least one power of $\frac{1}{Q^2}$ ($\frac{1}{Q}$) compared to $\sigma_L=\sigma_{00}^{++}$, therefore they are neglected in (5.1) for this Monte Carlo simulation.

Method of Event Generation

The steps to generate an exclusive event with the exclusive MC according to the cross section (5.1) are summarised below. More details can be found in Table B.1 on page 113). See also Fig. 3.1 and Table 3.1 for definition of the kinematic variables.

- The skeleton of the event is set up by generating random values for the azimuthal angle $\epsilon=-\Phi_{e^{+\prime}}-\pi$ of the scattering plane and the azimuthal angle ϕ between the production and the scattering planes.

- The independent kinematic variables x, Q^2, and t are randomly generated (Table B.1).

- Other kinematic variables are calculated using constraints on the scattering kinematics and masses of the participating particles, all of which are explicitly known. The particles are attached onto the scattering and production planes by a sequence of rotations (Table B.1).

- A generated event can either be a non-radiative one or a radiative event which includes the radiation of a real hard photon γ. The radiated photon with energy E_γ is here generated by RADGEN [7] as for the case of deep inelastic scattering. The influence of initial or final state radiation is taken into account by replacing the energies of either the incoming or outgoing positron, $E \to E - E_\gamma$ or $E' \to E' - E_\gamma$, respectively. Thus the observed energy transfer $\nu = E - E'$ in a radiative event is always decreased by the energy of the radiated photon, $\nu \to \nu - E_\gamma$, compared to a non-radiative event. This gives rise to asymmetric shapes, known as radiative tails, in the distributions of some kinematic variables. A rough estimate for the size of the radiative effects (due to bremsstrahlung, vertex and loop diagrams) in exclusive electroproduction is obtained with EXCLURAD [6] applied to the HERMES kinematics, and is found to be about 20% with almost no dependence on x and Q^2.

- The physics of the simulated process resides in the photoabsorption cross section σ_{00}^{++} (5.1) for the process $\gamma_L^* p \to n\pi^+$, where γ_L is the longitudinal virtual photon. Two different parameterisations of the kinematic dependences of $\frac{d\sigma_{++}^{00}(x,Q^2,t)}{dx\,dQ^2\,dt}$, based on GPD models, are implemented in the simulation

  - Piller parameterisation [50]: the cross section is calculated as a function of t for $Q^2 = 2.4\,\mathrm{GeV}^2$ and $x = 0.1$, and as a function of x for $Q^2 = 2.4\,\mathrm{GeV}^2$ and $t = t_0$, $t = -0.4\,\mathrm{GeV}^2$. To obtain a description of the full kinematics (see (3.27)) an x dependence as x^2 and a Q^2 dependence as Q^6 are assumed.
  - VGG parameterisation [73]: the cross section σ_{00}^{++} is calculated over the full kinematic range using a source code based on the VGG model for deeply virtual electroproduction of mesons on the nucleon. The option for power corrections on the GPD $\widetilde{E}$ is chosen and the t dependence is modified by e^{-bt}, with $b = 3$, to obtain a better description of data.

  As shown in [41], the VGG model describes the data well in the kinematic variables x, Q^2, and t, while the Piller model shows a steeper Q^2 dependence than the data and an x distribution which is shifted to lower x values (figures not shown here). The VGG model is chosen for the following Monte Carlo studies. In practice, the VGG-code is used to produce the cross section $\frac{1}{4\pi^2}\frac{d\sigma_{00}^{++}(x,Q^2,t)}{dx\,dQ^2\,dt\,d\epsilon\,d\phi}$ uniformly in the azimuthal angles $\epsilon = -\Phi_{e^{+\prime}} - \pi$ and $\phi = \phi_{\pi^+}$ (Tables B.1, 3.1) at the generated x, Q^2, and t values of the event.

- Finally the weight of the event is calculated as the product

$$\Gamma_T\,\varepsilon \frac{1}{4\pi^2}\frac{d\sigma_{00}^{++}(x,Q^2,t)}{dx\,dQ^2\,dt\,d\epsilon\,d\phi}. \tag{5.2}$$

The weight (5.2) does not serve to accept or reject the event at the level of generation but it is stored and used later to weight the event in order to obtain meaningful distributions. The difference between weighted and unweighted distributions is relatively small (Figs. B.8–B.9).

Fluxes of Virtual Photons

Since no attempt is made in the data analysis (Chapters 6, 7) to extract the contribution to the measurements of longitudinal virtual photons only, here we briefly study the fluxes of longitudinal (Γ_L) and transverse (Γ_T) photons and the flux ratio $\varepsilon = \frac{\Gamma_L}{\Gamma_T}$ for our kinematics. The only way to separate the two contributions is via ε-variation, which is not possible in the context of this analysis.

The values of $\Gamma_T(x, Q^2)$ (3.11) and $\varepsilon(x, Q^2)$ (3.12) depend on the kinematics of the individual event. The two independent kinematic variables y (via $x(y) = \frac{Q^2}{2M_p E y}$) and Q^2 are chosen to evaluate the expressions $\Gamma_T(y, Q^2)$ and $\varepsilon(y, Q^2)$ per event. The distributions obtained from a large number of events, as well as the values of the product $\Gamma_T\,\varepsilon$ and of the event weight (5.2), can be seen in Fig. 5.1. The plots in the left column contain the results for data and simulated events (using the exclusive MC and PYTHIA, see next section). Data and PYTHIA events are normalised as described in Sections 6.4.1 and 5.1.2, respectively. Since the exclusive MC cannot provide an absolute cross section, its distributions are scaled arbitrarily to the highest data point. The form of $\varepsilon(y, Q^2)$ as a function of y for a fixed $Q^2 = 2.4\,\mathrm{GeV}^2$ and its dependence on Q^2 at a fixed value of $y = 0.465$ are also shown on the figure.

The Γ_T and $\Gamma_L = \Gamma_T\,\varepsilon$ distributions are peaked at $0.002\,\frac{1}{\mathrm{GeV}^2}$. Values of $\varepsilon = \frac{\Gamma_L}{\Gamma_T} = 0.92$ are found for the largest fraction of events. The average ratio of the fluxes ($\langle\varepsilon\rangle_{Data} = 0.80$, $\langle\varepsilon\rangle_{PYTHIA} = 0.81$, and $\langle\varepsilon\rangle_{excl} = 0.86$) is still close to the maximum possible value of $\varepsilon = 1.0$. The distribution of the event weight (5.2) for the exclusive MC ranges between 0 and 2.5 with a peak at 0.2.

5.1.2 PYTHIA 6.2 Generator

In this study PYTHIA [55, 56] is chosen to generate simultaneously a wide range of processes assumed to take place in the experiment, excluding however exclusive and resonance production whose overall contributions are considered to be small. The original PYTHIA code is tuned to data from high energy collider experiments. In the default version for use at the moderate energy range of HERMES some of the fragmentation parameters are adjusted to the HERMES semi-inclusive data [45]. For this work, a special version of PYTHIA 6.2 is used, in which in addition the parameters for diffractive and exclusive vector meson production are carefully tuned [49]. The Monte Carlo studies presented here are based on the latest PYTHIA tune with the best set of parameters (denoted as '2004c').

The positron–proton cross section is factorised into the flux of virtual photons and the subsequent interaction of these photons with the target protons ([51]). In terms of the PYTHIA process numbering scheme, the main physics processes contributing to the total simulated cross section are

- 91, elastic scattering [54]
- 92, single diffraction $AB \to XB$ [54]
- 93, single diffraction, $AB \to AX$ [54]
- 95, low-p_T production [57]
- 99, $\gamma^* q \to q$ [35]

Further on, these processes are classified as belonging to one of the two different kinds of events

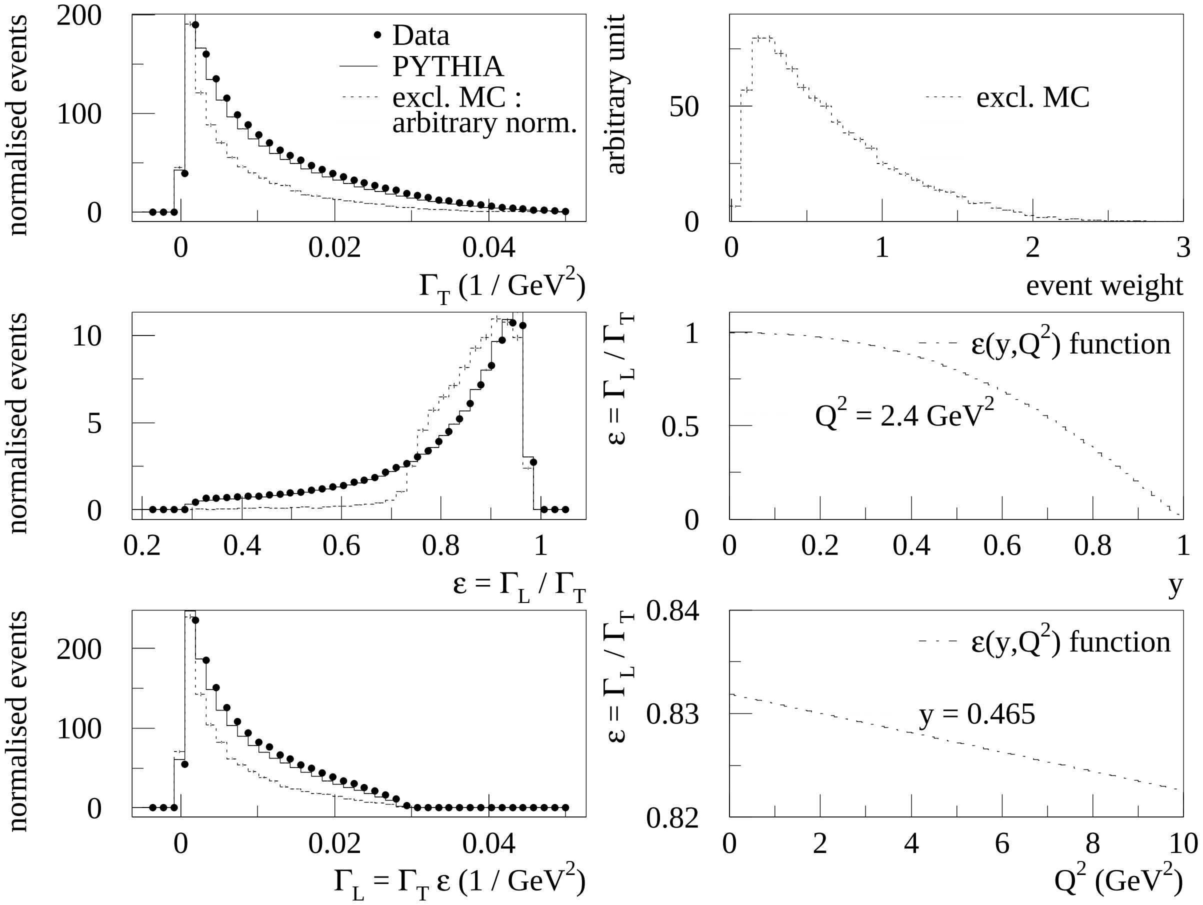

Figure 5.1: Left: The distributions of the transverse Γ_T (3.11) and longitudinal $\Gamma_L = \Gamma_T\,\varepsilon$ photon fluxes, and of their ratio ε (3.12). Right: Distribution of event weights (5.2) for the generated exclusive pion events, and the function $\varepsilon(y, Q^2)$ for HERMES kinematics. Event selection of Table 6.2 is applied.

- VMD: 91, 92, 93. The vector meson dominance (VMD) model is assumed for the structure of the photon, i.e., in a simulated VMD event (also called a resolved event) the photon fluctuates into a vector meson, predominantly a ρ^0. Therefore event classes known from hadron-hadron interactions occur here, such as elastic and diffractive events, e.g., production of ρ^0, ω, ϕ, and non-resonant $\pi^+\pi^-$ pairs.

- DIS: 95, 99. Unlike a hadron, the photon can act as an unresolved probe, having no underlying structure. Events, wherein the bare photon interacts directly with a parton from the proton, are called deep inelastic scattering (DIS or direct) processes. This is process 99 which is calculable in pQCD. A typical event structure at HERMES energies is the production from the target proton remnant of a bunch of hadrons (not more than 7-8, 3 on average) with lower momenta. The hadrons are pions, protons and kaons. Process 95, attached hereafter to the DIS part of the cross section, are the 'minimum bias' events that account for the 'whatever is left' part of the cross-section that cannot be parameterised by exclusive VMD and pQCD DIS processes.

Resonances, such as Δ^+, are not explicitly generated in PYTHIA but they are assumed to be described in the following way. Such excitations are defined in [56] as light single-resonance diffractive states (with a mass less than 1 GeV above the mass of the incoming particle), which are allowed to decay isotropically into a two-body state. It is via these decay products that resonances add up to the cross section.

Although the radiation of a real photon off the incoming or outgoing lepton on the generation level of events is not foreseen in the original PYTHIA version, radiative corrections to the generated cross section are applied using the RADGEN [7] generator. The implementation of RADGEN to PYTHIA is described in [49].

An alternative to the more complete generator PYTHIA described above is, e.g., to use two generators to model the two main background contributions, namely, LEPTO [47] for generation of semi-inclusive events and (the HERMES Monte Carlo) rhoMC for simulation of exclusive vector meson production in deep inelastic scattering (DIS). LEPTO generates events at the HERMES kinematics but considers a limited number of processes (i.e., only the leading and next-to-leading order processes in DIS). The rhoMC generator includes a number of phenomenological descriptions (as PYTHIA does) of the elastic cross section and a set of tunable parameters to match, e.g., the Q^2 slope, angular, and t distributions of the data, however, it allows only a comparison of shapes but not of absolute cross sections to be made between data and Monte Carlo (we refer to the rhoMC version current to this analysis).

Method of Event Generation

The task of PYTHIA is twofold: to generate events one at a time and to give an estimate of the generated total cross section.

Unlike most generators where the events are generated flat in phase-space and subsequently the event weights are calculated and stored along with the other event quantities, in PYTHIA the different event classes (DIS, VMD) are generated according to their cross section so that the relative process fractions are already correctly normalised to each other within the Monte Carlo sample. The need to normalise the total sample occurs when it has to be compared to the experimental data. The weight of any PYTHIA event is always 1.

The independent kinematic variables (e.g., τ, y, and z) are used in the generation of a physics process in PYTHIA [56]. The kinematic phase-space is determined by selecting the range of allowed values for each variable. The variables are generated separately not flat but according to simple functions (one per variable) chosen such that the kinematic dependence of the cross sections is approximately modelled. The variation of the cross section over the allowed phase-space is made known at initialisation of a PYTHIA run, so that the functions are optimised to closely follow the general behaviour of the physics cross section. After the kinematic variables are chosen, the event weight is constructed as being proportional to the physics cross section and inversely proportional to the before-mentioned functions. As the nominator and denominator balance each other, the non-unit weights of individual events cannot exhibit large fluctuations. The deviation of the weights from unity is due to the fact that the before-mentioned functions match only approximately the correct cross section. To achieve an exactly unit weight for all events, at initialisation the maximum weight is found and the generated event is retained with a probability equal to the actual event weight divided by the maximum weight.

Normalisation of Events

We note that the procedure below for converting event counts to a normalised yield (and vice versa) does not take into account all correction factors (for acceptance, etc.) required for a real cross section measurement, however, it is sufficient for our data-to-PYTHIA comparisons. The notation $\widetilde{\sigma}$ for the normalised yields is used throughout the text.

The generated absolute cross section (in units of μb) is obtained by Monte Carlo integration over the phase-space as the average of the (internal to PYTHIA non-unit) weights over all events. The so called average weight $\langle W \rangle_{N_{gen}}$ (which is in fact the total cross section in μb) and the total number of generated events N_{gen} are stored per run, while each of the accepted

PYTHIA	N_{gen} events	N_{acc} events	$\langle W\rangle_{N_{gen}}$ μb	$\widetilde{\sigma}$ μb	N_{DIS} events	Σ_{PYTHIA} $= \frac{\langle W\rangle_{N_{gen}}}{N_{gen}}$, nb
v1.HRC,v1.HSG	135992828	50000000	0.615257	0.2262	5338683	$4.5242 \cdot 10^{-6}$
v2.HSG	163437095	50000000	0.563476	0.1724	4068917	$3.4477 \cdot 10^{-6}$

Table 5.1: The numbers used for the normalisation of the events from three PYTHIA samples, PYTHIA.v1.HRC, PYTHIA.v1.HSG, and PYTHIA.v2.HSG.

events $N_{acc} \neq N_{gen}$ delivered by PYTHIA for analysis has a unit weight. The number N_{acc} is then converted to a normalised yield in units of μb using

$$\widetilde{\sigma} = \frac{N_{acc}}{N_{gen}} \langle W\rangle_{N_{gen}} = N_{acc}\,\Sigma_{PYTHIA}, \tag{5.3}$$

where $\Sigma_{PYTHIA} = \frac{\langle W\rangle_{N_{gen}}}{N_{gen}}$. The value of the yield (5.3) is converted to nb for consistency with the event normalisation of the data (Section 6.4.1). Differential yields computed as, e.g., $\frac{d\widetilde{\sigma}}{dM_X^2} = \frac{\Delta N_{acc}\Sigma_{PUTHIA}}{\Delta M_X^2}$ where ΔM_X^2 is the bin width, are also used in the following.

Knowing the total yield generated with PYTHIA, an estimate can be derived of the corresponding number of DIS events N_{DIS}. For production of 1 million DIS events on a hydrogen target at HERMES a luminosity of 23.6 pb^{-1} is required, which corresponds to a total cross section of 42.37 nb. Hence, the total number of DIS events contained in our PYTHIA sample is $N_{DIS} = \frac{\sigma\,(\mathrm{nb})}{42.37\,\mathrm{nb}}\,10^6$. The result can be read from Table 5.1. We conclude that the Monte Carlo statistics is by 33% larger compared to that of the data (Table 6.3 on page 57).

5.1.3 PYTHIA Samples

The generated PYTHIA events (Section 5.1.2) are passed through the HRC package (Section 4.5.3) which makes use of the complete description of the detector systems to perform a full track reconstruction, as done for data. An almost identical output but achieved on a much shorter time scale is provided by an alternative to the HRC code, namely the HERMES Smearing Generator (HSG) [45]. The time consuming simulation of the particle interactions with the detector material is replaced in HSG by look-up tables which contain information on how the kinematic variables are affected. For our studies an already available HRC production with the latest PYTHIA tune is used (PYTHIA.v1.HRC). In principle, HRC is preferred over HSG because the former provides more accurate information about the number of clusters in the calorimeter, whereas the latter uses a track extrapolation procedure to check for clusters associated to the track. Thus, in general, the use of HRC allows one to perform a more realistic data-to-PYTHIA comparison.

We use two PYTHIA productions, denoted here by version number one (v1) and two (v2). The fraction of VMD (vector meson) events in the generated sample is the main difference between these productions (Fig. B.11). The data from the second (first) version are processed with the HSG (and the HRC) package; the respective Monte Carlo samples and their HERMES labels are denoted as

1	PYTHIA.v1.HRC,	results_p99_q2cut_rad_mstp18_3_2004c_hrc
2	PYTHIA.v1.HSG	
3	PYTHIA.v2.HSG	results_p99_q2cut_rad_mstp18_3_2004c_msel2_std_new

Sample 2 is used only in comparisons of kinematic distributions (Figs. 6.7, 6.8, B.11, B.13, and Tables B.2, B.3) to demonstrate how it compares to sample 1. Sample 1 is used especially for the resolutions of kinematic variables (Figs. B.9–B.10), smearing studies (Section 7.2, Figs. C.1–C.6), and also in Fig. 6.3, 6.5. Sample 3 is used for extracting the DIS and VMD process fractions (Figs. 6.9 and Table 6.6), as v1 is found to overestimate the VMD fraction.

Chapter 6

Data Analysis

The data collected in the years 2002-2004 originating from the scattering of a 27.56 GeV unpolarised (helicity-balanced) positron beam off an internal transversely polarised hydrogen fixed target at the HERMES experiment, are considered throughout this work. In this chapter the analysis steps are described that ensure good data quality, and enhance the signal and reduce the background by means of event selection criteria. The amount of signal is estimated here using data only and with the help of Monte Carlo simulations.

6.1 Data Quality Cuts

A careful check of the data quality is an indispensable part of the analysis. The primary preselection of the data sample is performed on the burst level. A burst, defined as a 10 s-long period of data taking, may contain several events. The check is greatly facilitated by using the burstlist provided by the data quality group. This list contains one bit pattern per burst, each bit corresponding to a predefined condition and being set or not depending on the detector performance during the given burst. By constructing in the analysis program a bit mask with all bits set (to 1) and comparing (via the logical function `&` in C) against the burstlist bit pattern, only the good bursts that pass all predefined data quality conditions are accepted during processing of the μDST data. However, some of the conditions may be redundant. In this analysis a minimum number of bits are set so that potentially useful data are not discarded, while keeping the quality of the accepted data at a high level. The gain of statistics is 15% compared to a selection with all bits being set, i.e., with a bit pattern `0xffffffff`. A list of all bits can be found in Table 6.1. An explanation of the data quality conditions follows.

- **Target:** The target is required to be in a well defined polarisation state parallel or antiparallel to the target transverse magnetic field, which is not the case for the bursts during which the direction of the target polarisation is flipped (after every 90 s for < 10 s). The data with an unsettled polarisation state (1% of all bursts) are rejected as well as periods with low target performance due to malfunctioning components (ABS, BRP, TGA, magnet) or bad gas parameters (low density, low flux, high pollution). The target polarisation value, density, and atomic fractions, being provided separately by the target experts group, are not inspected here.

⋆ **Beam:** No beam polarisation is required for this analysis. The quality of the polarimeter measurements is not important as well. However the beam current is required to be in a reasonable range.

∨ **Burst:** Bursts are required to have reasonable values of the burst length. The first and the last bursts in a run are discarded as well as bursts with bad data records. Data with no available PID due to initialisation problems or an unknown calorimeter threshold are discarded. The run to which the burst belongs should be marked as analysable in the data-taking logbook. The cut on the luminosity detector rate discards data with very small count rates and very large fluctuations in the target density, however this cut is not included in the present data requirements.

◇ **Livetime:** The cuts on the livetime corrections ($\tau_{live} = \frac{N_{accepted}}{N_{generated}}$, $\tau_{artificial} = \frac{N_{missing}}{N_{generated}}$, defined as ratios of numbers of accepted and missing to generated events in the data stream) ensure that periods with unreasonably high background rates in the detector are discarded. The rate of accepted events (triggers) is defined by the DAQ system, while the number of generated triggers, when exceeding a certain limit, is sensitive to the beam conditions during data taking, which give rise to non-physics, i.e., background events.

▷ **HV trips:** Data-taking periods with HV trips, occurring because currents in certain detectors exceed a safe limit, are a signature of bad background conditions and are therefore discarded.

◁ **PID detectors:** Further cuts ensure that data taken during stable operation of the particle lepton-hadron separation and identification detectors are accepted.

\+ **Calorimeter:** Bursts in which at least one block in the calorimeter is dead are discarded, except if it is a single dead block in an outer row or column of the calorimeter. If dead blocks are traced back to problems with GMS the burst is not rejected. For the 2002 data one dead block in the calorimeter is allowed as it is traced back to ageing problems.

6.2 Event Selection

The exclusive production of a positively charged pion,

$$e^+p \rightarrow e^{+\prime}n\pi^+, \tag{6.1}$$

is characterised by the particles in the final state: the scattered positron $e^{+\prime}$, the recoiling neutron n, and the produced pion π^+. The change of the proton into a neutron (change of a u-quark into a d-quark without breakup of the nucleon) is required because the total charge in the initial and final states has to be conserved. In order to confirm that no additional particles are produced one has either to be able to detect all scattering products or one has to exclude processes with more than three particles in the final state. In contrast to a (semi-) inclusive analysis, in the exclusive analysis all produced particles have to be identified, directly or indirectly.

The strategy to select exclusive events of the type (6.1) with the HERMES spectrometer is outlined below.

- Only events with exactly 2 reconstructed charged tracks are accepted for analysis. The tracks have to be identified as a positron and a pion, respectively, by the lepton-hadron separation and particle identification detectors.

- The calorimeter has to show no signal (above threshold) caused by photon activity (0 clusters required).

- Although the neutron escapes direct detection in the experimental setup, an evidence for its production can be inferred using the measured four-momenta of the detected

bit	quantity	condition/action upon setting the bit	2002	2003	2004
$0^{\bullet}$	target polarisation state	well defined ($\uparrow$ or $\downarrow$)/accept	1	1	1
$1^{\star}$	beam polarisation value	$20(30) < P_{\text{beam}} < 80\%$ (2002)/accept	0	0	0
$2^{\diamond}$	livetime correction τ_{live}	$0.5 \leq \tau_{live} < 1.0$ $0.5 \leq \tau_{live} \cdot \tau_{artificial} \leq 1.0$ /reject $0.0 < \tau_{trigger-21} \leq 1.0$	1	1	1
$3^{\vee}$	burst length	$0 < t_{burst} \leq 11\,\text{s}$/accept	1	1	1
$4^{\star}$	beam current	$2 \leq I_{e^+} \leq 50\,\text{mA}$/accept	1	1	1
$5^{\vee}$	LUMI rate	$1 \leq R_{LUMI} \leq 50\,\text{Hz}$/accept	0	0	0
$6^{\vee}$	burst number	first burst in a run/reject	1	1	1
$7^{\vee}$	burst quality	bad μDST record or last burst in run /reject	1	1	1
$8^{\vee}$	PID information	not available/reject	1	1	1
$9^{\vee}$	run analysable	accept	1	1	1
$10^{\bullet}$	ABS in normal 2-state mode	normal data taking/accept	0	0	0
$11^{\bullet}$	unpolarised high-density gas	5...10× or 80× ABS density/reject	0	0	0
$12^{\bullet}$	ABS-mode information	not available/reject	0	0	0
$13^{\bullet}$	ABS in special 3-state mode	polarised Bhabha scattering/reject	0	0	0
$14^{\bullet}$	ABS n special 2-state mode	polarised Bhabha scattering/reject	0	0	0
$15^{\bullet}$	target gas type	unpolarised gas/reject	0	0	0
$16^{\bullet}$	target data quality	bad records/reject	1	1	1
17^{+}	calo dead blocks	≤ 1 dead block at the edges/reject	0	0	(1)
18^{+}	H2 and LUMI dead blocks	problems traced to GMS (undefined)	(0)	(0)	(0)
$19^{\triangleleft}$	TRD data quality	reject bad records	1	1	1
$20^{\triangleright}$	HV trips in FCs and BCs	reject	1	1	1
$21^{\triangleleft}$	RICH operated with N_2 (2002) or bad data (2004)	reject run ranges	1	(0)	0
$22^{\triangleright}$	HV trips in RICH	reject	1	1	1
$23^{\bullet}$	target gas atomic fraction	(not defined)	(0)	(0)	(0)
$24^{\bullet}$	atomic fraction quality	(not defined)	(0)	(0)	(0)
$25^{\triangleleft}$	RICH data quality	reject bad records	1	1	1
26	(empty)	(not defined)	(0)	(0)	(0)
$27^{\bullet}$	target polarisation	(not defined)	(0)	(0)	(0)
$28^{\star}$	time between polarimeter measurements	$t_{polarimeter} \leq 300\,\text{s}$/accept	0	0	0
$29^{\bullet}$	target polarisation	(not defined)	(0)	(0)	(0)
$30^{\diamond}$	livetime correction trigger-21	$\tau_{artificial} = 1.0$ $0.5 \leq \tau_{trigger-21} \leq 1.0$ /reject	0	0	0
31^{+}	calo dead blocks	≤ 1 dead block due to ageing/accept	1	(0)	(0)

Table 6.1: The 2002-2004 data quality cuts. The last three columns indicate whether a condition is applied to this analysis or not; 1/0 means that the bit is set/not set, (0) means that the condition is not defined and the bit is left unset. The bit number superscripts serve as a reference to the explanation in the text. The resulting hexadecimal numbers are `0x827903dd` (2002), `0x025903dd` (2003), and `0x025b03dd` (2004).

particles. This is a standard analysis method known as the 'missing mass technique'. It is based on the conservation of four-momentum in the reaction. Applied to the process $e^+p \rightarrow e^{+\prime}X\pi^+$ with X denoting one or more particles, it gives

$$q_{e^+} + q_p = q_{e^{+\prime}} + q_X + q_{\pi^+}, \quad : \quad q_X = q_{e^+} + q_p - q_{e^{+\prime}} - q_{\pi^+}. \tag{6.2}$$

The four-momentum q_X of the 'missing' particle(s) can be calculated from the known momenta (q_{e^+} and q_p) of the initial state particles and the measured momenta ($q_{e^{+\prime}}$ and q_{π^+}) of the final state particles. For exclusive events $e^+p \rightarrow e^{+\prime}n\pi^+$ ($X = n$) the invariant quantity q_X^2 should be equal to the squared mass of the neutron $M_n^2 = 0.88\,\mathrm{GeV}^2$, i.e., $q_X^2 = M_n^2$. To take into account also background events ($X \neq n$) that are inevitably present in our data sample, $q_X^2 = M_X^2$ (called the squared missing mass) is used in the following for both signal and background events. An upper cut on $M_X^2 \leq (M_n^2 + 3\,\sigma_{M_X^2})$ that accounts for the resolution of the squared missing mass $\sigma_{M_X^2}$ is usually required to limit the sample of events to the searched topology. The final value of the M_X^2 cut, however, needs to be optimised with respect to the statistical and systematic uncertainties of the results and is not fixed until much later in the analysis. Our studies of M_X^2 are described in Sections 6.4, 6.6.1, 6.6.2.

- Additional cuts, proven in the course of the analysis to enhance the sample of exclusive events, will be included.

6.2.1 Kinematic Cuts

The hard scale in the exclusive process, where factorisation (Section 3.2,[19]) is proven to work, is expected to set in at sufficiently large Q^2, e.g., $Q^2 \gg M_\pi^2 = 0.02\,\mathrm{GeV}^2$ [33], with the values of the transverse momentum transfer t and the Bjorken scaling variable x fixed. In this analysis $Q > 1\,\mathrm{GeV}^2$ is chosen as the HERMES data become sparse at larger Q^2.

An upper cut on the fractional energy transfer $y = \frac{E-E'}{E} < 0.85$ is set in order to reduce radiative effects on the measured quantities. In addition, this cut ensures that the scattered positron has sufficient energy E' to pass the calorimeter threshold E_{calo} and generate a trigger-21 (Section 4.5.1). With $E = 27.56\,\mathrm{GeV}$ being the beam energy, in fact $y < 0.87$ (0.95) is the upper limit of y for events triggered by trigger-21 with a threshold of $E_{calo} = 3.5\,\mathrm{GeV}$ ($E_{calo} = 1.4\,\mathrm{GeV}$).

The invariant squared mass of the hadronic final state W^2 for exclusive events is found to have a lower kinematic limit of about $10\,\mathrm{GeV}^2$ defined by the HERMES spectrometer acceptance (with upper angular limit of 220 mrad for hadrons) when a pion is required in coincidence with the scattered positron. To avoid this low acceptance region, we set the cut to $W^2 > 10\,\mathrm{GeV}^2$. With this cut only $< 5\%$ of the signal is rejected.

6.2.2 Geometry Cuts

The scattered positron and charged pion tracks originate from the interaction vertex in the target cell (9 cm diameter opening, 21 cm length along the beam pipe). The longitudinal vertex distribution has a triangular shape and is peaked at the centre of the target ($z = 0$), while the transverse distribution is sharply peaked at $x_{vertex} \approx y_{vertex} \approx 0$ (in the HERMES coordinate system, Section 4.3). Therefore only a z_{vertex}-cut is applied. Indeed, the spread of the perpendicular distance $r_{vertex}^2 = x_{vertex}^2 + y_{vertex}^2$ from the z axis of the vertex defined by the track and the z axis, given by $RMS(z_{vertex}) = 0.33\,\mathrm{cm}$, is much smaller than the lateral dimensions of the target (Section 4.2.2).

quantity	cut
charged track cuts	
DAQ trigger	trigger-21
short track stopped in MCs	0
number of tracks	2
charge of tracks	+1
sum of all track momenta	$p_{e^{+\prime}} + p_{\pi^+} < 29.0\,\mathrm{GeV}$
photon clusters in the calorimeter	0
reconstructed vertex inside target	$\lvert z_{vertex}\rvert \leq 18\,\mathrm{cm}$
horizontal fiducial cut at calorimeter position	$\lvert x_{calo}\rvert \leq 175\,\mathrm{cm}$
vertical fiducial cut at calorimeter position	$30\,\mathrm{cm} \leq \lvert y_{calo}\rvert \leq 108\,\mathrm{cm}$
front field clamp position	$\lvert y_{ffc}\rvert \leq 31\,\mathrm{cm}$
septum plate position	$\lvert y_{sp}\rvert \geq 7\,\mathrm{cm}$
horizontal rear clamp position (hit by bent tracks)	$\lvert x_{rc}\rvert \leq 100\,\mathrm{cm}$
vertical rear clamp position (hit by bent tracks)	$\lvert y_{rc}\rvert \leq 54\,\mathrm{cm}$
positron track cuts	
identification with PID system	$PID3 + PID5 > 1$
four-momentum transfer	$Q^2 > 1\,\mathrm{GeV}^2$
fractional energy transfer	$y < 0.85$
photon-nucleon invariant mass	$W^2 > 10\,\mathrm{GeV}^2$
pion track cuts	
identification with PID system	$-100 < PID3 + PID5 < -1$
RICH particle type	π
RICH quality parameter	$rQp > 0$
RICH momentum range for pions	$1 \leq p_\pi < 15\,\mathrm{GeV}$

Table 6.2: The standard cuts applied to the data to select event candidates for this analysis.

The geometric acceptance for charged tracks is limited in the horizontal (x) and vertical (y) direction by the outer dimensions of the detector systems. A sanity check on the track coordinates is performed at the positions of the front and rear field clamp plates of the spectrometer magnet and at the septum plate enclosing the beam pipe (Fig. 4.2). A box-like fiducial volume cut is defined at the position of the calorimeter to ensure that the positron track deposits all its energy in the calorimeter blocks, thus removing tracks from the edges where the measurement efficiency decreases because of shower leakage.

6.3 Luminosity Measurement

The absolute integrated luminosity L (4.28) is calculated from the same data which are analysed (2002-2004 data) but using processes that are different from the one studied here. There are two choices for the luminosity measurement at HERMES:

1. $L = L_{DIS} = \frac{N_{DIS}}{\sigma_{DIS}\,\epsilon_{DIS}}$, where N_{DIS} is the rate of deep inelastic scattering (DIS) events (selected with trigger-21, $Q^2 > 1\,\mathrm{GeV}^2$, $W^2 > 4\,\mathrm{GeV}^2$, $y < 0.85$ from the 2002-2004 data), $\sigma_{DIS} = 60.9\,\mathrm{nb}$ is the total DIS cross section obtained from world data (on the unpolarised structure function F_2 for a proton target) and integrated over the kinematic range covered by HERMES and corrected for radiative effects, $\epsilon_{DIS} = 0.81$ is the detection efficiency for DIS positrons as determined by data-to-Monte Carlo comparison of the inclusive DIS cross section in the HERMES acceptance for the 1996 data. An advantage of using L_{DIS}

year	N_{DIS} events	N_{LUMI} counts	C_{LUMI} $\frac{10^{-6}}{\text{nb}}$	L_{DIS} $\frac{10^4}{\text{nb}}$	L_{LUMI} $\frac{10^4}{\text{nb}}$
2002	796695	15455631	1046 ± 33	1.615	1.6167
2003	422483	8665904	949 ± 29	0.856	0.8224
2004	2774043	56296452	969 ± 29	5.624	5.4551
2002-04	3993221	80417987	-	8.095	7.8942
2002-04	1. $\Sigma_L = \Sigma_{L_{DIS}} = \frac{1}{L_{DIS}} = 1.235 \cdot 10^{-5}\,\text{nb}$ 2. $\Sigma_L = \Sigma_{L_{LUMI}} = \frac{1}{L_{LUMI}} = 1.267 \cdot 10^{-5}\,\text{nb}$ (used here)				

Table 6.3: The values of N_{DIS}, N_{LUMI}, and C_{LUMI} used to calculate the luminosity L in two alternative ways (see text). The inverse luminosity $\Sigma_L = \frac{1}{L}$ is given in units of nanobarn denoted as nb, where $1\,\text{nb} = 10^{-37}\,\text{cm}^2$.

is that through the N_{DIS} rate in the spectrometer corrections for dead time, tracking and trigger efficiencies, etc. are implicitly taken into account.

2. $L = L_{LUMI} = N_{LUMI}\, C_{LUMI}$, where $N_{LUMI} = \sum_{bursts}(R_{LUMI} \cdot \tau_{trigger-21}) \cdot t_{burst}$ is the integrated luminosity monitor rate calculated from the measured rate R_{LUMI} of detected coincident e^+e^- pairs in the luminosity monitor, corrected for dead time by $\tau_{trigger-21}$, and the length of the burst t_{burst} (10 s). The luminosity constant is given by $C_{LUMI} = \frac{C}{\sigma_{Bhabha}}$, where C is a normalisation constant which takes the efficiency and acceptance of the luminosity detector into account, and σ_{Bhabha} is the known cross section of Bhabha scattering ($e^+e^- \rightarrow e^+e^-$). The constant C_{LUMI} is obtained from a Monte Carlo simulation of the luminosity detector set-up with the relevant parameters (such as geometry, beam position, gas target) for each data taking year.

The values of N_{DIS}, N_{LUMI}, C_{LUMI}, and of the luminosities L_{DIS} and L_{LUMI} calculated according to 1. and 2. above, respectively, are given in Table 6.3. The latter choice, namely $L = L_{LUMI}$, is used to determine the absolute inverse luminosity $\Sigma_L = \frac{1}{L}$ for the cross section normalisation of the data (Section 6.4.1). The luminosity monitor rate is measured with a high statistical precision due to the high rate of Bhabha events. The statistical uncertainty of L_{LUMI} is about 1% within a time window of 100 s and is neglected, whereas the systematic uncertainty is ±3% for our data sample. A comparison between the two choices (1. and 2. above) reveals a difference of $\frac{\Sigma_{L_{LUMI}} - \Sigma_{L_{DIS}}}{\Sigma_{L_{LUMI}}} = +2.5\%$ which is well within the total uncertainty of L_{LUMI}.

6.4 Missing Mass Distribution

From (6.2) for the conservation of four-momentum in the positron-proton scattering process with production of a single pion or more particles, one can derive

$$M_X^2 = q_X^2 = (q_{e^+} + q_p - q_{e^{+\prime}} - q_{\pi^+})^2, \tag{6.3}$$

where M_X^2 is the squared missing mass for a given event. Although values of $M_X^2 < 0$ are non-physical they can arise due to finite detector smearing and resolution. In the laboratory frame where the proton target is at rest the four-momentum $q = (E, p_x, p_y, p_z)$ of each particle is calculated from the values of $|p| = \sqrt{p_x^2 + p_y^2 + p_z^2}$, the polar angle Θ and the azimuthal angle Φ of the reconstructed track in the spectrometer, and the particle mass m, according to the relation $m^2 = E^2 - p^2$, where $p = (p_x, p_y, p_z)$ is the three-momentum and E is the particle's energy. The expression for the four-momentum components of the beam positron

particle	E	p_x	p_y	p_z
e^+	$E_{e^+} = 27.56\,\mathrm{GeV}$	0	0	E_{e^+}
p	$M_p = 938.3\,\mathrm{MeV}$	0	0	0
$e^{+\prime}$	$\|p\|, \quad M_{e^+} \approx 0\,\mathrm{MeV}$	$\|p\| \sin\Theta \cos\Phi$	$\|p\| \sin\Theta \sin\Phi$	$\|p\| \cos\Theta$
π^+	$\sqrt{M_{\pi^+} + \|p\|^2}, \quad M_{\pi^+} = 139.6\,\mathrm{MeV}$	$\|p\| \sin\Theta \cos\Phi$	$\|p\| \sin\Theta \sin\Phi$	$\|p\| \cos\Theta$

Table 6.4: The components of the four-momentum $q = (E, p_x, p_y, p_z)$ of reconstructed tracks in the spectrometer used to calculate the event kinematics, in particular, M_X^2.

e^+, the target proton p, the scattered positron $e^{+\prime}$, and the produced pion π^+ are given in Table 6.4.

One M_X^2 value (6.3) is calculated per event. The M_X^2 values of all π^+ events that pass the standard cuts (Table 6.2) being accumulated in one plot form the squared missing mass distribution shown in Fig. 6.1.a) and denoted as 'Data π^+'. The M_X^2 distribution depicts how the amount of accepted pions changes as a function of the squared missing mass. It covers the range $-2 < M_X^2 \leq 40\,\mathrm{GeV}^2$ with a mean value of $\langle M_X^2 \rangle = 14\,\mathrm{GeV}^2$.

6.4.1 Normalisation of Events

The conversion of event counts to a normalised yield (and vice versa) is explained using the M_X^2 distribution in Fig. 6.1 as an example. We note that this conversion procedure does not take into account all correction factors (for acceptance, efficiencies, etc.) required for a real cross section measurement, however, it is sufficient for our data-to-PYTHIA comparisons. The notation $\widetilde{\sigma}$ for the normalised yields is used throughout the text.

The number of events ΔN falling in an M_X^2 bin on the horizontal axis of Fig. 6.1 is weighted by the inverse absolute luminosity $\Sigma_L = \frac{1}{L}$ (Section 6.3). The weighted number of events is divided by the bin width $\Delta M_X^2 = 0.4\,\mathrm{GeV}^2$. The result is a differential yield $\frac{d\widetilde{\sigma}}{dM_X^2} = \frac{N\Sigma_L}{\Delta M_X^2}$ in units of nanobarn per GeV^2 as displayed on the vertical axis of Fig. 6.1. The statistical error bar given by $\sqrt{N}$ is scaled accordingly. The integrated yield in units of nb is given by

$$\widetilde{\sigma} = N\,\Sigma_L, \tag{6.4}$$

where N is the total number of events and the value of $\Sigma_L = \Sigma_{L_{LUMI}}$ is given in Table 6.3.

In Fig. 6.1 the amount of π^+ data increases steeply in the region $M_X^2 = 0...2.5\,\mathrm{GeV}^2$ and beyond reaching a maximum value of $\frac{d\widetilde{\sigma}_{\pi^+}}{dM_X^2} = 0.141\,\frac{\mathrm{nb}}{\mathrm{GeV}^2}$ at $M_X^2 = 9.1\,\mathrm{GeV}^2$. A piling up of exclusive events in a clearly separated peak at the anticipated position of the squared neutron mass $M_X^2 = M_n^2 = 0.88\,\mathrm{GeV}^2$ is not observed. Further measures are required to separate the exclusive π^+ sample.

6.4.2 Background Subtraction

In addition to the M_X^2 distribution for π^+ studied above, the distribution of negatively charged pions is plotted in Fig. 6.1.a) and denoted as 'Data π^-'. The standard cuts (Table 6.2) are used except for the track charge cut (-1 instead of $+1$ is required for the pion). Notice that exclusive production of π^- from a proton target is forbidden by charge conservation and therefore no enhancement of the M_X^2 distribution for π^- at the squared neutron mass is expected. The mean value of the distribution is at $M_X^2 = 15\,\mathrm{GeV}^2$ and the maximum yield at $M_X^2 = 9.1\,\mathrm{GeV}^2$ is $\frac{d\widetilde{\sigma}_{\pi^-}}{dM_X^2} = 0.087\,\frac{\mathrm{nb}}{\mathrm{GeV}^2}$. The π^- yield is smaller than that for π^+ over the entire M_X^2 region. This can be explained by the favoured production of π^+ $(u\bar{d})$ over π^- $(d\bar{u})$ from a proton target p (uud).

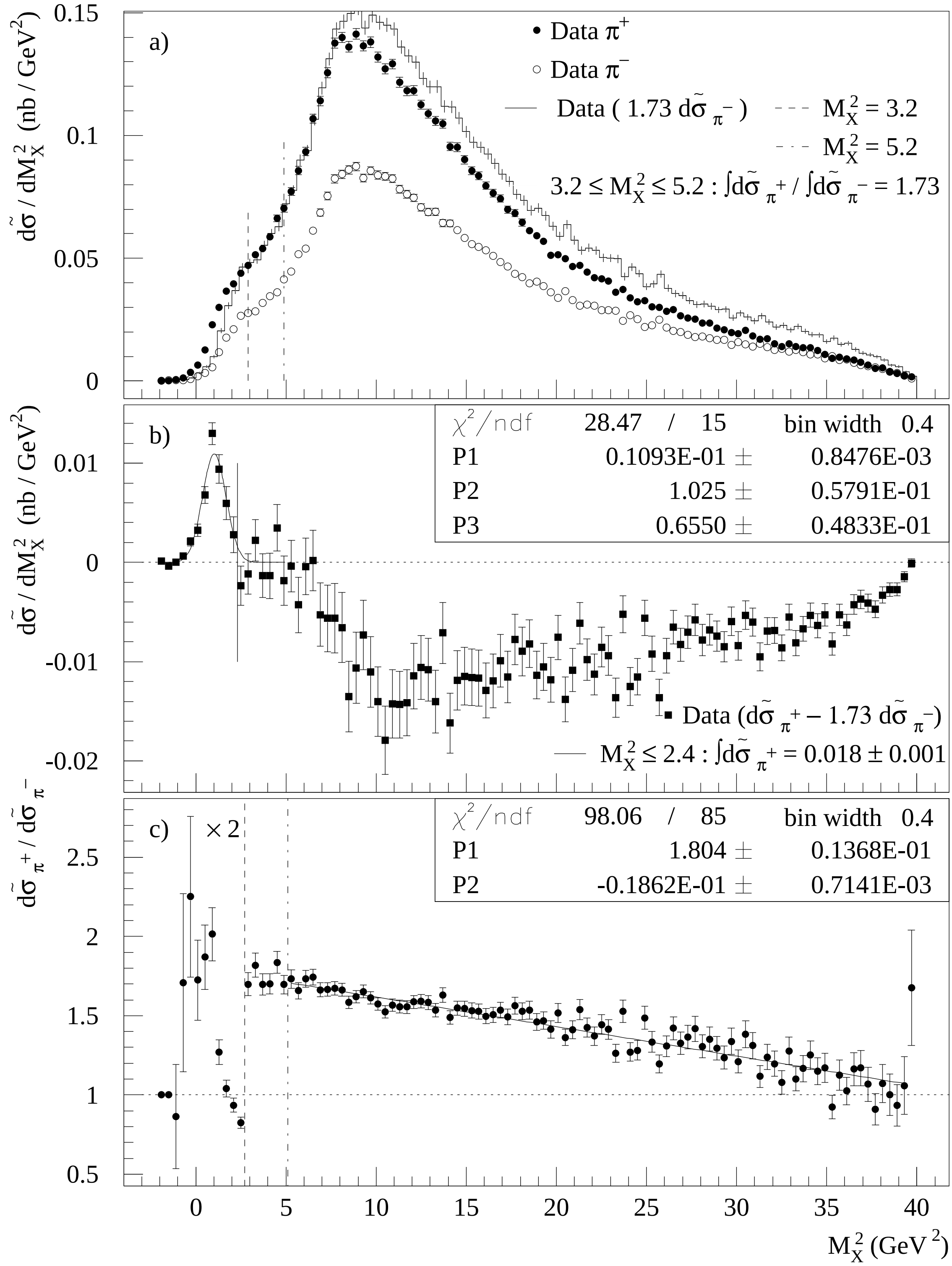

Figure 6.1: Separation of the exclusive π^+ peak using π^- data. As a function of the squared missing mass are shown a) the π^+, π^- and the normalised π^- yields, b) the exclusive π^+ yield after subtraction of the background, and c) the ratio of the π^+ yield to the π^- one. See text for explanations.

The M_X^2 distributions for π^+ and π^- (Fig. 6.1.a)) appear to have similar shapes and hence it is tempting to use the π^- data to evaluate the contribution from competing processes (altogether called background) to the π^+ distribution. The background consists of events with the same observed topology as an exclusive event, e.g., a pion produced in fragmentation processes with the rest of the produced particles escaping the detector acceptance, or production of other particles (for example Δ, ρ^0) which produce pion(s) in their decay. This type of events contributes to both the π^+ and π^- distributions. Note that the removal of such background is not possible on an event-by-event basis with the cuts fixed in Table 6.2 as both signal and background events pass those cuts. Therefore further treatment of the background in this section is based not on the properties of individual events but on the shapes of the M_X^2 distributions shown in Figure 6.1.a). The aim is to visually isolate and give an estimate of the amount of exclusive events in the data.

While a direct subtraction of the π^- from the π^+ distribution results in only partial reduction of the background, a full subtraction requires a rescaling of the π^- distribution, whereby one assumes that the total π^+ and π^- distributions for the background processes have matching shapes when scaled to each other by a constant normalisation factor—if not over the entire M_X^2 range then at least in a limited region around the expected position of the exclusive peak. As the needed normalisation factor is not known (valence-quark content arguments being too naive), it has to be measured from the data itself. This purpose serves the ratio of the integrated π^+ and π^- yields in the range $3.2 \leq M_X^2 \leq 5.2\,\mathrm{GeV}^2$ which amounts to $\frac{\widetilde{\sigma}_{\pi^+}}{\widetilde{\sigma}_{\pi^-}} = 1.73$. The rescaled π^- distribution is shown in Fig. 6.1.a) and denoted as 'Data ($1.73\, d\widetilde{\sigma}_{\pi^-}$)'.

The normalised π^- distribution is subtracted from the π^+ distribution and the result is shown in Fig. 6.1.b) denoted as 'Data ($d\widetilde{\sigma}_{\pi^+} - 1.73\, d\widetilde{\sigma}_{\pi^-}$)'. The shape of the resulting distribution as a function of M_X^2 has three distinct regions: a peak followed by a flat foot at zero level in the normalization region, followed by a wide valley below the zero level. Bearing in mind the steps that led to this result and therefore with some caution, one can attribute the peak to the contribution of exclusive events in the data. A Gaussian fit ($\chi^2/\mathrm{ndf} = 28.47/15$) to the excess points yields the peak position at $M_X^2 = (1.225 \pm 0.058)\,\mathrm{GeV}^2$ somewhat shifted above the expected value of $M_n^2 = 0.88\,\mathrm{GeV}^2$. The peak width, which is due to the detector resolution, is $\sigma_{M_X^2} = (0.655 \pm 0.048)\,\mathrm{GeV}^2$. The exclusive yield is $\frac{d\widetilde{\sigma}_{excl}}{dM_X^2} = 0.011\,\frac{\mathrm{nb}}{\mathrm{GeV}^2}$ at the peak position of the fit, while it is $\frac{d\widetilde{\sigma}_{excl}}{dM_X^2} = 0.013\,\frac{\mathrm{nb}}{\mathrm{GeV}^2}$ for the highest data point at $M_X^2 = 1.1\,\mathrm{GeV}^2$. The area below the peak for $M_X^2 \leq 2.4\,\mathrm{GeV}^2$ amounts to $\widetilde{\sigma}_{excl} = (0.018 \pm 0.001)\,\mathrm{nb}$. It corresponds to 28.6% of the π^+ data in that region and only 0.8% of the analysed π^+ data. For comparison, the area below the π^+ and the π^- distribution is $\widetilde{\sigma}_{\pi^+} = (2.153 \pm 0.005)\,\mathrm{nb}$ and $\widetilde{\sigma}_{\pi^-} = (1.394 \pm 0.004)\,\mathrm{nb}$, respectively, while it is $\widetilde{\sigma}_{\pi^+} = (0.061 \pm 0.001)\,\mathrm{nb}$ and $\widetilde{\sigma}_{\pi^-} = (0.025 \pm 0.001)\,\mathrm{nb}$ for $M_X \leq 2.4\,\mathrm{GeV}^2$, where (6.4) is used to compute the values of $\widetilde{\sigma}_{\pi^\pm}$. The errors of the reported results are the statistical uncertainties.

The negative values of the yield in the region $7 < M_X^2 < 40\,\mathrm{GeV}^2$ (Fig. 6.1.b)) obtained after the background subtraction point to the fact that the normalisation factor $\frac{\widetilde{\sigma}_{\pi^+}}{\widetilde{\sigma}_{\pi^-}} = 1.73$ as measured in $3.2 \leq M_X^2 \leq 5.2\,\mathrm{GeV}^2$ is not constant over the entire M_X^2 range. The π^+-to-π^- ratio of yields $\frac{d\widetilde{\sigma}_{\pi^+}}{d\widetilde{\sigma}_{\pi^-}}$ is shown in Fig. 6.1.c) as a function of M_X^2. Indeed the ratio can be approximated with a constant in the narrow normalisation region, while at $M_X^2 > 5.2\,\mathrm{GeV}^2$ it decreases slowly as $\frac{d\widetilde{\sigma}_{\pi^+}}{d\widetilde{\sigma}_{\pi^-}}(M_X^2) = 1.804 - 0.019\, M_X^2$ (from a straight-line fit with $\chi^2/\mathrm{ndf} = 98.06/85$). The ratio follows a peak-like behaviour in the region $M_X^2 < 3.2\,\mathrm{GeV}^2$ with a rapid increase up to $\frac{d\widetilde{\sigma}_{\pi^+}}{d\widetilde{\sigma}_{\pi^-}}(M_X^2 = 1.1\,\mathrm{GeV}^2) = 4.0 \pm 0.3$, then stays constant within the large statistical errors down to $M_X^2 = -0.5\,\mathrm{GeV}^2$, and further down becomes undetermined due to lack of statistics. Note that the vertical-axis scale in Fig. 6.1.c) should be increased by a factor of 2 in order to read the true values of the points in $M_X^2 < 3.2\,\mathrm{GeV}^2$.

6.4.3 Discussion

The squared missing mass (M_X^2) distribution of the selected π^+ events extends over a wide M_X^2 range without a clear peak at the expected position at the squared mass of the neutron

$M_n^2 = 0.88\,\text{GeV}^2$. This shows that the data sample is dominated by background events and the detector resolution is not sufficient to resolve the contributions to the M_X^2 distribution on a fine scale.

Subtraction of the background, using data only, results indeed in a peak centred slightly above the squared mass of the neutron with an area less than 1/3 of the area of the total π^+ yield in the squared missing mass range covered by the peak. Although this method of background subtraction gives evidence for exclusive π^+ production, it does not allow us to separate the exclusive events from the background events in the π^+ data sample.

Further analysis using Monte Carlo simulation will permits for search of more restrictive cuts in order to optimise the signal-to-background ratio, to identify the background processes, and to perform subtraction and correction for the main background contributions to the measured quantities (normalised yield and asymmetry).

6.5 Monte Carlo-Based Event Selection

6.5.1 Data-to-Monte Carlo Comparison

A detailed comparison of data and Monte Carlo distributions of kinematic variables is shown in Figs. B.2–B.4 (left). Two PYTHIA versions (Section 5.1.3) are used for the comparison. The standard cuts (Table 6.2) are applied to all samples. PYTHIA is not expected to describe the data perfectly in the entire kinematic phase-space, especially in the region with non-negligible fraction of exclusively produced pions in the data, as PYTHIA cannot generate exclusive events. For clearer comparison, the data-to-PYTHIA ratio is displayed in Figs. B.2–B.4 (right). The discrepancy is of the order of 25%. In order to show the overlap between signal and background, the exclusive MC events are scaled arbitrarily to the highest data point in each distribution and superimposed. Since the signal in the data cannot be separated event-by-event from the background and the exclusive MC cannot provide an absolute cross section estimate of the signal, a direct comparison between data and the exclusive MC is not possible at this stage.

6.5.2 PYTHIA-to-Exclusive MC Comparison

The purpose of comparing shapes of PYTHIA and exclusive MC distributions is to pick out those kinematic variables that give the most optimal signal–background separation. For such variables the signal (modelled by the exclusive MC) and the background (modelled by PYTHIA) should occupy a small region of the phase-space common to both. Thus a cut can be defined that reduces the background, while still preserving a large fraction of the signal in the data sample. In total 24 kinematic variables are considered (left panels of Figs. B.2–B.4) and 8 of them are selected for a more precise evaluation of the signal-to-background separation efficiency.

A cut that selects 90% of the signal (exclusive MC events) (i.e., $\frac{\int \tilde{\sigma}_{\text{selected}}}{\int \tilde{\sigma}} = 0.9$) is fixed and the fraction of background (PYTHIA events) passing the same cut is estimated for each of the 8 chosen variables. We note that each cut is applied separately in addition to the standard cuts (Table 6.2). The signal and background fractions of selected events as a function of the cut are shown in Fig 6.2 and the results are summarised below. The smaller the background (PYTHIA fraction), the more efficient the cut is. In order of decreasing but still acceptable separation efficiency, the variables are classified in the following three groups.

1. M_X^2, z, $p_{e^{+\prime}} + p_{\pi^+}$: The selected background fraction is 6.5% for $M_X^2 < 3.65\,\text{GeV}^2$, $z > 0.815$, and $p_{e^{+\prime}} + p_{\pi^+} > 25.7\,\text{GeV}$. Later on results are often given as a function of M_X^2, therefore it is not desirable to limit the M_X^2 range by an initial hard cut on this

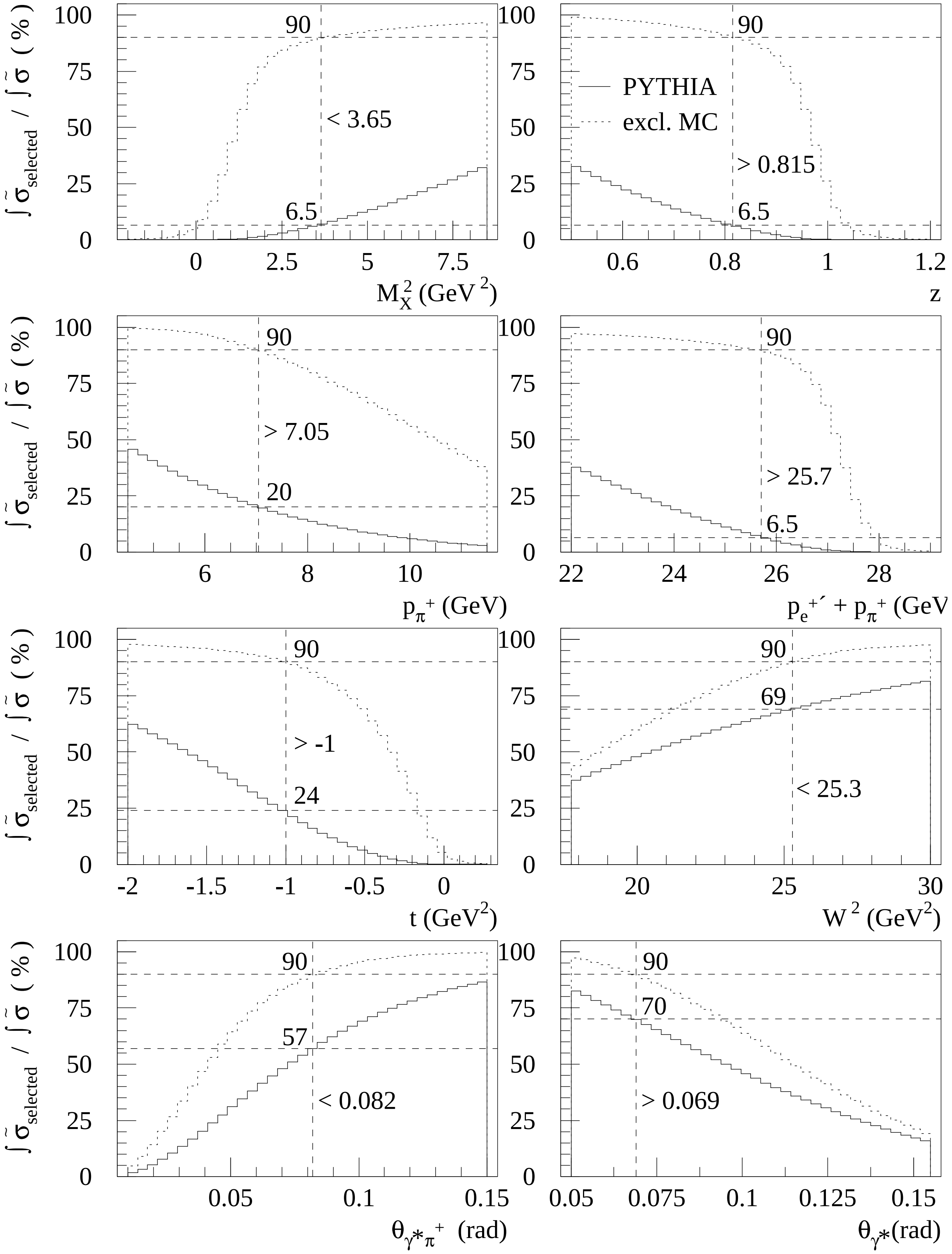

Figure 6.2: The fractions of accepted events ($\frac{\int \widetilde{\sigma}_{accepted}}{\int \widetilde{\sigma}}$) in percent as a function of the cuts on the kinematic variables M_X^2, z, p_{π^+}, $p_{e^{+'}} + p_{\pi^+}$, t, W^2, $\theta_{\gamma^*\pi^+}$, and θ_{γ^*} for exclusive MC and PYTHIA samples selected with the standard cuts (Table 6.2). The vertical line indicates either an upper (<) or a lower (>) bound for each cut, with the fractions corresponding to the cut indicated by horizontal lines.

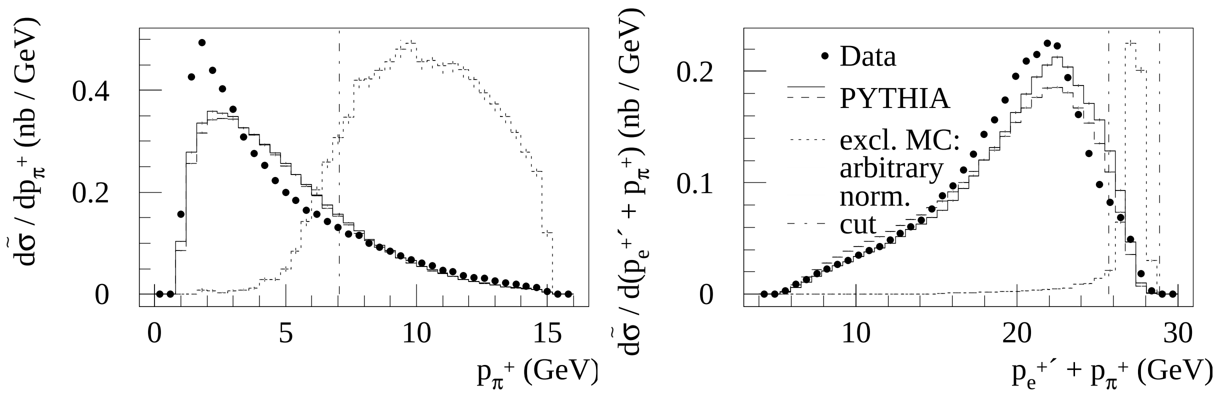

Figure 6.3: Comparison of the p_{π^+} and $p_{e^{+\prime}} + p_{\pi^+}$ distributions obtained from data, PYTHIA, and the exclusive Monte Carlo samples selected with the standard cuts (Table 6.2). Data and PYTHIA events are given as differential yields in units of $\frac{\text{nb}}{\text{GeV}^2}$, whereas the exclusive MC events are scaled arbitrarily to the highest data point in each distribution.

variable. Since z and $p_{e^{+\prime}}+p_{\pi^+}$ are correlated (Fig. E.9), a cut on either one gives the same effect. However, a cut on $p_{e^{+\prime}}+p_{\pi^+}$ is pursued further because it is more straightforward. In fact both momenta enter in the calculation of $z = \frac{E_{\pi^+}}{\nu} \overset{m_{e^{+\prime}} \approx 0}{\approx} \frac{\sqrt{m_{\pi^+}^2 + p_{\pi^+}^2}}{E - p_{e^{+\prime}}}$.

2. p_{π^+}: The selected background fraction is 20% for $p_{\pi^+} > 7.05\,\text{GeV}$. Although p_{π^+} and $p_{e^{+\prime}} + p_{\pi^+}$ are correlated (Fig. E.9), the cut $p_{e^{+\prime}} + p_{\pi^+} > 25.7\,\text{GeV}$ does not restrict the pion momenta above the before-mentioned value. A cut on p_{π^+} is therefore necessary for further background suppression.

3. t, $\theta_{\gamma^*\pi^+}$, W^2, θ_{γ^*}: The selected background is 24%, 57%, 69%, and 70% for $t > -1.0\,\text{GeV}^2$, $\theta_{\gamma^*\pi^+} < 0.082\,\text{rad}$, $W^2 < 25.3\,\text{GeV}^2$, and $\theta_{\gamma^*} > 0.069\,\text{rad}$, respectively. Cuts on these variables (if necessary) are to be chosen after the cuts in 1. and 2. above are fixed.

Note that the fractions above are relevant only within the corresponding MC sample (exclusive MC for the signal and PYTHIA for the background), the two samples being independent. Therefore a signal-to-background ratio cannot be estimated from these fractions. The distributions of the pion momentum p_{π^+} and of the sum of the measured momenta of the scattered positron and the produced pion $p_{e^{+\prime}} + p_{\pi^+}$, also called the two-track momentum, are shown in Fig. 6.3. The motivation for the choice of the cuts on these variables is described below.

Pion Momentum Cut

Since $p_{e^{+\prime}} + p_{\pi^+}$ depends on p_{π^+}, the cut on the latter variable is fixed first. Namely,

$$p_{\pi^+} > 7.05\,\text{GeV} \tag{6.5}$$

is required in the studies hereafter, unless otherwise noted. As seen from Fig. 6.2, this cut rejects 80% of the background while keeping 90% of the signal in the sample selected with the standard cuts (Table 6.2). The p_{π^+} cut is indicated by a vertical line in Fig. 6.3.

Two-track Momentum Cut

Fig. 6.2 shows a possible cut on the two-track momentum of $p_{e^{+\prime}} + p_{\pi^+} > 25.7\,\text{GeV}$ (for $p_{\pi^+} > 1.0\,\text{GeV}$). The exact (lower and upper) bounds of this cut are chosen as follows.

The distribution of $p_{e^{+\prime}} + p_{\pi^+}$ and its resolution (i.e., the distribution of the difference between reconstructed and generated values) are shown in Fig. 6.4 for the exclusive MC sample.

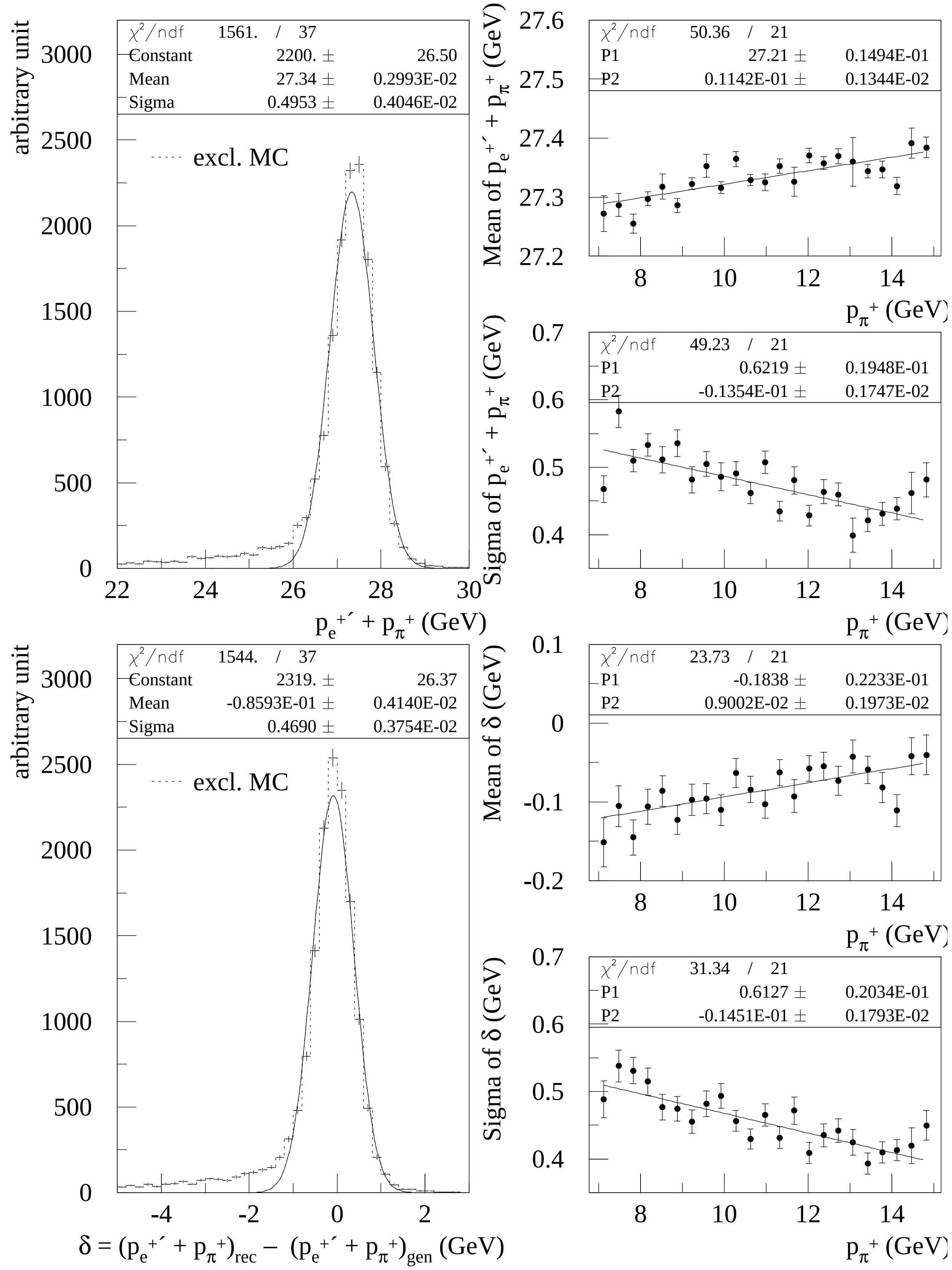

Figure 6.4: The two-track momentum distribution (upper left) and the resolution of the two-track momentum (lower left) obtained from the exclusive MC sample selected with the standard cuts (Table 6.2) and $p_{\pi^+} > 7.05\,\mathrm{GeV}$. The distributions are fitted with a Gaussian function. The dependence of the Gaussian fit parameters on the pion momentum is approximately described by a 2-parameter straight-line fit (right).

Both distributions exhibit a shape which can be fitted with a Gaussian function. The widths (Sigma) of the two distributions differ by only 5% meaning that the Gaussian-shaped spread, Sigma=0.495 GeV, of the two-track momentum (with Mean=27.3 GeV) is mainly due to the resolution, Sigma=0.469 GeV.

As seen from Fig. 6.4 (right), the Mean and Sigma Gaussian parameters of the two-track momentum and resolution distributions show a weak dependence on the pion momentum p_{π^+}. Plotting these parameters as a function of p_{π^+} and fitting them with a 2-parameter straight-line fit gives the Constant and Slope parameters of that dependence. The fit parameters for both the two-track momentum and the resolution are consistent with each other. Here the Constant and Slope parameters of the former are used to construct a pion-momentum dependent two-track momentum cut as

$$\mathrm{Mean}(p_{\pi^+}) - 3\ \mathrm{Sigma}(p_{\pi^+}) < p_{e^{+\prime}} + p_{\pi^+} < \mathrm{Mean}(p_{\pi^+}) + 3\ \mathrm{Sigma}(p_{\pi^+}), \tag{6.6}$$

where

$$\begin{aligned} \mathrm{Mean}(p_{\pi^+}) &= 27.210 + 0.011\, p_{\pi^+}, \\ \mathrm{Sigma}(p_{\pi^+}) &= 0.622 - 0.014\, p_{\pi^+}, \end{aligned} \tag{6.7}$$

are the p_{π^+} dependent Sigma and Mean parameters of the Gaussian fit to the two-track momentum distribution. Evaluated at the minimum and maximum pion momenta, the cut is

$$\begin{aligned} p_{\pi^+} = 7: &\quad 25.715 < p_{e^{+\prime}} + p_{\pi^+} < 28.859, \\ p_{\pi^+} = 15: &\quad 26.139 < p_{e^{+\prime}} + p_{\pi^+} < 28.611, \end{aligned} \tag{6.8}$$

respectively. The lowest and most upper bounds of the two-track momentum cut are indicated by vertical lines on Fig. 6.3.

The data, exclusive MC, and PYTHIA distributions of the kinematic variables are studied again (left panels of Figs. B.5–B.7), after applying the cuts (6.5) and (6.6) on the pion and two-track momenta, respectively, in addition to the standard cuts (Table 6.2). Although the shapes of the distributions do not match exactly, the overlap between the signal and the background is almost complete in all kinematic variables. Therefore there is no need to search for other variables to improve the background rejection, in particular, a cut on the variables t, $\theta_{\gamma^*\pi^+}$, W^2, and θ_{γ^*} (listed as candidates in 3. above) is not necessary.

6.5.3 Resolution Studies

The azimuthal angle ϕ_{π^+} between the scattering and production planes (Fig. 3.1) is an important quantity for the asymmetry measurement (Chapter 7). If the polar angle $\theta_{\gamma^*\pi^+}$ (Fig. 3.1) is of the same order as the $\theta_{\gamma^*\pi^+}$ resolution, then this angle is not well defined. As a consequence, the measurement of ϕ_{π^+} becomes unreliable and leads to large smearing effects in the results, e.g., of the asymmetry which depends on ϕ_{π^+}.

The resolution of $\theta_{\gamma^*\pi^+}$ is obtained from the PYTHIA sample selected with the standard cuts (Table 6.2). The difference between generated and reconstructed values of the angle, $\delta = \theta^{gen}_{\gamma^*\pi^+} - \theta^{rec}_{\gamma^*\pi^+}$, is fitted with a Gaussian function (not shown). The width σ from the fit as well as the RMS of the resolution distribution are shown in Fig. 6.5. The $\theta_{\gamma^*\pi^+}$ resolution is 0.003 rad, being constant in the range $0 < \theta_{\gamma^*\pi^+} < 0.100$ rad and increasing up to 0.015 rad at larger angles.

To avoid smearing effects due to the finite $\theta_{\gamma^*\pi^+}$ resolution (Fig. 6.5), only events with $\theta_{\gamma^*\pi^+} > 0.003$ rad should be accepted, however a safer bound of more than three times the resolution is chosen, namely, the lower cut on this polar angle is defined as

$$\theta_{\gamma^*\pi^+} > 0.010\,\mathrm{rad}. \tag{6.9}$$

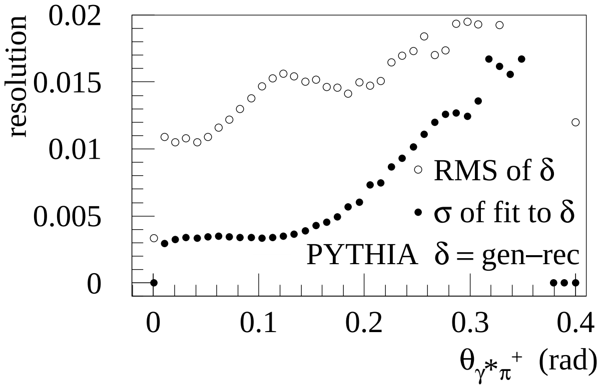

Figure 6.5: The $\theta_{\gamma^*\pi^+}$ resolution as a function of the $\theta_{\gamma^*\pi^+}$ angle obtained from a PYTHIA sample selected with the standard cuts (Table 6.2). Given are both the width σ (full circles) from a Gaussian fit to and the RMS (open circles) of the distribution of generated minus reconstructed values of the angle.

Reading Fig. 6.2 in the opposite direction, i.e., in terms of fractions of rejected (instead of accepted) events, one finds that this cut rejects less than 5% of the signal (selected with the standard cuts, Table 6.2). A more stringent cut (suggested by the larger resolution in terms of RMS), e.g., $\theta_{\gamma^*\pi^+} > 0.020\,\mathrm{rad}$, rejects already 15% of the useful statistics, and is not applied here. We note that the cut (6.9) is only used for the asymmetry measurement (Chapter 7).

The resolutions of ϕ_{π^+} and other kinematic variables are shown in Fig. B.9 (right) and Fig. B.10. Cuts on their values are not applied in this analysis.

6.6 Background Studies

The event selection cuts defined in the previous section are optimised to reject a large fraction of the background while having no or small influence on the signal. The final set of cuts (Table 6.5) used in this section includes the standard ones (Table 6.2), and the cuts (6.5) and (6.6) on the p_{π^+} and $p_{e^{+\prime}} + p_{\pi^+}$ momenta, respectively. The effect of the final cuts on the squared missing mass (M_X^2) distribution is presented for the exclusive MC (Section 6.6.1), and data and PYTHIA (Section 6.6.2).

Separation of the signal from the background is accomplished (Section 6.6.3) by use of the π^+ and π^- data and PYTHIA M_X^2 distributions. Results are compared to those of the background subtraction procedure using data only (Section 6.4.2). The fractions of signal and background processes, which contribute to the total M_X^2 distribution, are estimated in Section 6.6.4.

6.6.1 Missing Mass Distribution from Exclusive Monte Carlo

Fig. 6.6 shows the M_X^2 distribution of reconstructed events selected with the standard and final cuts. The events are generated with the exclusive MC (Section 5.1.1) at the exact position of the squared neutron mass, i.e, at $M_X^2 = M_n^2 = 0.88278\,\mathrm{GeV}^2$. The distribution is characterised by a Gaussian spread around the generated value and a radiative tail stretched towards higher M_X^2 values.

The fraction of events that pass the standard cuts but are removed by the final ones amounts to 21.9%, of which 7.7% consists of events in the Gaussian peak below $M_X^2 < 2.4\,\mathrm{GeV}^2$ and the rest 14.2% are events in the radiative tail. This relatively high percentage of the total signal loss can be accepted for this analysis, because the cleanest exclusive sample is located at low M_X^2, whereas the events in the radiative tail are associated with smearing effects for which no corrections (e.g., to the asymmetry (Chapter 7)) are known. The QED radiative effects can have large influence on the exclusive cross section, the measurement of which is however not the goal of this work.

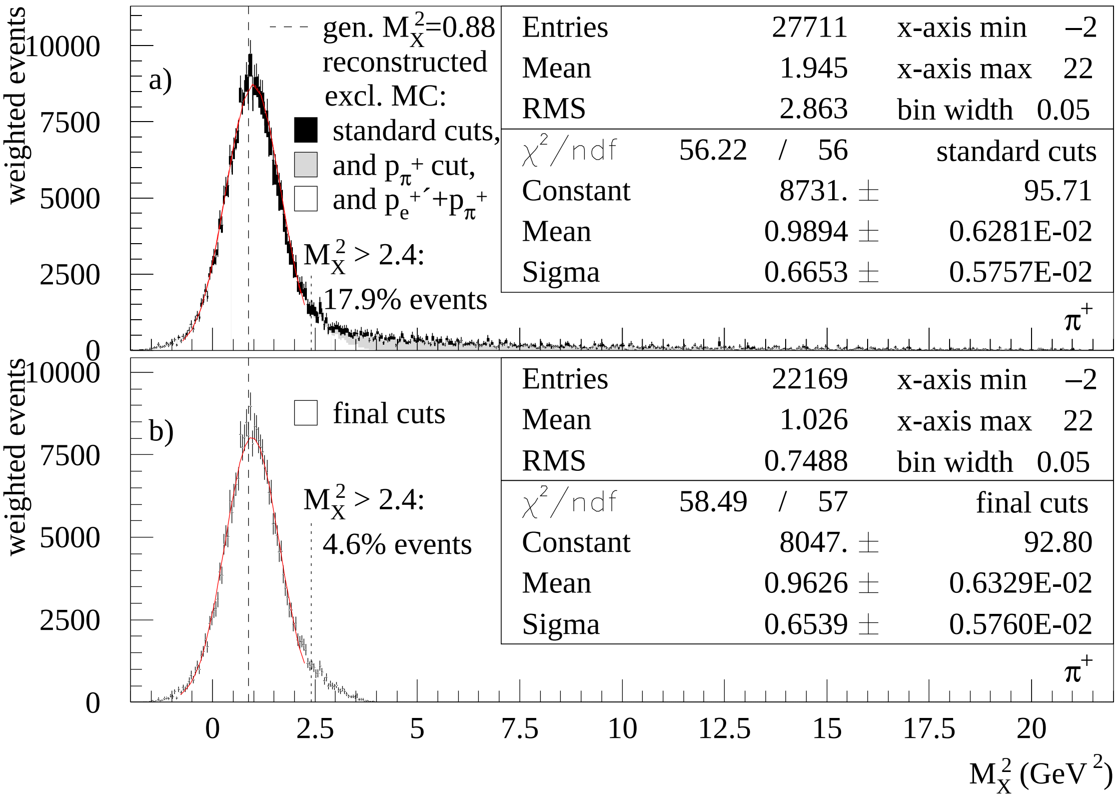

Figure 6.6: The M_X^2 distribution from the exclusive MC sample selected with a) the standard cuts (Table 6.2), the effect of the additional cuts is shown in grey scale; b) the final cuts (Table 6.5).

As seen from Fig. 6.6, it is mainly the cut on the pion momentum p_{π^+} that rejects events in the exclusive peak, while the cut on the two-track momentum $p_{e^{+\prime}} + p_{\pi^+}$ almost completely removes the radiative tail (as indicated by the grey-scale codes, see also Figs. E.5, E.9). The border line at $M_X^2 = 2.4\,\mathrm{GeV}^2$ between the peak and the tail is somewhat arbitrary, but it is used for consistency with the data studies (Section 6.4) where it appears first.

The best χ^2/ndf values are obtained when the Gaussian fit to the M_X^2 distributions is performed in the region $-0.75 < M_X^2 < 2.25\,\mathrm{GeV}^2$, thus minimising the effect of radiative events. The fit parameters given in the lower (upper) panel of Fig. 6.6 correspond to the distribution obtained with the final (standard) cuts; the resolution of the M_X^2 distribution is $\sigma_{M_X^2} = 0.65\,\mathrm{GeV}^2$ ($\sigma_{M_X^2} = 0.67\,\mathrm{GeV}^2$), while the centre of the peak is at $M_X^2 = (0.9626 \pm 0.0063)\,\mathrm{GeV}^2$ ($M_X^2 = (0.9894 \pm 0.0063)\,\mathrm{GeV}^2$). The position of the peak has a significant shift from the generated value that cannot be covered by the fit error. This shift can be explained as being due to, e.g., a residual effect from the radiative tail (at higher values of M_X^2) which is not parameterised in the fit, or a feature of the Monte Carlo production chain. In order to remove the effect of the binning on the fitted peak position a bin width of $0.05\,\mathrm{GeV}^2$ is chosen, i.e., much smaller than the resolution. The peak centre is found at $M_X^2 = 0.9975 \pm 0.0061$ ($M_X^2 = 1.0394 \pm 0.0060$) for a bin width of $0.4\,\mathrm{GeV}^2$ which is comparable to the resolution, for a sample selected the final (standard) cuts. Note that such binning effect may occur in the data, where due to the lack of statistics larger bins have to be used.

6.6.2 Missing Mass Distribution from Data and PYTHIA

In analogy to the background subtraction using data only (Section 6.4.2), the purpose is to obtain an exclusive peak by subtraction of the PYTHIA from the data distribution. Note that both distributions are given below as a normalised yield $\frac{d\tilde{\sigma}}{dM_X^2}$ in units of $\frac{\mathrm{nb}}{\mathrm{GeV}^2}$. The normalisa-

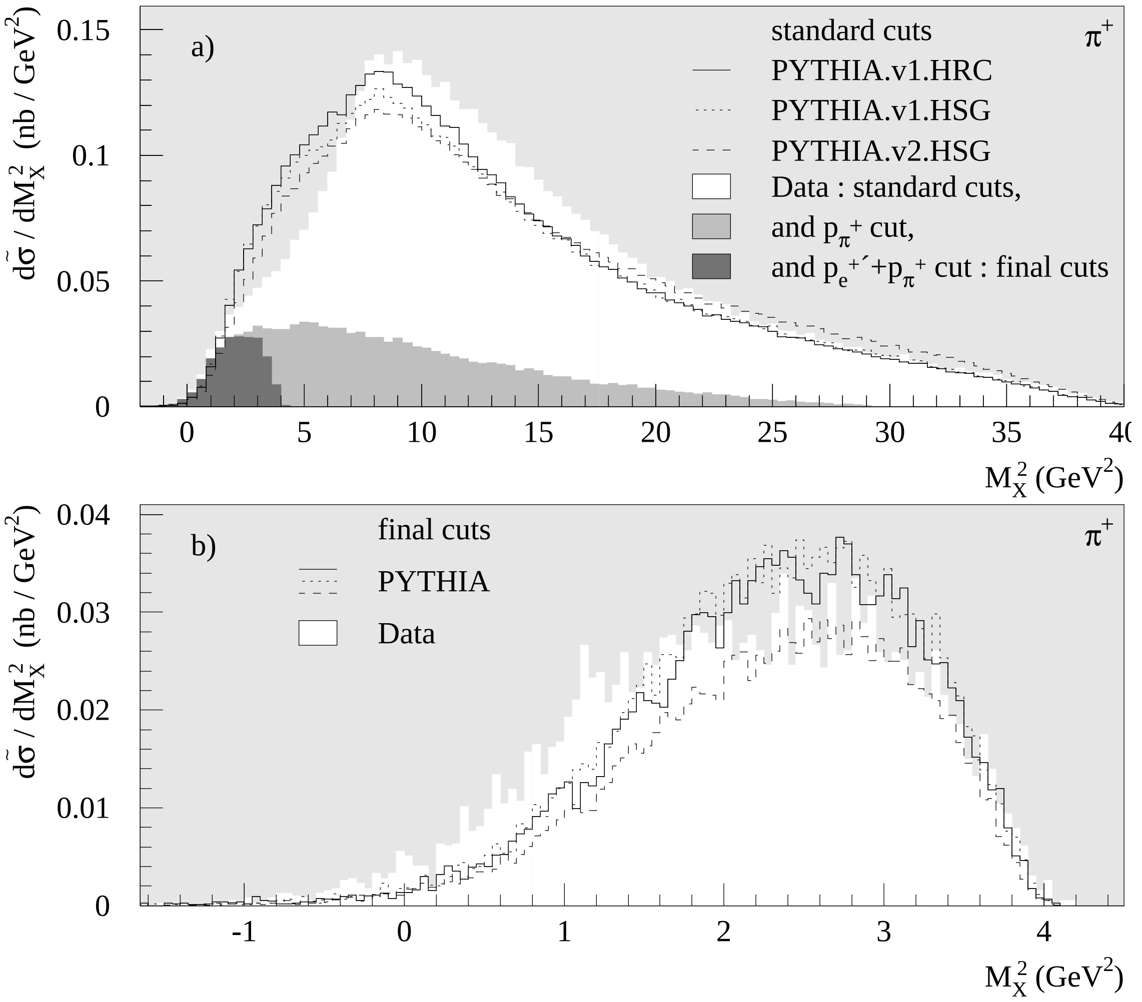

Figure 6.7: a) Comparison of the M_X^2 distributions among three PYTHIA samples and between data and PYTHIA samples selected with the standard cuts (Table 6.2). The effect of the cuts is shown in grey-scale. Bin width is $0.4\,\mathrm{GeV}^2$. b) Comparison among three PYTHIA samples and between data and PYTHIA samples selected with the final cuts (Table 6.5). Bin width is $0.05\,\mathrm{GeV}^2$.

tion of data and PYTHIA samples is described in Sections 6.4.1 and 5.1.2, respectively.

Fig. 6.7.a) shows (using grey scale) the squared missing mass (M_X^2) distributions of π^+ data events selected with the standard cuts (white), plus cuts on the pion momentum p_{π^+} (light-grey), and on the two-track momentum $p_{e^{+\prime}} + p_{\pi^+}$ (dark-grey). The final cuts reject all background events for $M_X^2 > 4\,\mathrm{GeV}^2$ (Fig. 6.7.b)). For comparison with data, the π^+ distributions from three PYTHIA samples, v1.HRC, v1.HSG, and v2.HSG (Section 5.1.3), selected with the standard (final) cuts are superimposed on the upper (lower) panel. The overall feature of the PYTHIA version v2 with respect to v1 is that it generates a smaller (larger) cross section at lower (higher) M_X^2 values. This feature is known to be due to the more realistic estimate of the fraction of VMD events in v2 (Fig. B.11). The agreement between HRC and HSG for v1 is reasonably good.

Data and PYTHIA M_X^2 distributions of events selected with the final cuts are compared in Fig. 6.7.b). PYTHIA.v1.HRC and PYTHIA.v1.HSG are in a good agreement with each other. Compared to the PYTHIA.v2.HSG distribution, the PYTHIA.v1.HRC one overestimates the yield in the entire M_X^2 range (by up to 20%). Therefore the PYTHIA.v1.HRC sample cannot be used directly for background subtraction. The PYTHIA.v2.HSG sample, in principle, can be used but it is not used here because even with reduced fraction of VMD events at lower M_X^2 (compared to PYTHIA.v1.HSG, see Fig. B.11), the data-to-PYTHIA comparison for π^+ is still not sufficiently good (see right panels of Figs. B.2–B.4). Further studies of the background are described in the next section.

6.6.3 Background Subtraction

An attempt is made to estimate the amount of exclusive events in the data sample by using PYTHIA to describe the background. The subtraction of the PYTHIA squared missing mass (M_X^2) distribution from that of the data is expected to give a peak due to the excess of exclusive events produced in the data but not simulated in PYTHIA.

The steps of the background subtraction procedure used for the results of this analysis are as follows.

1. The π^- distribution is subtracted from the π^+ one using the data sample: Data($d\widetilde{\sigma}_{\pi^+} - d\widetilde{\sigma}_{\pi^-}$).
2. Step 1. is performed with the PYTHIA.v1.HRC sample: PYTHIA($d\widetilde{\sigma}_{\pi^+} - d\widetilde{\sigma}_{\pi^-}$).
3. The difference between data (step 1.) and PYTHIA (step 2.) gives the double-difference which extracts the contribution of exclusive events to the π^+ data sample: Data($d\widetilde{\sigma}_{\pi^+} - d\widetilde{\sigma}_{\pi^-}$) − PYTHIA($d\widetilde{\sigma}_{\pi^+} - d\widetilde{\sigma}_{\pi^-}$). We write the latter expression also as

$$d\widetilde{\sigma}_{excl} = (d\widetilde{\sigma}^{\pi^+}_{Data} - d\widetilde{\sigma}^{\pi^-}_{Data}) - (d\widetilde{\sigma}^{\pi^+}_{PYTHIA} - d\widetilde{\sigma}^{\pi^-}_{PYTHIA}). \tag{6.10}$$

Both data and PYTHIA events should be normalised to a common unit. We note that $d\widetilde{\sigma}_{\pi^\pm} \equiv \frac{d\sigma_{\pi^\pm}}{dM_X^2}$ should be understood in case the M_X^2 distributions are considered. This procedure is of course applicable to the distributions of other kinematic variables (see right panels of Figs. B.5–B.7).

Fig. 6.8.a) shows as a function of M_X^2 the difference $d\widetilde{\sigma}_{\pi^+} - d\widetilde{\sigma}_{\pi^-}$ obtained from data and three PYTHIA samples selected with the final cuts. Unlike in the single π^+ and π^- distributions (Figs. 6.7, B.11) where PYTHIA's v1.HRC-to-v2.HSG discrepancies are relatively large, they disappear in the difference of the π^+ and π^- distributions. This is explained by the fact that the distinction between PYTHIA's v1 and v2 samples is only in the generation of the VMD part of the cross section, thus affecting the π^+ and π^- samples in the same way (Fig. B.11). Compared to PYTHIA, the $d\widetilde{\sigma}_{\pi^+} - d\widetilde{\sigma}_{\pi^-}$ difference for data shows an excess of events for $M_X^2 < 2\,\mathrm{GeV}^2$ as expected, while at higher M_X^2 values it is well described by the simulation.

The subtraction of PYTHIA from data according to (6.10) is possible at this point. Moreover, possible flaws in PYTHIA such as missing processes or inaccurate cross sections, that are common to both π^+ and π^-, should also cancel in this double difference.

The result of the double-difference background subtraction procedure (6.10) is presented in Fig. 6.8.b) (full circles). The goodness of this procedure can be estimated from its ability to give a clear exclusive peak at the expected position with a width consistent with the resolution, as well by the behaviour of the resulting distribution outside the exclusive region where only random fluctuations around zero should be observed. In both respects the obtained M_X^2 distribution is satisfactory. The peak is fitted with a Gaussian ($\chi^2/\mathrm{ndf} = 1.10$) giving the centre of the peak at $M_X^2 = (1.093 \pm 0.056)\,\mathrm{GeV}^2$ with a resolution of $\sigma_{M_X^2} = (0.673 \pm 0.048)\,\mathrm{GeV}^2$. Superimposed (dotted line) and fitted with a Gaussian (not shown) is the exclusive MC peak, after being scaled by an arbitrary factor to the Gaussian peak (P1 parameter) of the double difference result. The resolution of the latter is consistent with that obtained from the exclusive MC, whereas the centre of the peak is shifted towards higher values of M_X^2 by 2.32σ compared to that of the exclusive MC and by 3.75σ from the nominal position, where σ denotes here the error on the peak position from the fit.

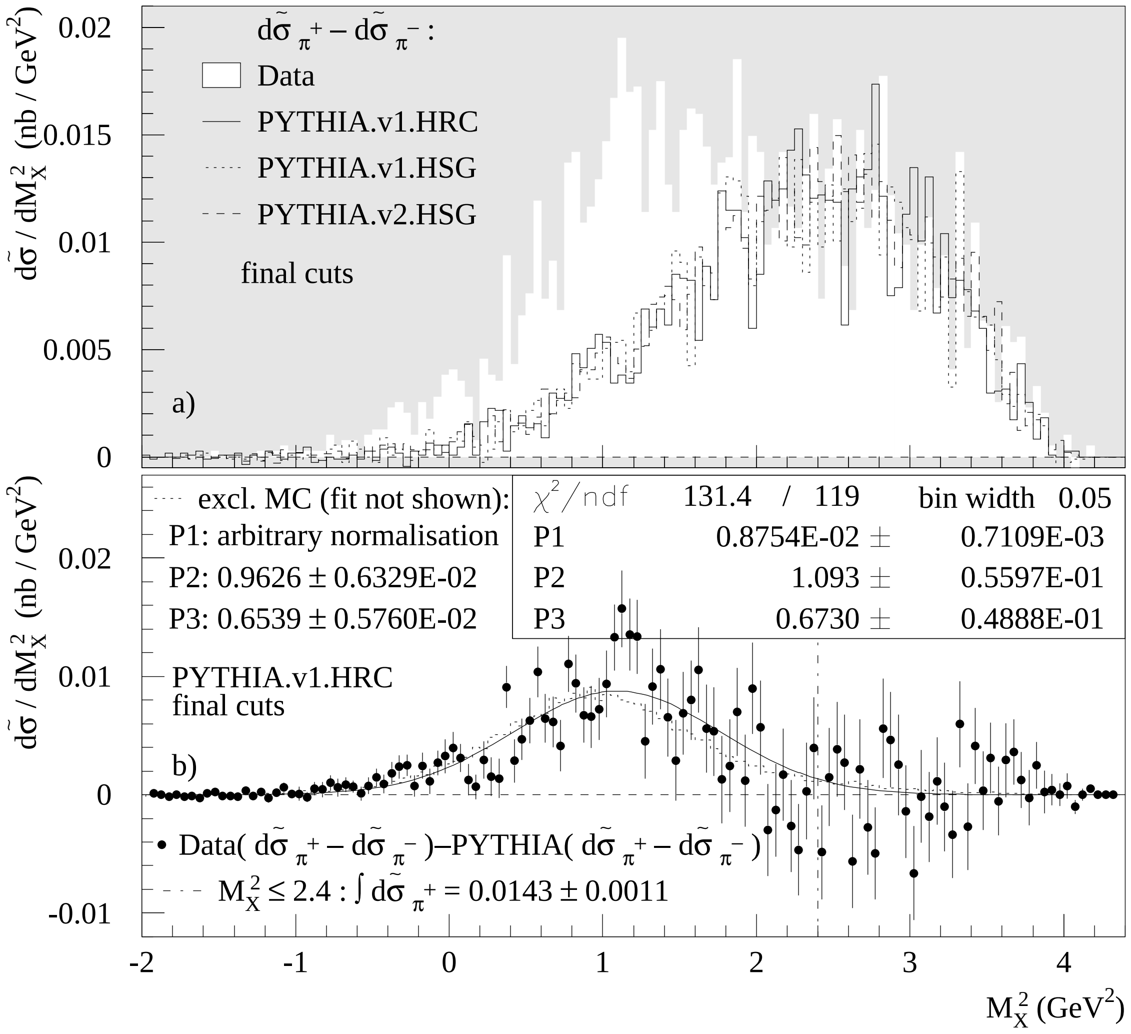

Figure 6.8: a) Comparison of the difference $d\widetilde{\sigma}_{\pi^+} - d\widetilde{\sigma}_{\pi^-}$ between π^+ and π^- M_X^2 distributions for three PYTHIA samples and between PYTHIA and data samples selected with the final cuts (Table 6.5). b) Double-difference distribution: the result from the difference $d\widetilde{\sigma}_{\pi^+} - d\widetilde{\sigma}_{\pi^-}$ for PYTHIA is subtracted from that for data. The PYTHIA.v1.HRC π^+ sample is used.

The measured yield of exclusive π^+ events, given by the area under the peak below $M_X^2 < 2.4\,\mathrm{GeV}^2$, is $\widetilde{\sigma}_{excl} = (0.00143 \pm 0.0011)\,\mathrm{nb}$, which is by 19% lower than the same quantity extracted with the normalised-π^- subtraction procedure (Section 6.4) using only data selected with the standard cuts. We note that this discrepancy is much larger than the expected 7.7% (Section 6.6.1) due to the final event selection cuts, which remove that much of the signal.

In order to show that the background subtraction (6.10) and the one using π^+ and π^- data only (Section 6.4) give better results compared to the alternative one (i.e., using only π^+ data and PYTHIA distributions), the exclusive peaks as obtained with the three procedures are displayed on the left and right panels of Figs. B.12–B.14 with the standard and final cuts, respectively. As seen from the figures, the double-difference procedure gives better results with the final cuts (Table 6.5) defined in this chapter, than with the standard cuts (Table 6.2).

By analogy with the M_X^2 distribution (Fig. 6.8), the double-difference background subtraction procedure (6.10) is applied to other kinematic variables. The resulting exclusive distributions are compared the in right panels of Figs. B.5–B.7 with those obtained from the exclusive MC using the same data-to-exclusive MC normalisation as for the comparison of the M_X^2 distributions (Fig. 6.8).

6.6.4 Process Fractions

We estimate the fractions of signal and background in the measured π^+ data sample. Fractions of the main processes contributing to the π^+ background and to the π^- sample are also given.

The yield of exclusive π^+ events $d\widetilde{\sigma}_{excl}$ (i.e., the signal) is obtained from the background subtraction procedure (Section 6.6.3, Fig. 6.8). The signal and background fractions, f_{excl} and f_{bg}, respectively, are then defined as the following ratios of yields

$$
\begin{aligned}
f_{excl} &= \frac{d\widetilde{\sigma}_{excl}}{d\widetilde{\sigma}_{Data}}, && (6.11)\\
f_{bg} &= \frac{d\widetilde{\sigma}_{bg}}{d\widetilde{\sigma}_{Data}} = \frac{d\widetilde{\sigma}_{Data} - d\widetilde{\sigma}_{excl}}{d\widetilde{\sigma}_{Data}} = 1 - f_{excl}, && (6.12)
\end{aligned}
$$

where $d\widetilde{\sigma}_{bg} = d\widetilde{\sigma}_{Data} - d\widetilde{\sigma}_{excl}$ is defined, and $d\widetilde{\sigma}_{Data}$ is the measured π^+ yield (Fig. 6.7).

The use of PYTHIA (Section 5.1.2) allows us to further separate the background into contributions from deep inelastic scattering (DIS) and vector meson production (VMD). The fractions of these processes in the data sample are obtained from the expressions

$$
\begin{aligned}
f_{DIS} &= \frac{d\widetilde{\sigma}_{DIS}}{d\widetilde{\sigma}_{PYTHIA}} \frac{d\widetilde{\sigma}_{PYTHIA}}{d\widetilde{\sigma}_{Data}}, && (6.13)\\
f_{VMD} &= \frac{d\widetilde{\sigma}_{VMD}}{d\widetilde{\sigma}_{PYTHIA}} \frac{d\widetilde{\sigma}_{PYTHIA}}{d\widetilde{\sigma}_{Data}}, && (6.14)
\end{aligned}
$$

where $d\widetilde{\sigma}_{DIS}$ and $d\widetilde{\sigma}_{VMD}$ are the yields obtained from PYTHIA, and $d\widetilde{\sigma}_{PYTHIA} = d\widetilde{\sigma}_{DIS} + d\widetilde{\sigma}_{VMD}$. Hence the correct knowledge of the process fractions in the background depends, on one hand, on the correct description of these fractions within PYTHIA, and, on the other hand, on the overall agreement between data and PYTHIA.

The results for the ratios of yields and process fractions defined above are shown in Fig. 6.9 as a function of the squared missing mass M_X^2 for π^+ and π^- data, and listed in Table 6.6 with the cut on $\theta_{\gamma^*\pi^+} > 0.010\,\text{rad}$ being applied. We remind that this cut is required only for the asymmetry measurement (Chapter 7). Although the PYTHIA.v1.HRC sample is used in the background subtraction procedure (Fig. 6.8), it cannot be used in the estimation of the process fractions as the VMD fraction is known to be overestimated in this sample (Fig. B.11). Therefore here PYTHIA.v2.HSG is used instead. We conclude that the exclusive signal dominates in the region $M_X^2 < 1.2\,\text{GeV}^2$, being on average 55%. There is practically no signal above $M_X^2 > 1.9\,\text{GeV}^2$.

6.7 Summary

The 2002-2004 HERMES data taken with a transversely polarised proton target and an unpolarised (helicity-balanced) positron beam are analysed in the search of positively charged pions produced in the exclusive process $e^+p \rightarrow e^{+\prime}n\pi^+$. Data quality cuts are applied such as to minimise the loss of data due to problematic detector performance. Further cuts (on the kinematic phase-space, geometry, and event topology) are used to filter out the exclusive π^+ data and reduce the number of background events. An attempt is made, using data only, to separate the exclusive π^+ peak by subtracting the normalised π^- from the π^+ M_X^2 distribution.

Using two Monte Carlo generators, exclusive MC and PYTHIA, three more cuts in addition to the standard ones (Table 6.2) are defined for the selection of exclusive events. The final set of cuts is given in Table 6.5.

Over the entire squared missing mass region ($-2 < M_X^2 \leq 40\,\text{GeV}^2$) the pion and the two-track momentum cuts together reject 96.2% of the background and 21.9% of the signal events in the π^+ data sample selected with the standard cuts (see Table B.2 on page 114).

quantity	cut	reference
pion momentum	$p_\pi > 7.05\,\mathrm{GeV}$	(6.5), Fig. 6.3
two-track momentum	$p_\pi + p_{e^{+\prime}} > 26\,\mathrm{GeV}$	(6.6), Fig. 6.3
$\theta_{\gamma^*\pi^+}$ angle	$\theta_{\gamma^*\pi^+} > 0.010\,\mathrm{rad}$	(6.9), Fig. 6.5
standard cuts		Table 6.2

Table 6.5: The final cuts applied to the data to select event candidates for this analysis. Note: the above full set of cuts is only used for the asymmetry measurement (Chapter 7), whereas in the studies of this chapter and Appendix E the $\theta_{\gamma^*\pi^+}$ cut is omitted unless otherwise noted.

Although the final cuts reject a large amount (96.2%) of the background events, the gain is mostly of practical benefit—we deal with less data in the following. The background removed from the region $-2 < M_X^2 < 2.4\,\mathrm{GeV}^2$ is only 25%. No possibility is found that allows us to further separate the signal from the background.

The exclusive signal is isolated only by subtraction of event distributions (Section 6.6.3) using π^+ and π^- data and PYTHIA samples. Therefore any results extracted from the π^+ data sample still contain contributions from both the signal and the background. However, the estimates of the signal fraction and of the contributions of the main processes (DIS, VMD) to the background, obtained with the PYTHIA generator (Section 6.6.4), allow us to perform background correction to those results.

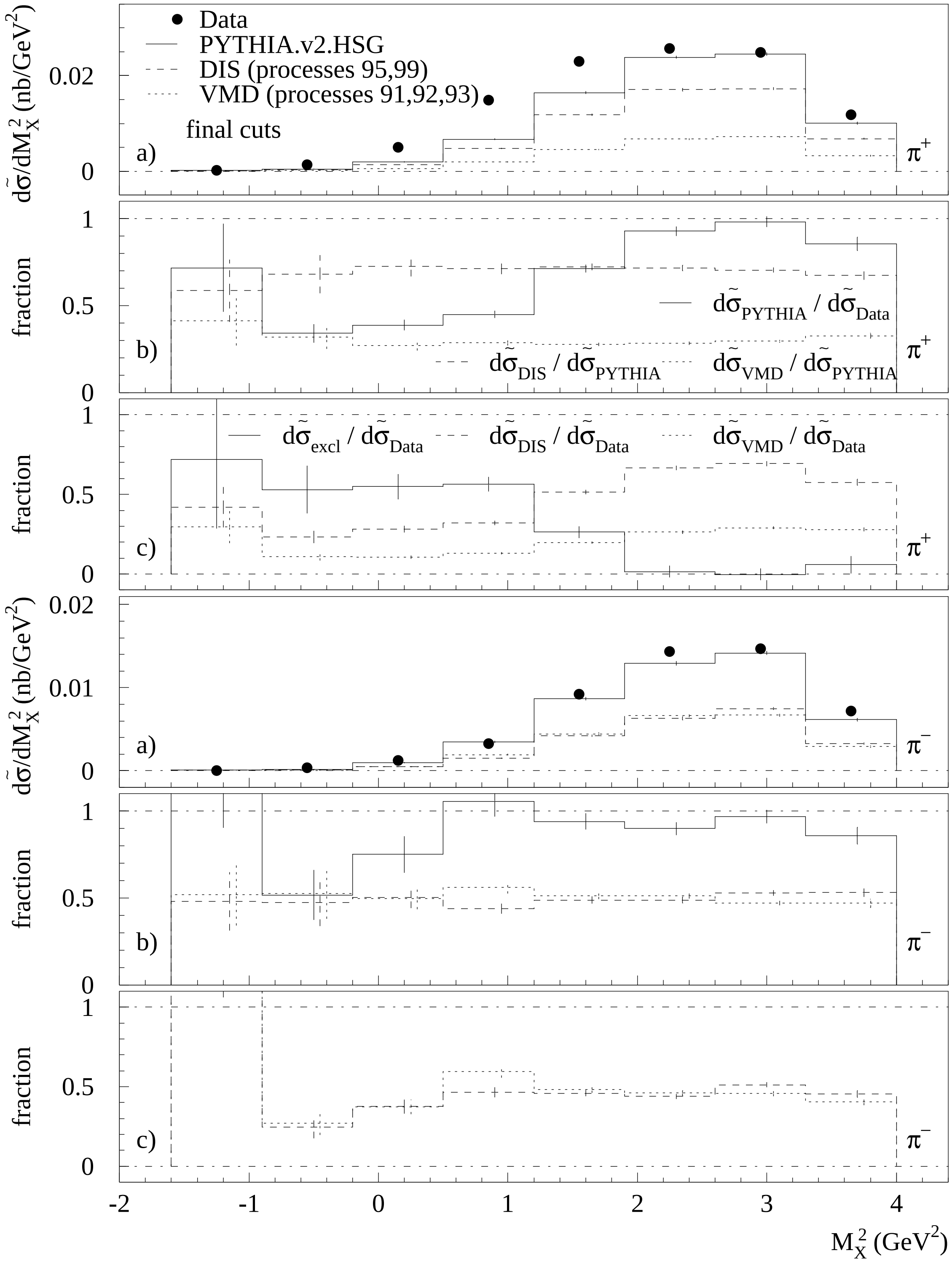

Figure 6.9: Unpolarised yields (a) and process fractions (b,c) for the DIS (deep inelastic scattering), VMD (vector meson dominance) and exclusive reactions for the π^+ (upper half) and π^- (lower half) samples selected with the final cuts (Table 6.5, $\theta_{\gamma^*} > 0.010$ rad is applied). Bin width is 0.7 GeV^2.

M_X^2 bin	GeV^2	-1.6-0.5	0.5-1.2	1.2-1.9	1.9-2.6	2.6-3.3	3.3-4.0	average
f_{excl}	%	π^+ 55.0	56.3	26.3	1.4	-0.2	5.9	24.1
$= \frac{\widetilde{\sigma}_{excl}}{\widetilde{\sigma}_{Data}}$	%	± 6.9	4.6	3.7	3.7	3.8	5.5	2.0
f_{bg}	%	π^+ 45.0	43.7	73.7	98.6	100.2	94.1	75.9
$= \frac{\widetilde{\sigma}_{bg}}{\widetilde{\sigma}_{Data}}$		± 8.5	5.6	5.0	5.2	5.4	7.7	2.6
f_{DIS}	%	π^+ 27.5	32.1	51.5	66.6	69.3	57.6	50.8
$= \frac{\widetilde{\sigma}_{DIS}}{\widetilde{\sigma}_{Data}}$		± 2.0	1.5	1.8	2.1	2.2	2.7	0.9
		π^- 37.6	46.3	45.9	43.9	51.1	45.5	45.0
		± 5.2	4.3	2.6	2.0	2.2	2.9	1.4
f_{VMD}	%	π^+ 11.2	12.9	19.8	26.3	29.0	27.9	21.2
$= \frac{\widetilde{\sigma}_{VMD}}{\widetilde{\sigma}_{Data}}$		± 1.1	0.8	0.9	1.0	1.1	1.5	0.4
		π^- 38.2	59.4	48.2	46.1	45.6	40.3	46.3
		± 5.2	5.3	2.7	2.1	2.0	2.6	1.5
$\frac{\widetilde{\sigma}_{PYTHIA}}{\widetilde{\sigma}_{Data}}$	%	π^+ 38.8	45.0	71.3	92.9	98.3	85.5	72.0
		± 2.7	2.0	2.3	2.8	3.0	3.8	1.2
		π^- 75.8	105.7	94.0	89.9	96.7	85.8	91.3
		± 9.2	8.8	4.7	3.6	3.9	4.9	2.6
$\frac{\widetilde{\sigma}_{DIS}}{\widetilde{\sigma}_{PYTHIA}}$	%	π^+ 70.9	71.2	72.2	71.6	70.5	67.4	70.7
		± 4.8	3.0	1.9	1.6	1.6	2.3	1.1
		π^- 49.6	43.8	48.8	48.8	52.8	53.0	49.5
		± 5.4	3.0	2.0	1.7	1.7	2.5	1.2
$\frac{\widetilde{\sigma}_{VMD}}{\widetilde{\sigma}_{PYTHIA}}$	%	π^+ 28.9	28.8	27.8	28.3	29.5	32.6	29.3
		± 2.7	1.7	1.0	0.9	0.9	1.5	0.6
		π^- 50.4	56.2	51.2	51.2	47.2	47.0	50.5
		± 5.4	3.5	2.1	2.1	1.6	2.4	1.3
$\widetilde{\sigma}_{Data}$	pb	π^+ 4.586	10.387	16.126	17.976	17.431	8.247	12.459
	±	0.241	0.363	0.452	0.477	0.470	0.323	0.162
		π^- 1.165	2.293	6.460	10.058	10.261	5.029	5.878
	±	0.122	0.170	0.286	0.357	0.361	0.252	0.111
$\widetilde{\sigma}_{PYTHIA}$	pb	π^+ 1.779	4.675	11.498	16.707	17.137	7.050	9.808
	±	0.078	0.127	0.199	0.240	0.243	0.156	0.075
		π^- 0.883	2.424	6.075	9.046	9.926	4.317	5.445
	±	0.055	0.091	0.145	0.177	0.185	0.122	0.056
$\widetilde{\sigma}_{DIS}$	pb	π^+ 1.262	3.330	8.305	11.970	12.084	4.751	6.950
	±	0.066	0.107	0.169	0.203	0.204	0.128	0.063
		π^- 0.438	1.062	2.962	4.413	5.244	2.289	2.735
	±	0.039	0.061	0.101	0.123	0.134	0.088	0.040
$\widetilde{\sigma}_{VMD}$	pb	π^+ 0.514	1.345	3.193	4.734	5.054	2.300	2.856
	±	0.042	0.068	0.105	0.128	0.132	0.089	0.041
		π^- 0.445	1.362	3.113	4.634	4.682	2.027	2.710
	±	0.039	0.069	0.104	0.126	0.127	0.084	0.039
$\widetilde{\sigma}_{excl}$	pb	π^+ 2.524	5.843	4.243	0.258	-0.042	0.484	2.218
	±	0.286	0.430	0.589	0.666	0.666	0.455	0.218
$\widetilde{\sigma}_{bg}$	pb	π^+ 2.062	4.544	11.883	17.718	17.473	7.763	10.241
$= \widetilde{\sigma}_{Data} - \widetilde{\sigma}_{excl}$	±	0.374	0.563	0.742	0.819	0.815	0.558	0.272

Table 6.6: Process fractions, unpolarised yields, and ratios of the yields obtained from data, PYTHIA.v2.HSG, and the exclusive MC samples selected with the final cuts (Table 6.5, $\theta_{\gamma^*} > 0.010\,\mathrm{rad}$ is applied). The process fractions fulfill the equality $f_{excl} + f_{DIS} + f_{VMD} \approx 1$. The numbers correspond to Fig. 6.9.

Chapter 7

Analysis of the Azimuthal Asymmetry

The extraction of the azimuthal asymmetry amplitudes is described in the following. The values of the amplitudes are measured from the π^+ and π^- data samples selected with the final cuts (Table 6.5). Non-exclusive processes are present in both samples, while exclusive pion production which is of primary interest in this analysis, contributes only to the π^+ sample. A method is described to estimate the effect of smearing on the measured amplitudes using Monte Carlo simulation. Correction for the background contribution to the leading amplitude for π^+ is applied.

7.1 Extraction of Asymmetry Amplitudes

The definition of the azimuthal asymmetry $A(\phi, \phi_S)$ given in (3.20) is used. To measure this asymmetry we need to compute the azimuthal angles ϕ (3.2) and ϕ_S (3.3) for each event and to separate the data sample into two subsamples of events corresponding to the two target polarisation states. In this analysis ϕ_S is always computed with respect to the fixed axis $\vec{S} = (0, -1, 0)$ in the HERMES coordinate system (Section 4.3, C' frame in Fig. 3.1), while the target polarisation state, which is available per event, is actually used to identify events as belonging to one of the two subsamples. Conventionally [9], ϕ_S and $\phi_S + \pi$ in (3.20) just denote the positive ($P_T > 0$ or 'spin-up') and negative ($P_T < 0$ or 'spin-down') states for the case of transversely polarised target. We remind that at HERMES the polarisation of the target is flipped every 90 s during data taking.

The asymmetry $A(\phi, \phi_S)$ is predicted to exhibit six sine modulations as shown in (3.23). The physical information describing the details of the scattering process is contained in the amplitudes of these modulations. Only the size of the leading amplitude $A_{UT}^{\sin(\phi-\phi_S)}$, i.e., the one that gives the largest contribution to the asymmetry for exclusive pion production, is predicted by theory. None of the amplitudes is measured so far.

Our goal is to estimate the six asymmetry amplitudes (3.23) of the sine modulations of the asymmetry $A_{meas}(\phi, \phi_S)$ measured from our data. This is achieved by performing a fit to the values of $A_{meas}(\phi, \phi_S)$ with the free parameters of the fit giving the extracted amplitudes.

A 2-dimensional 6-parameter unbinned maximum likelihood (UML) fit is used to extract the amplitudes in this analysis. This choice is based on a comparison with other extraction methods (moments method [27, 30], binned 2D [30, 31] and 1D [60] fits). Monte Carlo simulations show that the UML fit is best suited for use with a low statistics data sample as ours [46]. The fit proceeds in a similar manner as a 2-dimensional binned χ^2 fit, however, without breaking the sample into bins. The fit procedure is described in Section 7.1.1 and the measured amplitudes are presented in Section 7.1.2.

7.1.1 Unbinned Maximum Likelihood Fit

We assume that the azimuthal asymmetry to be measured from our data, $A_{meas}(\phi, \phi_S)$, can be described by six sine modulations and their amplitudes as predicted by the theory of pion electroproduction in Section 3.1. That is, we work under the hypothesis that the asymmetry is given by (3.23)

$$A_{meas}(\phi, \phi_S) = \sum_{k=1}^{6} A_{UT,meas}^{\sin(\mu\phi+\lambda\phi_S)_k} \sin(\mu\phi + \lambda\phi_S)_k, \tag{7.1}$$

where $k = 1, \ldots, 6$ (see (3.21), (3.22), and table following (3.17)). The sign of the asymmetry is flipped in (7.1) for convenience and accord with a more widely accepted convention.

From (3.20) and the expression $d\sigma(\phi, \phi_S) + d\sigma(\phi, \phi_S + \pi) = 2d\sigma_{UU}(\phi)$ (3.19) it follows for the cross sections

$$\begin{aligned} d\sigma(\phi, \phi_S) &= [1 + |P_T|\, A(\phi, \phi_S)]\; d\sigma_{UU}(\phi), & (7.2)\\ d\sigma(\phi, \phi_S + \pi) &= [1 - |P_T|\, A(\phi, \phi_S)]\; d\sigma_{UU}(\phi), & (7.3) \end{aligned}$$

where $d\sigma_{UU}(\phi)$ is the unpolarised cross section (3.16). In the calculations with data $d\sigma(\phi, \phi_S)$ ($d\sigma(\phi, \phi_S + \pi)$) corresponds to the event counts N^+ (N^-) with positive $P_T > 0$ (negative $P_T < 0$) target polarisation, and the asymmetry $A(\phi, \phi_S)$ is replaced by (7.1). The azimuthal angles ϕ and ϕ_S (see Fig. 3.1, (3.2), (3.3)) are computed per event.

Using (7.2) and (7.3), the probability density function (p.d.f) [70] is constructed as

$$f_\pm(\phi, \phi_S; \theta_k) = \frac{1}{C_\pm}\left[1 \pm |P_T| \sum_{k=1}^{6} \theta_k \sin(\mu\phi + \lambda\phi_S)_k\right], \tag{7.4}$$

where the + (−) sign refers to polarisation states with $P_T > 0$ ($P_T < 0$), θ_k are the parameters of the fit, and $C_\pm$ is a normalisation constant; $C_\pm = 1$ is taken in this work.

The extracted asymmetry amplitudes $A_{UT,meas}^{\sin(\mu\phi+\lambda\phi_S)_k}$ are those values of θ_k that maximise the likelihood function

$$L(\theta_k) = L_+(\theta_k)L_-(\theta_k) = \prod_{i=1}^{N^+} f_+(\phi, \phi_S; \theta_k) \prod_{j=1}^{N^-} f_-(\phi, \phi_S; \theta_k), \tag{7.5}$$

or minimise the negative log-likelihood function

$$-\ln L(\theta_k) = -\ln L_+(\theta_k) - \ln L_-(\theta_k) = -\sum_{i=1}^{N^+} \ln f_+(\phi, \phi_S; \theta_k) - \sum_{j=1}^{N^-} \ln f_-(\phi, \phi_S; \theta_k). \tag{7.6}$$

The function minimisation is performed with the MIGRAD or HESSE routines from the MINUIT package [3].

7.1.2 Measured Asymmetry Amplitudes

Each of the π^+ and π^- data samples is divided into six bins of the squared missing mass M_X^2. The M_X^2 binning and the number of events per bin N^+ (N^-) for the positive $P_T > 0$ (negative $P_T < 0$) target polarisation are given in Table 7.1.

In order to balance between resolution effects and sufficient statistics, the M_X^2-bin width (0.7 GeV^2) is chosen to be equal to the M_X^2 resolution (Figs. 6.6, 6.8), except for the first bin which is three times wider in order to collect enough event counts. For each of the M_X^2 bins the

M_X^2 bin	GeV^2	-1.6-0.5	0.5-1.2	1.2-1.9	1.9-2.6	2.6-3.3	3.3-4.0	total
N^+ ($P_T > 0$)	events	π^+ 185	405	622	718	686	346	2962 ± 54
		π^- 51	87	267	417	407	191	1420 ± 38
N^- ($P_T < 0$)	events	π^+ 177	415	651	701	690	305	2939 ± 54
		π^- 41	94	243	377	403	206	1364 ± 37
$N^+ + N^-$	events	π^+ 362	820	1273	1419	1376	651	5901 ± 77
		π^- 92	181	510	794	810	397	2784 ± 53

Table 7.1: The π^+ and π^- data samples used for the extraction of the asymmetry amplitudes (Fig. 7.1, Table 7.2). The squared missing mass (M_X^2) binning and the number of events per bin N^+ (N^-) for positive $P_T > 0$ (negative $P_T < 0$) target polarisation are given.

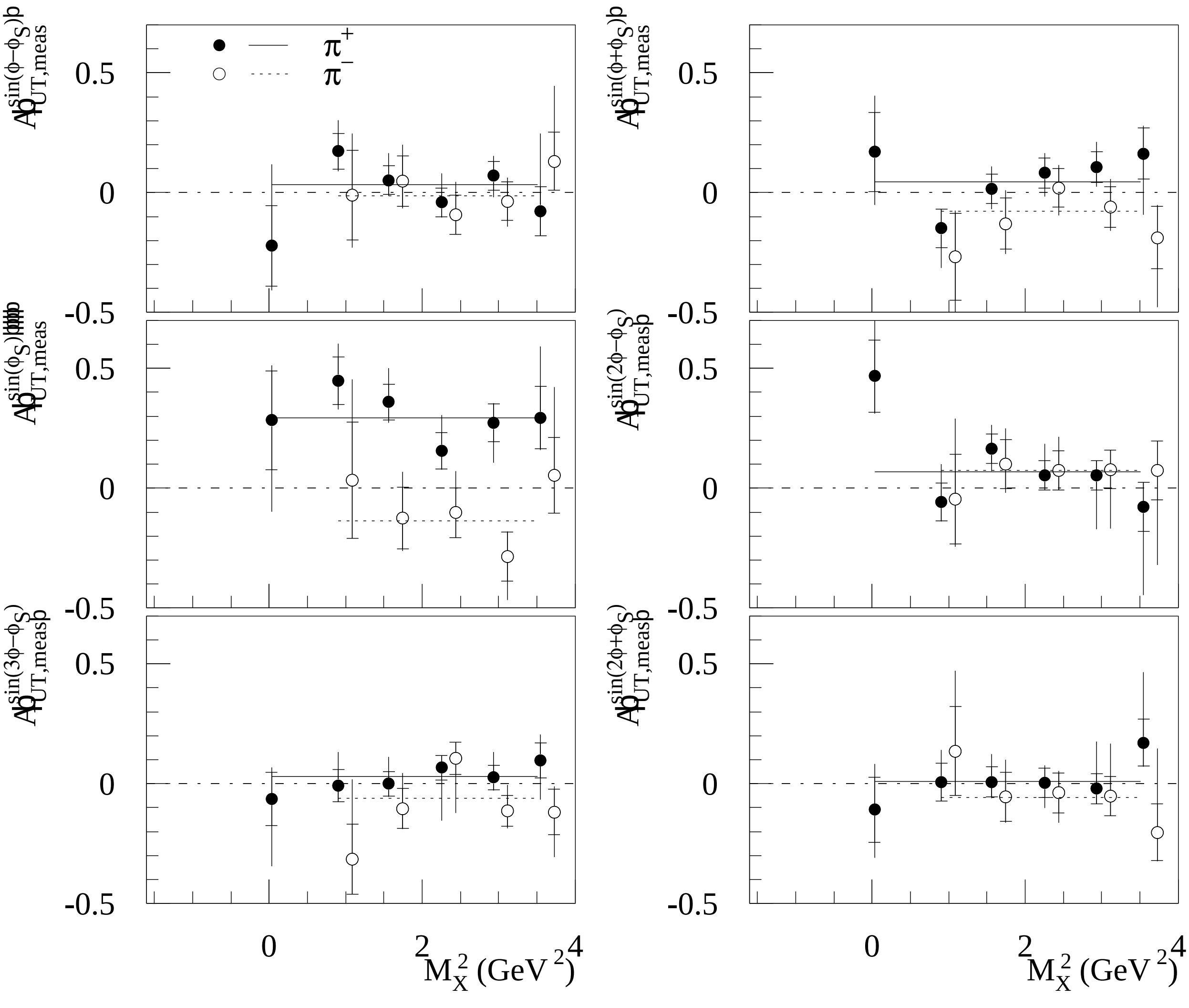

Figure 7.1: The measured six asymmetry amplitudes (7.1) as a function of the squared missing mass M_X^2 for the π^+ (full circles) and π^- (open circles) data samples (Table 7.1). The small horizontal bars enclose the statistical uncertainty, while the full vertical error bars show the total uncertainty obtained from a quadratic sum of the statistical and systematic uncertainties. The long horizontal lines are straight-line fits to the data points. Values are listed in Tables 7.2, 7.5.

values of the azimuthal angles ϕ and ϕ_S are computed per event. The ϕ, ϕ_S values are inserted in the log-likelihood function (7.6), which upon minimisation with the UML fit (Section 7.1.1) yields the six asymmetry amplitudes (7.1). The UML fit package, developed at HERMES by J. Dreschler [29], is kindly provided to us by the author.

	M_X^2 bin, GeV^2					
	-1.6-0.5	0.5-1.2	1.2-1.9	1.9-2.6	2.6-3.3	3.3-4.0
	$A_{UT,meas}^{\sin(\phi-\phi_S)}$	$\pi^+:\ 0.034\pm0.030\,(\chi^2/\mathrm{ndf}=1.8)$ $\pi^-:\ -0.013\pm0.045\,(\chi^2/\mathrm{ndf}=0.68)$				
π^+	-0.22 ± 0.17	0.17 ± 0.07	0.05 ± 0.06	-0.04 ± 0.06	0.07 ± 0.06	-0.08 ± 0.10
π^-	1.58 ± 0.75	-0.01 ± 0.19	0.05 ± 0.10	-0.09 ± 0.08	-0.04 ± 0.08	0.13 ± 0.12
	$A_{UT,meas}^{\sin(\phi+\phi_S)}$	$\pi^+:\ 0.046\pm0.031\,(\chi^2/\mathrm{ndf}=1.8)$ $\pi^-:\ -0.077\pm0.046\,(\chi^2/\mathrm{ndf}=0.88)$				
π^+	0.17 ± 0.16	-0.15 ± 0.08	0.02 ± 0.06	0.08 ± 0.06	0.11 ± 0.07	0.16 ± 0.11
π^-	-1.56 ± 0.71	-0.27 ± 0.18	-0.13 ± 0.11	0.02 ± 0.08	-0.06 ± 0.08	-0.19 ± 0.13
	$A_{UT,meas}^{\sin\phi_S}$	$\pi^+:\ 0.293\pm0.038\,(\chi^2/\mathrm{ndf}=1.3)$ $\pi^-:\ -0.135\pm0.057\,(\chi^2/\mathrm{ndf}=1.05)$				
π^+	0.28 ± 0.21	0.45 ± 0.10	0.36 ± 0.08	0.16 ± 0.08	0.27 ± 0.08	0.29 ± 0.13
π^-	2.11 ± 0.87	0.03 ± 0.24	-0.13 ± 0.13	-0.10 ± 0.10	-0.29 ± 0.10	0.05 ± 0.16
	$A_{UT,meas}^{\sin(2\phi-\phi_S)}$	$\pi^+:\ 0.068\pm0.030\,(\chi^2/\mathrm{ndf}=2.8)$ $\pi^-:\ 0.073\pm0.045\,(\chi^2/\mathrm{ndf}=1.2)$				
π^+	0.47 ± 0.15	-0.06 ± 0.08	0.16 ± 0.06	0.05 ± 0.06	0.05 ± 0.06	-0.08 ± 0.10
π^-	-0.85 ± 0.51	-0.05 ± 0.19	0.10 ± 0.10	0.07 ± 0.08	0.08 ± 0.08	0.07 ± 0.12
	$A_{UT,meas}^{\sin(3\phi-\phi_S)}$	$\pi^+:\ 0.029\pm0.025\,(\chi^2/\mathrm{ndf}=0.56)$ $\pi^-:\ -0.061\pm0.036\,(\chi^2/\mathrm{ndf}=2.6)$				
π^+	-0.06 ± 0.11	-0.01 ± 0.07	-0.00 ± 0.05	0.07 ± 0.05	0.03 ± 0.05	0.10 ± 0.07
π^-	0.17 ± 0.24	-0.31 ± 0.15	-0.10 ± 0.08	0.11 ± 0.07	-0.11 ± 0.07	-0.12 ± 0.10
	$A_{UT,meas}^{\sin(2\phi+\phi_S)}$	$\pi^+:\ 0.010\pm0.030\,(\chi^2/\mathrm{ndf}=0.74)$ $\pi^-:\ -0.059\pm0.045\,(\chi^2/\mathrm{ndf}=0.66)$				
π^+	-0.11 ± 0.14	0.01 ± 0.08	0.01 ± 0.06	0.00 ± 0.06	-0.02 ± 0.06	0.17 ± 0.10
π^-	0.69 ± 0.41	0.14 ± 0.19	-0.05 ± 0.10	-0.04 ± 0.08	-0.05 ± 0.08	-0.20 ± 0.12

Table 7.2: The values of the measured π^+ and π^- six asymmetry amplitudes (7.1) for the six M_X^2 bins shown in Fig. 7.1. The values (and the χ^2/ndf) from a straight-line fit to the data points are given.

Fig. 7.1 shows the six asymmetry amplitudes, $A_{UT,meas}^{\sin(\phi-\phi_S)}$, $A_{UT,meas}^{\sin(\phi+\phi_S)}$, $A_{UT,meas}^{\sin\phi_S}$, $A_{UT,meas}^{\sin(2\phi-\phi_S)}$, $A_{UT,meas}^{\sin(3\phi-\phi_S)}$, and $A_{UT,meas}^{\sin(2\phi+\phi_S)}$ with their statistical uncertainties extracted with the UML fit from the π^+ and π^- data samples (Table 7.1). The measurements for π^+ (full circles) and π^- (open circles) are plotted as a function of M_X^2. A straight line is fitted through the data points. The amplitude values and their statistical uncertainties are listed in Table 7.2, while the evaluation of the systematic uncertainties is discussed in Section 7.3. Most of the measured amplitudes are either zero or not significantly far from zero within the statistical error bars. Only $A_{UT,meas}^{\sin\phi_S}$ is found to be relatively large. Its average value is positive (negative) for π^+ (π^-).

The display of the amplitudes in the entire region $-1.6 < M_X^2 \leq 4.0\,\mathrm{GeV}^2$ (Fig. 7.1) allows one to check whether a distinct behaviour is observed around $M_X^2 \approx 1\,\mathrm{GeV}^2$ for π^+, which corresponds to the position the exclusive peak (Fig. 6.8). From an unbiased point of view there is no significant indication for such a behaviour. We remind that although the event selection (Table 6.5) is optimised for the study of exclusive π^+ production, the resulting π^+ data sample and therefore the measurements in Fig. 7.1 correspond to a mixture of both exclusive and background events. According to Monte Carlo simulation, the background is described by DIS (deep inelastic scattering) and VMD (vector meson dominance) production, while the π^- sample consists entirely of DIS and VMD events. The process fractions for π^+ and π^- in the six M_X^2 bins are estimated in Chapter 6 (Fig. 6.9) and listed in Table 6.6. As can be read from this table, the fraction of exclusive π^+ events is only slightly larger than that of the background in the first two M_X^2 bins and becomes negligible for $M_X^2 > 1.9\,\mathrm{GeV}^2$.

Thus the results in Fig. 7.1 for π^+ do not give information about the exclusive process only. In order to provide a measurement of the exclusive π^+ amplitudes, in addition to the process fractions one needs a knowledge of the amplitudes for each background process. A method for a background correction to the measured π^+ amplitudes is discussed in Section 7.4. The final results and their interpretation are presented in Chapter 8.

Fig. 7.1 and Table 7.2 together with the process fractions in Table 6.9 and the systematic uncertainties in Table 7.5 present our results for the measured six amplitudes of the sine modulations of the transverse-target single-spin azimuthal asymmetry. More details about the extraction of the amplitudes are given in the rest of this section.

Goodness of UML fit

An attempt is made to give a measure of goodness of the UML fit used in Section 7.1.2 to extract the asymmetry amplitudes from data.

The (ϕ, ϕ_S)-plane is divided into 8×8 bins. For a given M_X^2 bin the asymmetry and its statistical uncertainty are computed in each (ϕ, ϕ_S) bin i, $i = 1, \ldots 64$ as

$$A_{i,Data} = \frac{N_i^+ - N_i^-}{N_i^+ + N_i^-}, \quad \delta A_{i,Data} = \frac{\sqrt{(2\,N_i^-\,\delta N_i^+)^2 + (2\,N_i^+\,\delta N_i^-)^2}}{(N_i^+ + N_i^-)^2}, \tag{7.7}$$

where N_i^+ (N_i^-) is the number of events for $P_T > 0$ $(P_T < 0)$, and $\delta N_i^\pm = \sqrt{N_i^\pm}$ is the statistical uncertainty; if $N_i^\pm = 0$ then $\delta N_i^\pm = 1$ is taken. The π^+ data sample is used.

The values of the six amplitudes for π^+ (Table 7.2) obtained from the UML fit and the average values of the azimuthal angles $\langle\phi\rangle_i$, $\langle\phi_S\rangle_i$ are used to compute the asymmetry and its statistical uncertainty in each bin i as

$$\begin{aligned} A_{i,UML} &= \sum_{k=1}^{6} A_{UT,meas}^{\sin(\phi+\lambda\phi_S)_k}\ \sin(\mu\langle\phi\rangle_i + \lambda\langle\phi_S\rangle_i)_k, \\ \delta A_{i,UML} &= \sqrt{\sum_{k=1}^{6} \left[\delta A_{UT,meas}^{\sin(\phi+\lambda\phi_S)_k}\ \sin(\mu\langle\phi\rangle_i + \lambda\langle\phi_S\rangle_i)_k\right]^2}. \end{aligned} \tag{7.8}$$

The bin asymmetries $A_{i,Data}$ and $A_{i,UML}$ are shown in Fig. 7.2 (top) as a 2-dimensional grey-scale scatter plot in the range from -1 to 1 with 8×8 (ϕ, ϕ_S) bins for $0.5 < M_X^2 \leq 1.9\,\mathrm{GeV}^2$. The asymmetry values as a function of the (ϕ, ϕ_S) bin number i are also shown in Fig. 7.2 (middle). As an estimate of the degree of agreement between the two sets of points (full and open circles for Data and UML, respectively), the following quantity is computed per bin i

$$\frac{A_{i,Data} - A_{i,UML}}{\sqrt{(\delta A_{i,Data})^2 + (\delta A_{i,UML})^2}}, \tag{7.9}$$

whose values are displayed with open squares in Fig. 7.2 (bottom). Since most of the square points appear to be randomly scattered in the range between -1 and 1 we conclude that the parameters extracted with the UML fit describe the measured asymmetry sufficiently well.

The quantity (7.9) is computed for six M_X^2 bins using the π^+ sample and shown in Fig. 7.3. Although the number of events varies among the M_X^2 bins (Table 7.1) the UML fit gives equally good results for all of them.

Sign of Extracted Amplitudes

A remark follows about the signs of the theoretical and experimental asymmetry amplitudes. The azimuthal angles ϕ and ϕ_S (Fig. 3.1), and the asymmetry $A(\phi, \phi_S)$ (3.20, 3.23) are defined in agreement with the Trento conventions [9], which require that

- For a positive (negative) target polarisation $P_T > 0$ $(P_T < 0)$ the target polarisation vector S_T (Fig. 3.1) points parallel (antiparallel) to the positive direction of the vertical y axis.

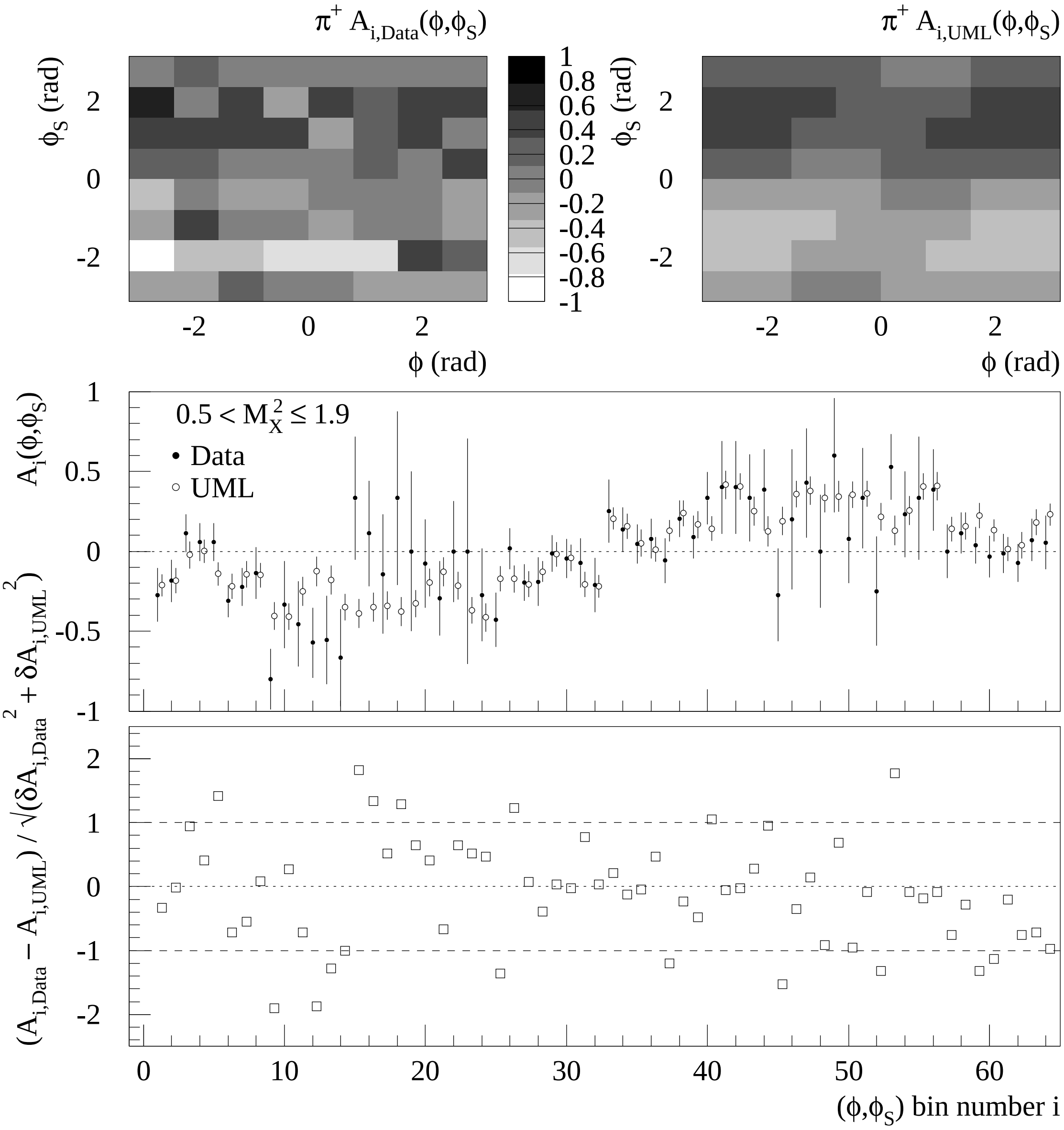

Figure 7.2: The bin asymmetries $A_{i,Data}$ (7.7) and $A_{i,UML}$ (7.8) are presented for the π^+ data sample in $0.5 < M_X^2 \leq 1.9\,\mathrm{GeV}^2$ as a 2-dimensional grey-scale scatter plot in the range from -1 to 1 with 8×8 (ϕ, ϕ_S) bins (top), and as a function of the (ϕ, ϕ_S) bin number i (middle) with $\delta A_{i,Data}$ and $\delta A_{i,UML}$ being the statistical uncertainties. The open squares (bottom) give an estimate of the degree of agreement between the two sets of points (full and open circles for Data and UML, respectively).

- The asymmetry is defined as the difference of the cross sections for $P_T > 0$ and $P_T < 0$ (with the appropriate $|P_T|$ normalisation as in (3.20)).

These definitions and the conventions for σ_{mn}^{ij} in [27] give the minus sign in (3.21) for the theoretical asymmetry, and, in particular, the minus signs for the amplitudes in (3.23).

The asymmetry amplitude results obtained in this thesis can be directly compared with other measurement and predictions which conform with the Trento conventions [9].

Beam Polarisation

The measurement of the asymmetry amplitudes $A_{UT,meas}^{\sin(\mu\phi+\lambda\phi_S)_k}$ (7.1) for an unpolarised (U) beam is achieved in this analysis by balancing the helicity states of the otherwise longitudinally polarised HERA beam. The helicity of the beam was flipped several times during data taking

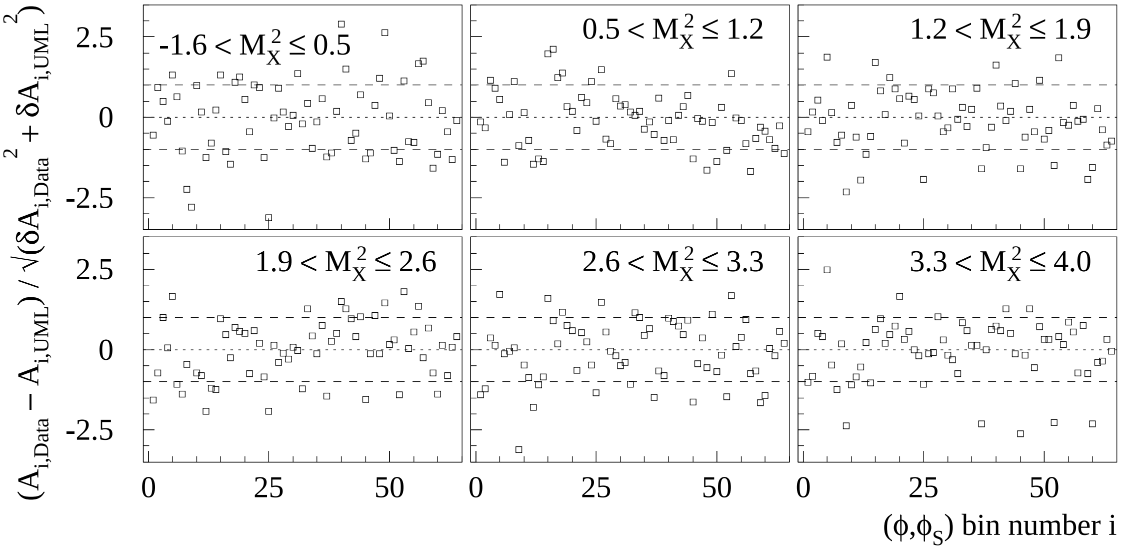

Figure 7.3: An estimate of the of the degree of agreement between the bin asymmetries $A_{i,Data}$ (7.7) and $A_{i,UML}$ (7.8) for the π^+ data sample and for six M_X^2 bins. $\delta A_{i,Data}$ and $\delta A_{i,UML}$ are the statistical uncertainties. See also Fig. 7.2.

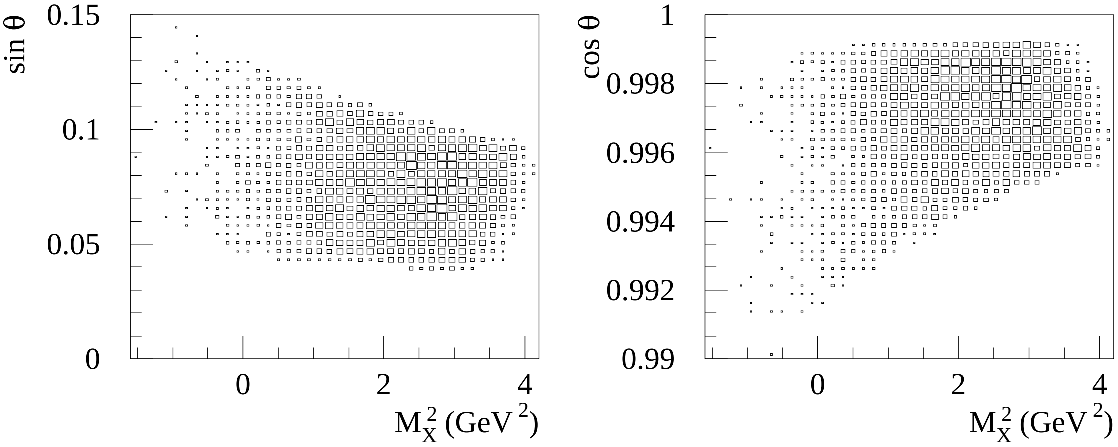

Figure 7.4: The values of $\sin\theta$ and $\cos\theta$ versus the squared missing mass M_X^2 for the π^+ data sample selected with the final cuts (Table 6.5). The angle $\theta \equiv \theta_{\gamma^*}$ defined through (3.5) is the polar angle between the incoming positron and the virtual photon (Fig. 3.1).

so that an almost zero net polarisation ($\langle P_{e^+}\rangle = 0.072$) is obtained for the combined 2002-2004 data sample. This value is considered to be too small to cause an observable background asymmetry therefore no further attempt is made here, neither by rejecting part of the data nor by means of corrections, to perfectly bring $\langle P_{e^+}\rangle$ to zero.

Kinematic Approximation

Besides neglecting the positron mass, the approximation (3.18) is assumed to hold for this analysis. The largest deviation from unity for a maximum value of $\sin\theta = 0.15$ at $\sin\phi_S = 1$ is $\Gamma = 1.011$. The $\sin\theta$ and $\cos\theta$ distributions with the final cuts (Table 6.5) versus M_X^2 are shown in Fig.7.4. The average values are $\langle\gamma\rangle = 0.101$, $\langle\sin\theta\rangle = 0.081$, and $\langle\cos\theta\rangle = 0.997$ for $0.5 < M_X^2 \leq 1.2\,\text{GeV}^2$, where θ and γ are defined in (3.5). The values $\gamma = 0.095$, $\sin\theta = 0.074$, and $\cos\theta = 0.997$ are obtained for the average HERMES kinematics (Table B.3, final cuts), therefore $\sin\theta \approx 0$ and $\cos\theta \approx 1$ can be used also in the table following (3.17).

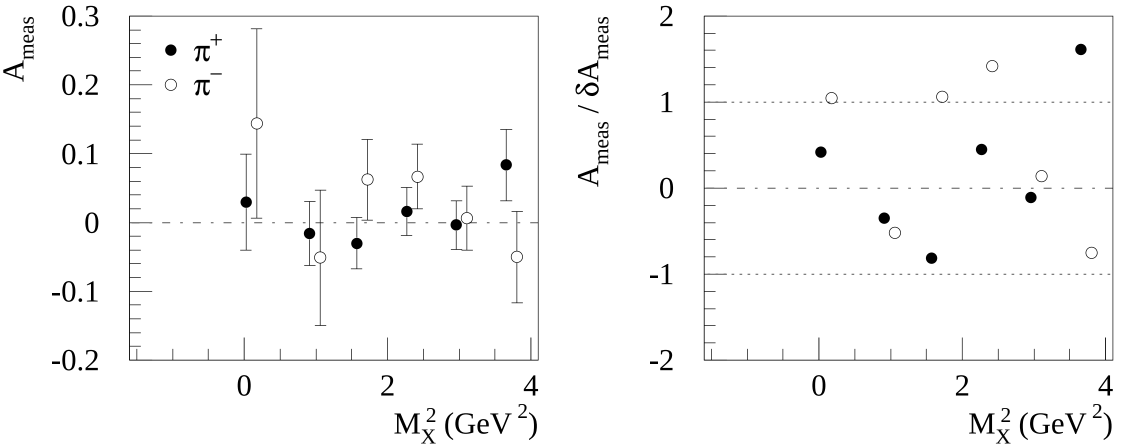

Figure 7.5: The measured asymmetry A_{meas} integrated over the azimuthal angles ϕ and ϕ_S (left) and the relative deviation from zero (right) as a function of the squared missing mass M_X^2 for π^+ and π^- data. The error δA_{meas} is statistical only. For most of the points the deviation is $\leq 1\,\sigma$ (maximum $1.5\,\sigma$) from the expected zero value. No systematic deviation is visible. The average values are $\langle A_{meas}\rangle = 0.005 \pm 0.017$ for π^+ and $\langle A_{meas}\rangle = 0.028 \pm 0.025$ for π^-.

Zero Constant Term

According to (3.19), the cross sections $d\sigma(\phi, \phi_S)$ and $d\sigma(\phi, \phi_S + \pi)$ for the two target polarisation states $P_T > 0$ and $P_T < 0$, respectively, integrated over the azimuthal angle ϕ_S (and ϕ) should be equal to each other. This requirement serves as a quality check of the data and is equivalent to showing for the asymmetry $A(\phi, \phi_S)$ (3.20) that

$$A \equiv \int_{-\pi}^{\pi} d\phi \int_{-\pi}^{\pi} d\phi_S \; A(\phi, \phi_S) = 0. \tag{7.10}$$

The measured values A_{meas} as a function of the squared missing mass M_X^2 are shown in Fig.7.5 for π^+ and π^- data. Most of the points are zero within the statistical error bars, δA_{meas}. For several points the deviation is $1\,\sigma$, maximum $1.5\,\sigma$ from the expected zero value, where σ is the standard deviation. A deviation from zero in (7.10), also called a 'constant term' of the asymmetry, can be due to an incomplete cancellation of the measured unpolarised event yields $d\widetilde{\sigma}_{UU}$ in (3.20). However, since $\langle A_{meas}\rangle = 0.005 \pm 0.017$ and $\langle A_{meas}\rangle = 0.028 \pm 0.025$ averaged over M_X^2 for π^+ and π^-, respectively, are consistent with zero and $\frac{A_{meas}}{\delta A_{meas}}$ in Fig.7.5 shows no systematic deviations, we conclude that no significant discrepancy is observed between data and the requirement (7.10).

Asymmetry of Polarised Samples

Although the transverse polarisation of the target is flipped on a regular basis (every 90 s), the data taken with positive ($P_T > 0$) and negative ($P_T < 0$) target polarisation may contain additional differences due to, e.g., a possible detector top-bottom asymmetry.

The six amplitudes are extracted from a fit to the unpolarised yield (i.e., events with both $P_T > 0$ and $P_T < 0$ enter (7.4, 7.5) with the same sign in front of $|P_T|$) as well as from fits to the polarised yields, but separately for positive and negative target polarisation; we denote the values of the corresponding amplitudes as A_{UU}, and A_{UT+} and A_{UT-}, respectively, for a given sine modulation $\sin(\mu\phi + \lambda\phi_S)_k$. While the unpolarised amplitudes should be consistent with zero, the polarised ones should agree with each other. We note that the 6-parameter UML fit (Section 7.1.1) is used without adding additional terms to take into account possible non-zero unpolarised amplitudes.

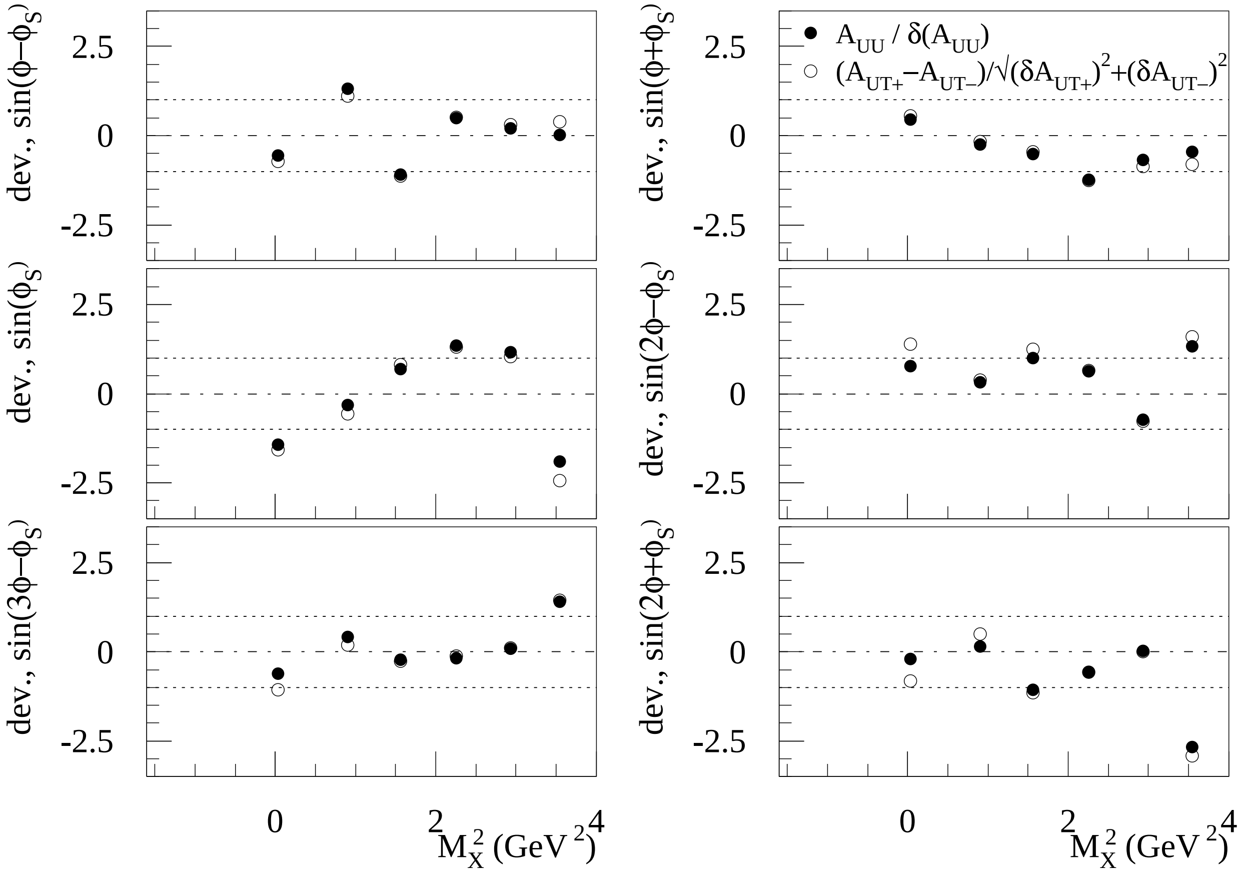

Figure 7.6: The deviation of the unpolarised amplitudes A_{UU} from zero (full circles) and of the polarised amplitudes for positive (A_{UT+}) from those for negative (A_{UT-}) target polarisation (open circles) for the six sine modulations $\sin(\mu\phi + \lambda\phi_S)_k$ as a function of the squared missing mass M_X^2 for the π^+ data sample.

For a given sine modulation, the deviation from zero of the unpolarised amplitude and the discrepancy between the values obtained from the two polarised samples are computed as

$$\left.\begin{array}{c} \dfrac{A_{UU}}{\delta(A_{UU})} \\ \dfrac{A_{UT+} - A_{UT-}}{\sqrt{(\delta A_{UT+})^2 + (\delta A_{UT-})^2}} \end{array}\right\} \text{ for } A_{UU,meas}^{\sin(\mu\phi+\lambda\phi_S)_k} \text{ from } \left\{\begin{array}{l} \text{unpolarised yield} \\ \text{polarised yields} \end{array}\right. \tag{7.11}$$

and plotted in Fig. 7.6 for the unpolarised (full circles) and polarised (open circles) amplitudes for the six M_X^2 bins. Most of the values are close or within the range from -1 to 1, except for a few points at higher M_X^2.

We conclude that the amplitudes caused by an asymmetry in the samples for positive and negative target polarisation are within a reasonable range. Therefore the deviations in Fig. 7.6 are not included in the systematic uncertainties of the measured amplitudes. We note that the possibility that the extracted amplitudes are fake is partly accounted for by the systematic uncertainties due to smearing (Section 7.2).

7.2 Smearing Studies

The extraction of the six amplitudes in (7.1) with the UML fit may be influenced by factors unrelated to the fit procedure itself, e.g., the detector resolutions and smearing. To evaluate such external effects on the extracted amplitudes, the values obtained from the UML fit are compared with the well known 'true' amplitudes implemented in Monte Carlo-generated data samples. The discrepancies between reconstructed and generated amplitudes are taken into account for the systematic uncertainty of the results (Section 7.3.1).

The Monte Carlo events used in the following studies are generated in the HERMES acceptance.

7.2.1 Polarisation in the Monte Carlo Samples

Since the available Monte Carlo programs (Sections 5.1.1, 5.1.2) do not take account of the target polarisation states at the generator level, the produced sample is artificially polarised by randomly assigning to each event a spin state according to

$$\left.\begin{array}{l} P_T = 1 \\ P_T = -1 \end{array}\right\} \text{ if } \mathit{RANDOM} \left\{ \begin{array}{c} < \\ > \end{array} \right\} 0.5\,[1 + A_{UT}^{\sin(\mu\phi+\lambda\phi_S)_k} \sin(\mu\phi + \lambda\phi_S)_k], \tag{7.12}$$

where RANDOM is a random number between 0 and 1, and $A_{UT}^{\sin(\mu\phi+\lambda\phi_S)_k}$ (3.22), being the generated amplitude for a given k ($k = 1, \ldots, 6$), is a number chosen in the range from -1 to 1.

7.2.2 Smearing in M_X^2

Scan of All Six Asymmetry Amplitudes

In separate samples for each of the six sine modulations (7.1), 21 asymmetry amplitudes from -1 to 1 are generated simultaneously using (7.12) with the exclusive MC (Section 5.1.1) and PYTHIA (Section 5.1.2); a GEANT simulation [16] of the detector is included. For each sample, though only one of the amplitudes is generated, all amplitudes are extracted with the UML fit (Section 7.1.1). The statistics of the PYTHIA samples are comparable to those of the data, whereas the size of the exclusive MC sample is such that there are enough events in the last M_X^2 bin; the numbers of reconstructed events are given in Table 7.3 for six M_X^2 bins and for the two polarisation states.

M_X^2(GeV^2) bin	-1.6-0.5	0.5-1.2	1.2-1.9	1.9-2.6	2.6-3.3	3.3-4.0	total
events	PYTHIA.v1.HRC DIS						
$N^+(P_T = 1)$	π^+ 85	196	490	710	736	278	2495 ± 50
$N^-(P_T = -1)$	π^+ 82	201	474	723	712	265	2457 ± 50
$N^+ + N^-$	π^+ 167	397	964	1433	1448	543	4952 ± 70
events	excl. MC						
$N^+(P_T = 1)$	π^+ 2457	3979	2823	887	362	223	10731 ± 104
$N^-(P_T = -1)$	π^+ 2545	3997	2754	878	367	216	10757 ± 104
$N^+ + N^-$	π^+ 5002	7976	5577	1765	729	439	21488 ± 147

Table 7.3: The π^+ PYTHIA and exclusive MC samples used for the smearing studies (Figs. C.1–C.6). The squared missing mass (M_X^2) binning and the number of reconstructed events per bin N^+ (N^-) for positive $P_T = 1$ (negative $P_T = -1$) target polarisation are given.

Both PYTHIA (left) and exclusive MC (right) reconstructed amplitudes are shown in Figs. C.1–C.6 for six M_X^2 bins. Each row corresponds to a separate MC sample, with the generated amplitude ($gen.A_{UT}$) marked with a diagonal dotted line and the reconstructed values ($rec.A_{UT}$) denoted by full circles. The reconstructed values of the middle point and the last one are fitted to a straight line and the fit parameters $p1$ (the offset) and $p2$ (the slope) are given in the plot. Only these two points are used for the fit in order to obtain realistic error bars for $p1$ and $p2$; being implemented in and extracted from the same sample, each set of 21 reconstructed amplitudes has correlated error bars. The fit parameters can be related to the amplitudes as $rec.A_{UT} = p1 + p2\, gen.A_{UT}$.

The following comments refer to Figs.C.1–C.6:

- For each sample (i.e., row) the generated amplitude is reconstructed reasonably well. The quality of the reconstruction in terms of the straight-line-fit parameters with expectation values $p1 = 0$ and $p2 = 1$, is worst for the lowest (highest) M_X^2 bins for PYTHIA (exclusive MC).

- Non-zero fake amplitudes (i.e., amplitudes that are not generated) are reconstructed for each sample. In terms of the deviation from the reference parameters, $p1 = 0$ and $p2 = 0$, the largest deviations are observed again in the first and last M_X^2 bins.

- For those reconstructed amplitudes that are generated (along the diagonal of Figs. C.1–C.6), the $p2$ parameters differ from the nominal value $p2 = 1$ most strongly in the first two M_X^2 bins for PYTHIA and in the last three M_X^2 bins for the exclusive MC. The size of the deviation depends on the amplitude $A_{UT}^{\sin(\mu\phi\pm\phi_S)_k}$ being reconstructed, in particular, on the value of μ, where $\mu = 0, 1, 2, 3$. The agreement between reconstructed and generated amplitudes is best for $A_{UT}^{\sin\phi_S}$ ($\mu = 0$) and worst for $A_{UT}^{\sin(3\phi-\phi_S)}$ ($\mu = 3$).

- The best agreement between generated and reconstructed amplitude values is found in $1.2 < M_X^2 \leq 1.9\,\mathrm{GeV}^2$ for PYTHIA and in $0.5 < M_X^2 \leq 1.2\,\mathrm{GeV}^2$ for the exclusive MC.

Smearing of Events versus M_X^2

The dependence of the quality of the reconstructed asymmetry amplitudes on the squared missing mass M_X^2 observed in Figs. C.1–C.6 can be studied on the level of the events used to construct the asymmetry. Beyond the comparison between reconstructed and generated amplitudes, a comparison between generated and reconstructed event counts as a function of M_X^2 is presented.

In Fig. 7.7 for PYTHIA (left) and the exclusive MC (right) the solid-line histograms show the distributions of generated events (top), converted to a normalised yield for PYTHIA, see Section 5.1.2, and the corresponding distributions of reconstructed events (bottom). The difference between generated and reconstructed distributions is due to the smearing which causes migration of events among M_X^2 bins. The smearing effect is illustrated by the solid, dashed, dotted, and dash-dotted broken-line histograms of reconstructed events, each of which corresponds to one M_X^2 bin of generated events depicted in the same line code. As expected, practically (almost) no events are generated for $M_X^2 < 0.5\,\mathrm{GeV}^2$ ($< 1.9\,\mathrm{GeV}^2$) with the exclusive MC (PYTHIA); the distribution in this low M_X^2 range consists of smeared-back events from the next (two) M_X^2 bin(s), as seen from Fig. 7.7 (bottom). As far as the smearing is due to the finite detector resolution, events are also smeared forth from a lower to a higher M_X^2 bin.

The smearing effect shown in Fig. 7.7 is quantified by generating events in a given M_X^2 bin, counting the number of reconstructed events in the same as well as in the neighbouring bins, and normalising the counts to the total number of reconstructed events in the corresponding M_X^2 bin. The resulting percentages and the particular choice of the M_X^2 bins are given in Table 7.4. The last column serves as a cross check and reminds that the normalisation is done with respect to the number of reconstructed events (for PYTHIA) in the corresponding

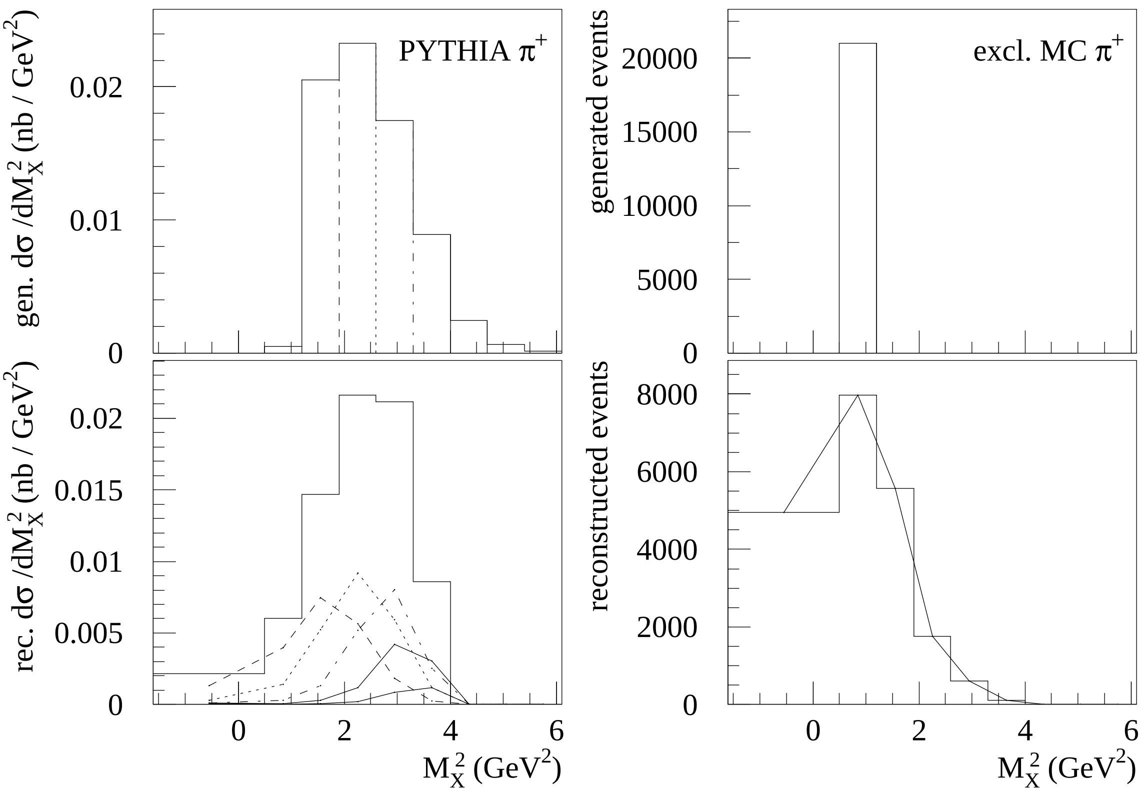

Figure 7.7: The smearing effect in terms of the squared missing mass (M_X^2) of the π^+ distribution for PYTHIA (left) and the exclusive MC (right). The solid-line histograms show the total generated (top) and reconstructed (bottom) distributions. The bin contributions are drawn with solid, dashed, dotted, and dash-dotted (broken) lines for the generated (reconstructed) distributions, where the M_X^2 bins are defined in both cases by a non-overlapping upper and lower cuts on the generated M_X^2 values.

M_X^2 bin. Excluding the region $-1.6 < M_X^2 \leq 1.2\,\mathrm{GeV}^2$ for PYTHIA, the largest fraction of reconstructed events in a given M_X^2 bin is generated in that same bin, however this fraction is not more than 50.9% for $1.2 < M_X^2 \leq 1.9\,\mathrm{GeV}^2$ and it is 38.7% on average for the next three bins. For the exclusive MC all events are generated with a fixed value of $M_X^2 = 0.88\,\mathrm{GeV}^2$, i.e., in the single bin $0.5 < M_X^2 \leq 1.2\,\mathrm{GeV}^2$, however only 38% of the reconstructed events fall in that bin. We note that unlike for PYTHIA, for the exclusive MC the normalisation of the reconstructed event counts in a given M_X^2 bin is performed with respect to the total number of generated events (in the single M_X^2 bin). A consequence of the smearing of events among M_X^2 bins is that the M_X^2 dependence of the extracted asymmetry amplitudes cannot be determined precisely, instead the measured amplitude in any M_X^2 bin is in fact a smeared-out average of the amplitude in that bin and the ones in the neighbouring bins.

The smearing effect in M_X^2 discussed in the previous paragraph is something to be kept in mind for the measured asymmetry amplitudes presented as a function of M_X^2 in Section 7.1.2. The M_X^2-dependent deviation (Figs. C.1–C.6) of some of the reconstructed Monte Carlo amplitudes from the generated values cannot be due to the smearing in M_X^2 alone, because the generated amplitudes are independent of M_X^2. As seen from (7.12), the azimuthal angles ϕ and ϕ_S are the only kinematic variables involved in the generation of the amplitudes. We recall that the agreement between reconstructed and generated amplitudes $A_{UT}^{\sin(\mu\phi\pm\phi_S)_k}$ depends on the values of $\mu = 0, 1, 2, 3$ (Figs. C.1–C.6). This observation points to an additional smearing effect in the azimuthal angles.

	generated PYTHIA π^+ events in M_X^2 (GeV^2)								
	0.5-1.2	1.2-1.9	1.9-2.6	2.6-3.3	3.3-4.0	4.0-4.7	4.7-5.4	5.4-6.1	total
rec. in M_X^2(GeV^2)	%								
-1.6-0.5	3.4	62.1	13.2	5.9	5.7	3.1	2.9	0.8	97.1
0.5-1.2	2.7	65.9	23.7	5.1	1.0	0.6	0.5	0.1	99.6
1.2-1.9	1.2	50.9	35.8	8.8	1.9	0.5	0.2	0.2	99.5
1.9-2.6	0.3	26.1	42.5	23.9	5.5	0.9	0.4	0.1	99.7
2.6-3.3	0.1	8.7	27.9	37.9	19.8	4.1	0.7	0.2	99.4
3.3-4.0	0.1	3.1	13.6	29.6	35.7	14.0	3.2	0.6	99.9
> 4.0	0	0	14.3	14.3	28.6	42.9	0	0	100.1

	generated exclusive MC π^+ events at $M_X^2 = 0.88\,\mathrm{GeV}^2$						
rec. in M_X^2 (GeV^2)	-1.6-0.5	0.5-1.2	1.2-1.9	1.9-2.6	2.7-3.3	3.3-4.0	total
%	23.6	38.0	26.6	8.3	2.9	0.5	99.9

Table 7.4: The fractions (in percent) of reconstructed π^+ events in a given M_X^2 bin are separated according to the M_X^2 bins in which the reconstructed events are generated. The normalisation is to the total number of reconstructed events in the given M_X^2 bin for PYTHIA, while it is to the number of generated events in the single M_X^2 bin for the exclusive MC. The numbers correspond to Fig. 7.7.

7.2.3 Smearing in ϕ and ϕ_S

In a similar way as in Fig. 7.7 for M_X^2, the smearing effect in the azimuthal angles $\phi \equiv \phi_{\pi^+}$ and ϕ_S is illustrated in Figs. 7.8 and 7.9, respectively, for PYTHIA (left) and for the exclusive MC (right); each row corresponds to a M_X^2 bin. The solid-line histograms show the ϕ and ϕ_S total distributions of reconstructed events in 12 bins, while the break-down into contributions from each bin is presented by the solid, dashed, dotted, and dash-dotted broken-line histograms beneath. The generated distributions are not shown.

As a way to estimate the smearing effect in ϕ from Fig. 7.8 one can draw as a reference for each bin a two-equal-sides triangle with the remaining side being equal to the bin width and the height—to the bin height, and with a peak at the centre of the bin. No bin distribution matches this reference triangular shape for the ϕ angle, however the distributions in $1.2 < M_X^2 \leq 1.9\,\mathrm{GeV}^2$ for PYTHIA and in $0.5 < M_X^2 \leq 1.2\,\mathrm{GeV}^2$ for the exclusive MC are closest to the reference ones. The largest deviations are observed for the lowest (highest) M_X^2 bin for PYTHIA (exclusive MC), where events are drawn towards $\phi = 0$ ($\phi = \pm\pi$), i.e., smeared out of the bin centre. Comparing the deviations among the M_X^2 bins it is also seen that the smearing effect in ϕ depends on M_X^2.

In contrast to ϕ, there is no smearing in ϕ_S as shown in Fig. 7.9 for the $-1.6 < M_X^2 \leq 0.5\,\mathrm{GeV}^2$ bin; for the other M_X^2 bins the ϕ_S bin distributions have the same perfect triangular shape and therefore are not shown. Note that both the PYTHIA and the exclusive MC reconstructed ϕ_S distributions are entirely comprised of smeared events (no events are generated in the region $-1.6 < M_X^2 \leq 0.5\,\mathrm{GeV}^2$) and despite this maximal smearing in M_X^2 the reconstructed ϕ_S values are preserved to be the same as the generated ones.

We conclude that the two main features emerging from Figs. C.1–C.6 of the Monte Carlo smearing studies, namely, the M_X^2 and $\mu\phi$ (where $\mu = 0, 1, 2, 3$) dependence of the discrepancies between generated and reconstructed amplitudes, can be qualitatively understood as both being caused by the smearing effect in the azimuthal angle ϕ. More precisely, the smearing effect in ϕ gives the largest contribution to these discrepancies.

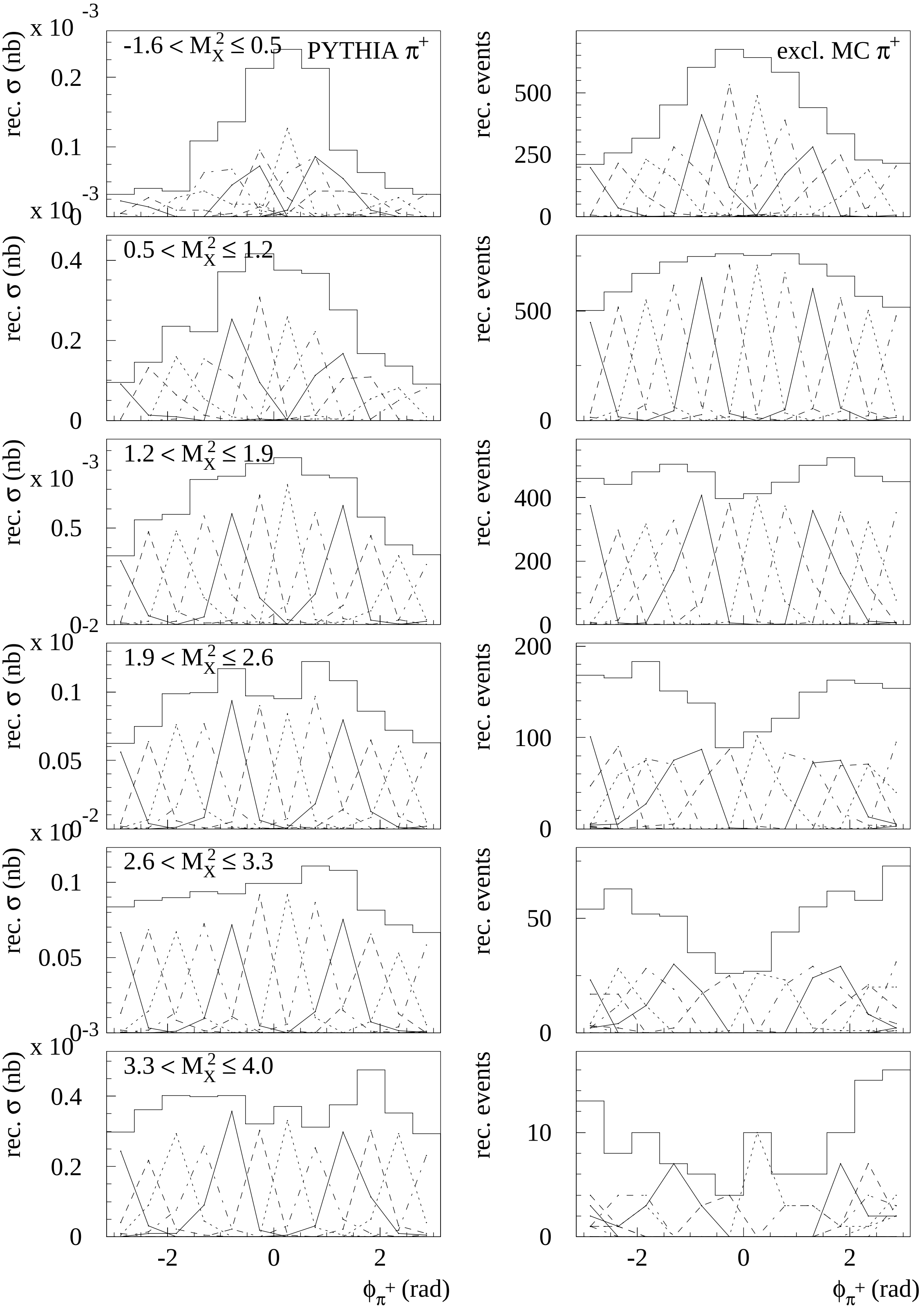

Figure 7.8: Solid-line histograms: Total reconstructed ϕ distributions of π^+ events generated with PYTHIA (left) and the exclusive Monte Carlo (right) for six squared missing mass M_X^2 bins (rows). Broken-line histograms: Contributions to the total distribution from each ϕ bin. The total distribution is a sum of the bin distributions. Note that σ (nb) denotes $\frac{d\sigma}{d\phi_{\pi^+}}\,(\frac{\text{nb}}{\text{rad}})$.

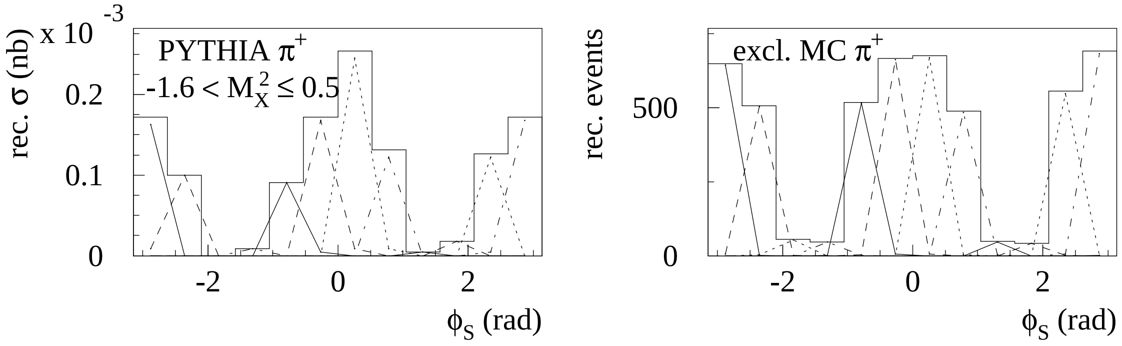

Figure 7.9: Solid-line histograms: Total reconstructed ϕ_S distributions of π^+ events generated with PYTHIA (left) and the exclusive Monte Carlo (right) for the squared missing mass bin $-1.6 < M_X^2 \leq 0.5\,\mathrm{GeV}^2$. Broken-line histograms: Contributions to the total distribution from each ϕ_S bin. The total distribution is a sum of the bin distributions. Note that $\sigma\,(\mathrm{nb})$ denotes $\frac{d\sigma}{d\phi_S}\,(\frac{\mathrm{nb}}{\mathrm{rad}})$.

7.3 Systematic Uncertainties of Measured Amplitudes

7.3.1 Effect of Smearing

The smearing effect is estimated from the discrepancy between generated and reconstructed amplitudes shown in Figs. C.1–C.6. The effect is expressed in terms of the straight-line-fit parameters, $p1$ and $p2$, where for each amplitude (see (7.1))

$$A_{UT,rec}^{\sin(\mu\phi+\lambda\phi_S)_k} = p1 + p2\, A_{UT,gen}^{\sin(\mu\phi+\lambda\phi_S)_k}. \tag{7.13}$$

The systematic correction and deviation described below are used to assign systematic uncertainties to the measured asymmetry amplitudes. The uncertainties take into account smearing and other effects, e.g., related to the extraction method, the detector acceptance, the statistics of the sample, etc., which are automatically included in the Monte Carlo smearing studies presented above. We note that when applying (7.16) and (7.18) to data the reconstructed/generated amplitudes are replaced with the measured/corrected ones, and

$$\Delta_{syst.cor./dev.}^{\sin(\mu\phi+\lambda\phi_S)_k} = (1-f_{excl})\,\Delta_{syst.cor./dev.}^{\sin(\mu\phi+\lambda\phi_S)_k,\mathrm{PYTHIA}} + f_{excl}\,\Delta_{syst.cor./dev.}^{\sin(\mu\phi+\lambda\phi_S)_k,\mathrm{excl.MC}}. \tag{7.14}$$

Systematic Correction

The generated (corrected) amplitude is obtained from the reconstructed (measured) one using the relation (see (7.13))

$$A_{UT,gen}^{\sin(\mu\phi+\lambda\phi_S)_k} = -\frac{p1}{p2} + \frac{1}{p2}\,A_{UT,rec}^{\sin(\mu\phi+\lambda\phi_S)_k}. \tag{7.15}$$

We construct a systematic correction to the reconstructed amplitudes as

$$\Delta_{syst.cor.}^{\sin(\mu\phi+\lambda\phi_S)_k} = -A_{UT,rec}^{\sin(\mu\phi+\lambda\phi_S)_k} + \begin{cases} \delta_+^k, & \text{if } \delta_-^k > A_{UT,rec}^{\sin(\mu\phi+\lambda\phi_S)_k}, \\ \delta_-^k, & \text{if } \delta_+^k < A_{UT,rec}^{\sin(\mu\phi+\lambda\phi_S)_k}, \\ \delta_\pm^k, & \text{otherwise}, \end{cases} \tag{7.16}$$

where $\delta_\pm^k = A_{UT,gen}^{\sin(\mu\phi+\lambda\phi_S)_k} \pm \delta A_{UT,gen}^{\sin(\mu\phi+\lambda\phi_S)_k}$, and the statistical uncertainty $\delta A_{UT,gen}^{\sin(\mu\phi+\lambda\phi_S)_k}$ is obtained from (7.15) by propagation of the errors of $p1$ and $p2$.

Systematic Deviation

We also construct a systematic deviation from zero of a given reconstructed amplitude (fake amplitude), e.g., $A_{UT,rec}^{\sin(\mu\phi+\lambda\phi_S)_k} \neq 0$, (due to another generated amplitude, e.g., $A_{UT,gen}^{\sin(\mu\phi+\lambda\phi_S)_l} > 0$, $l \neq k$) which gives an estimate of the size the given reconstructed amplitude can assume while being zero in reality, i.e., $A_{UT,gen}^{\sin(\mu\phi+\lambda\phi_S)_k} = 0$. The fake amplitude is given by

$$A_{UT,rec}^{\sin(\mu\phi+\lambda\phi_S)_k} = p1 + p2\, A_{UT,gen}^{\sin(\mu\phi+\lambda\phi_S)_l} \quad (\text{for } A_{UT,gen}^{\sin(\mu\phi+\lambda\phi_S)_k} = 0,\ l \neq k), \tag{7.17}$$

where the parameters $p1$ and $p2$ in (7.17) are taken from a fit to $A_{UT,rec}^{\sin(\mu\phi+\lambda\phi_S)_k}$. The deviation is computed as

$$\Delta_{syst.dev.}^{\sin(\mu\phi+\lambda\phi_S)_l} = -A_{UT,rec}^{\sin(\mu\phi+\lambda\phi_S)_k} \pm \delta A_{UT,rec}^{\sin(\mu\phi+\lambda\phi_S)_k}, \tag{7.18}$$

where the statistical uncertainty $\delta A_{UT,rec}^{\sin(\mu\phi+\lambda\phi_S)_k}$ is obtained from (7.17) by propagation of the errors of $p1$ and $p2$. The maximal (positive and negative) deviations among the values of $\Delta_{syst.dev.}^{\sin(\mu\phi+\lambda\phi_S)_l}$ computed from the other five amplitudes are taken for the systematic uncertainty of a given amplitude $A_{UT,rec}^{\sin(\mu\phi+\lambda\phi_S)_k}$.

7.3.2 Target Polarisation

The contribution to the systematic uncertainty of an amplitude $A_{UT,meas}^{\sin(\mu\phi+\lambda\phi_S)_k}$ due to the uncertainty of the transverse target polarisation value $|P_T| \pm \delta P_T = 0.754 \pm 0.050$ (Section 4.2.3) is given as

$$\begin{aligned} \Delta_{pol}^{\sin(\mu\phi+\lambda\phi_S)_k} &= \pm |A_{UT,meas}^{\sin(\mu\phi+\lambda\phi_S)_k}| \frac{\Delta}{2}, \\ \frac{\Delta}{2} = \frac{|P_T|}{2} \left| \frac{1}{|P_T| + \delta P_T} - \frac{1}{|P_T| - \delta P_T} \right| &= \frac{0.754}{2} \left| \frac{1}{0.804} - \frac{1}{0.704} \right| = 0.0666. \end{aligned} \tag{7.19}$$

7.3.3 Total Systematic Uncertainty

The total systematic uncertainty ($syst$) of the measured amplitudes $A_{UT,meas}^{\sin(\mu\phi+\lambda\phi_S)_k}$ is obtained from the quadratic sum of the contributions numbered 1 to 3 in Table 7.5, and explained above. The total uncertainty is the quadratic sum of the statistical and systematic uncertainties. For the six M_X^2 bins the total uncertainty of the measured amplitudes is denoted by the full vertical error bars in Fig. 7.1, while the small horizontal bars enclose the statistical uncertainty.

7.4 Asymmetry Background Correction

In order to compare the values of the asymmetry amplitudes measured from data (Section 7.1.2) with theoretical predictions for exclusive pion production, the contributions from background processes to the measured values have to be taken into account.

The measured amplitudes for π^+ (Fig 7.1, Table 7.2) are extracted from our data sample, which contains both signal (exclusive pion production) and background (DIS, VMD) events (Fig. 6.9, Table 6.6). For such a composite sample the measured polarised yield is given by

$$\widetilde{\sigma}_{UT,Data} = \widetilde{\sigma}_{UT,excl} + \widetilde{\sigma}_{UT,DIS} + \widetilde{\sigma}_{UT,VMD}, \tag{7.20}$$

$$\widetilde{\sigma}_{UU,Data} = \widetilde{\sigma}_{UU,excl} + \widetilde{\sigma}_{UU,DIS} + \widetilde{\sigma}_{UU,VMD}. \tag{7.21}$$

	M_X^2 bin GeV^2	-1.6-0.5	0.5-1.2	1.2-1.9	1.9-2.6	2.6-3.3	3.3-4.0	ave.
1	$\Delta_{syst.cor.}$	$^{+0.11}_{-0.05}$	$^{+0.07}_{-0.02}$	$^{+0.06}_{-0.02}$	$^{+0.07}_{-0.01}$	$^{+0.04}_{-0.04}$	$^{+0.17}_{-0.00}$	$^{+0.09}_{-0.02}$
2	$\Delta_{syst.dev.}$	$^{+0.27}_{-0.07}$	$^{+0.08}_{-0.02}$	$^{+0.07}_{-0.02}$	$^{+0.08}_{-0.02}$	$^{+0.04}_{-0.05}$	$^{+0.26}_{-0.00}$	$^{+0.13}_{-0.03}$
3	Δ_{pol}	±0.01	±0.01	±0.00	±0.00	±0.00	±0.01	±0.01
$A_{UT,meas}^{\sin(\phi-\phi_S)}$	$(syst)$	$^{+0.30}_{-0.08}$	$^{+0.11}_{-0.04}$	$^{+0.09}_{-0.02}$	$^{+0.10}_{-0.02}$	$^{+0.06}_{-0.07}$	$^{+0.31}_{-0.01}$	$^{+0.16}_{-0.04}$
1	$\Delta_{syst.cor.}$	$^{+0.11}_{-0.09}$	$^{+0.00}_{-0.11}$	$^{+0.04}_{-0.04}$	$^{+0.04}_{-0.05}$	$^{+0.06}_{-0.03}$	$^{+0.00}_{-0.15}$	$^{+0.04}_{-0.08}$
2	$\Delta_{syst.dev.}$	$^{+0.13}_{-0.12}$	$^{+0.00}_{-0.10}$	$^{+0.05}_{-0.04}$	$^{+0.04}_{-0.06}$	$^{+0.06}_{-0.04}$	$^{+0.04}_{-0.18}$	$^{+0.05}_{-0.09}$
3	Δ_{pol}	±0.01	±0.01	±0.00	±0.01	±0.01	±0.01	±0.01
$A_{UT,meas}^{\sin(\phi+\phi_S)}$	$(syst)$	$^{+0.17}_{-0.15}$	$^{+0.01}_{-0.14}$	$^{+0.07}_{-0.06}$	$^{+0.05}_{-0.08}$	$^{+0.08}_{-0.05}$	$^{+0.04}_{-0.23}$	$^{+0.07}_{-0.12}$
1	$\Delta_{syst.cor.}$	$^{+0.06}_{-0.14}$	$^{+0.08}_{-0.05}$	$^{+0.08}_{-0.03}$	$^{+0.08}_{-0.02}$	$^{+0.01}_{-0.10}$	$^{+0.17}_{-0.02}$	$^{+0.08}_{-0.06}$
2	$\Delta_{syst.dev.}$	$^{+0.08}_{-0.29}$	$^{+0.08}_{-0.04}$	$^{+0.09}_{-0.02}$	$^{+0.10}_{-0.01}$	$^{+0.02}_{-0.10}$	$^{+0.20}_{-0.03}$	$^{+0.09}_{-0.08}$
3	Δ_{pol}	±0.02	±0.03	±0.02	±0.01	±0.02	±0.02	±0.02
$A_{UT,meas}^{\sin\phi_S}$	$(syst)$	$^{+0.10}_{-0.32}$	$^{+0.12}_{-0.07}$	$^{+0.12}_{-0.04}$	$^{+0.13}_{-0.03}$	$^{+0.02}_{-0.15}$	$^{+0.27}_{-0.04}$	$^{+0.13}_{-0.11}$
1	$\Delta_{syst.cor.}$	$^{+0.30}_{-0.00}$	$^{+0.10}_{-0.00}$	$^{+0.06}_{-0.03}$	$^{+0.08}_{-0.01}$	$^{+0.00}_{-0.16}$	$^{+0.00}_{-0.27}$	$^{+0.09}_{-0.08}$
2	$\Delta_{syst.dev.}$	$^{+0.18}_{-0.03}$	$^{+0.10}_{-0.02}$	$^{+0.05}_{-0.06}$	$^{+0.08}_{-0.01}$	$^{+0.00}_{-0.14}$	$^{+0.01}_{-0.23}$	$^{+0.07}_{-0.08}$
3	Δ_{pol}	±0.03	±0.00	±0.01	±0.00	±0.00	±0.01	±0.01
$A_{UT,meas}^{\sin(2\phi-\phi_S)}$	$(syst)$	$^{+0.35}_{-0.04}$	$^{+0.14}_{-0.02}$	$^{+0.08}_{-0.07}$	$^{+0.12}_{-0.01}$	$^{+0.00}_{-0.22}$	$^{+0.01}_{-0.35}$	$^{+0.12}_{-0.12}$
1	$\Delta_{syst.cor.}$	$^{+0.05}_{-0.18}$	$^{+0.08}_{-0.00}$	$^{+0.07}_{-0.01}$	$^{+0.00}_{-0.16}$	$^{+0.07}_{-0.01}$	$^{+0.05}_{-0.09}$	$^{+0.05}_{-0.08}$
2	$\Delta_{syst.dev.}$	$^{+0.05}_{-0.18}$	$^{+0.09}_{-0.02}$	$^{+0.07}_{-0.01}$	$^{+0.00}_{-0.14}$	$^{+0.06}_{-0.02}$	$^{+0.06}_{-0.12}$	$^{+0.06}_{-0.08}$
3	Δ_{pol}	±0.00	±0.00	±0.00	±0.00	±0.00	±0.01	±0.00
$A_{UT,meas}^{\sin(3\phi-\phi_S)}$	$(syst)$	$^{+0.07}_{-0.26}$	$^{+0.12}_{-0.02}$	$^{+0.10}_{-0.01}$	$^{+0.00}_{-0.22}$	$^{+0.09}_{-0.02}$	$^{+0.08}_{-0.15}$	$^{+0.08}_{-0.11}$
1	$\Delta_{syst.cor.}$	$^{+0.09}_{-0.09}$	$^{+0.07}_{-0.01}$	$^{+0.06}_{-0.01}$	$^{+0.03}_{-0.06}$	$^{+0.13}_{-0.00}$	$^{+0.21}_{-0.00}$	$^{+0.10}_{-0.03}$
2	$\Delta_{syst.dev.}$	$^{+0.10}_{-0.12}$	$^{+0.09}_{-0.01}$	$^{+0.08}_{-0.03}$	$^{+0.03}_{-0.06}$	$^{+0.14}_{-0.00}$	$^{+0.18}_{-0.01}$	$^{+0.10}_{-0.04}$
3	Δ_{pol}	±0.01	±0.00	±0.00	±0.00	±0.00	±0.01	±0.00
$A_{UT,meas}^{(\sin(2\phi+\phi_S)}$	$(syst)$	$^{+0.13}_{-0.15}$	$^{+0.11}_{-0.01}$	$^{+0.10}_{-0.03}$	$^{+0.04}_{-0.09}$	$^{+0.19}_{-0.00}$	$^{+0.28}_{-0.02}$	$^{+0.14}_{-0.05}$

Table 7.5: The contributions to and the systematic uncertainty ($syst$) of the measured asymmetry amplitudes $A_{UT,meas}^{\sin(\mu\phi+\lambda\phi_S)_k}$ (Fig. 7.1, Table 7.2) for the π^+ data sample. See text for more explanation.

From (7.20) and using (3.17), (3.21), and (3.22) one obtains for the measured amplitudes

$$\begin{aligned} A_{UT,meas}^{\sin(\mu\phi+\lambda\phi_S)_k} =& \frac{1}{\widetilde{\sigma}_{UU,Data}} \big(A_{UT,excl}^{\sin(\mu\phi+\lambda\phi_S)_k}\, \widetilde{\sigma}_{UU,excl} \\ &+ A_{UT,DIS}^{\sin(\mu\phi+\lambda\phi_S)_k}\, \widetilde{\sigma}_{UU,DIS} + A_{UT,VMD}^{\sin(\mu\phi+\lambda\phi_S)_k}\, \widetilde{\sigma}_{UU,VMD}\big), \end{aligned} \tag{7.22}$$

where the unpolarised yields $\widetilde{\sigma}_{UU,proc}$ are given in Table 6.6 with the subscript UU being omitted (also in the following), and $A_{UT,proc}^{\sin(\mu\phi+\lambda\phi_S)_k} \gtreqless 0$ depending on the process, $proc = Data, excl, DIS, VMD$. Thus, e.g., $A_{UT,meas}^{\sin(\mu\phi+\lambda\phi_S)_k} = 0$ in (7.22) can be the (accidental) result of a cancellation of possibly large amplitudes appearing with opposite signs for different processes.

From (7.22) follows that in order to obtain the amplitudes for exclusive pion production $A_{UT,excl}^{\sin(\mu\phi+\lambda\phi_S)_k}$ one needs a knowledge of the background amplitudes $A_{UT,DIS}^{\sin(\mu\phi+\lambda\phi_S)_k}$ and $A_{UT,VMD}^{\sin(\mu\phi+\lambda\phi_S)_k}$. However, values of the latter are presently unavailable for the kinematic range of our data (Fig. B.1, [46]). The alternative method described below is used for the final results.

7.4.1 Effective Asymmetry of π^+ Background

The asymmetry amplitudes for exclusive pion production $A_{UT,excl}^{\sin(\mu\phi+\lambda\phi_S)_k}$ in (7.22), denoted as $A_{UT,bg.cor}^{\sin(\mu\phi+\lambda\phi_S)_k}$ in the following, are obtained from the measured ones $A_{UT,meas}^{\sin(\mu\phi+\lambda\phi_S)_k}$ using the

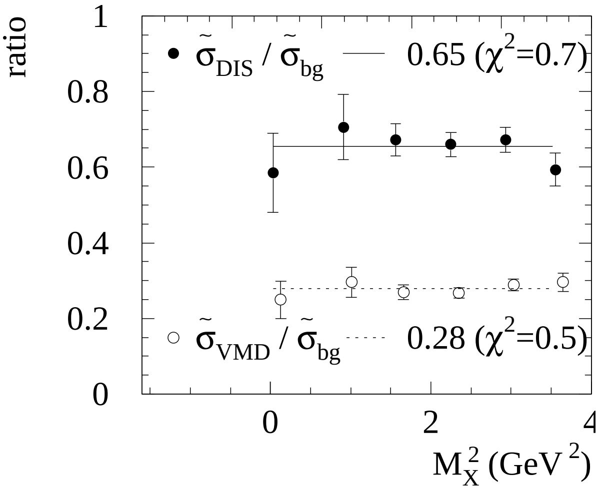

Figure 7.10: The fractions of DIS and VMD π^+ yields in the background as a function of the squared missing mass M_X^2. The fractions are constant within the statistical error bars.

M_X^2 bin	GeV^2	−1.6-0.5	0.5-1.2	1.2-1.9
$\frac{\tilde\sigma_{DIS}}{\tilde\sigma_{bg}}$	%	π^+ 61.2	73.3	69.9
	%	±11.6	±9.4	±4.6
$\frac{\tilde\sigma_{VMD}}{\tilde\sigma_{bg}}$	%	π^+ 24.9	29.6	26.9
	%	±5.0	±4.0	±1.9

M_X^2 bin	GeV^2	1.9-2.6	2.6-3.3	3.3-4.0
$\frac{\tilde\sigma_{DIS}}{\tilde\sigma_{bg}}$	%	π^+ 67.6	69.2	61.2
	%	±3.3	±3.4	±4.7
$\frac{\tilde\sigma_{VMD}}{\tilde\sigma_{bg}}$	%	π^+ 26.7	28.9	29.6
	%	±1.4	±1.5	±2.4

Table 7.6: The values and their statistical errors of the DIS and VMD fractions for the π^+ data sample plotted on the figure to the left for six M_X^2 bins.

relations

$$\begin{aligned} A_{UT,meas}^{\sin(\mu\phi+\lambda\phi_S)_k} &= \frac{1}{\tilde\sigma_{Data}}\left(A_{UT,bg.cor}^{\sin(\mu\phi+\lambda\phi_S)_k}\,\tilde\sigma_{excl} + A_{UT,bg}^{\sin(\mu\phi+\lambda\phi_S)_k}\,\tilde\sigma_{bg}\right), \\ :A_{UT,bg.cor}^{\sin(\mu\phi+\lambda\phi_S)_k} &= \frac{1}{f_{excl}}A_{UT,meas}^{\sin(\mu\phi+\lambda\phi_S)_k} - \frac{1-f_{excl}}{f_{excl}}A_{UT,bg}^{\sin(\mu\phi+\lambda\phi_S)_k}, \end{aligned} \tag{7.23}$$

$$\text{where } A_{UT,bg}^{\sin(\mu\phi+\lambda\phi_S)_k} = \frac{\tilde\sigma_{DIS}}{\tilde\sigma_{bg}}A_{UT,DIS}^{\sin(\mu\phi+\lambda\phi_S)_k} + \frac{\tilde\sigma_{VMD}}{\tilde\sigma_{bg}}A_{UT,VMD}^{\sin(\mu\phi+\lambda\phi_S)_k} + \ldots. \tag{7.24}$$

The unpolarised yields $\tilde\sigma_{proc}$ ($proc = Data, excl, bg$) and the fraction f_{excl} are given in Table 6.6, and $A_{UT,bg}^{\sin(\mu\phi+\lambda\phi_S)_k}$ are the unknown asymmetry amplitudes of the background.

The advantage of (7.23) compared to (7.22) is that for a given amplitude the contribution from all background sources is contained in a single effective quantity, namely, the amplitude $A_{UT,bg}^{\sin(\mu\phi+\lambda\phi_S)_k}$. Another advantage of (7.23) is that the background amplitudes can be measured from our data sample, instead of using external measurements or predictions. Also no explicit calculation from the terms in the right-hand side of (7.24) is needed. Note that for the correction of $A_{UT,meas}^{\sin(\mu\phi+\lambda\phi_S)_k}$ in a given M_X^2 bin $A_{UT,bg}^{\sin(\mu\phi+\lambda\phi_S)_k}$ in that same bin is needed.

7.4.2 Corrected Asymmetry Amplitudes

The background correction (7.23) is carried out for the asymmetry amplitudes $A_{UT,meas}^{\sin(\mu\phi+\lambda\phi_S)_k}$ measured in the squared missing mass region $0.5 < M_X^2 \leq 1.9\,\text{GeV}^2$ (Table 7.7) as well as in the two bins within this region (Table 7.2) for the π^+ data sample. These regions, also called exclusive bins in the following, are chosen to be optimal with respect to the fraction of exclusive events (Table 6.6) and the smearing effect (Section 7.2). Because the background asymmetry amplitudes cannot be measured in the exclusive bins, we make the following assumptions.

- Assume $A_{UT,bg}^{\sin(\mu\phi+\lambda\phi_S)_k}$ is constant in the vicinity of the exclusive bin. When $A_{UT,DIS}^{\sin(\mu\phi+\lambda\phi_S)_k} \neq A_{UT,VMD}^{\sin(\mu\phi+\lambda\phi_S)_k} \neq 0$, $A_{UT,bg}^{\sin(\mu\phi+\lambda\phi_S)_k} = const$ is possible in various scenarios for the behaviour of the terms in (7.24). For example, we show in Fig. 7.10 (Table 7.6) the ratios $\frac{\tilde\sigma_{DIS}}{\tilde\sigma_{bg}}$ and $\frac{\tilde\sigma_{VMD}}{\tilde\sigma_{bg}}$, and observe that both are nearly flat within the statistical errors as a function

M_X^2 bin, GeV^2	0.5-1.2	1.2-1.9	0.5-1.9	0.5-1.9	1.9-4.0
$A_{UT}^{\sin(\mu\phi+\lambda\phi_S)_k}$		*bg.cor*		*meas*	*bg*
$A_{UT}^{\sin(\phi-\phi_S)}$	0.30 ± 0.14	0.18 ± 0.25	0.22 ± 0.13	0.09 ± 0.05	0.01 ± 0.04
$A_{UT}^{\sin(\phi+\phi_S)}$	-0.34 ± 0.15	-0.21 ± 0.27	-0.23 ± 0.14	-0.05 ± 0.05	0.10 ± 0.04
$A_{UT}^{\sin\phi_S}$	0.63 ± 0.18	0.75 ± 0.33	0.69 ± 0.16	0.38 ± 0.06	0.22 ± 0.05
$A_{UT}^{\sin(2\phi-\phi_S)}$	-0.13 ± 0.14	0.53 ± 0.27	0.15 ± 0.13	0.07 ± 0.05	0.03 ± 0.04
$A_{UT}^{\sin(3\phi-\phi_S)}$	-0.06 ± 0.12	-0.17 ± 0.22	-0.08 ± 0.11	-0.01 ± 0.04	0.06 ± 0.03
$A_{UT}^{\sin(2\phi+\phi_S)}$	-0.00 ± 0.14	-0.03 ± 0.26	-0.00 ± 0.13	0.01 ± 0.05	0.02 ± 0.04

Table 7.7: The values and the statistical uncertainties of the π^+ six asymmetry amplitudes corrected for the background contribution (*bg.cor*) for three M_X^2 regions. The measured amplitudes (*meas*) are given here and in Table 7.2. The background amplitude (*bg*) is measured in the neighbouring M_X^2 region using the same π^+ data sample as for the measured amplitudes (*meas*).

of M_X^2. In order to keep $A_{UT,bg}^{\sin(\mu\phi+\lambda\phi_S)_k}$ constant versus M_X^2, we assume that also the amplitudes $A_{UT,DIS}^{\sin(\mu\phi+\lambda\phi_S)_k}$, $A_{UT,VMD}^{\sin(\mu\phi+\lambda\phi_S)_k}$ in (7.24) do not vary over the given M_X^2 range.

- As far as $A_{UT,bg}^{\sin(\mu\phi+\lambda\phi_S)_k}(M_X^2) = const$ is a good assumption, the background amplitude can be measured in the neighbouring region to the right of the exclusive bin (i.e., at higher M_X^2) and the same value can be used for the correction of the amplitude in the exclusive bin.

The results of the background correction (7.23) are given in Table 7.7 for three M_X^2 regions. The values of the measured amplitudes in the exclusive bins are taken from Table 7.2. The background amplitudes $A_{UT,bg}^{\sin(\mu\phi+\lambda\phi_S)_k}$ are measured from the π^+ data sample (Table 7.1) in the region $1.9 < M_X^2 \leq 4.0\,\mathrm{GeV}^2$, whose lower limit corresponds to $M_X^2 \approx (M_n^2 + 1.3\,\sigma_{M_X^2})$, $M_n^2 \approx 1\,\mathrm{GeV}^2$ being the centre of the exclusive peak (Fig. 6.8) and $\sigma_{M_X^2} \approx 0.7\,\mathrm{GeV}^2$ is the resolution of the squared missing mass. Larger values of this limit reduce the sample of background events and lead to large error bars of the measured background amplitudes.

Most of the corrected amplitudes remain small or consistent with zero within the statistical uncertainties, like the measured ones. The values of $|A_{UT,bg.cor}^{\sin(\phi\pm\phi_S)}|$ are larger with respect to the measured ones, however, they are only about 2 (1.5) standard deviations away from zero in the region $0.5 < M_X^2 \leq 1.2(1.9)\,\mathrm{GeV}^2$. $A_{UT,bg.cor}^{\sin\phi_S}$ remains the largest one of all six amplitudes.

7.4.3 Systematic Uncertainties of Corrected Amplitudes

We discuss the sources, which in addition to those presented in Section 7.3, contribute to the systematic uncertainty of the corrected amplitudes.

Background Asymmetry Amplitude

Instead of $1.9\,\mathrm{GeV}^2$ used for the results in Table 7.7, a lower limit of $M_X^2 \approx (M_n^2 + 2.0\,\sigma_{M_X^2}) = 2.4\,\mathrm{GeV}^2$ is taken for the squared missing mass region in which the background amplitudes $A_{UT,bg}^{\sin(\mu\phi+\lambda\phi_S)_k}$ are measured. The difference,

$$\Delta_{bg}^{\sin(\mu\phi+\lambda\phi_S)_k} = A_{UT,bg.cor}^{\sin(\mu\phi+\lambda\phi_S)_k}(bg \text{ for } M_X^2 > 2.4) - A_{UT,bg.cor}^{\sin(\mu\phi+\lambda\phi_S)_k}(bg \text{ for } M_X^2 > 1.9), \tag{7.25}$$

is added to the systematic uncertainty of the corrected amplitudes.

M_X^2 bin GeV^2	0.5-1.2	1.2-1.9	0.5-1.9	0.5-1.2	1.2-1.9	0.5-1.9	0.5-1.2	1.2-1.9	0.5-1.9
	$A_{UT,meas}^{\sin(\phi-\phi_S)}$			$A_{UT,meas}^{\sin(\phi+\phi_S)}$			$A_{UT,meas}^{\sin\phi_S}$		
Δ_{bg}	-0.01	-0.02	-0.01	-0.01	-0.04	-0.02	-0.01	-0.03	-0.02
$\Delta_{f_{excl}}$	-0.04	-0.02	-0.03	$+0.06$	$+0.04$	$+0.05$	-0.05	-0.07	-0.05
Δ_{pol}	±0.02	±0.01	±0.01	±0.02	±0.01	±0.02	±0.04	±0.05	±0.05
$(syst)$	$^{+0.11}_{-0.06}$	$^{+0.10}_{-0.04}$	$^{+0.10}_{-0.04}$	$^{+0.06}_{-0.15}$	$^{+0.08}_{-0.07}$	$^{+0.07}_{-0.10}$	$^{+0.12}_{-0.09}$	$^{+0.13}_{-0.10}$	$^{+0.13}_{-0.09}$
	$A_{UT,meas}^{\sin(2\phi-\phi_S)}$			$A_{UT,meas}^{\sin(3\phi-\phi_S)}$			$A_{UT,meas}^{\sin(2\phi+\phi_S)}$		
Δ_{bg}	$+0.01$	$+0.03$	$+0.02$	$+0.01$	$+0.04$	$+0.02$	-0.01	-0.02	-0.01
$\Delta_{f_{excl}}$	$+0.02$	-0.07	-0.01	$+0.02$	$+0.03$	$+0.02$	$+0.00$	$+0.01$	$+0.00$
Δ_{pol}	±0.01	±0.04	±0.01	±0.00	±0.01	±0.01	±0.00	±0.00	±0.00
$(syst)$	$^{+0.14}_{-0.02}$	$^{+0.09}_{-0.10}$	$^{+0.11}_{-0.05}$	$^{+0.12}_{-0.02}$	$^{+0.11}_{-0.02}$	$^{+0.11}_{-0.02}$	$^{+0.11}_{-0.02}$	$^{+0.10}_{-0.04}$	$^{+0.11}_{-0.02}$

Table 7.8: The contributions to and the systematic uncertainty ($syst$) of the corrected asymmetry amplitudes $A_{UT,bg.cor}^{\sin(\mu\phi+\lambda\phi_S)_k}$ (Table 7.7) for the π^+ data sample. See text for more explanation.

Fraction of Exclusive Events

The results from different methods for subtraction of the background yield from the π^+ data sample are used to estimate the systematic uncertainty of the exclusive yield $\widetilde{\sigma}_{excl}$, and thus of the fraction of exclusive events $f_{excl} = \frac{\widetilde{\sigma}_{excl}}{\widetilde{\sigma}_{Data}}$ (Table 6.6). The largest discrepancy between the chosen method and the one using data only is found to be about 15% from the ratio of the exclusive yields in the region $0.5 < M_X^2 \leq 1.9\,\mathrm{GeV}^2$, and also from the ratio of the yields at peak position, as shown on the right-hand side of Fig. B.14 (top and bottom). Thus, the results for f_{excl} (Table 6.6) appear to be underestimated by 15%.

The difference between the amplitudes corrected with the two values of the fractions,

$$\Delta_{f_{excl}}^{\sin(\mu\phi+\lambda\phi_S)_k} = A_{UT,bg.cor}^{\sin(\mu\phi+\lambda\phi_S)_k}(f_{excl} \to f_{excl} + 0.15 \cdot f_{excl}) - A_{UT,bg.cor}^{\sin(\mu\phi+\lambda\phi_S)_k}(f_{excl}), \tag{7.26}$$

gives the systematic uncertainty of the latter due to the uncertainty of the fraction for exclusive events.

Total Systematic Uncertainty

The systematic uncertainty ($syst$) of the corrected amplitudes $A_{UT,bg.cor}^{\sin(\mu\phi+\lambda\phi_S)_k}$ (Table 7.7) is given in Table 7.8. It is obtained by summing quadratically the contributions from the uncertainty of the background amplitude (7.25), of the fraction of exclusive events (7.26), of the target polarisation ((7.19) is computed with the corrected values), and the uncertainties due to the systematic correction (7.16) and deviation (7.18) of the measured amplitudes (Table 7.5). For the value of ($syst$) in $0.5 < M_X^2 \leq 1.9\,\mathrm{GeV}^2$ the averages $\langle\Delta_{syst.cor}\rangle$ and $\langle\Delta_{syst.dev}\rangle$ from the two exclusive bins within this region are used.

7.5 Summary

All six amplitudes of the azimuthal asymmetry (Section 3.1.3) are extracted from data using the 2-dimensional 6-parameter unbinned maximum likelihood (UML) fit (Section 7.1.1). Comparison with other fits and Monte Carlo studies show that the UML fit is best suited for treatment of our low statistics data sample.

By comparing reconstructed with generated distributions the smearing of events among bins is studied as a function of the squared missing mass M_X^2 (Section 7.2.2), and of the azimuthal angles ϕ and ϕ_S (Section 7.2.3). The effect of smearing on the extracted amplitudes is estimated in terms of the fit parameters to the reconstructed amplitudes. Using these parameters a systematic correction and deviation are defined (Section 7.3.1) and used to compute the systematic uncertainty of the results. The smearing effect is found to be largest in the region $-1.6 < M_X^2 \leq 0.5\,\mathrm{GeV}^2$ and therefore the asymmetry results for this bin should be discarded.

The correction of the measured asymmetry amplitudes for contributions from background processes is complicated by the fact that the amplitudes of these processes are unknown for our kinematics. Therefore several assumptions are made and an effective background correction (Section 7.4.1) is applied in this analysis. The corrected amplitudes are reported and the leading one, $A_{UT,bg.cor}^{\sin(\phi-\phi_S)}$, can finally be compared with the predictions for exclusive pion production as discussed in Chapter 8.

Chapter 8

Results and Theoretical Interpretation

The transverse-target single-spin azimuthal asymmetry is analysed in Chapter 7. There the values of the measured and corrected amplitudes of all six allowed sine modulations of the asymmetry and their uncertainties are presented. No previous measurements of these amplitudes are available for comparison. As discussed in Chapter 3, a theoretical prediction exists only for the amplitude $A_{UT}^{\sin(\phi-\phi_S)}$ of the $\sin(\phi-\phi_S)$ modulation, which appears at leading order in $\frac{1}{Q}$. Among all six amplitudes $A_{UT}^{\sin\phi_S}$ is found in this analysis to be the largest one. Therefore only $A_{UT}^{\sin(\phi-\phi_S)}$ and $A_{UT}^{\sin\phi_S}$ are discussed next, except for the kinematic dependences which are given for all six amplitudes.

We note that only longitudinal virtual photons are considered for the prediction of $A_{UT}^{\sin(\phi-\phi_S)}$ (Chapter 3), while the results of this analysis involve contributions from both longitudinal and transverse photons, e.g., via the photon flux ratio, whose value is found to be $\langle\varepsilon\rangle = 0.8$ (Fig. 5.1). No attempt is made here to separate the two contributions. Effects from transverse photons in the measurement of this amplitude are expected to be suppressed by at least $\frac{1}{Q^2}$ compared to those from longitudinal photons (Section 3.2), i.e., 2.3 times for $\langle Q^2\rangle = 2.3\,\mathrm{GeV}^2$ at our kinematics.

8.1 Results for $A_{UT}^{\sin(\phi-\phi_S)}$ and $A_{UT}^{\sin\phi_S}$ versus M_X^2

The values, the statistical and systematic uncertainties of the measured asymmetry amplitudes $A_{UT,meas}^{\sin(\phi-\phi_S)}$ and $A_{UT,meas}^{\sin\phi_S}$ for the two exclusive squared missing mass (M_X^2) bins are given in (8.1). (The values are taken from Tables 7.2, 7.8, see also Fig. 7.1).

M_X^2 bin, GeV^2	0.5-1.2	1.2-1.9	0.5-1.9
$A_{UT,meas}^{\sin(\phi-\phi_S)}$	$0.17 \pm 0.07^{+0.11}_{-0.04}$	$0.05 \pm 0.06^{+0.09}_{-0.02}$	$0.09 \pm 0.05^{+0.10}_{-0.03}$
$A_{UT,meas}^{\sin\phi_S}$	$0.45 \pm 0.10^{+0.12}_{-0.07}$	$0.36 \pm 0.08^{+0.12}_{-0.04}$	$0.38 \pm 0.06^{+0.12}_{-0.06}$

(8.1)

The corrected amplitudes $A_{UT,bg.cor}^{\sin(\phi-\phi_S)}$ and $A_{UT,bg.cor}^{\sin\phi_S}$, reported in (8.2), are obtained by applying a correction for the non-exclusive background contribution to the measured ones (Section 7.4.2). (The values are taken from Tables 7.7, 7.8).

M_X^2 bin, GeV^2	0.5-1.2	1.2-1.9	0.5-1.9
$A_{UT,bg.cor}^{\sin(\phi-\phi_S)}$	$0.30 \pm 0.14^{+0.11}_{-0.06}$	$0.18 \pm 0.25^{+0.10}_{-0.04}$	$0.22 \pm 0.13^{+0.10}_{-0.04}$
$A_{UT,bg.cor}^{\sin\phi_S}$	$0.63 \pm 0.18^{+0.12}_{-0.09}$	$0.75 \pm 0.33^{+0.13}_{-0.10}$	$0.69 \pm 0.16^{+0.13}_{-0.09}$

(8.2)

In Fig. 8.1 the measured (full circles) and the corrected (open circles) amplitudes are shown versus the squared missing mass M_X^2. The data point in each M_X^2 bin is the result for the given amplitude averaged (integrated) over the kinematic variables x, Q^2, and t at the kinematics and in the acceptance of HERMES.

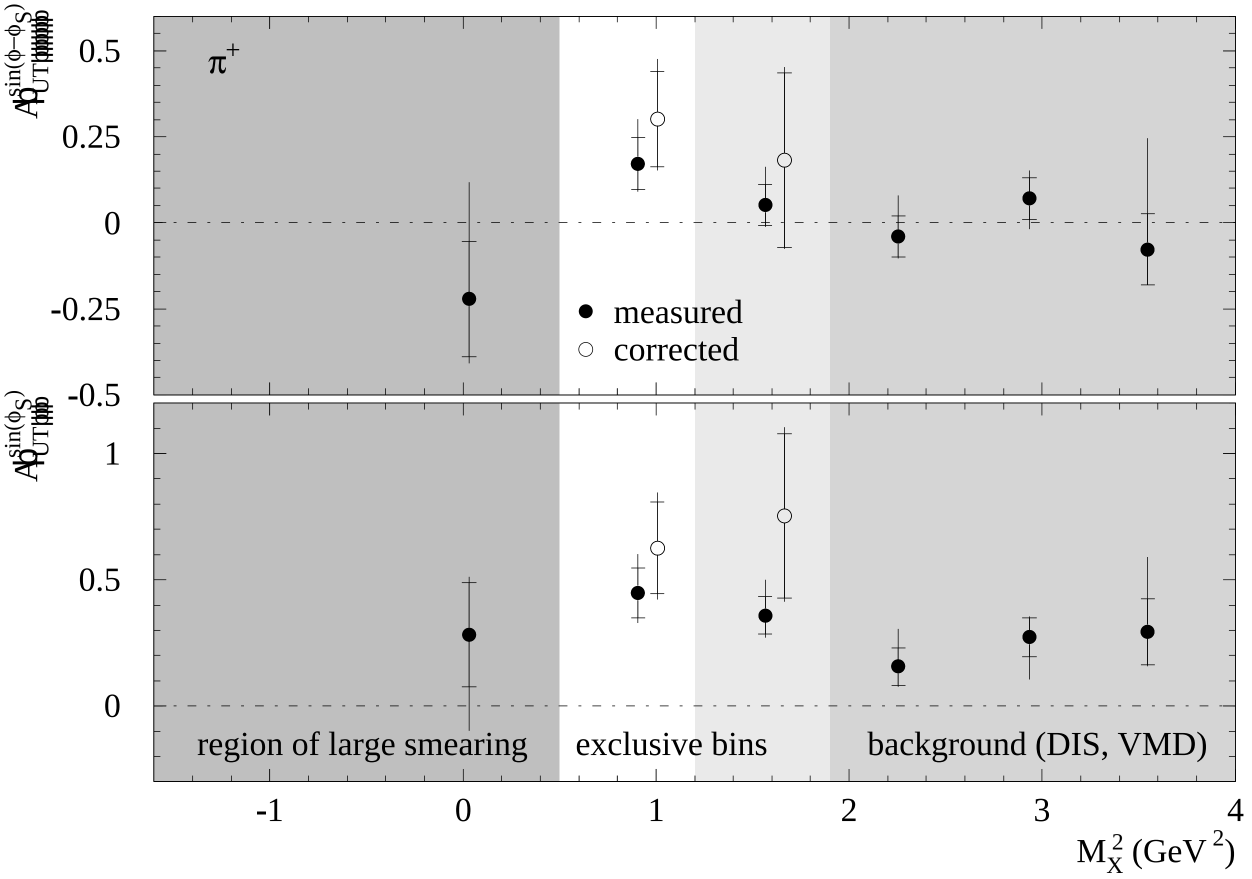

Figure 8.1: Results for the measured (full circles) and corrected (open circles) π^+ asymmetry amplitudes $A_{UT}^{\sin(\phi-\phi_S)}$ and $A_{UT}^{\sin\phi_S}$ as a function of the squared missing mass M_X^2. The small horizontal bars enclose the statistical uncertainty, while the full vertical error bars show the total uncertainty obtained from a quadratic sum of the statistical and systematic uncertainties.

8.2 Kinematic Dependences of All Six Amplitudes

The measured six amplitudes of the sine modulations of the transverse-target single-spin azimuthal asymmetry $A_{meas}(\phi, \phi_S)$ (7.1) are presented so far as a function of the squared missing mass M_X^2 (Figs. 7.1, 8.1).

In order to show the amplitudes' dependence on other kinematic variables an M_X^2 cut needs to be fixed. Despite the significant amount of signal ($f_{excl} = 0.55 \pm 0.07$, see Table 7.2), in the region $-1.6 < M_X^2 \leq 0.5\,\mathrm{GeV}^2$, it is discarded due to the large smearing effect (Fig. C.1). Hence a lower cut of $M_X^2 = 0.5\,\mathrm{GeV}^2$ is chosen. Fig. 8.2 shows the fraction of exclusive events $f_{excl} = \frac{\widetilde{\sigma}_{excl}}{\widetilde{\sigma}_{Data}}$ and its relative statistical uncertainty $\frac{\delta f_{excl}}{f_{excl}}$ as a function of the M_X^2 upper cut.

With an upper cut of $M_X^2 = 1.2\,\mathrm{GeV}^2$ the fraction of exclusive π^+ events is largest ($f_{excl} = 0.56 \pm 0.05(stat) : \frac{\delta f_{excl}}{f_{excl}} = 8.9\%$), while for $M_X^2 \leq 1.9\,\mathrm{GeV}^2$ more signal as well as background events are included, however, without reducing the statistical significance of the signal ($f_{excl} = 0.38 \pm 0.03(stat) : \frac{\delta f_{excl}}{f_{excl}} = 7.9\%$). In both regions the smearing effect is minimal (Figs. C.2–C.3). A choice of an upper M_X^2-cut for $M_X^2 > 1.9\,\mathrm{GeV}^2$ results in fast decrease of the signal fraction and increase of its statistical uncertainty, as seen from Fig. 8.2. Therefore the exclusive bin $0.5 < M_X^2 \leq 1.9\,\mathrm{GeV}^2$ is chosen for our results on the kinematic dependences of the amplitudes. This bin contains the entire exclusive sample.

We note that an intermediate upper cut of, e.g. $M_X^2 = 1.55\,\mathrm{GeV}^2$ is not chosen here in order to be consistent with the binning used in Section 8.1 to present the results versus M_X^2. A new M_X^2 binning requires that the Monte Carlo asymmetry amplitude scan (Section 7.2.2)

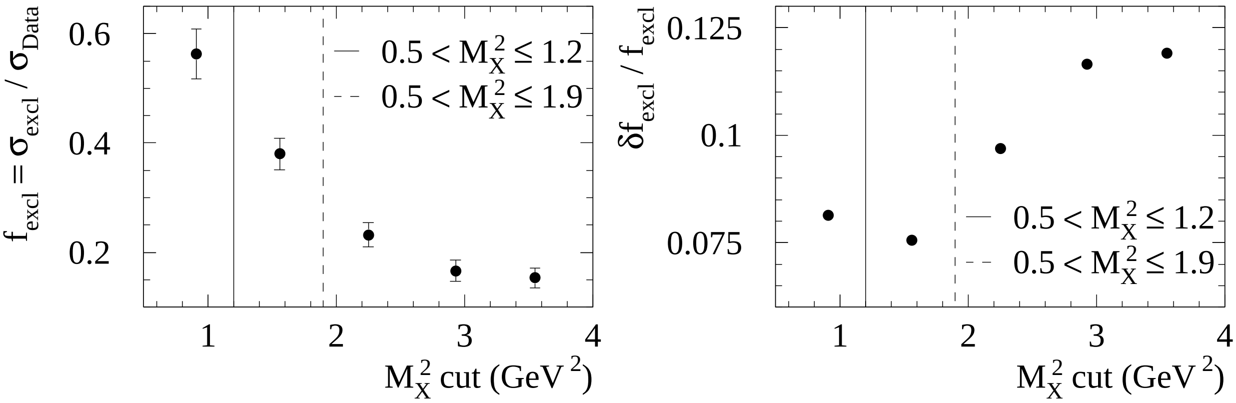

Figure 8.2: The fraction of exclusive π^+ events $f_{excl} = \frac{\widetilde{\sigma}_{excl}}{\widetilde{\sigma}_{Data}}$ and its relative statistical uncertainty $\frac{\delta f_{excl}}{f_{excl}}$ as a function of the squared missing mass (M_X^2) upper cut. A cut of $M_X^2 = 1.2\,\mathrm{GeV}^2$ selects a sample with the largest fraction of signal with small statistical uncertainty, while for $M_X^2 \leq 1.9\,\mathrm{GeV}^2$ the signal fraction decreases but its statistical uncertainty still remains small. See also Figs. 6.8, 6.9, and Table 7.2 (the region $0.5 < M_X^2 \leq 1.9\,\mathrm{GeV}^2$ contains the entire signal; $-1.6 < M_X^2 \leq 0.5\,\mathrm{GeV}^2$ is excluded here because of smearing).

to extract the systematic correction and deviation to the results be repeated.

In Figs. 8.3, 8.4, 8.5 (full circles) the dependences of all six amplitudes on the kinematic variables $t' = t - t_0$, Q^2, and x are presented for the exclusive bin $0.5 < M_X^2 \leq 1.9\,\mathrm{GeV}^2$. The variable t' is chosen in order to remove effects due to t_0 (3.28), which is the smallest kinematically allowed value of t in a given event. More details about the calculation of t' are discussed in Appendix D. The background amplitudes (full triangles) measured in the neighbouring region $1.9 < M_X^2 \leq 4.0\,\mathrm{GeV}^2$ from the same π^+ data sample are used for the background correction (7.23) of the measured ones. The corrected amplitudes for $0.5 < M_X^2 \leq 1.9\,\mathrm{GeV}^2$ are shown with open circles. These figures and the information given below each figure are our main result on the separation of the measured asymmetry amplitudes with respect to the kinematic dependences of the involved six sine modulations.

8.3 Theoretical Interpretation

Exclusive pion electroproduction from protons is very well suited for comparison between data and theory studies of exclusive meson processes. According to the QCD factorisation theorem (Section 3.2) the process can be understood as a convolution of a hard scattering part (T), the pion distribution amplitude (Φ_{π^+}), and the proton generalised parton distributions ($\widetilde{H}$ and $\widetilde{E}$). The hard part T is calculable in perturbative QCD, while the non-perturbative quantities are parameterised within models, in particular, the chiral quark-soliton model is used to calculate $\widetilde{H}$ and $\widetilde{E}$, and the asymptotic or Chernyak-Zhitnitsky models are used to evaluate Φ_{π^+}.

With regard to the hard part T of the scattering process, unlike the exclusive pion cross section for which leading-order (LO) calculations are known to be insufficient at HERMES kinematics [72], it is expected that the transverse-target single-spin azimuthal asymmetry is less sensitive to higher order effects (such as next-to-leading order (NLO) [10] and next-to-NLO (NNLO) corrections in QCD). The NLO-corrections to the LO-prediction for the asymmetry amplitude $A_{UT}^{\sin(\phi-\phi_S)}$ are found to be negligible [10].

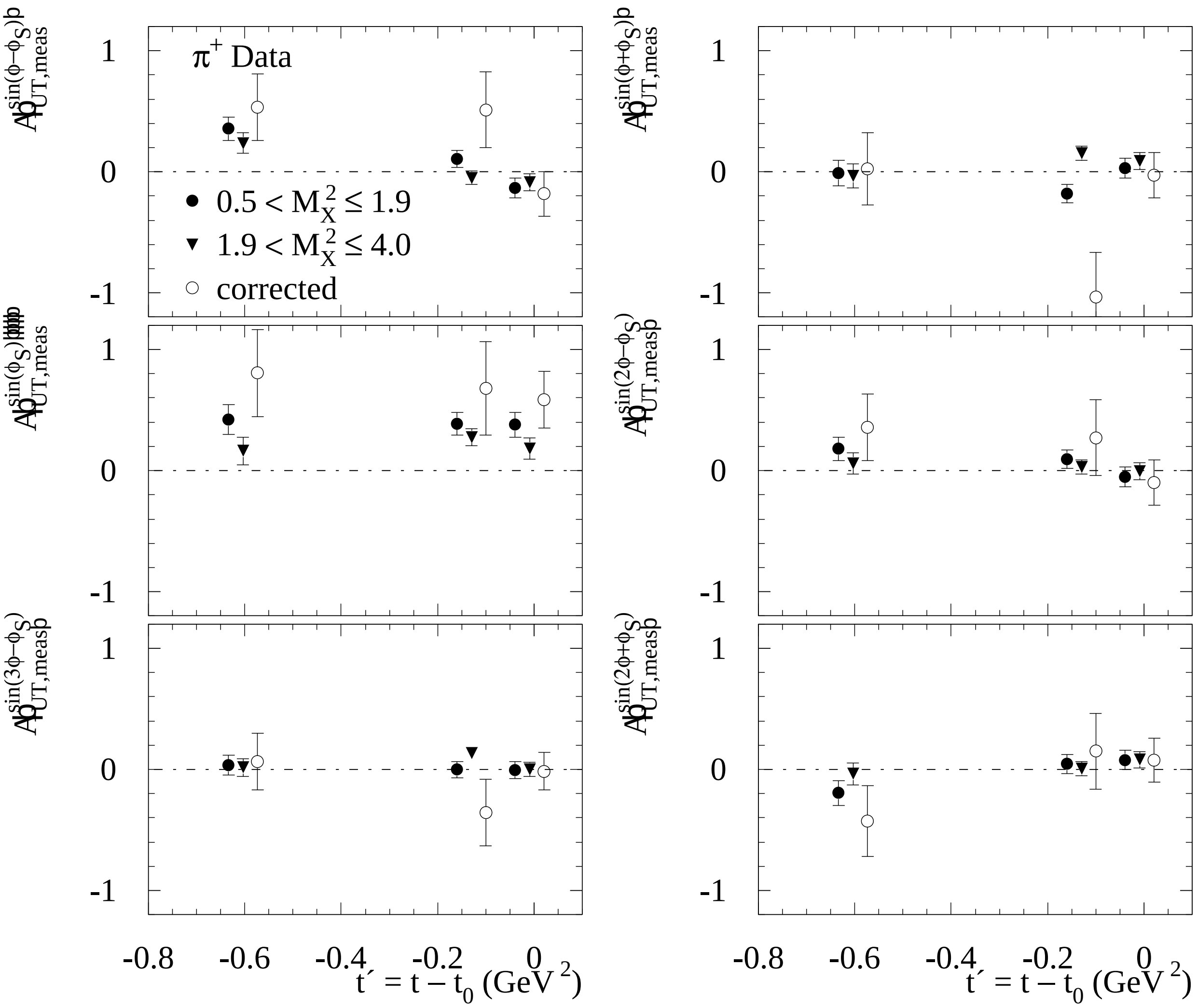

t' binning, GeV^2	1 [−10.0... − 0.300] 2 [−0.300... − 0.075] 3 [−0.075...1.200]					
t' bins	1	2	3	1	2	3
M_X^2 GeV^2	0.5-1.2			1.9-4.0		
$\langle M_X^2\rangle$ GeV^2	1.30	1.31	1.31	2.63	2.79	2.84
$\langle x\rangle$	0.147	0.135	0.121	0.115	0.112	0.101
$\langle Q^2\rangle$ GeV^2	2.97	2.63	2.33	2.38	2.27	2.04
$\langle t'\rangle$ GeV^2	−0.634	−0.160	−0.039	−0.524	−0.162	−0.041
$\langle z\rangle$	0.936	0.963	0.970	0.873	0.982	0.887
$A_{UT}^{\sin(\phi-\phi_S)}$	0.36±0.10 0.53±0.27	0.11±0.07 0.51±0.31	−0.13±0.08 −0.18±0.18	0.23±0.09	−0.05±0.06	−0.09±0.07
$A_{UT}^{\sin(\phi+\phi_S)}$	−0.01±0.10 0.02±0.30	−0.18±0.08 −1.03±0.37	0.03±0.08 −0.03±0.19	−0.04±0.10	0.15±0.06	0.09±0.07
$A_{UT}^{\sin\phi_S}$	0.42±0.12 0.80±0.36	0.39±0.09 0.68±0.39	0.38±0.10 0.59±0.23	0.16±0.11	0.28±0.07	0.18±0.09
$A_{UT}^{\sin(2\phi-\phi_S)}$	0.18±0.10 0.36±0.27	0.10±0.08 0.27±0.31	−0.06±0.08 −0.10±0.19	0.06±0.09	0.03±0.06	−0.01±0.07
$A_{UT}^{\sin(3\phi-\phi_S)}$	0.03±0.08 0.06±0.23	−0.00±0.07 −0.36±0.28	−0.01±0.07 −0.01±0.15	0.02±0.07	0.13±0.05	0.00±0.06
$A_{UT}^{\sin(2\phi+\phi_S)}$	−0.19±0.10 −0.43±0.29	0.04±0.08 0.15±0.31	0.08±0.08 0.08±0.18	−0.04±0.09	0.00±0.06	0.08±0.07
π^+ events	531	841	721	756	1582	1108
π^- events	156	296	239	303	922	776
f_{excl} %	40.3 ± 5.7	27.8 ± 4.5	48.3 ± 4.9	25.7 ± 4.9	−3.0 ± 3.6	−8.2 ± 4.4
f_{DIS} %	53.8 ± 2.9	51.1 ± 2.2	28.2 ± 1.5	62.4 ± 2.7	71.2 ± 2.1	60.8 ± 2.2
f_{VMD} %	9.1 ± 0.8	21.4 ± 1.1	18.1 ± 1.1	15.6 ± 0.9	31.1 ± 1.1	31.1 ± 1.3

Figure 8.3: The measured six amplitudes as a function of $t' = t - t_0$ for two M_X^2 ranges (full circles and triangles), used to obtain the corrected amplitudes (open circles). The average kinematics and the fractions of signal and background for each bin are given in the table; when two values are given for the amplitudes, the upper (lower) is without (with) background correction.

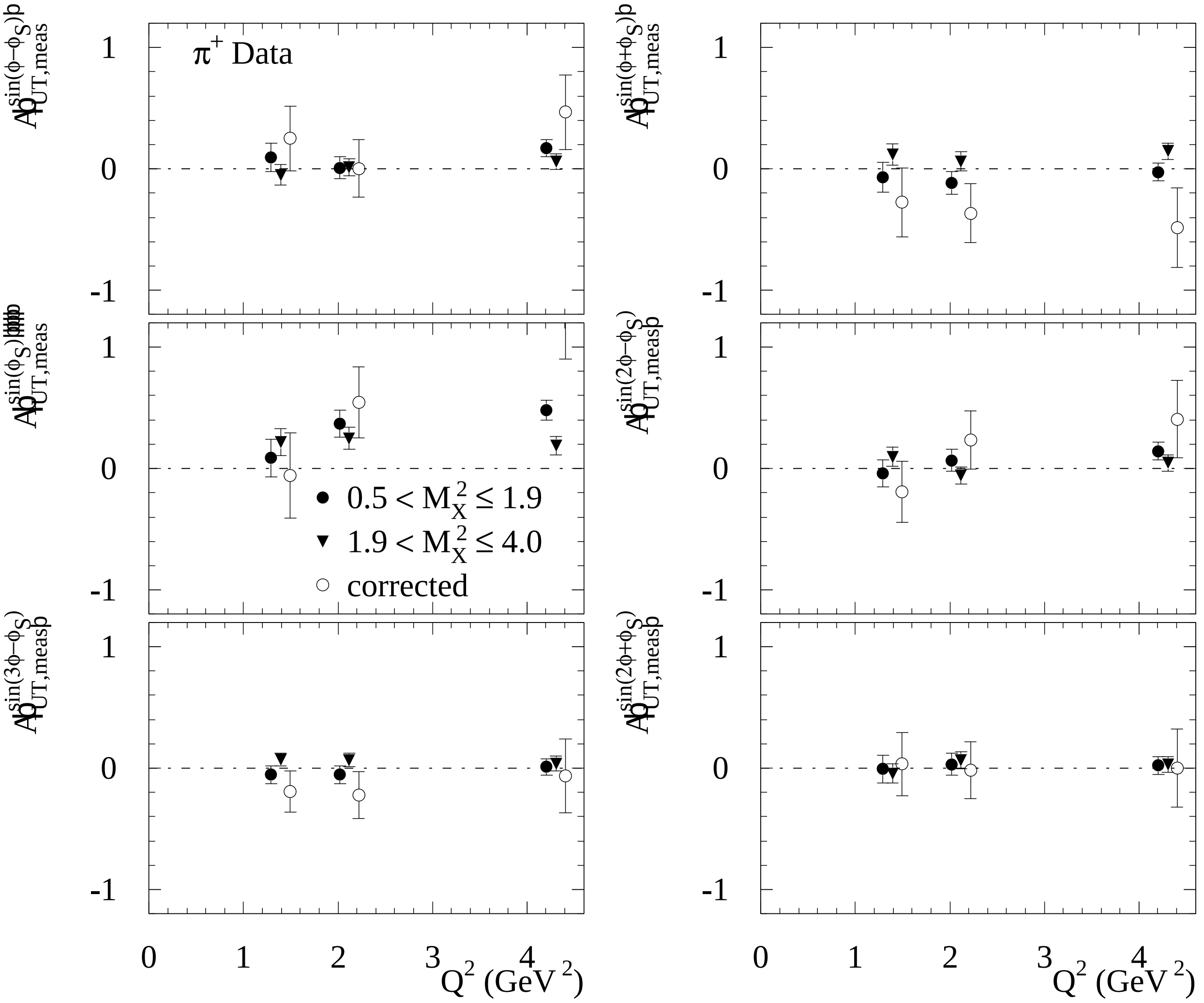

Q^2 binning, GeV^2	1 [0...1.6] 2 [1.6...2.5] 3 [2.5...15.0]					
Q^2 bins	1	2	3	1	2	3
M_X^2 GeV^2		0.5-1.2			1.9-4.0	
$\langle M_X^2\rangle$ GeV^2	1.32	1.30	1.30	2.86	2.79	2.62
$\langle x\rangle$	0.071	0.109	0.205	0.066	0.100	0.178
$\langle Q^2\rangle$ GeV^2	1.29	2.02	4.20	1.27	1.98	3.76
$\langle t'\rangle$ GeV^2	−0.206	−0.222	−0.278	−0.187	−0.206	−0.219
$\langle z\rangle$	0.962	0.961	0.953	0.881	0.881	0.883
$A_{UT}^{\sin(\phi-\phi_S)}$	0.09±0.12 0.25±0.27	0.01±0.09 0.00±0.24	0.17±0.07 0.47±30	−0.05±0.08	0.01±0.07	0.06±0.06
$A_{UT}^{\sin(\phi+\phi_S)}$	−0.07±0.12 −0.28±0.28	−0.12±0.09 −0.37±0.24	−0.03±0.07 −0.48±0.33	0.12±0.09	0.06±0.08	0.14±0.07
$A_{UT}^{\sin\phi_S}$	0.09±0.15 −0.06±0.35	0.37±0.11 0.54±0.29	0.48±0.08 1.26±0.36	0.22±0.11	0.25±0.09	0.19±0.08
$A_{UT}^{\sin(2\phi-\phi_S)}$	−0.04±0.11 −0.19±0.25	0.07±0.09 0.24±0.24	0.14±0.07 0.40±0.32	0.10±0.08	−0.06±0.07	0.05±0.07
$A_{UT}^{\sin(3\phi-\phi_S)}$	−0.06±0.08 −0.19±0.17	−0.05±0.07 −0.22±0.19	0.01±0.07 −0.06±0.30	0.07±0.05	0.07±0.06	0.04±0.06
$A_{UT}^{\sin(2\phi+\phi_S)}$	−0.01±0.11 0.03±0.26	0.03±0.09 −0.02±0.24	0.02±0.07 0.00±0.32	−0.04±0.08	0.06±0.07	0.03±0.06
π^+ events	652	657	784	1360	1087	999
π^- events	234	213	244	875	663	463
f_{excl} %	47.3 ± 5.3	41.8 ± 5.1	27.2 ± 4.6	10.5 ± 3.9	4.1 ± 4.3	−13.3 ± 4.4
f_{DIS} %	32.5 ± 1.7	39.1 ± 2.0	57.3 ± 2.5	46.1 ± 1.6	63.5 ± 2.3	95.7 ± 3.4
f_{VMD} %	25.2 ± 1.4	17.6 ± 1.1	10.0 ± 0.7	36.3 ± 1.3	27.2 ± 1.2	16.5 ± 0.9

Figure 8.4: The measured six amplitudes as a function of Q^2 for two M_X^2 ranges (full circles and triangles), used to obtain the corrected amplitudes (open circles). The average kinematics and the fractions of signal and background for each bin are given in the table; when two values are given for the amplitudes, the upper (lower) is without (with) background correction.

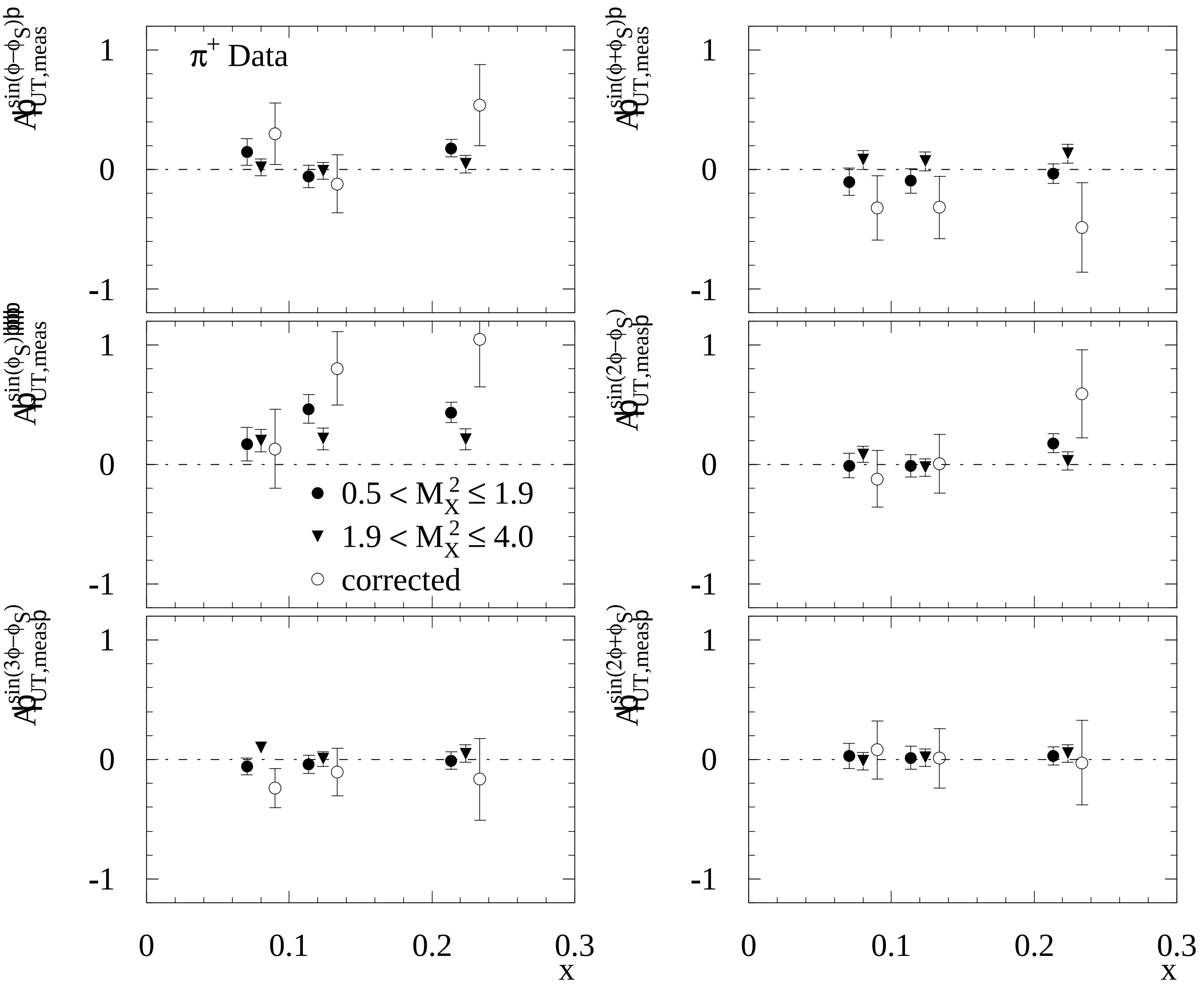

x binning	1 [0...0.0916] 2 [0.0916...0.1390] 3 [0.1390...1.2]					
x bins	1	2	3	1	2	3
M_X^2 GeV^2	0.5-1.2			1.9-4.0		
$\langle M_X^2 \rangle$ GeV^2	1.33	1.30	1.29	2.85	2.76	2.60
$\langle x \rangle$	0.070	0.114	0.214	0.068	0.112	0.197
$\langle Q^2 \rangle$ GeV^2	1.40	2.13	4.24	1.41	2.23	4.02
$\langle t' \rangle$ GeV^2	−0.236	−0.205	−0.269	−0.196	−0.199	−0.219
$\langle z \rangle$	0.963	0.961	0.951	0.885	0.879	0.875
$A_{UT}^{\sin(\phi-\phi_S)}$	0.15±0.11 0.30±0.26	−0.06±0.09 −0.12±0.24	0.18±0.07 0.53±0.34	0.02±0.07	−0.01±0.07	0.05±0.07
$A_{UT}^{\sin(\phi+\phi_S)}$	−0.10±0.12 −0.32±0.27	−0.09±0.10 −0.32±0.26	−0.03±0.08 −0.48±0.38	0.08±0.08	0.07±0.08	0.13±0.08
$A_{UT}^{\sin\phi_S}$	0.17±0.14 0.13±0.33	0.46±0.12 0.80±0.31	0.43±0.09 1.05±0.40	0.20±0.09	0.21±0.09	0.21±0.09
$A_{UT}^{\sin(2\phi-\phi_S)}$	−0.01±0.10 −0.12±0.24	−0.01±0.10 0.01±0.25	0.18±0.08 0.59±0.37	0.08±0.07	−0.03±0.07	0.03±0.08
$A_{UT}^{\sin(3\phi-\phi_S)}$	−0.06±0.07 −0.24±0.16	−0.04±0.08 −0.11±0.20	−0.01±0.08 −0.17±0.34	0.10±0.05	0.00±0.06	0.05±0.07
$A_{UT}^{\sin(2\phi+\phi_S)}$	0.03±0.10 0.08±0.24	0.01±0.10 0.01±0.24	0.03±0.08 −0.03±0.35	−0.01±0.07	0.02±0.07	0.05±0.07
π^+ events	742	617	734	1708	973	765
π^- events	271	204	216	1081	566	354
f_{excl} %	45.5 ± 5.0	42.4 ± 5.3	26.8 ± 4.7	12.1 ± 3.4	4.2 ± 4.5	-25.2 ± 5.1
f_{DIS} %	30.5 ± 1.5	41.1 ± 2.1	59.8 ± 2.7	45.3 ± 1.4	66.4 ± 2.5	111.2 ± 4.5
f_{VMD} %	25.2 ± 1.3	15.4 ± 1.0	10.4 ± 0.7	34.9 ± 1.1	24.3 ± 1.1	15.9 ± 0.9

Figure 8.5: The measured six amplitudes as a function of x for two M_X^2 ranges (full circles and triangles), used to obtain the corrected amplitudes (open circles). The average kinematics and the fractions of signal and background for each bin are given in the table; when two values are given for the amplitudes, the upper (lower) is without (with) background correction.

8.3.1 Discussion of $A_{UT}^{\sin\phi_S}$

The measured amplitude $A_{UT,meas}^{\sin\phi_S}$ ((8.1), Fig. 8.1) is found to be large in the exclusive as well as in the background region at higher M_X^2. In theory, $\sin\phi_S$ is an allowed modulation of the polarised cross section and its amplitude $A_{UT}^{\sin\phi_S}$ is proportional to the photoabsorption cross section σ_{+0}^{+-} (see table following 3.17). The subscript +0 denotes a change of photon polarisation states, which means that transverse (helicity +) apart from longitudinal (helicity 0) virtual photons should be involved in the dynamics of the process. The QCD factorisation theorem (Section 3.2) states that in the Bjorken limit (large Q^2, large W^2, small t) σ_{+0}^{+-} is suppressed by at least $\frac{1}{Q}$, i.e., 0.7 times, which is not a big factor at HERMES kinematics with $\langle Q^2\rangle = 2.3\,\mathrm{GeV}^2$. Moreover, it is known from other experimental studies at HERMES that amplitudes which are formally suppressed are not so small even in the Bjorken limit. However, the value of $A_{UT}^{\sin\phi_S}$ for exclusive pion production is not reliably predicted by theory and models so far. Also no QCD factorisation theorem is proved for transverse virtual photons (helicity ±1).

8.3.2 Discussion of $A_{UT}^{\sin(\phi-\phi_S)}$

In the Bjorken limit (large Q^2, large W^2, small t) the only term of the polarised cross section $d\sigma_{UT}$ (3.17) which is leading in $\frac{1}{Q}$ is $\varepsilon\sin(\phi-\phi_S)\sigma_{00}^{+-}$ (Section 3.2), thus $A_{UT}^{\sin(\phi-\phi_S)}$ is expected to be the leading amplitude. The latter is also the amplitude which can be estimated using the GPD formalism, as outlined in Chapter 3. The leading-twist prediction for the size of $A_{UT}^{\sin(\phi-\phi_S)}$ is of order unity (Fig. 3.4) on a scale from minus one to one.

The measured amplitude $A_{UT,meas}^{\sin(\phi-\phi_S)}$ ((8.1), Fig. 8.1) cannot be compared directly to the available prediction as the signal-to-background ratio is 1 : 1 for our π^+ data sample. The measured amplitude corrected for background, $A_{UT,bg.cor}^{\sin(\phi-\phi_S)}$ ((8.2), Fig. 8.1), is better suited for such comparison. It, however, still contains contribution from transverse photons via the flux ratio ε (see table following (3.17)), even when the cross section for transverse photons σ_{++}^{+-} is assumed to be suppressed. We remind that the theoretical prediction considers only longitudinal virtual photons.

In addition, the amplitude $A_{UT,bg.cor}^{\sin(\phi-\phi_S)}$ includes a contribution from soft pion production (i.e., hard exclusive production of a π^+ accompanied by an emission of a soft pion) since the latter is inseparable within the HERMES resolution from the hard reaction. According to a recent theoretical study [52], the asymmetry amplitude $A_{UT}^{\sin(\phi-\phi_S)}$ for the exclusive process with soft pion emission is predicted to be one order of magnitude smaller than that for the process without it. Hence the amplitude for the combined process is expected to be smaller by about 10% compared to that for the pure hard process, i.e., the one predicted in [10, 33] and shown in Fig.3.4.

Considering the soft pion production and the flux factor ($\langle\varepsilon\rangle = 0.8$, see Fig. 5.1), as discussed above, the maximal predicted value for $A_{UT}^{\sin(\phi-\phi_S)}$ becomes 0.72 instead of unity. This value can be further reduced depending on the choice of the model for the pion distribution amplitude (see Fig. 3.4).

Guided by the theoretical prediction (3.27), one may argue that a $\sqrt{-t'}$ dependence is indeed recognised in the $t' = t - t_0$ distribution of the measured amplitude (top-left panel of Fig. 8.3). In Fig. 8.6 a two parameter fit $p1 + p2\sqrt{-t'}$ is performed to the measured (full circles), as well as to the background (full triangles) amplitudes. The latter are used for the background correction of the former resulting in the corrected amplitudes (open triangles). A less conservative correction (open circles) is performed with the background amplitudes taken to be zero. This is justified by the fact that for $1.9 < M_X^2 \leq 4.0\,\mathrm{GeV}^2$ a non-zero fraction of exclusive events is found in the first t' bin where the background amplitude is

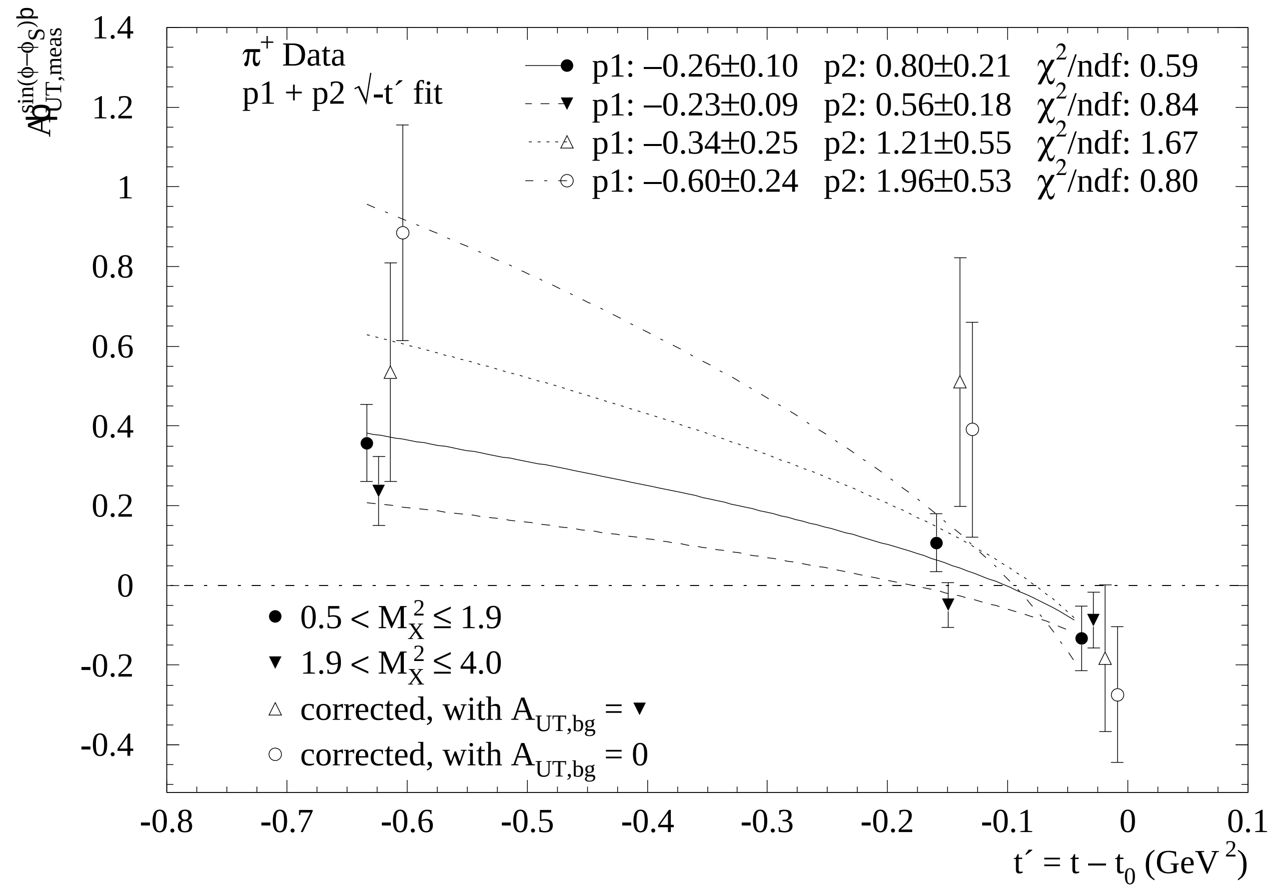

t' binning, GeV^2	1 [$-10.0... - 0.300$]	2 [$-0.300... - 0.075$]	3 [$-0.075...1.200$]	M_X^2 bin
$A_{UT,meas}^{\sin(\phi-\phi_S)}$	0.36 ± 0.10	0.11 ± 0.07	-0.13 ± 0.08	0.5-1.9
$A_{UT,bg}^{\sin(\phi-\phi_S)}$	0.23 ± 0.09	-0.05 ± 0.06	-0.09 ± 0.07	1.9-4.0
$A_{UT,bg.cor;A_{UT,bg}\neq 0}^{\sin(\phi-\phi_S)}$	0.53 ± 0.27	0.51 ± 0.31	-0.18 ± 0.18	0.5-1.9
$A_{UT,bg.cor;A_{UT,bg}=0}^{\sin(\phi-\phi_S)}$	0.89 ± 0.27	0.39 ± 0.27	-0.27 ± 0.17	
f_{excl} %	40.3 ± 5.7	27.8 ± 4.5	48.3 ± 4.9	0.5-1.9
f_{DIS} %	53.8 ± 2.9	51.1 ± 2.2	28.2 ± 1.5	
f_{VMD} %	9.1 ± 0.8	21.4 ± 1.1	18.1 ± 1.1	

Figure 8.6: Result for the measured and corrected asymmetry amplitude $A_{UT}^{\sin(\phi-\phi_S)}$ as a function of the exclusive kinematic variable $t' = t - t_0$. See text for more explanation.

largest (Fig. 8.3). We remind that both corrected results are based on assumptions since the background amplitude is unknown in the exclusive region $0.5 < M_X^2 \leq 1.9\,\text{GeV}^2$. The t' dependence of the corrected amplitude $A_{UT,bg.cor}^{\sin(\phi-\phi_S)}$ (Fig. 8.6) indicates that this amplitude is indeed large for higher $|t'|$ values, so that the data appear to support the theoretical prediction, however, within the large statistical uncertainties. This is the main result of this thesis.

A more detailed comparison cannot be performed at this moment, as a (presently unavailable) theoretical t' dependence similar to the predicted x dependence in Fig. 3.4, would be needed to allow us to directly superimpose theoretical curves over data points. We note that due to our limited statistics a detailed x dependence for each of the three t' bins in Fig 8.3 cannot be obtained (for comparison with the theoretical curves in Fig. 3.4) and thus the two pion models ($\eta = 1$ and $\eta = \frac{5}{3}$) cannot be distinguished. Notice also that the average values of t' are different for the three x bins in Fig 8.5 so that a fit to the x dependence of these data points cannot be performed.

Chapter 9

Summary and Conclusion

A QCD factorisation theorem for hard exclusive production of mesons by longitudinal virtual photons (helicity 0) was proved in 1997 [19]. Since 1999 the theorem has been applied to the theoretical investigation of hard exclusive production of pions from transversely polarised protons [10, 33, 34, 52]. In leading order and within the leading-twist approximation, and in terms of the light-cone distribution amplitude of the produced pion and of the generalised parton distributions (GPDs) for the proton to neutron transition, the value of the transverse-target single-spin azimuthal asymmetry was predicted to be of order unity on a scale from minus one to one. The role of the proton transverse polarisation with respect to the virtual photon is to select a particular combination of GPDs, in particular, via the interference between the pseudoscalar ($\widetilde{\mathcal{E}}$) and pseudovector ($\widetilde{\mathcal{H}}$) scattering amplitudes. This combination is inaccessible through other observables like the unpolarised cross section. The generalised parton distributions are of great interest, because they provide a wealth of information about the parton structure of the nucleon.

No experimental measurement of the above mentioned asymmetry exists to our knowledge. For the first time in 2002 at HERMES a relatively large asymmetry for longitudinally polarised protons was measured [60] which, in the absence of theoretical estimates, could be interpreted as possibly arising from the small transverse component of the proton polarisation.

In 2001 a fixed internal gas target with transversely polarised protons was installed in the HERMES experiment. Data were recorded in the years 2002-2004 with this target, whose average transverse polarisation was 0.754 ± 0.050, and a 27.56 GeV positron beam from the HERA accelerator. The HERMES forward spectrometer provided excellent lepton-hadron separation and pion identification in the 1-15 GeV momentum range.

The analysis of the HERMES data with transversely polarised target, which is the main subject of this thesis, is based to a large extent on the techniques developed previously for the longitudinally polarised target data [60]. As the recoiling neutron was not detected, exclusive production of π^+ pions was selected by requiring that the squared missing mass in the reaction corresponded to the squared neutron mass of about $1\,\mathrm{GeV}^2$. However, with this technique the signal could not be separated entirely from the non-exclusive background. Therefore, the π^+ background was estimated from the normalised number of π^- passing the same requirements as the π^+. An estimate about the signal was obtained by subtraction of the background from the total π^+ number.

The main focus of this thesis was to further optimise and improve the asymmetry data analysis methods. The progress of this work benefited from regular discussions as well as developments in similar analyses of azimuthal asymmetries at HERMES. The π^+ and π^- yields were simulated with the PYTHIA Monte Carlo generator. Exclusive pion production, which is not included in PYTHIA, was simulated by a dedicated generator. By exploring the kinematic regions of π^+ samples obtained from the two generators, additional requirements were imposed on the data sample. This resulted in partial reduction (elimination) of the background at lower (higher) squared missing mass. Another goal of the Monte Carlo studies was to use PYTHIA for subtraction of the background. Since the data-to-PYTHIA comparison for the π^+ yield was not sufficiently good, the following procedure was invented. The π^- yield was subtracted from the π^+ one for data, and the same was done for PYTHIA; then the result for PYTHIA was subtracted from that for data. The difference between the signal obtained in this way and using data only was assigned as a systematic uncertainty to the exclusive yield.

A substantial part of this work was devoted to the extraction of the asymmetry amplitudes. Results obtained with different extraction methods and fit parameters were compared, and the two-dimensional six-parameter unbinned maximum likelihood fit was chosen to be the most suitable one for this analysis. The effects of detector smearing and resolution on the extracted amplitudes was studied by implementing different amplitudes in 'unpolarised' PYTHIA and exclusive Monte Carlo samples by randomly assigning polarisation states to events. By comparing reconstructed with generated amplitudes the smearing effect was quantified and used to assign systematic uncertainties to the results. All six asymmetry amplitudes were extracted from the π^+ data as a function of the squared missing mass, but averaged over other kinematic variables. The asymmetry amplitude of interest was measured to be $A_{UT,meas}^{\sin(\phi-\phi_S)} = 0.09 \pm 0.05(stat)^{+0.10}_{-0.03}(syst)$ in the exclusive region of the squared missing mass from 0.5 to 1.9 GeV^2. In the same region, the amplitude of another allowed asymmetry modulation of the polarised cross section, which however was expected to be dynamically suppressed, was found to be relatively large, namely, $A_{UT,meas}^{\sin\phi_S} = 0.38 \pm 0.06(stat)^{+0.12}_{-0.06}(syst)$. The amplitudes of the other four modulations were found to be small or consistent with zero. In addition, the values of the six amplitudes measured in the exclusive region were presented as a function of the three independent kinematic variables t', Q^2, and x, whose average values for this analysis are $\langle t'\rangle = -0.18\,\mathrm{GeV}^2$, $\langle Q^2\rangle = 2.3\,\mathrm{GeV}^2$, and $\langle x\rangle = 0.12$.

In view of a signal-to-background ratio of about 1 : 1 in the exclusive region at lower squared missing mass, a direct comparison between our measurement of the asymmetry amplitudes and theoretical predictions [10, 33] is not possible. In order to evaluate the amplitudes for exclusive pion production a background correction to the measured ones was applied. Two parameters are needed to correct for each background process: the yield for the process and its asymmetry amplitude. According to PYTHIA, the π^+ background consists mainly of pions produced in semi-inclusive deep inelastic scattering and a contribution of decay pions from exclusively produced vector mesons (dominated by exclusive ρ^0 decays). The yields of these background processes are obtained from PYTHIA, however their amplitudes cannot be determined since the generator is 'unpolarised'. Therefore, instead of considering each background process separately, these processes were combined in an effective background yield and an effective asymmetry amplitude. The former was taken as the result of the background subtraction procedure and the latter was estimated to be the amplitude from the neighbouring squared missing mass region where the contribution of exclusive π^+ events could be neglected. The results for the corrected amplitudes are not discussed in detail as no predictions exist so far, except for $A_{UT}^{\sin(\phi-\phi_S)}$.

The main results of this thesis are the values of the leading azimuthal asymmetry amplitude, $A_{UT,meas}^{\sin(\phi-\phi_S)} = 0.09 \pm 0.05(stat)^{+0.10}_{-0.03}(syst)$, and of the one corrected for the contribution of background processes, namely, $A_{UT,bg.cor}^{\sin(\phi-\phi_S)} = 0.22 \pm 0.13(stat)^{+0.10}_{-0.04}(syst)$ in the region of the squared missing mass from 0.5 to 1.9 GeV^2. The contributions to the systematic uncertainty from various sources was evaluated. The dominant systematic uncertainty comes from the smearing effect. Assuming the background amplitude is zero and performing a naive fit of the form $p1 + p2\sqrt{-t'}$ to the t' dependence of the corrected amplitude, we observe that the amplitude approaches large values of order unity in the higher $|t'|$ region. Thus, in this kinematic region our final result appears to support the prediction for the large size of this amplitude. A conclusive interpretation of the results, however, requires larger statistics and improved detector capabilities.

Important note: After the present analysis was completed, it was found out that the sign of the predicted asymmetry amplitude $A_{UT}^{\sin(\phi-\phi_S)}$, defined according to the Trento conventions [9], is negative [25].

Appendix A

Hydrogen Atom in Magnetic Field

A.1 Hyperfine Structure

The hydrogen atom consists of an electron, e, and a proton, p. The atom is described by the Hamiltonian (i.e., sum of the kinetic energy of the atom and the Coulomb interaction energy)

$$\mathcal{H}_0 = \frac{P^2}{2\mu} - \frac{q^2}{4\pi\varepsilon_0 r}, \tag{A.1}$$

where $\mu = \frac{m_e M_p}{m_e + M_p}$. A more exact description must consider the magnetic interaction energy due to the spins of the electron, S, and of the proton, I. For the ground state of hydrogen (principal quantum number $n = 1$ and orbital angular momentum $l = 0$) in a magnetic field B, the Hamiltonian is

$$\mathcal{H} = \mathcal{H}_0 + \mathcal{A}\, S \cdot I + \frac{g_S \mu_B}{\hbar}\, B \cdot S - \frac{g_I \mu_N}{\hbar}\, B \cdot I, \tag{A.2}$$

where $\mathcal{A} = \frac{4}{3} g_I \frac{m_e}{M_p} m_e c^2 \alpha_{\mathrm{em}}^4 (1 + \frac{m_e}{M_p})^{-3} \frac{1}{\hbar^2}$ describes the strength of the interaction between the electron and proton spins, $\mu_B = \frac{e\hbar}{2m_e} = 5.7884 \times 10^{-5}\,\mathrm{eV/T}$ is the Bohr magneton and $\mu_N = \frac{e\hbar}{2M_p} = 3.1525 \times 10^{-8}\,\mathrm{eV/T}$ is the nuclear magneton, $g_S = 2.0023$ and $g_I = 5.5857$ are the respective gyromagnetic factors. $\mu_S = q_e g_S \frac{e}{2m_e} S = q_e g_S \mu_B m_S$ and $\mu_I = q_p g_I \frac{e}{2M_p} I = q_p g_I \mu_N m_I$ are the electron and proton spin magnetic moments (with $e = +1$, $q_e = -e$, $q_p = +e$), respectively. The scalar products among the vectors $S(S_x, S_y, S_z)$, $I(I_x, I_y, I_z)$, and $B(B_x, B_y, B_z)$ can be expanded as

$$\begin{aligned} S \cdot I &= S_z I_z + \frac{1}{2}(S_+ I_- + S_- I_+), & \text{(A.3)} \\ B \cdot S &= B_z S_z + \frac{1}{2}(B_x - iB_y) S_+ + \frac{1}{2}(B_x + iB_y) S_-, & \text{(A.4)} \\ B \cdot I &= B_z I_z + \frac{1}{2}(B_x - iB_y) I_+ + \frac{1}{2}(B_x + iB_y) I_-, & \text{(A.5)} \end{aligned}$$

where $I_\pm = I_x \pm i I_y$ and $S_\pm = S_x \pm i S_y$. In the representation $|S^2, I^2; m_S, m_I\rangle$ (where $m_S = \pm\frac{1}{2}$ and $m_I = \pm\frac{1}{2}$ refer to the operators S_z and I_z), a basis ($|j_S, j_I; m_S, m_I\rangle \equiv |\frac{1}{2}, \frac{1}{2}; m_S, m_I\rangle \equiv |m_S, m_I\rangle$ of states common to S^2, I^2, S_z, and I_z) for the Hamiltonian operator is given by

$$|+\frac{1}{2}, +\frac{1}{2}\rangle \quad , \quad |+\frac{1}{2}, -\frac{1}{2}\rangle \quad , \quad |-\frac{1}{2}, -\frac{1}{2}\rangle \quad , \quad |-\frac{1}{2}, +\frac{1}{2}\rangle \quad . \tag{A.6}$$

Using the recursion relations [18] (with $j_S = \frac{1}{2}$ and $j_I = \frac{1}{2}$)

$$\begin{aligned} S_z|j_S, j_I; m_S, m_I\rangle &= \hbar\ m_S|j_S, j_I; m_S, m_I\rangle, \\ I_z|j_S, j_I; m_S, m_I\rangle &= \hbar\ m_I|j_S, j_I; m_S, m_I\rangle, \\ S_\pm|j_S, j_I; m_S, m_I\rangle &= \hbar\ \sqrt{j_S(j_S+1) - m_S(m_S \pm 1)}|j_S, j_I; m_S \pm 1, m_I\rangle, \\ I_\pm|j_S, j_I; m_S, m_I\rangle &= \hbar\ \sqrt{j_I(j_I+1) - m_I(m_I \pm 1)}|j_S, j_I; m_S, m_I \pm 1\rangle, \end{aligned} \tag{A.7}$$

one can write the operators in the following matrix representation

$$S_z = \frac{\hbar}{2}\begin{pmatrix} 1 & 0 & 0 & 0 \\ 0 & 1 & 0 & 0 \\ 0 & 0 & -1 & 0 \\ 0 & 0 & 0 & -1 \end{pmatrix}, \quad S_+ = \frac{\hbar}{2}\begin{pmatrix} 0 & 0 & 0 & 0 \\ 0 & 0 & 0 & 0 \\ 0 & 1 & 0 & 0 \\ 1 & 0 & 0 & 0 \end{pmatrix}, \quad S_- = \frac{\hbar}{2}\begin{pmatrix} 0 & 0 & 0 & 1 \\ 0 & 0 & 1 & 0 \\ 0 & 0 & 0 & 0 \\ 0 & 0 & 0 & 0 \end{pmatrix},$$

$$I_z = \frac{\hbar}{2}\begin{pmatrix} 1 & 0 & 0 & 0 \\ 0 & -1 & 0 & 0 \\ 0 & 0 & -1 & 0 \\ 0 & 0 & 0 & 1 \end{pmatrix}, \quad I_+ = \frac{\hbar}{2}\begin{pmatrix} 0 & 0 & 0 & 0 \\ 1 & 0 & 0 & 0 \\ 0 & 0 & 0 & 1 \\ 0 & 0 & 0 & 0 \end{pmatrix}, \quad I_- = \frac{\hbar}{2}\begin{pmatrix} 0 & 1 & 0 & 0 \\ 0 & 0 & 0 & 0 \\ 0 & 0 & 0 & 0 \\ 0 & 0 & 1 & 0 \end{pmatrix}.$$

Consequently (A.3), (A.4), (A.5) take the form

$$S \cdot I = \frac{\hbar^2}{4}\begin{pmatrix} 1 & 0 & 0 & 0 \\ 0 & -1 & 0 & 2 \\ 0 & 0 & 1 & 0 \\ 0 & 2 & 0 & -1 \end{pmatrix}, \frac{B}{B_C} \cdot S = \frac{\hbar}{2}\begin{pmatrix} \chi & 0 & 0 & 0 \\ 0 & \chi & 0 & 0 \\ 0 & 0 & -\chi & 0 \\ 0 & 0 & 0 & -\chi \end{pmatrix}, \frac{B}{B_C} \cdot I = \frac{\hbar}{2}\begin{pmatrix} \chi & 0 & 0 & 0 \\ 0 & -\chi & 0 & 0 \\ 0 & 0 & -\chi & 0 \\ 0 & 0 & 0 & \chi \end{pmatrix},$$

where a static magnetic field along the z direction is taken, $B = (0, 0, B)$, and $\chi = \frac{B}{B_C}$, $B_C = \frac{\mathcal{A}\hbar^2}{g_S \mu_B}$ ($= 50.7\,\text{mT}$ for hydrogen) being the critical field of the hyperfine interaction. Then (A.2) can be written in the form

$$\mathcal{H} = \mathcal{H}_0 + \mathcal{H}_0^{static} = \mathcal{H}_0 + \mathcal{A}\hbar^2\Big[\frac{S \cdot I}{\hbar^2} + \frac{B}{B_C} \cdot \big(\frac{S}{\hbar} - \varepsilon\frac{I}{\hbar}\big)\Big], \tag{A.8}$$

with $\varepsilon = \frac{g_I \mu_N}{g_S \mu_B}$ and $\mathcal{H}_0^{static}$ denoting the part of the Hamiltonian for the hyperfine interactions in a static magnetic field. The matrix representation of the operator is

$$\mathcal{H}_0^{static} = \frac{\mathcal{A}\hbar^2}{4}\begin{pmatrix} 1 + 2\chi(1-\varepsilon) & 0 & 0 & 0 \\ 0 & -1 + 2\chi(1+\varepsilon) & 0 & 2 \\ 0 & 0 & 1 - 2\chi(1-\varepsilon) & 0 \\ 0 & 2 & 0 & -1 - 2\chi(1+\varepsilon) \end{pmatrix}. \tag{A.9}$$

Since the matrix (A.9) is not diagonal, the basis (A.6) is not a set of eigenstates of $\mathcal{H}_0^{static}$. The diagonalisation is achieved via an orthogonal transformation

$$\mathcal{H}_1^{static} = U_0 \mathcal{H}_0^{static} U_0^T, \qquad U_0 = \begin{pmatrix} 1 & 0 & 0 & 0 \\ 0 & \cos\theta & 0 & \sin\theta \\ 0 & 0 & 1 & 0 \\ 0 & -\sin\theta & 0 & \cos\theta \end{pmatrix}, \tag{A.10}$$

which imposes the relation, $2\chi(1+\varepsilon)\cos\theta\sin\theta = \cos^2\theta - \sin^2\theta$, equivalent to

$$\cos 2\theta = \frac{\chi(1+\varepsilon)}{\sqrt{\chi^2(1+\varepsilon)^2 + 1}}, \ \sin 2\theta = \frac{1}{\sqrt{\chi^2(1+\varepsilon)^2 + 1}} \quad : \tan 2\theta = \frac{1}{\chi(1+\varepsilon)}. \tag{A.11}$$

The diagonal elements, and thus the eigenenergies of $\mathcal{H}_1^{static}$ are

$$\begin{aligned} E_1 &= \frac{E_{hfs}}{4}(1+2\chi(1-\varepsilon)), & E_3 &= \frac{E_{hfs}}{4}(1-2\chi(1-\varepsilon)), \\ E_2 &= \frac{E_{hfs}}{4}(-1+2\sqrt{\chi^2(1+\varepsilon)^2+1}), & E_4 &= \frac{E_{hfs}}{4}(-1-2\sqrt{\chi^2(1+\varepsilon)^2+1}), \end{aligned} \tag{A.12}$$

where $E_{hfs} = \mathcal{A}\hbar^2$. The new basis of eigenstates of $\mathcal{H}_1^{static}$ is given by

$$\begin{aligned} |1\rangle &= |+\frac{1}{2},+\frac{1}{2}\rangle, & |3\rangle &= |-\frac{1}{2},-\frac{1}{2}\rangle, \\ |2\rangle &= \cos\theta\,|+\frac{1}{2},-\frac{1}{2}\rangle + \sin\theta\,|-\frac{1}{2},+\frac{1}{2}\rangle, & |4\rangle &= \cos\theta\,|-\frac{1}{2},+\frac{1}{2}\rangle - \sin\theta\,|+\frac{1}{2},-\frac{1}{2}\rangle. \end{aligned} \tag{A.13}$$

The hydrogen hyperfine splitting is also known in terms of the frequency $\nu_{hfs} = \frac{E_{hfs}}{2\pi\hbar} = 1420.4\,\mathrm{MHz}$, which corresponds to the zero-field splitting due to the S–I spin interaction.

In Fig. A.1 the hydrogen hyperfine eigenenergies corresponding to the four eigenstates are plotted as a function of the external static magnetic field in units $\chi = \frac{B}{B_C}$. ① refers to state $|1\rangle$, etc.

A.2 Polarisation

Polarisation is not used here in the same sense as in 'polarisation of a photon', therefore the expression 'polarisation of a single proton/an electron' does not exist. The polarisation of a sample of spin= $\frac{1}{2}$ particles is described by a polarisation vector. The component of polarisation along some axis (z) is defined as

$$P_z = n_+ - n_- \quad \text{with } n_\pm = \frac{N_\pm}{N_+ + N_-}, \tag{A.14}$$

where n_+ and n_- are the fractions of particles with spin I along z ($m_I = +\frac{1}{2}$) and opposite to z ($m_I = -\frac{1}{2}$), respectively.

The electron and proton polarisations (P_e and P_z) of the state $|i\rangle$ are given by (the expectation values of the spin operators)

$$P_e = \sum_{i=1}^{4} = n_i\langle i|\frac{2}{\hbar}S_z|i\rangle = n_1 - n_3 + (n_2 - n_4)\cos 2\theta, \tag{A.15}$$

$$P_z = \sum_{i=1}^{4} = n_i\langle i|\frac{2}{\hbar}I_z|i\rangle = n_1 - n_3 - (n_2 - n_4)\cos 2\theta, \tag{A.16}$$

where $\sum_i n_i = 1$ and $\tan 2\theta \sim \frac{B_C}{B}$. The proton polarisation P_z (or P_p) for the four hydrogen hyperfine states is plotted in Fig. A.1 as a function of the external static magnetic field in units $\chi = \frac{B}{B_C}$. The electron polarisation P_e (not shown) is similar with the states ② and ④ interchanged. Usually, the atoms of a polarised sample are located in a uniform external static magnetic field (guide or holding field), in which case the polarisation vector is along the field.

The external field is referred to as 'weak' or 'strong' depending on the field strength, B, compared with the critical field, B_C, of the hyperfine interaction. The two limits are

- $B \ll B_C$ ($\theta \to \frac{\pi}{4}$, Zeeman limit). In a weak magnetic field, the electron spin, S, and the proton spin, I, couple to a total angular momentum, F. For the mixed states ($m_F = 0$, states ② and ④) the electron and proton spins precess one about the other so that they have zero magnetic moment and zero nuclear polarisation.

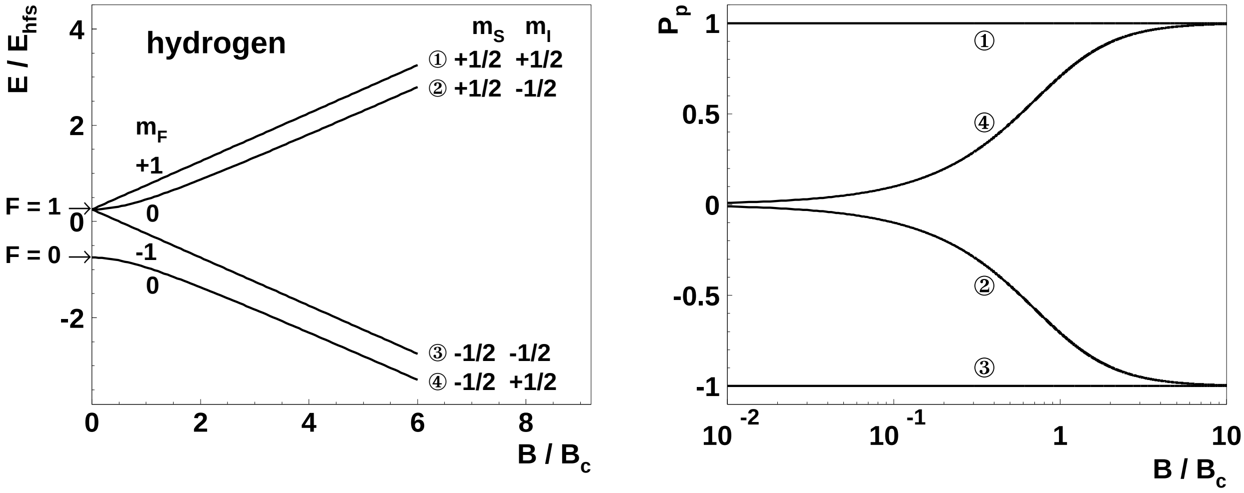

Figure A.1: Energy (left) and proton polarisation of the four hyperfine states of the hydrogen atom as a function of the external static magnetic (guide, holding) field, B, given in units $\chi = \frac{B}{B_C}$.

- $B \gg B_C$ ($\theta \rightarrow 0$, Paschen-Back limit). In a strong magnetic field, electron and proton spins are decoupled. The proton polarisation reaches $P_z = \pm 1$ asymptotically and the magnetic moment of the atom approaches the electron magnetic moment, μ_B. Note that $\mu_N/\mu_B = m_e/M_p \approx 1/1836$.

For the two pure spin states (states ① and ③) the polarisation $|P| = 1$ independent of field strength.

A.3 Hyperfine Transitions

In the presence of a time dependent external magnetic field (apart from the static holding field) the hyperfine energy levels get distorted, so that transitions may originate between pairs of hyperfine states, $|i\rangle \leftrightarrow |j\rangle$. Each transition is characterised by the angular frequency

$$\omega_{ij} = \frac{|E_i - E_j|}{\hbar}, \tag{A.17}$$

which too depends on the holding field (as do the energy levels E_i and E_j (A.12). Hyperfine transitions are classified [59] depending on the relative orientations of the static holding field, B^{static}, and the time dependent one, $B(t)$.

A.3.1 σ transitions: $B(t) \| B^{static}$

The external magnetic field has the form $B = (0, 0, B^{static} + B(t))$. Applying the Schrödinger equation to the states in the two bases (A.6) and (A.13) (both being related to each other via the orthogonal matrix (A.10) as $|i\rangle = U_0 |m_S, m_I\rangle$, $|m_S, m_I\rangle = U_0^T |i\rangle$, where $m_S = \pm\frac{1}{2}$, $m_I = \pm\frac{1}{2}$, $i = 1, 2, 3, 4$) gives

$$\begin{aligned} i\hbar \frac{\partial |m_S, m_I\rangle}{\partial t} &= \mathcal{H}_0^{static} |m_S, m_I\rangle \\ :i\hbar \frac{\partial |i\rangle}{\partial t} &= (\mathcal{H}_1^{static} - i\hbar \frac{\partial U_0^T}{\partial t} U_0)|i\rangle = (\mathcal{H}_1^{static} - \mathcal{H}_1^{\sigma})|i\rangle, \end{aligned} \tag{A.18}$$

where

$$\mathcal{H}_1^\sigma = i\hbar \begin{pmatrix} 0 & 0 & 0 & 0 \\ 0 & s\dot{s}+c\dot{c} & 0 & -s\dot{c}+c\dot{s} \\ 0 & 0 & 0 & 0 \\ 0 & s\dot{c}-c\dot{s} & 0 & s\dot{s}+c\dot{c} \end{pmatrix} = i\hbar \begin{pmatrix} 0 & 0 & 0 & 0 \\ 0 & 0 & 0 & -\dot{\theta} \\ 0 & 0 & 0 & 0 \\ 0 & \dot{\theta} & 0 & 0 \end{pmatrix} = \frac{i\hbar}{2}\dot{\chi} \begin{pmatrix} 0 & 0 & 0 & 0 \\ 0 & 0 & 0 & \sin^2 2\theta \\ 0 & 0 & 0 & 0 \\ 0 & -\sin^2 2\theta & 0 & 0 \end{pmatrix} \tag{A.19}$$

Here $c = \cos\theta$, $s = \sin\theta$, $\dot{} = \frac{\partial}{\partial t}$ and $\varepsilon \ll 1$ is neglected. This leads to the possible transition

$$\sigma|2\rangle \leftrightarrow |4\rangle \qquad (\Delta F = \pm 1, \Delta m_F = 0)$$

A.3.2 π transitions: $B(t) \perp B^{static}$

The external magnetic field is directed either along x or along y. Choosing the x direction for the following example, the field has the form $B = (B(t), 0, B^{static})$. The time dependent part of the Hamiltonian in the basis $|m_S, m_I\rangle$ is given by

$$\mathcal{H}_0^\pi = \frac{g_S\mu_B}{\hbar}B(t)S_x, \quad \text{where } S_x = \frac{1}{2}(S_+ + S_-) = \frac{\hbar}{2}\begin{pmatrix} 0 & 0 & 0 & 1 \\ 0 & 0 & 1 & 0 \\ 0 & 1 & 0 & 0 \\ 1 & 0 & 0 & 0 \end{pmatrix}. \tag{A.20}$$

In the basis $|i\rangle$ the Hamiltonian has the form

$$\mathcal{H}_1^\pi = U_0\mathcal{H}_0^\pi U_0^T \quad : \quad \mathcal{H}_1^\pi = \frac{g_S\mu_B}{2}B(t)\begin{pmatrix} 0 & \sin\theta & 0 & \cos\theta \\ \sin\theta & 0 & \cos\theta & 0 \\ 0 & \cos\theta & 0 & -\sin\theta \\ \cos\theta & 0 & -\sin\theta & 0 \end{pmatrix}, \tag{A.21}$$

where the constant $\varepsilon \ll 1$ is neglected. This leads to the possible transitions

$$\begin{aligned} &\pi|1\rangle \leftrightarrow |2\rangle && (\Delta F = 0, \Delta m_F = \pm 1) \\ &\pi|2\rangle \leftrightarrow |3\rangle && (\Delta F = 0, \Delta m_F = \pm 1) \\ &\pi|1\rangle \leftrightarrow |4\rangle && (\Delta F = \pm 1, \Delta m_F = \pm 1) \\ &\pi|3\rangle \leftrightarrow |4\rangle && (\Delta F = \pm 1, \Delta m_F = \pm 1). \end{aligned}$$

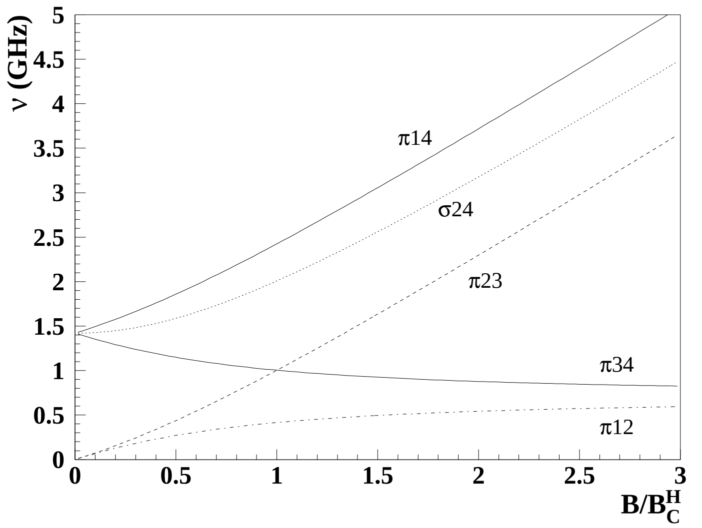

Figure A.2: Frequencies of hydrogen hyperfine transitions plotted as a function of the static holding field. The field values are normalised to the critical field B_C.

Appendix B

Data and Monte Carlo Studies

The following tables and figures serve as a supplement to Chapter 6.

generation of an exclusive pion event	
ϵ, ϕ	random in $(0, 2\pi)$ are generated isotropically the angle $\epsilon = -\Phi_{e^{+\prime}} - \pi$ of the scattering plane and the angle ϕ between the production and the scattering planes (in the lab-frame)
x	x is generated random and flat in $(0, 1)$
Q^2	to increase the efficiency of the simulation, instead of Q^2 in the range $(0.5, 20)$, $\frac{1}{Q^2}$ is generated random and flat in $(0.05, 2)$
t	the t dependence is approximated by a simple exponential fall-off (by analogy with the elastic/diffractive cross section at not too large t); instead of t $(t < 0)$ in the range $(-8, 0)$, $e^{-b\|t\|}$ is generated random and flat in $(e^{-8b}, 1)$ with the slope parameter $b = 3$

kinematic variable	comment
$\nu = \frac{Q^2}{2M_p x}$	calculated
$y = \frac{\nu}{E}$	
$W^2 = M_p^2 + 2M_p\nu - Q^2$	
$E' = E - \nu$	kinematics in the scattering plane
$E_{\gamma^*} = \nu$	
$\|l\| = E$	
$\|l'\| = \sqrt{E'^2 - m_{e^{+\prime}}^2}$	
$\|q\| = \sqrt{\nu^2 + Q^2}$	
$\Theta_{e^{+\prime}} = \arccos \frac{\|l'\|^2 + \|l\|^2 - \|q\|^2}{2\|l'\|\|l\|}$	law of cosines
$\Theta_{\gamma^*} = \arccos \frac{\|q\|^2 + \|l\|^2 - \|l'\|^2}{2\|q\|\|l\|}$	
$l'_x = -\sin\Theta_{e^{+\prime}}\|l'\|$	x-projection in the scattering plane
$l'_y = 0$	
$l'_z = \cos\Theta_{e^{+\prime}}\|l'\|$	z-projection in the scattering plane
$q_x = \sin\Theta_{\gamma^*}\|q\|$	
$q_y = 0$	
$q_z = \cos\Theta_{\gamma^*}\|q\|$	
$(l'_x, l'_y, l'_z) = R(\epsilon; z)(l'_x, 0, l'_z)$	rotation about z-axis by the angle ϵ
$(q_x, q_y, q_z) = R(\epsilon; z)(q_x, 0, q_z)$	
$\Phi_{e^{+\prime}} = \arctan \frac{l'_y}{l'_x}$	
$\Phi_{\gamma^*} = \arctan \frac{q_y}{q_x}$	
$E_{\pi^+} = E_{\gamma^*} + M_p - E'_n$	kinematics in the production plane
$E'_n = \frac{M_p^2 + M_n^2 - t}{2M_p}$	
$\|p_{\pi^+}\| = \sqrt{E_{\pi^+}^2 - m_{\pi^+}^2}$	
$\|P'\| = \sqrt{E_n'^2 - M_n^2}$	
$\Theta_{\pi^+} = \arccos \frac{\|p_{\pi^+}\|^2 + \|q\|^2 - \|P'\|^2}{2\|p_{\pi^+}\|\|q\|}$	
$\Theta_n = \arccos \frac{\|P'\|^2 + \|q\|^2 - \|p_{\pi^+}\|^2}{2\|P'\|\|q\|}$	
$p_x = -\sin\Theta_{\pi^+}\|p_{\pi^+}\|$, $p_y = 0$, $p_z = \cos\Theta_{\pi^+}\|p_{\pi^+}\|$	
$P'_x = \sin\Theta_n\|P'\|$, $P'_y = 0$, $P'_z = \cos\Theta_n\|P'\|$	
$(p_x, p_y, p_z) = R(\epsilon; z)R(-\Theta_{\gamma^*}; y)R(-\phi; z)(p_x, 0, p_z)$	sequence of rotations
$(P'_x, P'_y, P'_z) = R(\epsilon; z)R(-\Theta_{\gamma^*}; y)R(-\phi; z)(P'_x, 0, P'_z)$	
$\Phi_{\pi^+} = \arctan \frac{p_y}{p_x}$	
$\Phi_n = \arctan \frac{P'_y}{P'_x}$	

Table B.1: Generation and calculation of the kinematic variables of an exclusive pion event.

M_X^2 cut		$-2 < M_X^2 \le 40.0\,\mathrm{GeV}^2$			$-2 < M_X^2 \le 2.4\,\mathrm{GeV}^2$		
other cuts		standard	final		standard	final	
yield		$\widetilde{\sigma}^s$	$\widetilde{\sigma}^f$	$\frac{\widetilde{\sigma}^f}{\widetilde{\sigma}^s}$	$\widetilde{\sigma}^s$	$\widetilde{\sigma}^f$	$\frac{\widetilde{\sigma}^f}{\widetilde{\sigma}^s}$
unit		pb	pb	%	pb	pb	%
excl. [a]	π^+	-	-	-	17.6 ± 1.3	15.1 ± 1.1	86
excl [b,d]	π^+	-	-	-	14.7 ± 0.9	14.5 ± 0.8	99
excl [b,e]	π^+				14.3 ± 0.9	14.1 ± 0.9	99
excl [b,f]	π^+				14.6 ± 0.9	14.3 ± 0.9	98
excl [c,d]	π^+	-	-	-	8.3 ± 0.7	10.0 ± 0.7	120
excl [c,e]	π^+				7.2 ± 0.7	8.6 ± 0.7	119
excl [c,f]	π^+				15.0 ± 0.8	16.2 ± 0.8	108
Data	π^+	2152.8 ± 5.2	81.2 ± 1.0	3.8	61.1 ± 0.9	46.7 ± 0.8	76
Data	π^-	1394.3 ± 4.2	39.3 ± 0.7	2.8	25.1 ± 0.6	18.2 ± 0.6	73
PYTHIA [d]	π^+	2074.8 ± 3.1	78.3 ± 0.6	3.8	60.4 ± 0.5	39.1 ± 0.4	65
PYTHIA [e]	π^+	2018.3 ± 3.0	81.6 ± 0.6	4.0	62.2 ± 0.5	41.2 ± 0.4	66
PYTHIA [f]	π^+	2036.7 ± 2.6	62.4 ± 0.5	3.1	46.9 ± 0.4	30.4 ± 0.3	65
PYTHIA [d]	π^-	1457.6 ± 2.6	51.3 ± 0.5	3.5	37.6 ± 0.4	24.8 ± 0.3	66
PYTHIA [e]	π^-	1438.3 ± 2.6	54.8 ± 0.5	3.8	40.0 ± 0.4	26.8 ± 0.3	67
PYTHIA [f]	π^-	1415.9 ± 2.2	34.9 ± 0.2	2.5	25.1 ± 0.3	16.3 ± 0.2	65
excl. MC [g]	π^+	17739 ± 131	13849 ± 116	78	14427 ± 118	13126 ± 113	91
DIS [d]	π^+	1853.0 ± 2.9	46.1 ± 0.5	2.5	37.7 ± 0.4	22.7 ± 0.3	60
DIS [e]	π^+	1773.0 ± 2.8	47.0 ± 0.5	2.7	38.0 ± 0.4	23.6 ± 0.3	62
DIS [f]	π^+	1808.2 ± 2.5	43.9 ± 0.4	2.4	35.0 ± 0.3	21.7 ± 0.3	62
DIS [d]	π^-	1240.8 ± 2.4	18.7 ± 0.3	1.5	15.2 ± 0.3	8.6 ± 0.2	57
DIS [e]	π^-	1196.3 ± 2.3	19.4 ± 0.3	1.6	15.5 ± 0.3	9.0 ± 0.2	58
DIS [f]	π^-	1193.7 ± 2.0	17.2 ± 0.2	1.4	13.3 ± 0.2	7.7 ± 0.2	58
VMD [d]	π^+	203.7 ± 1.0	32.3 ± 0.4	16	22.7 ± 0.3	16.4 ± 0.3	72
VMD [e]	π^+	226.5 ± 1.0	34.7 ± 0.4	15	24.2 ± 0.3	17.6 ± 0.3	73
VMD [f]	π^+	209.7 ± 0.9	18.5 ± 0.3	9	11.8 ± 0.2	8.7 ± 0.2	74
VMD [d]	π^-	202.4 ± 1.0	32.6 ± 0.4	16	22.4 ± 0.3	16.2 ± 0.3	72
VMD [e]	π^-	227.7 ± 1.0	35.4 ± 0.4	16	24.5 ± 0.3	17.8 ± 0.3	73
VMD [f]	π^-	208.5 ± 0.8	17.7 ± 0.2	9	11.8 ± 0.2	8.6 ± 0.2	73

[a] = Data $(d\widetilde{\sigma}_{\pi^+} - 1.73\, d\widetilde{\sigma}_{\pi^-})$

[b] = Data $(d\widetilde{\sigma}_{\pi^+} - d\widetilde{\sigma}_{\pi^-})$ − PYTHIA $(d\widetilde{\sigma}_{\pi^+} - d\widetilde{\sigma}_{\pi^-})$

[c] = Data $(d\widetilde{\sigma}_{\pi^+})$ − PYTHIA $(d\widetilde{\sigma}_{\pi^+})$

[d] v1.HRC production

[e] v1.HSG production

[f] v2.HSG production

[g] yield in unit of weighted events

Table B.2: The π^+ and π^- yields with the standard cuts (Table 6.2) and with the final cuts (Table 6.5) for two M_X^2 cuts: the entire missing mass range ($-2 < M_X^2 \le 40\,\mathrm{GeV}^2$) and the exclusive region ($-2 < M_X^2 \le 2.4\,\mathrm{GeV}^2$).

	cuts	standard				final				standard excl. MC	final excl. MC	
	quantity	Data	PYTHIA v1.HRC	PYTHIA v1.HSG	PYTHIA v2.HSG	Data	PYTHIA v1.HRC	PYTHIA v1.HSG	PYTHIA v2.HSG			unit
1	$\langle x \rangle$	0.112	0.118	0.116	0.113	0.119	0.124	0.123	0.128	0.184	0.197	-
2	$\langle y \rangle$	0.461	0.452	0.458	0.475	0.389	0.382	0.382	0.383	0.401	0.401	-
3	$\langle \nu \rangle$	12.7	12.5	12.6	13.1	10.7	10.5	10.5	10.6	11.1	11.0	GeV
4	$\langle Q^2 \rangle$	2.41	2.49	2.50	2.49	2.34	2.40	2.38	2.48	3.74	4.07	GeV^2
5	$\langle W^2 \rangle$	22.3	21.7	22.1	22.9	18.7	18.2	18.2	18.2	17.8	17.5	GeV^2
6	$\langle \theta_{\gamma^*} \rangle$	0.0984	0.103	0.101	0.0965	0.110	0.114	0.113	0.115	0.135	0.138	rad
7	$\langle p_{\pi^+} \rangle$	4.66	4.88	4.95	4.90	9.88	9.54	9.55	9.56	10.2	10.8	GeV^2
8	$\langle P_{\pi^+\perp} \rangle$	0.341	0.332	0.335	0.337	0.361	0.354	0.351	0.360	0.386	0.347	GeV
9	$\langle M_X^2 \rangle$	14.0	13.1	13.3	14.2	2.09	2.30	2.29	2.31	1.94	1.03	GeV^2
10	$\langle \theta_{\pi^+\gamma^*} \rangle$	0.0928	0.0848	0.0841	0.0847	0.0380	0.0386	0.0381	0.0391	0.0409	0.0338	rad
11	$\langle \phi_{\pi^+} \rangle$	0.00251	0.00352	0.00103	0.00207	0.00787	−0.0202	−0.0133	0.0215	0.0146	−0.00190	rad
12	$\langle \phi_S \rangle$	0.0419	−0.0354	−0.0241	−0.0223	−0.0124	0.0434	0.0104	−0.00959	0.00516	0.00376	rad
13	$\langle \Theta_{\pi^+} \rangle$	0.115	0.115	0.113	0.114	0.111	0.111	0.110	0.112	0.134	0.133	rad
14	$\langle \Phi_{\pi^+} \rangle$	3.15	3.14	3.14	3.14	3.19	3.14	3.14	3.14	3.14	3.15	rad
15	$\langle t \rangle$	−1.95	−1.85	−1.86	−1.92	−0.401	−0.430	−0.421	−0.446	−0.478	−0.295	GeV^2
16	$\langle z \rangle$	0.381	0.418	0.420	0.403	0.919	0.905	0.906	0.904	0.936	0.980	-
17	$\langle \Theta_{e^{+\prime}} \rangle$	0.0769	0.0776	0.0781	0.0796	0.0693	0.0697	0.0696	0.0710	0.0897	0.0934	rad
18	$\langle \Phi_{e^{+\prime}} \rangle$	3.13	3.15	3.15	3.14	3.08	3.15	3.16	3.14	3.13	3.13	rad
19	$\langle p_{e^{+\prime}} \rangle$	14.9	15.1	14.9	14.5	16.9	17.0	17.0	17.0	16.5	16.5	GeV
20	$\langle p_{\pi^+} + p_{e^{+\prime}} \rangle$	19.5	20.0	19.9	19.4	26.7	26.6	26.6	26.6	26.7	27.3	GeV
21	$\langle x_F \rangle$	0.336	0.373	0.375	0.360	0.862	0.848	0.849	0.847	0.872	0.918	GeV
22	$\langle \mathrm{rapidity} \rangle$	1.41	1.52	1.51	1.49	2.36	2.33	2.34	2.31	2.29	2.41	GeV
23	$\langle t_0 \rangle$	−1.52	−1.47	−1.51	−1.47	−0.196	−0.238	−0.235	−0.248	−0.226	−0.121	GeV
24	$\langle t' \rangle$	−0.428	−0.387	−0.393	−0.410	−0.180	−0.176	−0.172	−0.180	−0.219	−0.162	GeV

Table B.3: Average values of the kinematic variables from data, PYTHIA and exclusive Monte Carlo events selected with the standard cuts (Table 6.2) and with the final cuts (Table 6.5). The numbers are extracted from the distributions in Figs. B.2–B.4 (left) with the standard cuts, and in Figs. B.5–B.7 (left) with the final cuts.

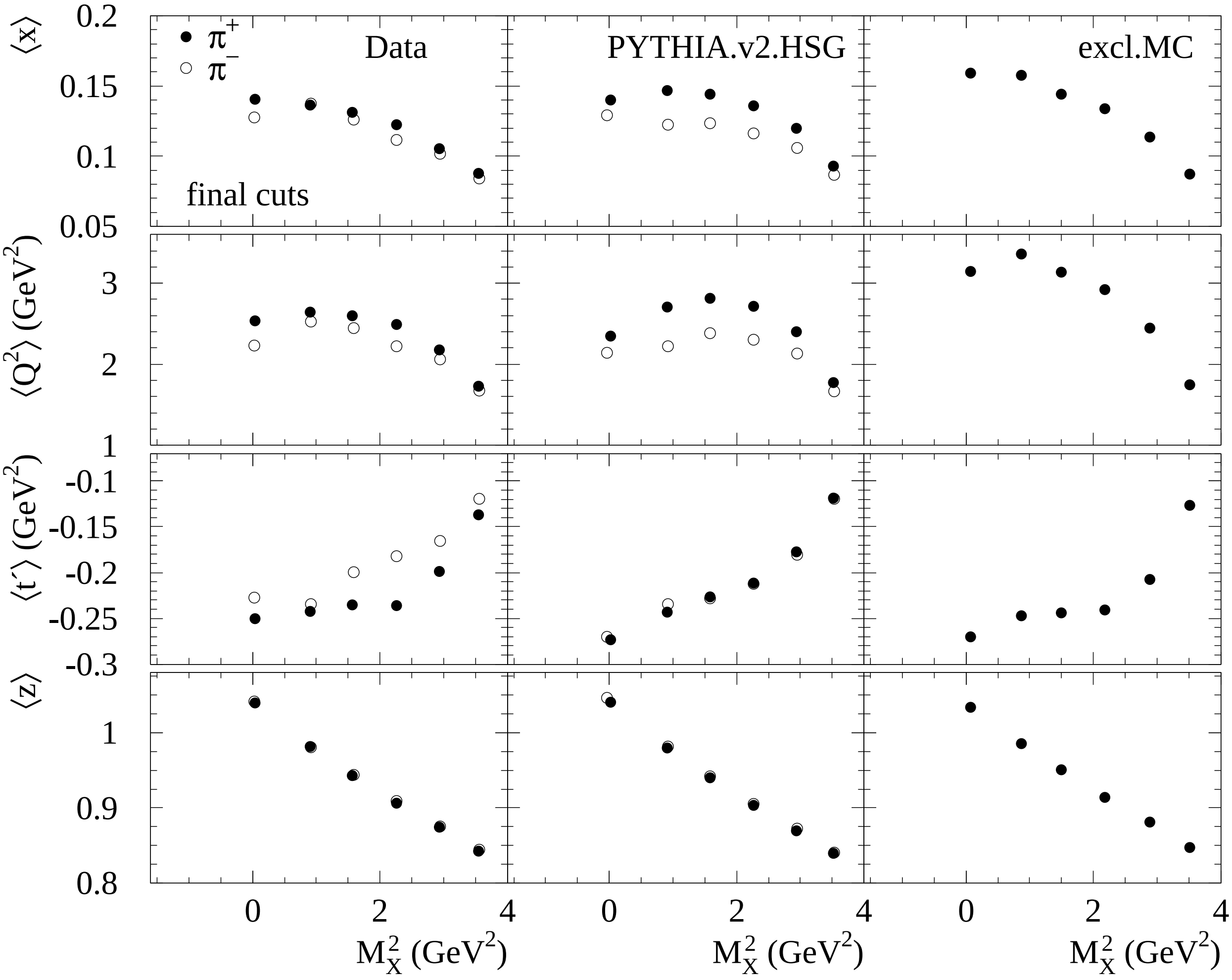

M_X^2 bin	GeV^2	-1.6-0.5	0.5-1.2	1.2-1.9	1.9-2.6	2.6-3.3	3.3-4.0	average
		Data						
$\langle M_X^2\rangle$	GeV^2	π^+ 0.03 π^- 0.02	0.91 0.92	1.56 1.59	2.25 2.26	2.93 2.94	3.55 3.56	1.87 1.88
$\langle x\rangle$		π^+ 0.140 π^- 0.128	0.136 0.137	0.131 0.126	0.122 0.111	0.105 0.102	0.088 0.084	0.120 0.113
$\langle Q^2\rangle$	GeV^2	π^+ 2.53 π^- 2.23	2.64 2.53	2.59 2.45	2.49 2.22	2.17 2.06	1.73 1.67	2.36 2.19
$\langle t'\rangle$	GeV^2	π^+ -0.250 π^- -0.227	-0.242 -0.234	-0.236 -0.200	-0.236 -0.182	-0.199 -0.165	-0.137 -0.120	-2.17 -1.88
$\langle z\rangle$		π^+ 1.04 π^- 1.04	0.98 0.98	0.94 0.94	0.91 0.91	0.87 0.87	0.84 0.84	0.93 0.93
		PYTHIA.v2.HSG						
$\langle M_X^2\rangle$	GeV^2	π^+ 0.02 π^- -0.04	0.91 0.92	1.59 1.58	2.26 2.26	2.93 2.94	3.52 3.53	1.87 1.88
$\langle x\rangle$		π^+ 0.140 π^- 0.129	0.147 0.122	0.144 0.124	0.136 0.116	0.120 0.106	0.093 0.087	0.130 0.114
$\langle Q^2\rangle$	GeV^2	π^+ 2.35 π^- 2.14	2.71 2.22	2.81 2.38	2.72 2.30	2.40 2.13	1.78 1.67	2.46 2.14
$\langle t'\rangle$	GeV^2	π^+ -0.274 π^- -0.270	-0.243 -0.235	-0.227 -0.228	-0.212 -0.212	-0.177 -0.180	-0.118 -0.120	-0.209 -0.208
$\langle z\rangle$		π^+ 1.04 π^- 1.05	0.98 0.98	0.94 0.94	0.90 0.91	0.87 0.87	0.84 0.84	0.93 0.93
		excl.MC						
$\langle M_X^2\rangle$	GeV^2	π^+ 0.07	0.86	1.50	2.18	2.88	3.51	1.83
$\langle x\rangle$		π^+ 0.159	0.158	0.144	0.134	0.113	0.087	0.133
$\langle Q^2\rangle$	GeV^2	π^+ 3.14	3.36	3.13	2.92	2.44	1.74	2.79
$\langle t'\rangle$	GeV^2	π^+ -0.270	-0.247	-0.244	-0.241	-0.207	-0.127	-0.223
$\langle z\rangle$		π^+ 1.03	0.99	0.95	0.91	0.88	0.85	0.94

Figure B.1: The mean values of the kinematic variables x, Q^2, t', and z as a function of the squared missing mass M_X^2 for data, PYTHIA and exclusive MC π^+ samples selected with the final cuts (Table 6.5).

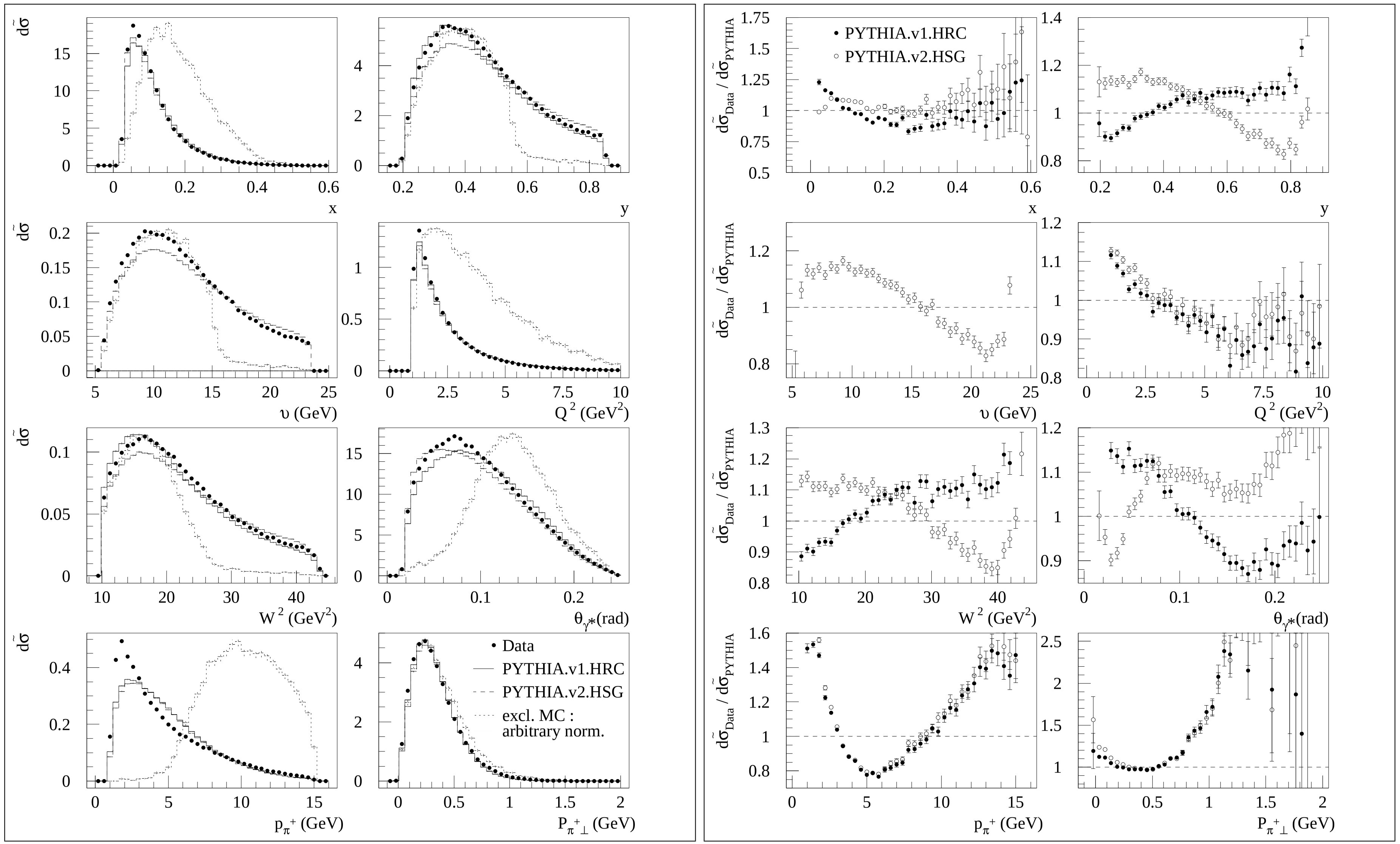

Figure B.2: Distributions (left) and ratios (right) for x, y, ν, Q^2, W^2, θ_{γ^*}, p_{π^+}, and $P_{\pi^+\perp}$ for π^+ data, PYTHIA and exclusive Monte Carlo samples, selected with the standard cuts (Table 6.2). Data and PYTHIA events are given as normalised yields in units of nb differential in the corresponding kinematic variable (e.g., $d\tilde{\sigma} \equiv \frac{d\tilde{\sigma}}{dQ^2}$ in $\frac{\text{nb}}{\text{GeV}^2}$); the exclusive MC events are scaled arbitrarily to the highest data point in each distribution.

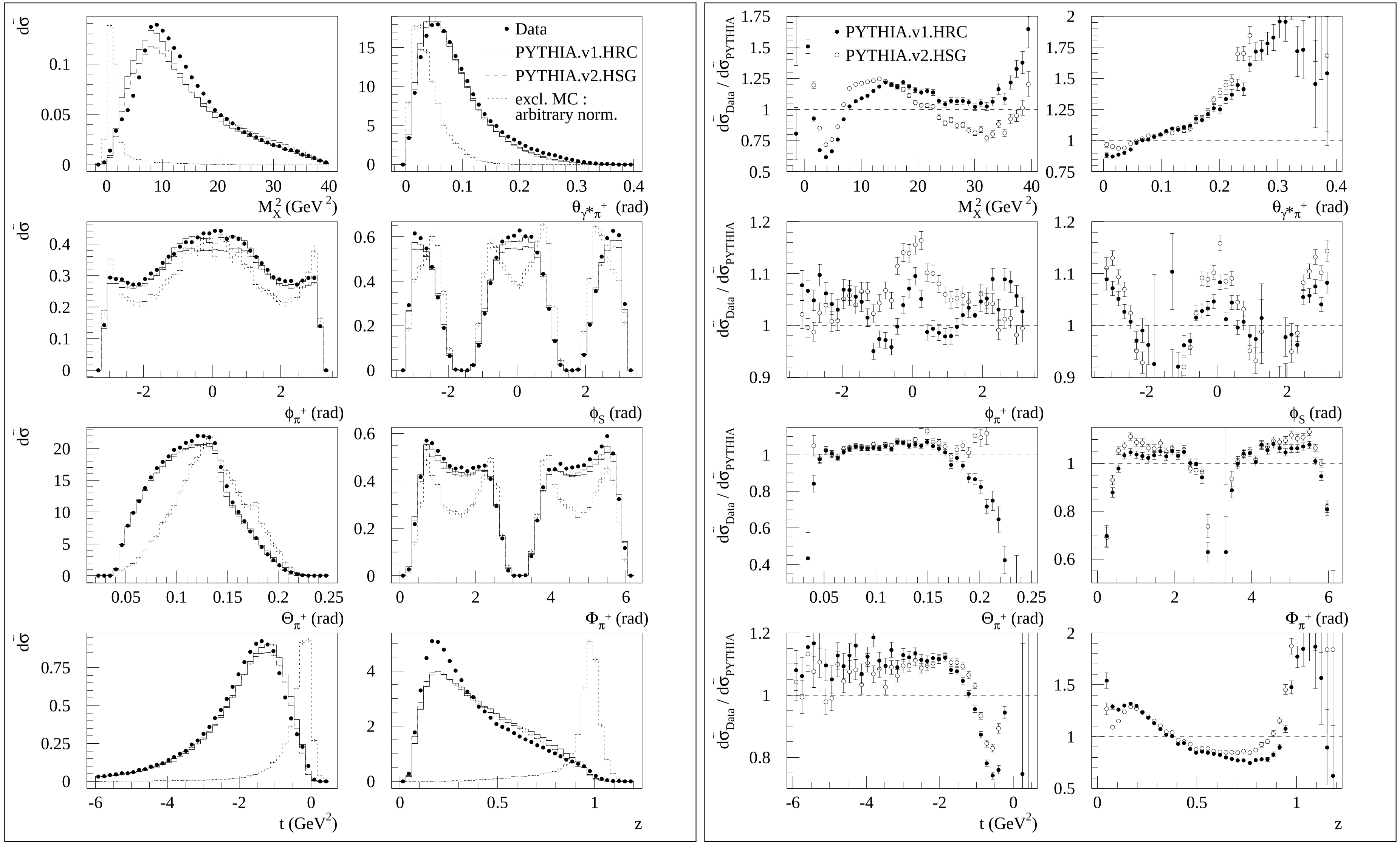

Figure B.3: Distributions (left) and ratios (right) for M_X^2, $\theta_{\gamma^*\pi}$, ϕ_{π^+}, ϕ_S, Θ_{π^+}, Φ_{π^+}, t, and z for π^+ data, PYTHIA and exclusive Monte Carlo samples, selected with the standard cuts (Table 6.2). Data and PYTHIA events are given as normalised yields in units of nb differential in the corresponding kinematic variable (e.g., $d\widetilde{\sigma} \equiv \frac{d\widetilde{\sigma}}{dM_X^2}$ in $\frac{\mathrm{nb}}{\mathrm{GeV}^2}$); the exclusive MC events are scaled arbitrarily to the highest data point in each distribution.

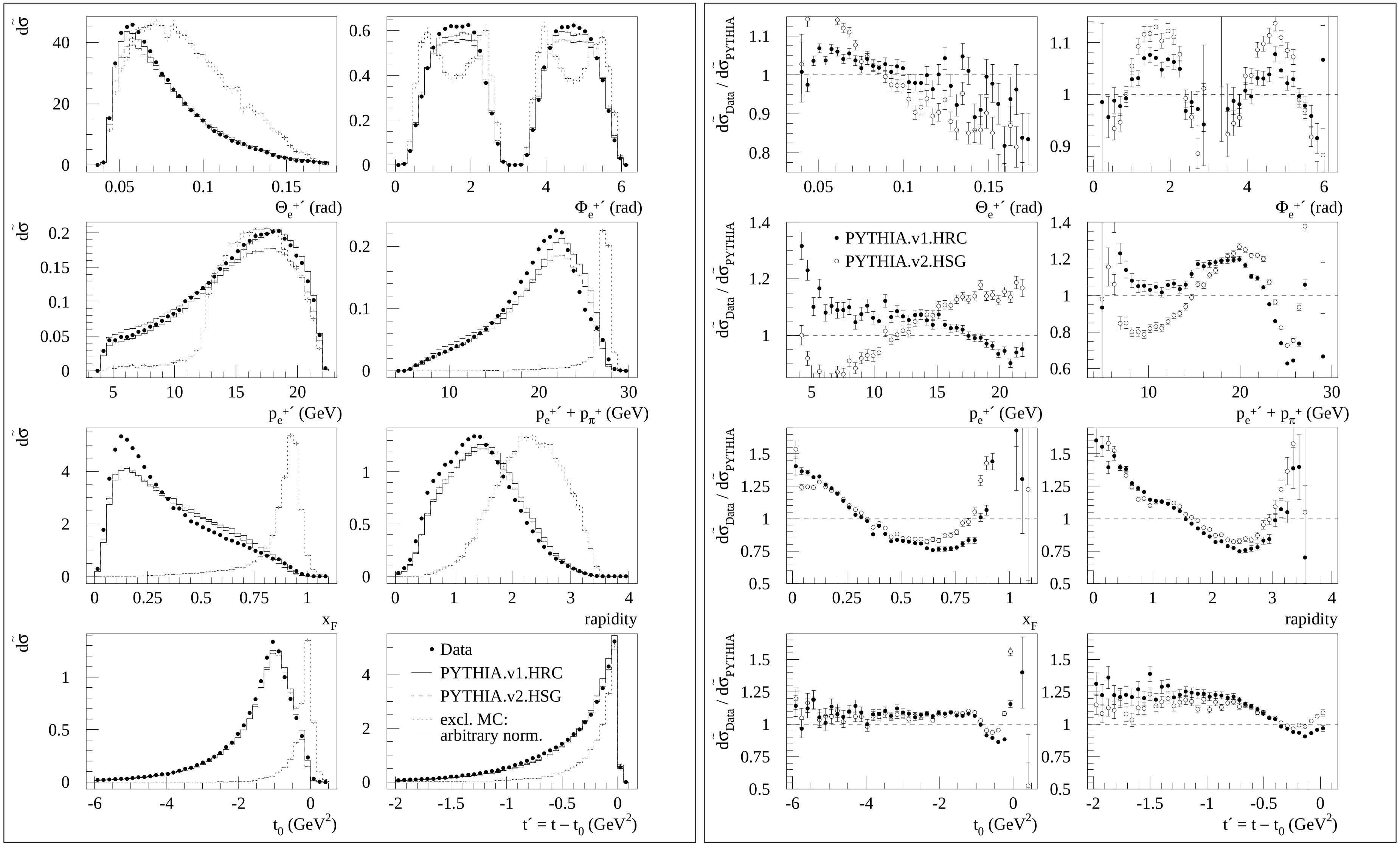

Figure B.4: Distributions (left) and ratios (right) for $\Theta_{e^{+\prime}}$, $\Phi_{e^{+\prime}}$, $p_{e^{+\prime}}$, $p_{e^{+\prime}} + p_{\pi^+}$, x_F, $rapidity$, t_0, and t' for π^+ data, PYTHIA and exclusive Monte Carlo samples, selected with the standard cuts (Table 6.2). Data and PYTHIA events are given as normalised yields in units of nb differential in the corresponding kinematic variable (e.g., $d\widetilde{\sigma} \equiv \frac{d\widetilde{\sigma}}{d\Theta_{e^{+\prime}}}$ in $\frac{\text{nb}}{\text{rad}}$); the exclusive MC events are scaled arbitrarily to the highest data point in each distribution.

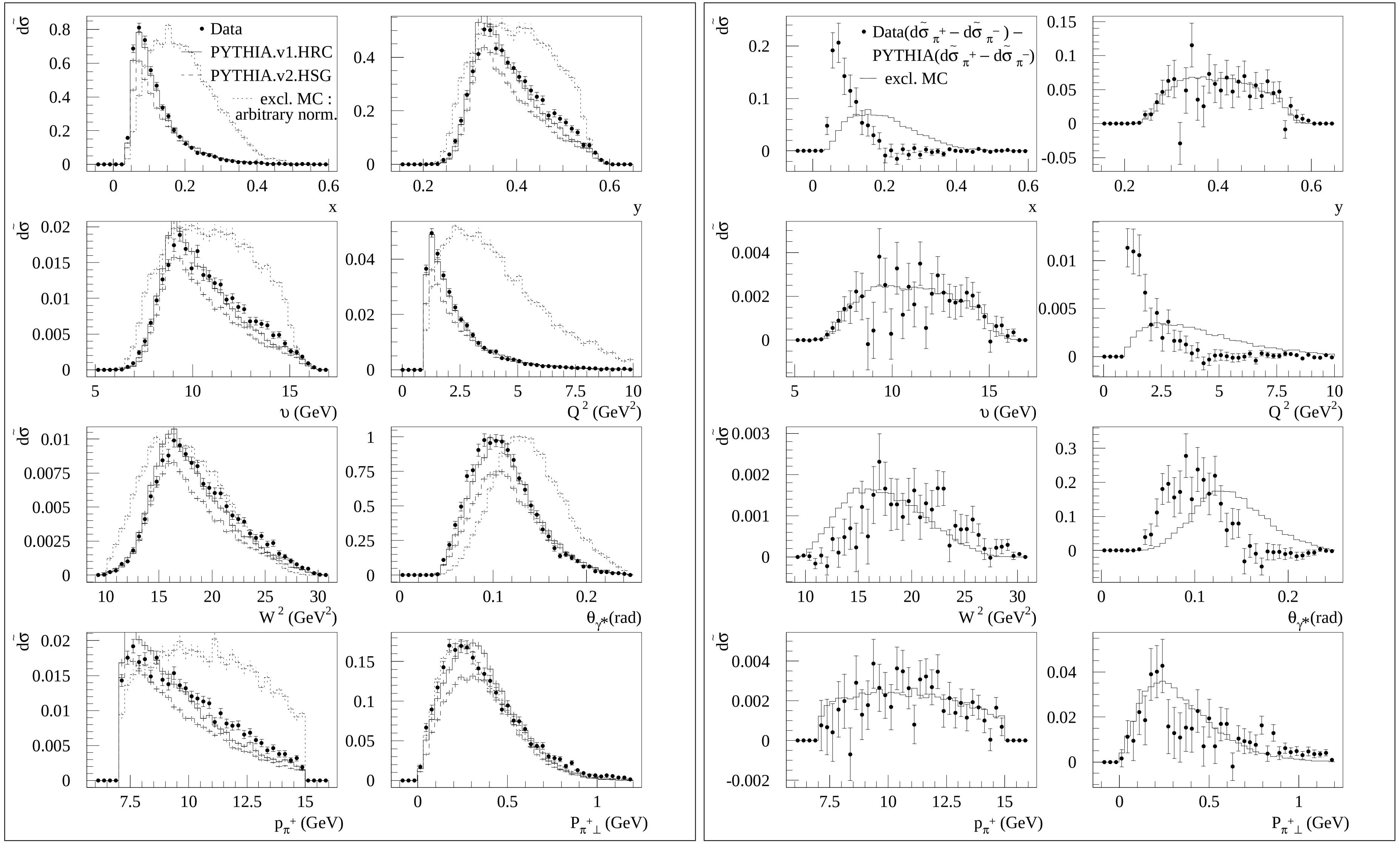

Figure B.5: The π^+ (left) and 'double-difference' (right) distributions for x, y, ν, Q^2, W^2, θ_{γ^*}, p_{π^+}, and $P_{\pi^+\perp}$ obtained from data, PYTHIA and exclusive Monte Carlo samples, selected with the final cuts (Table 6.5). Left: vertical-axis unit as in Fig. B.2 (left). Right: the exclusive MC events are scaled by a common arbitrary factor tuned to the M_X^2 distribution. PYTHIA.v2.HSG is used for the 'double-difference'; π^- distributions are not shown.

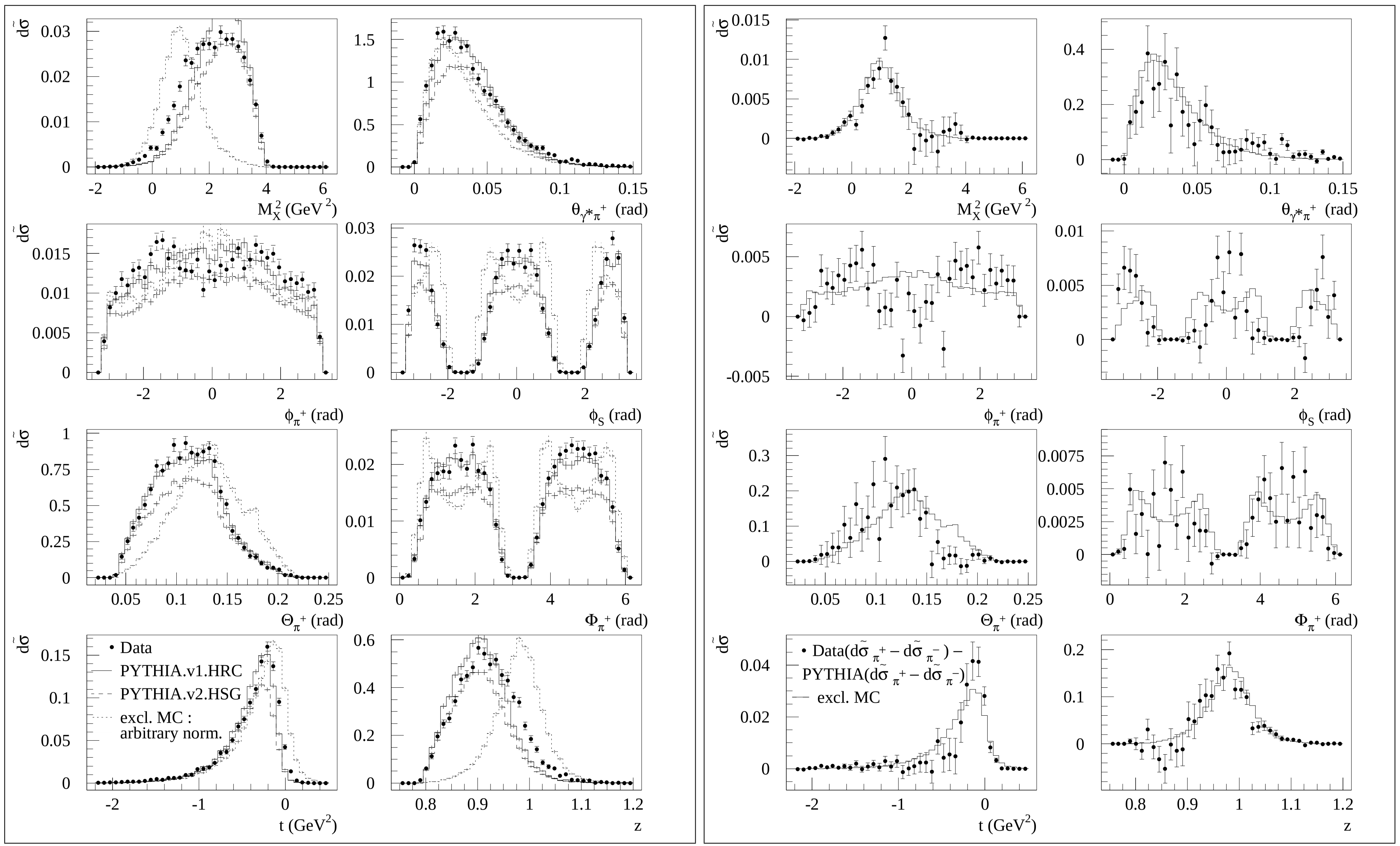

Figure B.6: The π^+ (left) and 'double-difference' (right) distributions for M_X^2, $\theta_{\gamma^*\pi}$, ϕ_{π^+}, ϕ_S, Θ_{π^+}, Φ_{π^+}, t, and z obtained from data, PYTHIA and exclusive Monte Carlo samples, selected with the final cuts (Table 6.5). Left: vertical-axis unit as in Fig. B.3 (left). Right: the exclusive MC events are scaled by a common arbitrary factor tuned to the M_X^2 distribution. PYTHIA.v2.HSG is used for the 'double-difference'; π^- distributions are not shown.

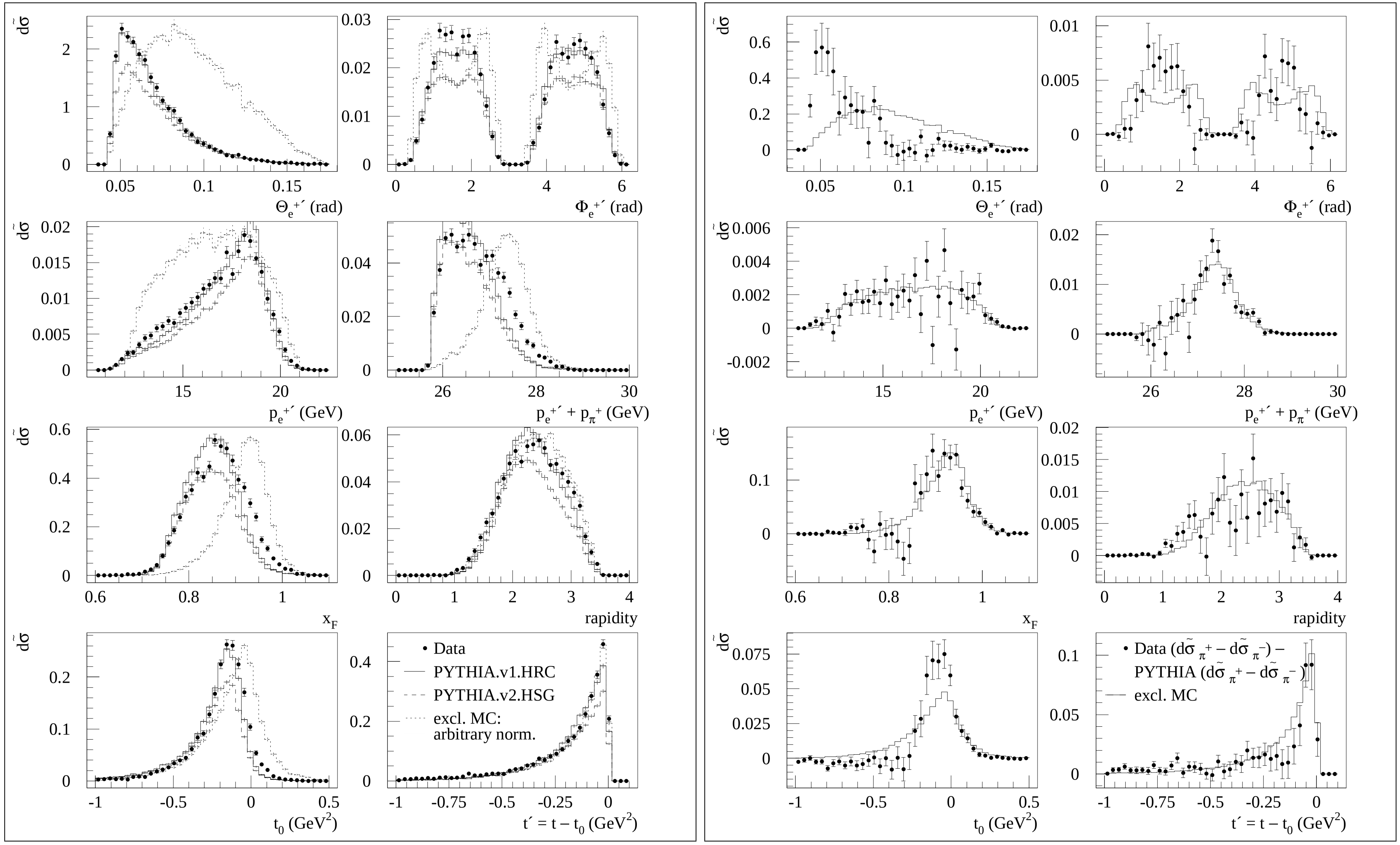

Figure B.7: The π^+ (left) and 'double-difference' (right) distributions for $\Theta_{e^{+\prime}}$, $\Phi_{e^{+\prime}}$, $p_{e^{+\prime}}$, $p_{e^{+\prime}} + p_{\pi^+}$, x_F, *rapidity*, t_0, and t' for data, PYTHIA and exclusive Monte Carlo samples, selected with the final cuts (Table 6.5). Left: vertical-axis unit as in Fig. B.4 (left). Right: the exclusive MC events are scaled by a common arbitrary factor tuned to the M_X^2 distribution. PYTHIA.v2.HSG is used for the 'double-difference'; π^- distributions are not shown.

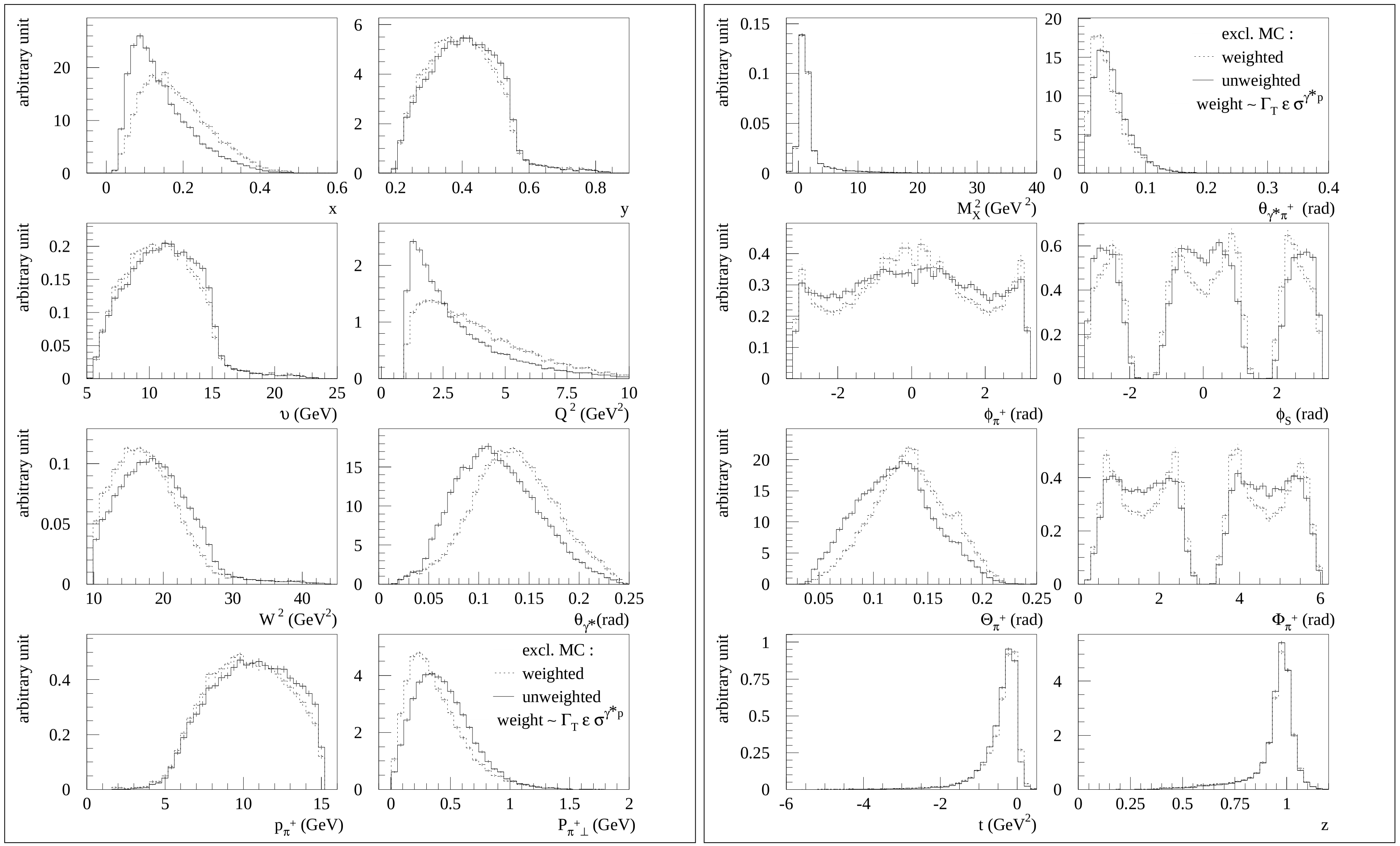

Figure B.8: Weighted and unweighted distributions of the kinematic variables x, y, ν, Q^2, W^2, θ_{γ^*}, p_{π^+}, and $P_{\pi^+\perp}$ (left) and M_X^2, $\theta_{\gamma^*\pi}$, ϕ_{π^+}, ϕ_S, Θ_{π^+}, Φ_{π^+}, t, and z (right) obtained from the exclusive MC sample selected with the standard cuts (Table 6.2).

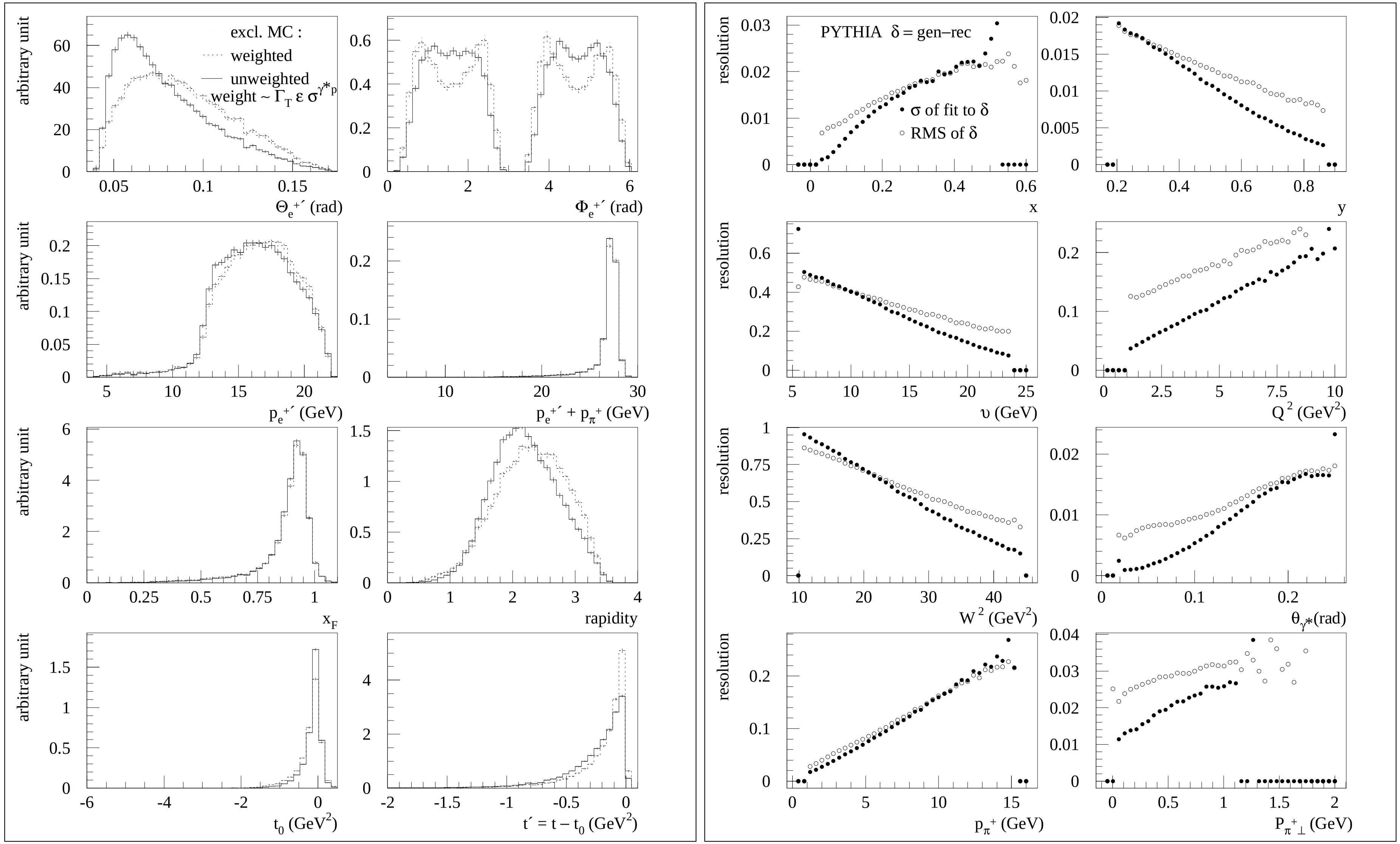

Figure B.9: Left: same as Fig. B.8 but for the kinematic variables $\Theta_{e^+\prime}$, $\Phi_{e^+\prime}$, $p_{e^+\prime}$, $p_{e^+\prime} + p_{\pi^+}$, x_F, *rapidity*, t_0, and t'. Right: same as Fig. B.10 but for the kinematic variables x, y, ν, Q^2, W^2, θ_{γ^*}, p_{π^+}, and $P_{\pi^+\perp}$.

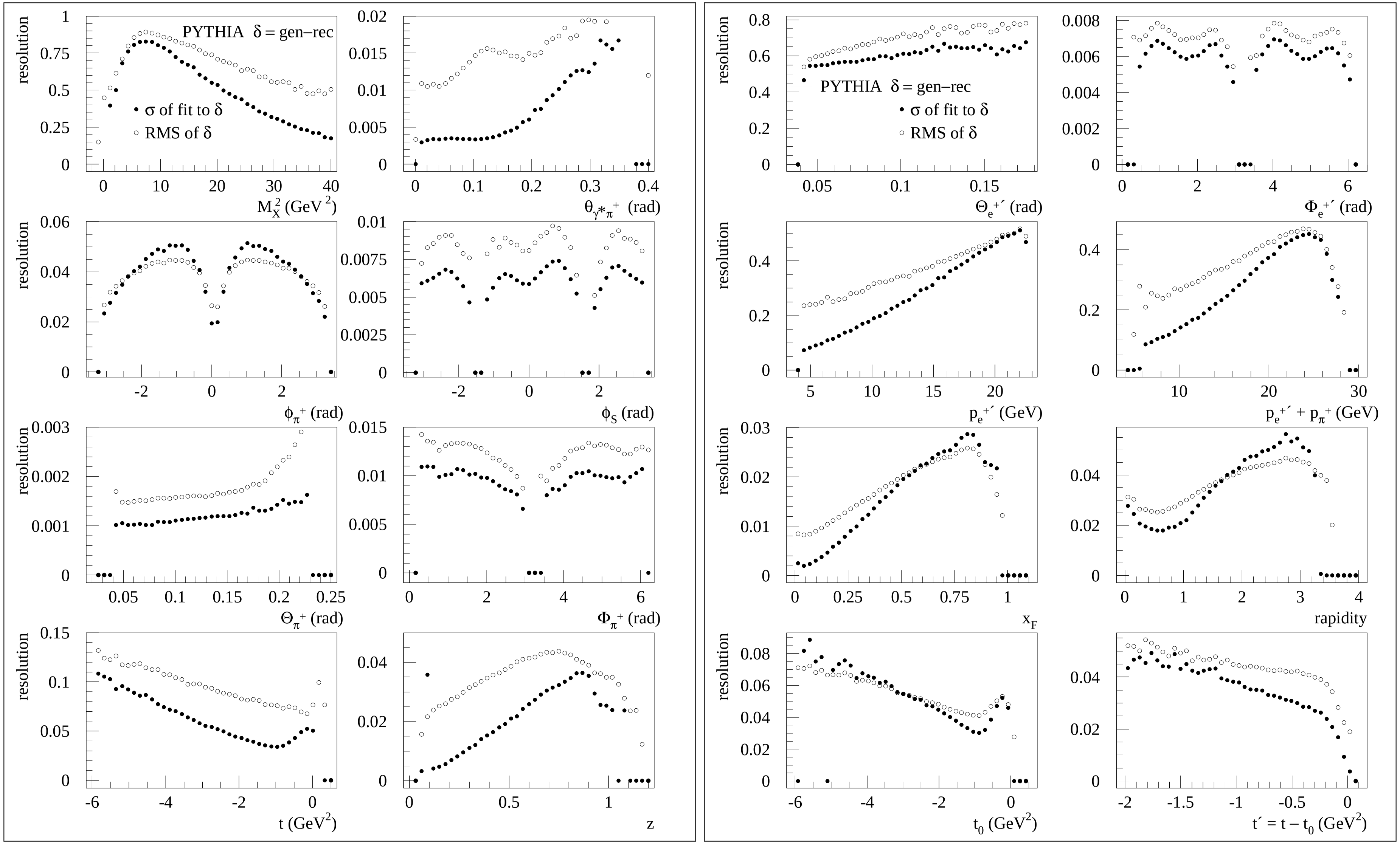

Figure B.10: Resolutions of the kinematic variables M_X^2, $\theta_{\gamma^*\pi}$, ϕ_{π^+}, ϕ_S, Θ_{π^+}, Φ_{π^+}, t, and z (left) and $\Theta_{e^{+\prime}}$, $\Phi_{e^{+\prime}}$, $p_{e^{+\prime}}$, $p_{e^{+\prime}} + p_{\pi^+}$, x_F, *rapidity*, t_0, and t' (right) as a function of the same variables measured from the PYTHIA.v1.HRC π^+ sample selected with the standard cuts (Table 6.2). The width σ from a Gaussian fit to the distribution of the differences δ between generated and reconstructed values, as well as the RMS of the distribution are given.

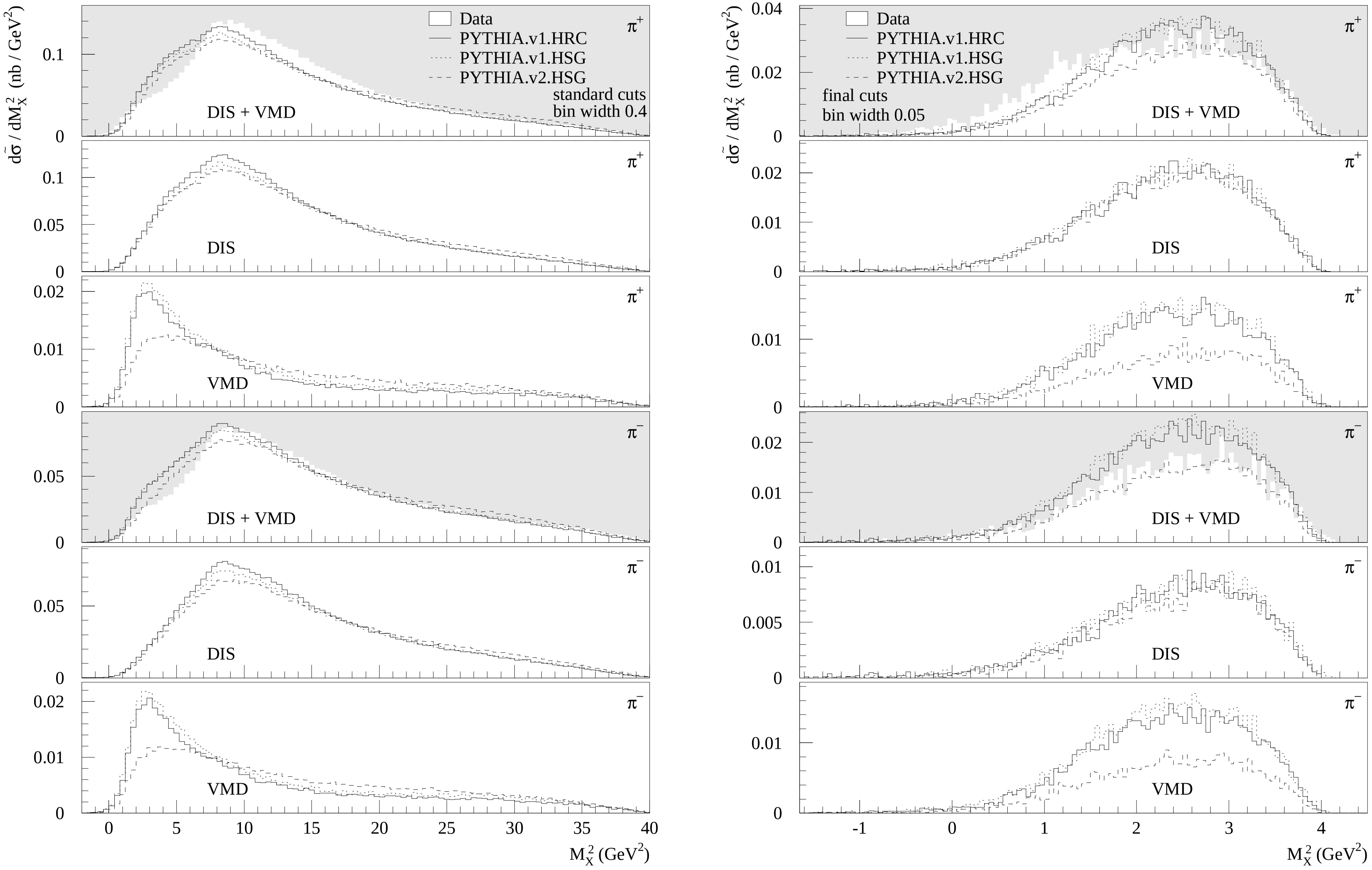

Figure B.11: Data-to-PYTHIA comparison of the M_X^2 distributions for π^+ and π^- samples selected with the standard cuts (Table 6.2; left) and with the final cuts (Table 6.5; right). Three PYTHIA samples are used: PYTHIA.v1.HRC, PYTHIA.v1.HSG, and PYTHIA.v2.HSG (Section 6.6.2).

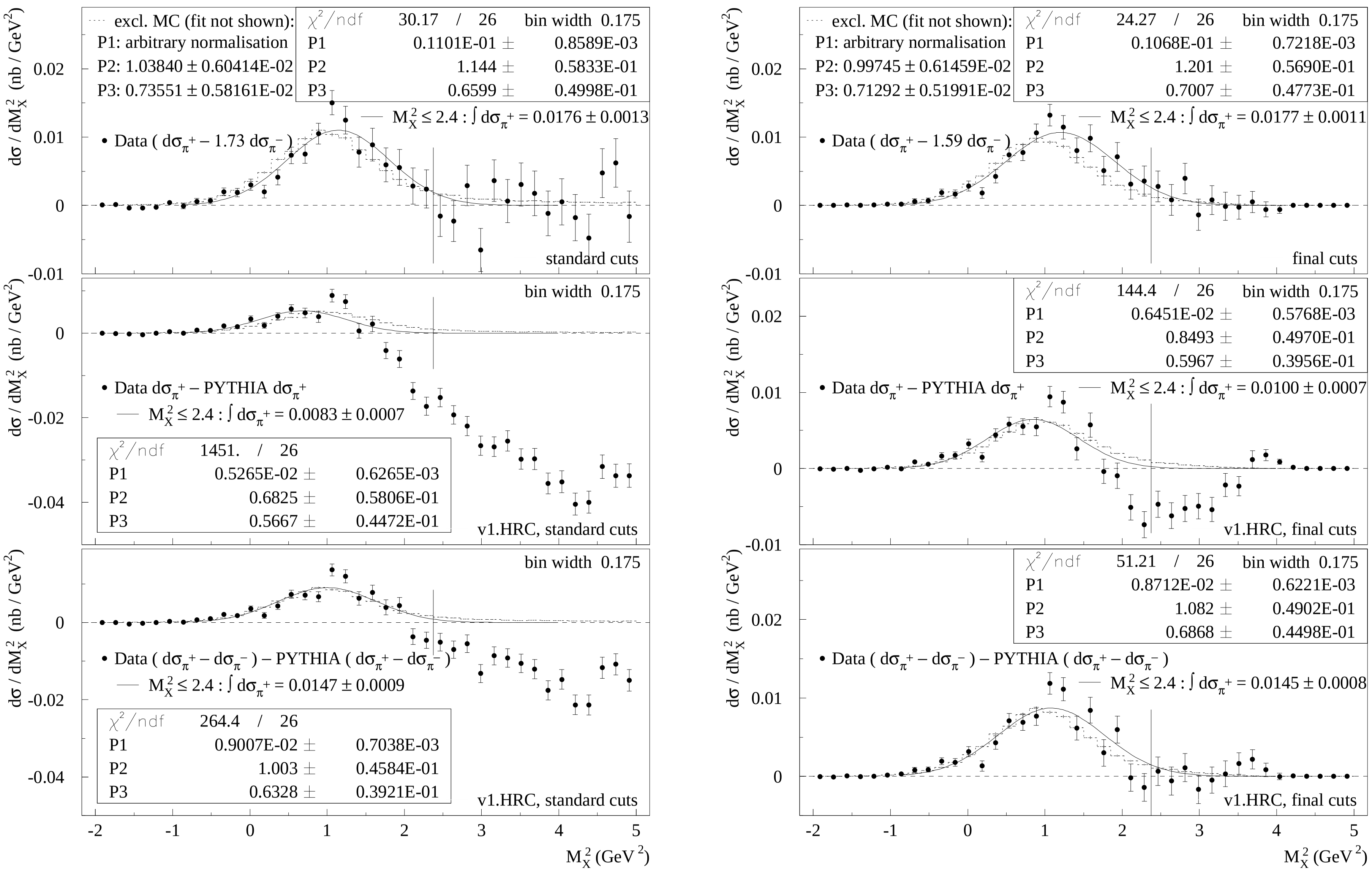

Figure B.12: The results for the π^+ exclusive peak obtained from three background subtraction procedures (Sections 6.4.2, 6.6.3) with the standard (left) and final (right) cuts. The PYTHIA.v1.HRC sample is used.

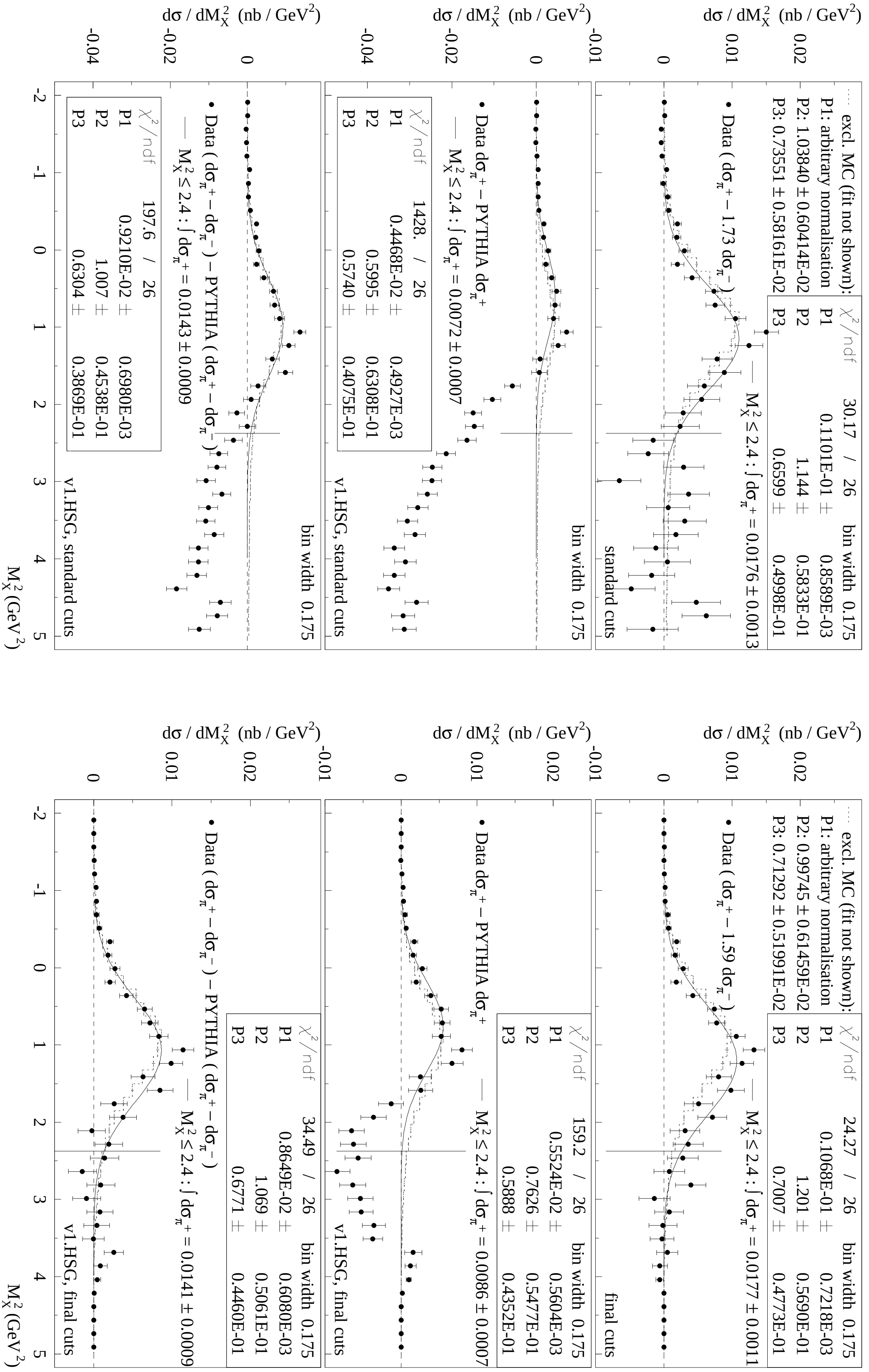

Figure B.13: As Fig. B.12 but the PYTHIA.v1.HSG sample is used.

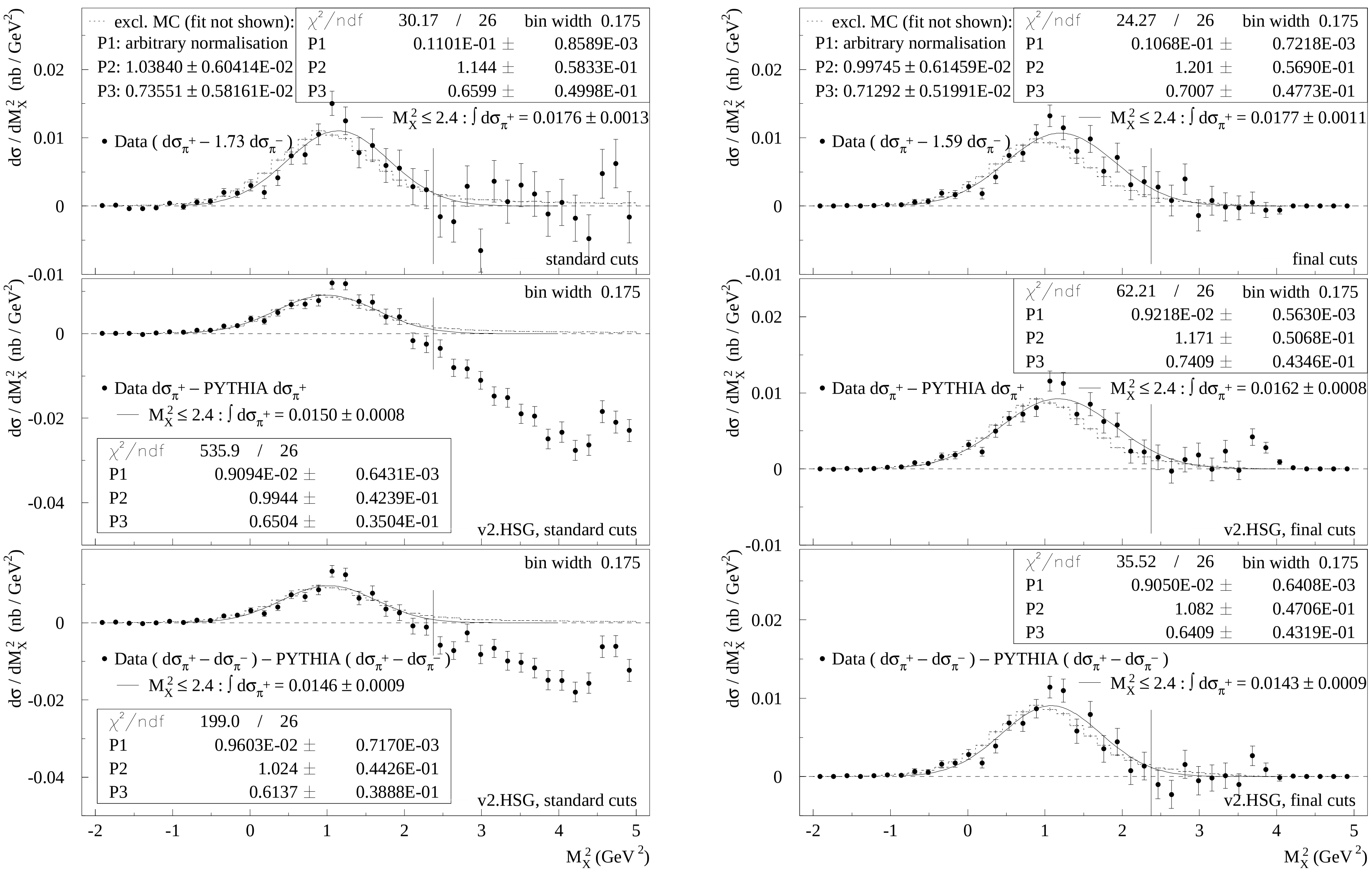

Figure B.14: As Fig. B.12 but the PYTHIA.v2.HSG sample is used.

Appendix C

Azimuthal Asymmetry Studies

The following figures serve as a supplement to Chapter 7.

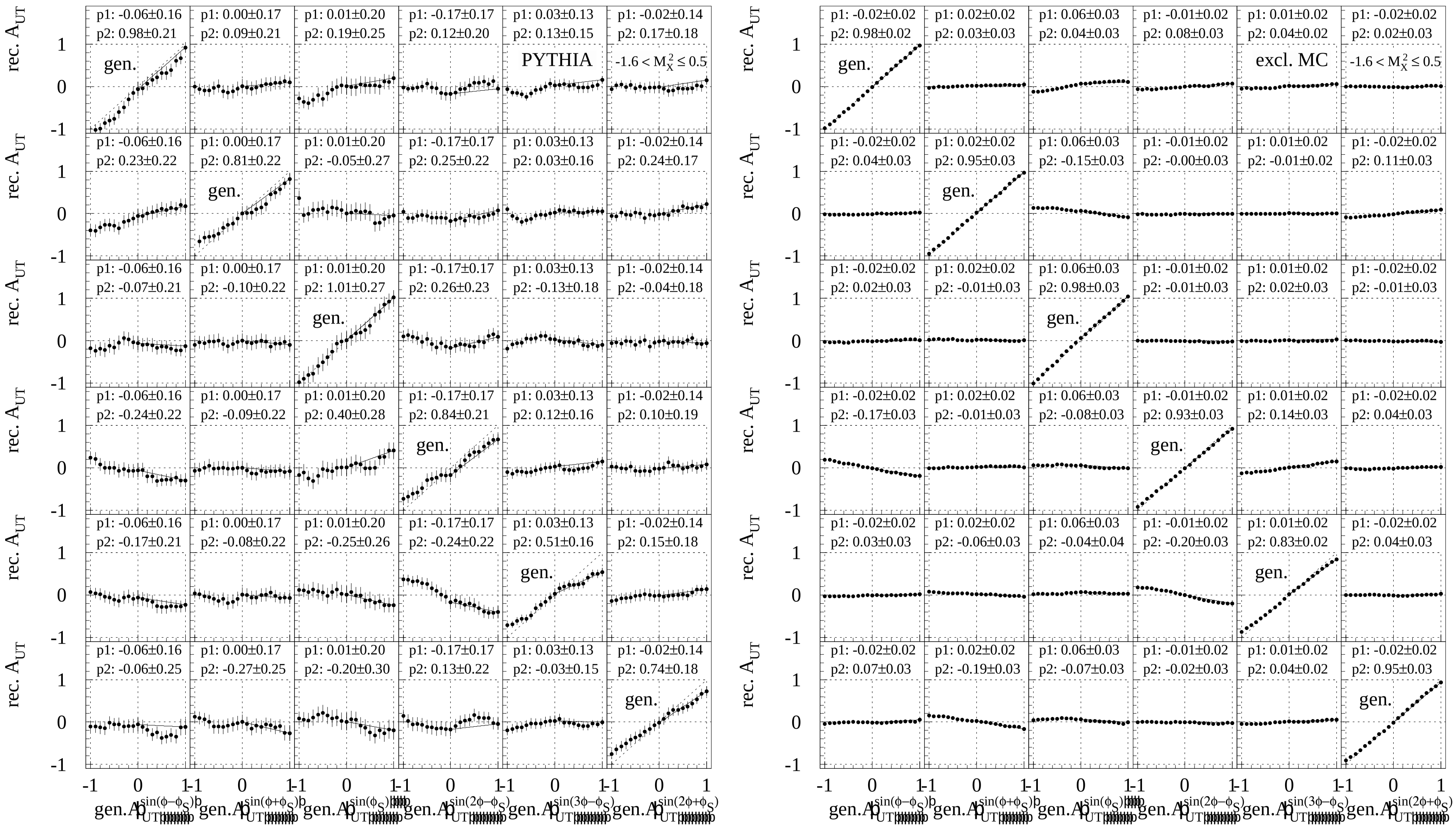

Figure C.1: Generated and reconstructed (full circles) asymmetry amplitudes for PYTHIA.v1.HRC DIS (left) and exclusive Monte Carlo (right) π^+ samples in the squared missing mass region $-1.6 < M_X^2 \leq 0.5\,\mathrm{GeV}^2$. The diagonal dotted lines mark the 21 generated amplitudes with values from -1 to 1. The parameters from a straight-line fit through the middle and the last reconstructed points are given. See Section 7.2.2 for details.

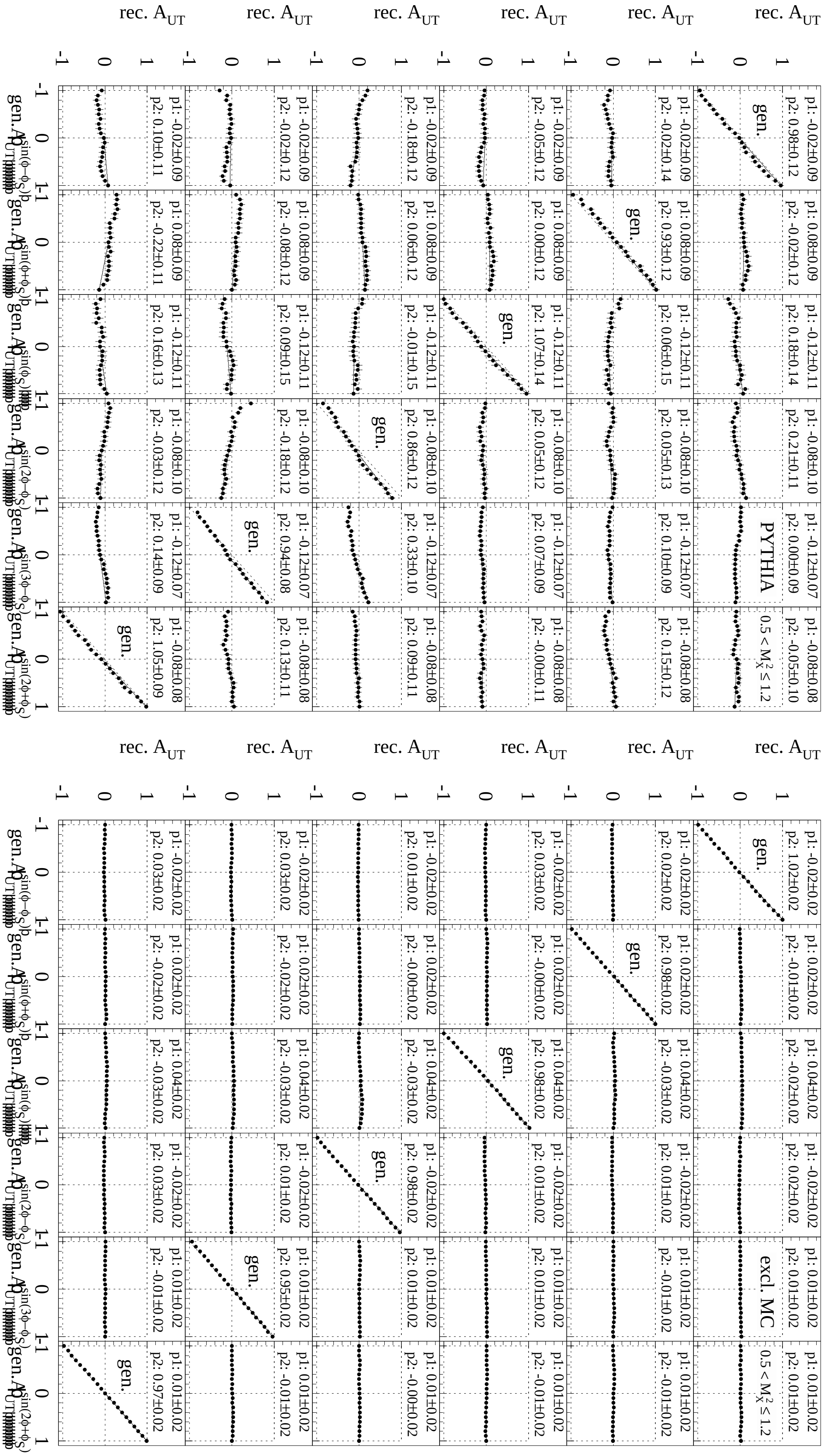

Figure C.2: As Fig. C.1 but for $0.5 < M_X^2 \leq 1.2\,\mathrm{GeV}^2$.

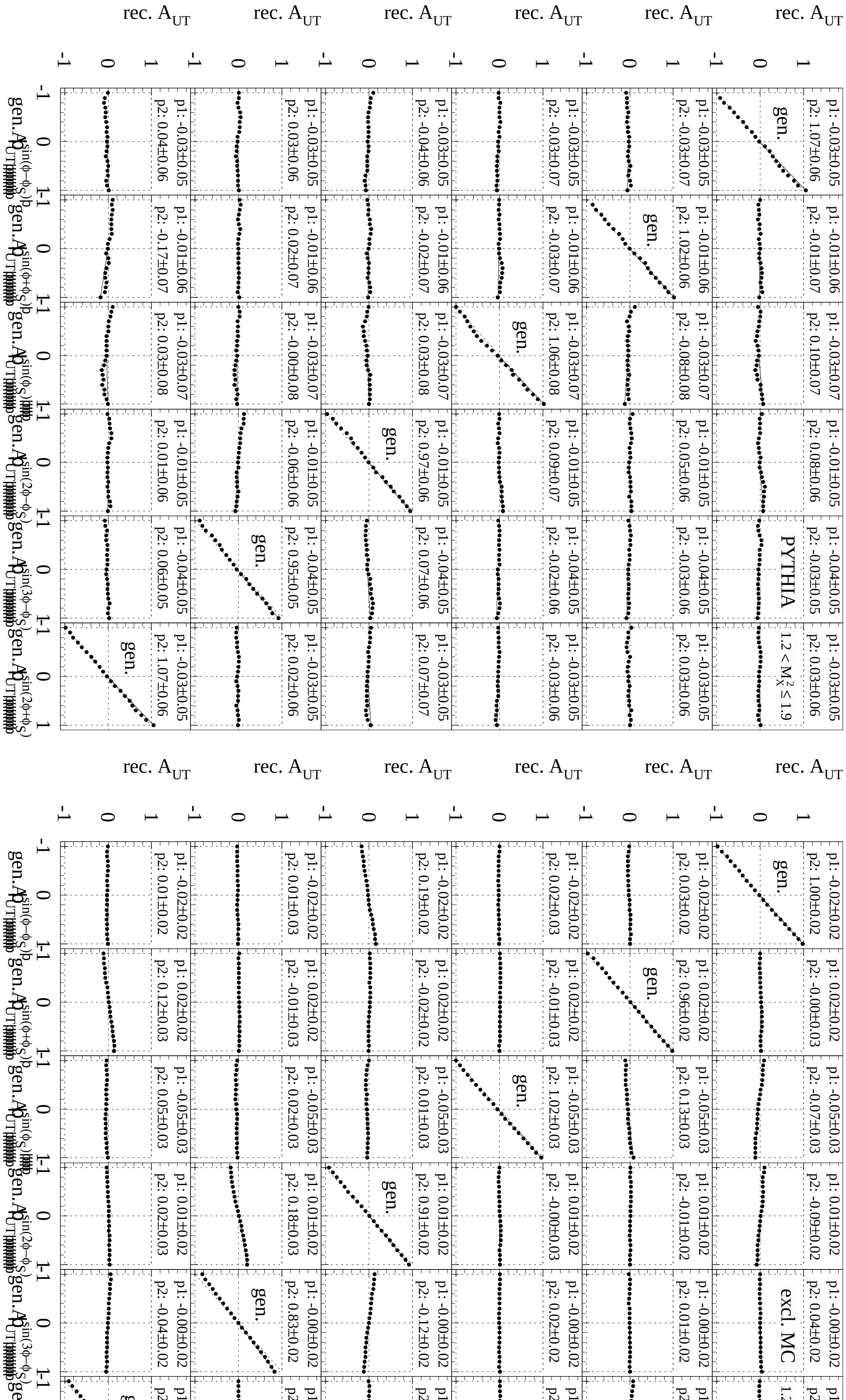

Figure C.3: As Fig. C.1 but for $1.2 < M_X^2 \leq 1.9\,\mathrm{GeV}^2$.

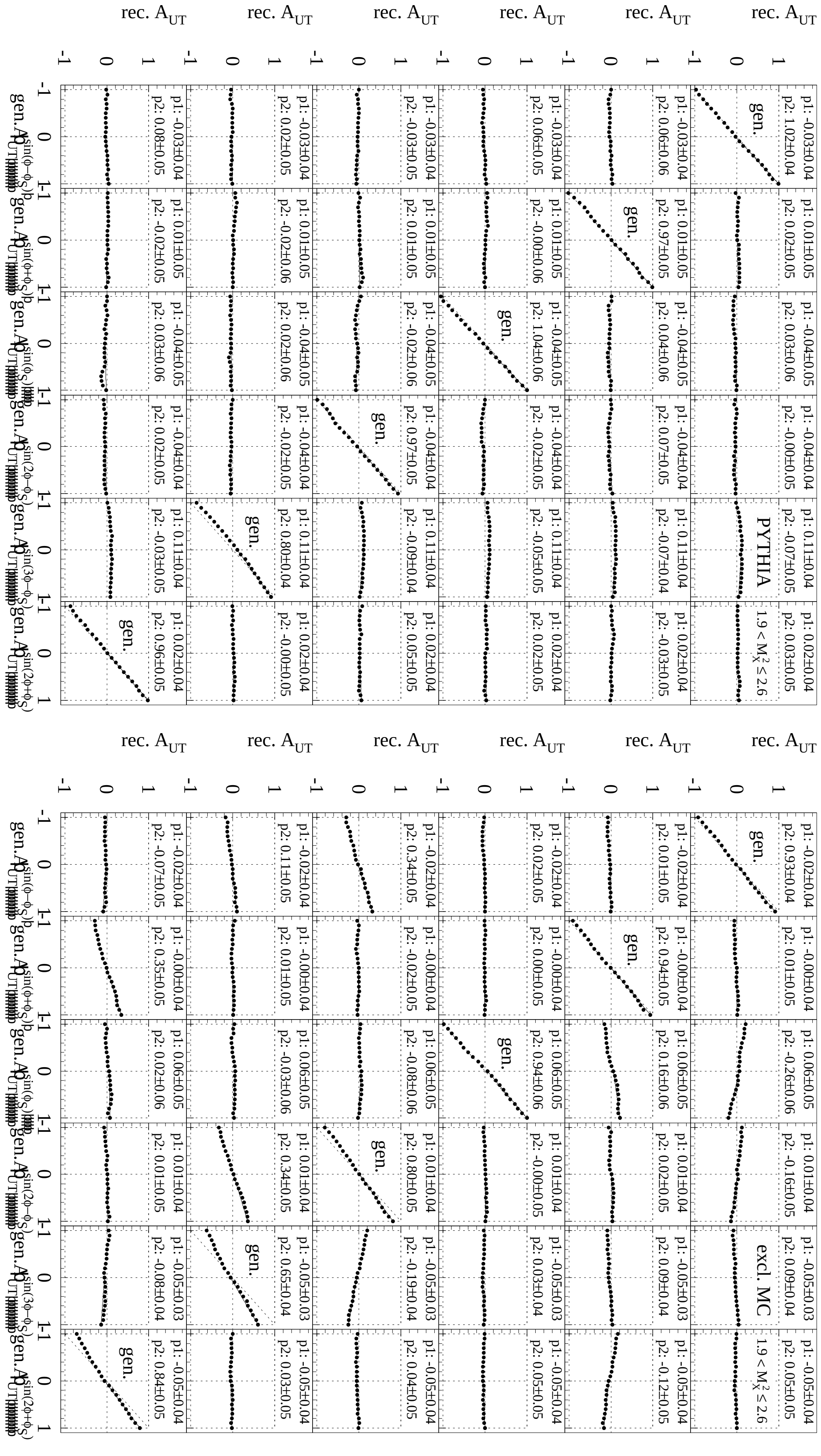

Figure C.4: As Fig. C.1 but for $1.9 < M_X^2 \leq 2.6\,\mathrm{GeV}^2$.

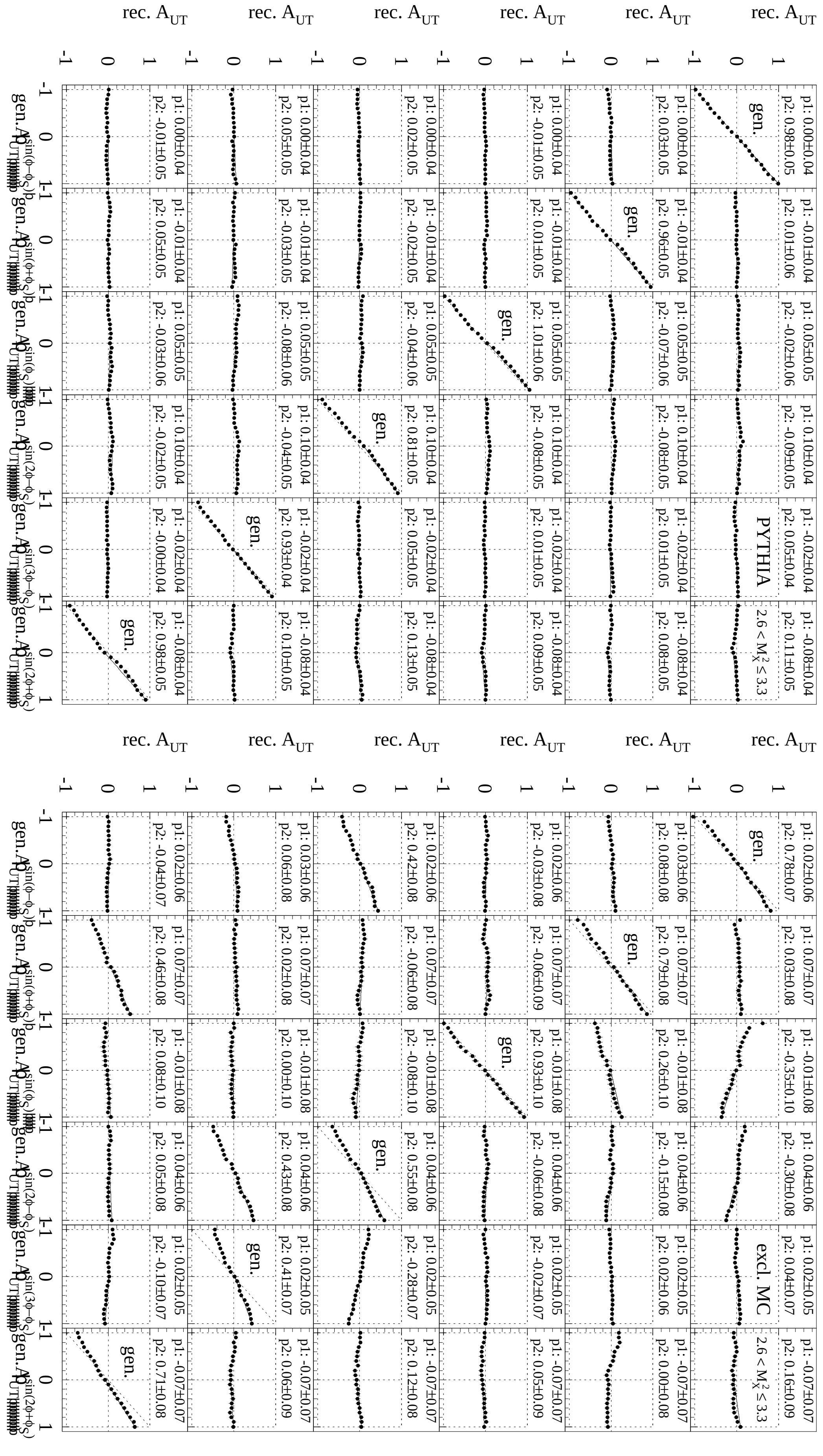

Figure C.5: As Fig. C.1 but for $2.6 < M_X^2 \leq 3.3\,\mathrm{GeV}^2$.

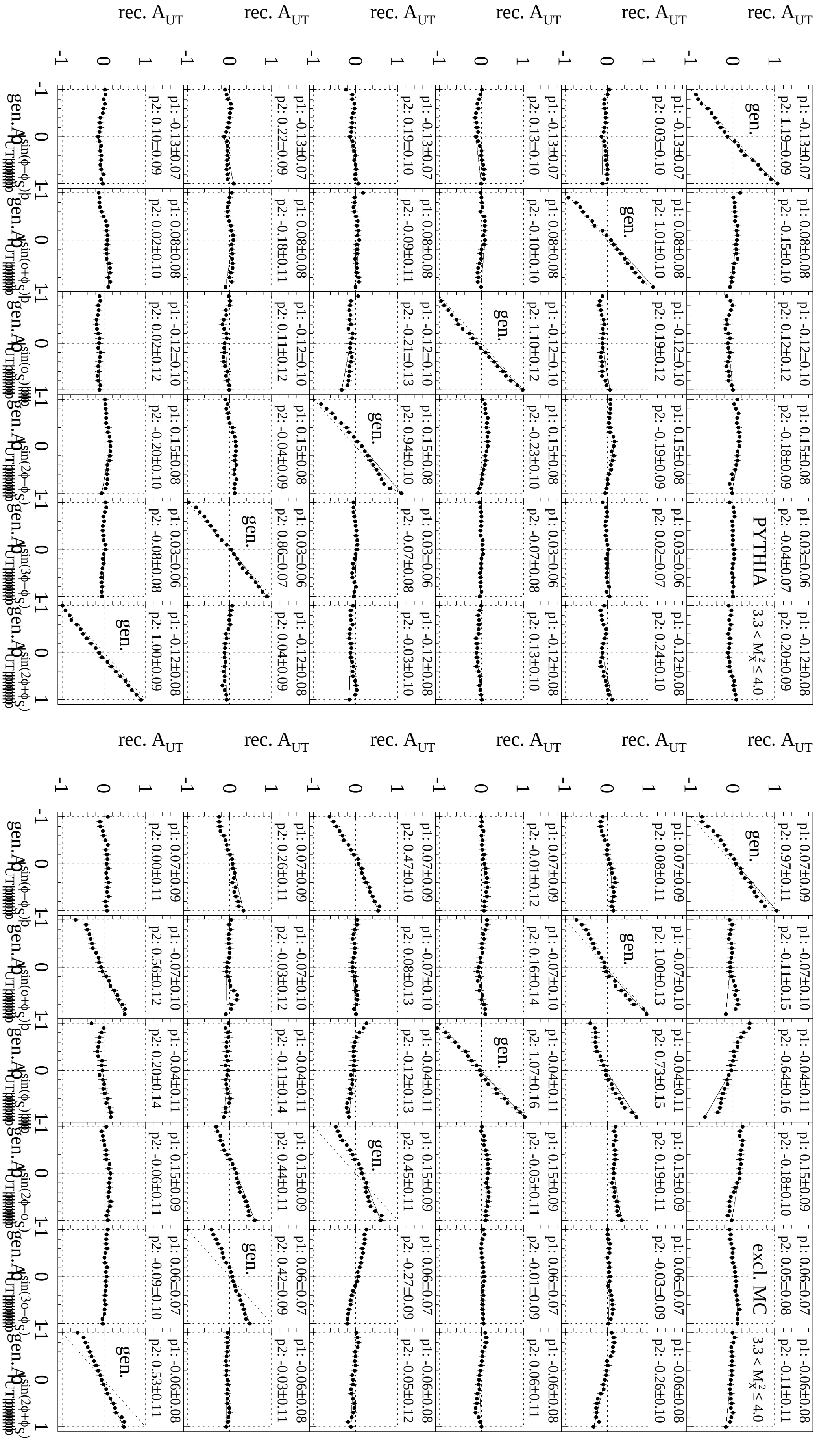

Figure C.6: As Fig. C.1 but for $3.3 < M_X^2 \leq 4.0\,\mathrm{GeV}^2$.

Appendix D

A Note on t and t'

In the analysis of the hard exclusive process, $\gamma^* p \rightarrow n\pi^+$, of interest is the dependence of measured azimuthal asymmetry on the invariant transverse four-momentum transfer $t = (q_{\gamma^*} - q_{\pi^+})^2$. The particles' four-momenta in the laboratory frame, q_{γ^*}, q_p, q_n, and q_{π^+}, are defined in Table 3.1.

The invariant variable t has a kinematical limit denoted as t_0 (3.28), therefore $t' = t - t_0$ is used for the final results (Chapter 8). The definitions of t and t_0 are given below in the centre-of-mass and in the laboratory frame. We explain how t' is computed in this analysis.

D.1 Kinematics in the $\gamma^* p$ Centre-of-Mass Frame

The transition from the laboratory (*lab*) frame, in which the target proton is at rest, to the virtual photon–proton centre-of-mass (*cm*) frame proceeds via the formation of the four-momentum of the *cm*-frame in the *lab*-frame, denoted as $q_{CM,lab}$. For consistency with the notation used throughout the text, the *lab*-subscript of the kinematic variables is omitted in the following. The transition four-vector is computed as $q_{CM} = q_{\gamma^*} + q_p$ and its components are $q_{CM} = (E_{CM}, \vec{p}_{CM}) = (\nu + M_p, \vec{q})$. The velocity of the centre-of-mass (CM) in the *lab*-frame is written as

$$\vec{\beta}_{CM} = \frac{\vec{p}_{CM}}{E_{CM}} = \frac{\vec{q}}{\nu + M_p}, \quad |\vec{\beta}_{CM}| = \frac{\sqrt{\nu^2 + Q^2}}{\nu + M_p}. \tag{D.1}$$

It is useful to write the expressions

$$\gamma_{CM} = \frac{1}{\sqrt{1 - \vec{\beta}^2_{CM}}} = \frac{E_{CM}}{M_{CM}} = \frac{\nu + M_p}{\sqrt{W^2}}, \tag{D.2}$$

$$\vec{\eta}_{CM} = \gamma_{CM}\, \vec{\beta}_{CM} = \frac{\vec{p}_{CM}}{M_{CM}} = \frac{\vec{q}}{\sqrt{W^2}}, \quad |\vec{\eta}_{CM}| = \sqrt{\gamma^2_{CM} - 1} = \frac{\sqrt{\nu^2 + Q^2}}{\sqrt{W^2}}, \tag{D.3}$$

where $M_{CM} = \sqrt{q^2_{CM}} = \sqrt{(\nu + M_p)^2 - \vec{q}^2} = \sqrt{\nu^2 - \vec{q}^2 + 2M_p\nu + M_p^2} = \sqrt{M_p^2 + 2M_p\nu - Q^2} = \sqrt{W^2}$.

The four-momentum of a particle h in the *cm*-frame is related to its four-momentum in the *lab*-frame as follows

$$E_{h,cm} = \gamma_{CM} E_h - \vec{\eta}_{CM}\, \vec{p}_h, \tag{D.4}$$

$$|\vec{p}_{h,cm}| = \sqrt{E^2_{h,cm} - m^2_h}, \tag{D.5}$$

where m_h is the particle's mass. This gives the *cm*-energies of the particles (virtual photon, proton, neutron, and pion) as a function of the kinematic variables in the *lab*-frame

$$\begin{aligned} E_{\gamma^*,cm} \equiv \nu_{cm} &= \frac{W^2 - Q^2 - M_p^2}{2\sqrt{W^2}}, & E_{n,cm} &= \frac{W^2 + M_n^2 - m_{\pi^+}^2}{2\sqrt{W^2}}, \\ E_{p,cm} &= \frac{W^2 + Q^2 + M_p^2}{2\sqrt{W^2}}, & E_{\pi^+,cm} &= \frac{W^2 + m_{\pi^+}^2 - M_n^2}{2\sqrt{W^2}}. \end{aligned} \tag{D.6}$$

Splitting $\vec{p}_h = \vec{p}_h^L + \vec{p}_h^T$ into components parallel and normal to $\vec{\beta}_{CM}$, where $\vec{p}_h^L = \frac{\vec{p}_h\cdot\vec{\eta}}{\vec{\eta}^2}\vec{\eta}$ and $\vec{p}_h^T = \vec{p}_h - \vec{p}_h^L$, the transformation of the three-vector can be written as

$$\vec{p}_{h,cm}^L = \gamma_{CM}\vec{p}_h^L - \vec{\eta}_{CM}E_h, \quad \vec{p}_{h,cm}^T = \vec{p}_h^T, \tag{D.7}$$

$$\vec{p}_{h,cm} = \vec{p}_{h,cm}^L + \vec{p}_{h,cm}^T = \vec{p}_h + \frac{\vec{q}}{\sqrt{W^2}}\Big(\frac{\vec{p}_h\cdot\vec{q}}{\nu + M_p + \sqrt{W^2}} - E_h\Big). \tag{D.8}$$

D.2 t in the *cm*-frame

In the *cm*-frame, the expressions for t and t_0 take the form

$$\begin{aligned} t &= (q_{\gamma^*,cm} - q_{\pi^+,cm})^2 = (\nu_{cm} - E_{\pi^+,cm})^2 - (\vec{q}_{cm} - \vec{p}_{\pi^+,cm})^2 \\ &= (\nu_{cm} - E_{\pi^+,cm})^2 - |\vec{q}_{cm}|^2 - |\vec{p}_{\pi^+,cm}|^2 + 2|\vec{q}_{cm}||\vec{p}_{\pi^+,cm}|\cos\theta_{\gamma^*\pi^+,cm} \\ &= (\nu_{cm} - E_{\pi^+,cm})^2 - (|\vec{q}_{cm}| - |\vec{p}_{\pi^+,cm}|)^2 - 4|\vec{q}_{cm}||\vec{p}_{\pi^+,cm}|\sin^2\frac{\theta_{\gamma^*\pi^+,cm}}{2}, \\ t_0 &= (\nu_{cm} - E_{\pi^+,cm})^2 - (|\vec{q}_{cm}| - |\vec{p}_{\pi^+,cm}|)^2, \end{aligned} \tag{D.9}$$

where ((D.4), (D.5), (D.6))

$$\begin{aligned} E_{\pi^+,cm} &= \frac{W^2 + m_{\pi^+}^2 - M_n^2}{2\sqrt{W^2}} & |\vec{p}_{\pi^+,cm}| &= \sqrt{E_{\pi^+}^2 - m_{\pi^+}^2}, \\ \nu_{cm} &= \frac{W^2 - Q^2 - M_p^2}{2\sqrt{W^2}} & |\vec{q}_{cm}| &= \sqrt{\nu_{cm}^2 + Q^2}. \end{aligned} \tag{D.10}$$

There are two ways to compute the t value

(i) $M_n^2 = M_X^2$, where $M_X^2 = (q_{\gamma^*} + q_p - q_{\pi^+})^2$ is the value of the measured squared missing mass in the exclusive process, in which the neutron is not detected.

(ii) $M_n^2 = (0.939565360)^2\,\mathrm{GeV}^2$ is the PDG-value of the neutron mass.

The definition of the so called 'constrained t' relies on the latter choice. Inserting M_n^2 in (D.10) for $E_{\pi^+,cm}$ and the latter in (D.9) allows us to obtain the constrained t values in the *cm*-frame in a straightforward way. Comparison between the two choices (i) and (ii) is discussed in Section D.4.

D.3 t in the *lab*-frame

In the *lab*-frame, the expressions for t and t_0 take the form

$$\begin{aligned} t &= (q_{\gamma^*} - q_{\pi^+})^2 = q_{\gamma^*}^2 + q_{\pi^+}^2 - 2q_{\gamma^*}q_{\pi^+} = -Q^2 + m_{\pi^+}^2 - 2\nu E_{\pi^+} + 2|\vec{q}||\vec{p}_{\pi^+}|\cos\theta_{\gamma^*\pi^+} \\ &= -Q^2 + m_{\pi^+}^2 - 2\nu E_{\pi^+} + 2\sqrt{\nu^2 + Q^2}\sqrt{E_{\pi^+}^2 - m_{\pi^+}^2}\cos\theta_{\gamma^*\pi^+}, \\ t_0 &= -Q^2 + m_{\pi^+}^2 - 2\nu E_{\pi^+} + 2\sqrt{\nu^2 + Q^2}\sqrt{E_{\pi^+}^2 - m_{\pi^+}^2}. \end{aligned} \tag{D.11}$$

The definition of the 'constrained t' relies on the dependence of t on M_n^2 (the squared neutron mass) and the subsequent substitution of M_n^2 with the PDG-value. In (D.11) the dependence on M_n^2 is made explicit via E_{π^+}. Both variables are related to each other via

$$M_n^2 = [(q_{\gamma^*} - q_{\pi^+}) + q_p]^2 = (q_{\gamma^*} - q_{\pi^+})^2 + q_p^2 + 2(q_{\gamma^*} - q_{\pi^+})q_p = t + M_p^2 + 2M_p(\nu - E_{\pi^+}), \quad \text{(D.12)}$$

$$:E_{\pi^+} = \frac{t}{2M_p} + \nu - \frac{M_n^2 - M_p^2}{2M_p}. \quad \text{(D.13)}$$

One sees from (D.13) that E_{π^+} depends on t as well. Inserting the expression for E_{π^+} from (D.13) into (D.11) leads to a non-straightforward solution (of a quadratic equation) with respect to t, due to the $\sqrt{E_{\pi^+}^2 - m_{\pi^+}^2}$ term. Without using kinematic approximations, the computation of 'constrained t' is more complicated, e.g., compared with that in the analysis of Deeply-Virtual Compton Scattering (DVCS) [30], because in this analysis:

(i) The pion mass $m_{\pi^+} \neq 0$, in contrast to the massless γ^* produced in DVCS.

(ii) The nucleons, a proton in the initial and a neutron in the final state, have different masses, $M_p \neq M_n$, in contrast to DVCS with a proton both in the inital and final state.

While (ii) is a minor point, the approximation $m_{\pi^+} = 0$ in (i) is not made in this analysis, and hence 'constrained t' in the *lab*-frame is not used to present the t-dependence of our results (Chapter 8).

D.4 Resolutions of t and $t' = t - t_0$

The minimal value $|t_0|$ of $|t|$, where $t < 0$ and $t_0 < 0$, is obtained from t when the polar angle $\theta_{\gamma^*\pi^+}$ between the virtual photon (γ^*) and the produced pion (π^+) is put to zero, see (D.9), (D.11). Since t is an invariant quantity, t_0 and $t' = t - t_0$ for $\theta_{\gamma^*\pi^+} \neq 0$ are not invariants.

Fig. D.1 shows a comparison of the t, t_0, and $t' = t - t_0$ distributions as computed in the *lab*-frame with the neutron mass $M_n^2 = M_X^2$ (solid line), and in the *cm*-frame with $M_n^2 = (0.9396)^2\,\mathrm{GeV}^2$ (dotted line) and $M_n^2 = M_X^2$ (dashed line), where M_X^2 is the squared missing mass in the exclusive process $\gamma^* p \to n\pi^+$. The plots on the left (right) side of the figure are obtained from the PYTHIA (exclusive MC) sample selected with the final cuts (Table 6.5). The spread in t and t_0 becomes smaller when the PDG-value of $M_n^2 = (0.9396)^2\,\mathrm{GeV}^2$ instead M_X^2 is used in the calculation. However, the $t' = t - t_0$ distribution appears to be insensitive to these two choices of M_n^2 values, and also to the choice of the reference frame (the centre-of-mass or the laboratory frame). The fact that the t_0 and t' distributions differ only slightly between the *lab*-frame and the *cm*-frame is explained by the small $\theta_{\gamma^*\pi^+}$ angle. In this analysis $t' = t - t_0$ as computed in the *lab*-frame with $M_n^2 = M_X^2$ is chosen to present the t'-dependence of the azimuthal asymmetry amplitude (Fig. 8.6).

The resolution of t and t' (obtained from the difference between generated and reconstructed values) is shown in Fig. D.2. The values are computed with $M_n^2 = M_X^2$ (full points) and $M_n^2 = (0.9396)^2\,\mathrm{GeV}^2$ (open points) in the *cm*-frame. Below (above) $t \approx -0.4\,\mathrm{GeV}^2$ the resolution of t is larger (smaller) when computed with $M_n^2 = (0.9396)^2\,\mathrm{GeV}^2$, while the t' resolution is not sensitive to the choice of M_n^2 values. The PYTHIA sample selected with the final cuts (Table 6.5) is used for this resolution study since the exclusive MC distributions (δ) of generated minus reconstructed values are not symmetric to be fitted with a Gaussian.

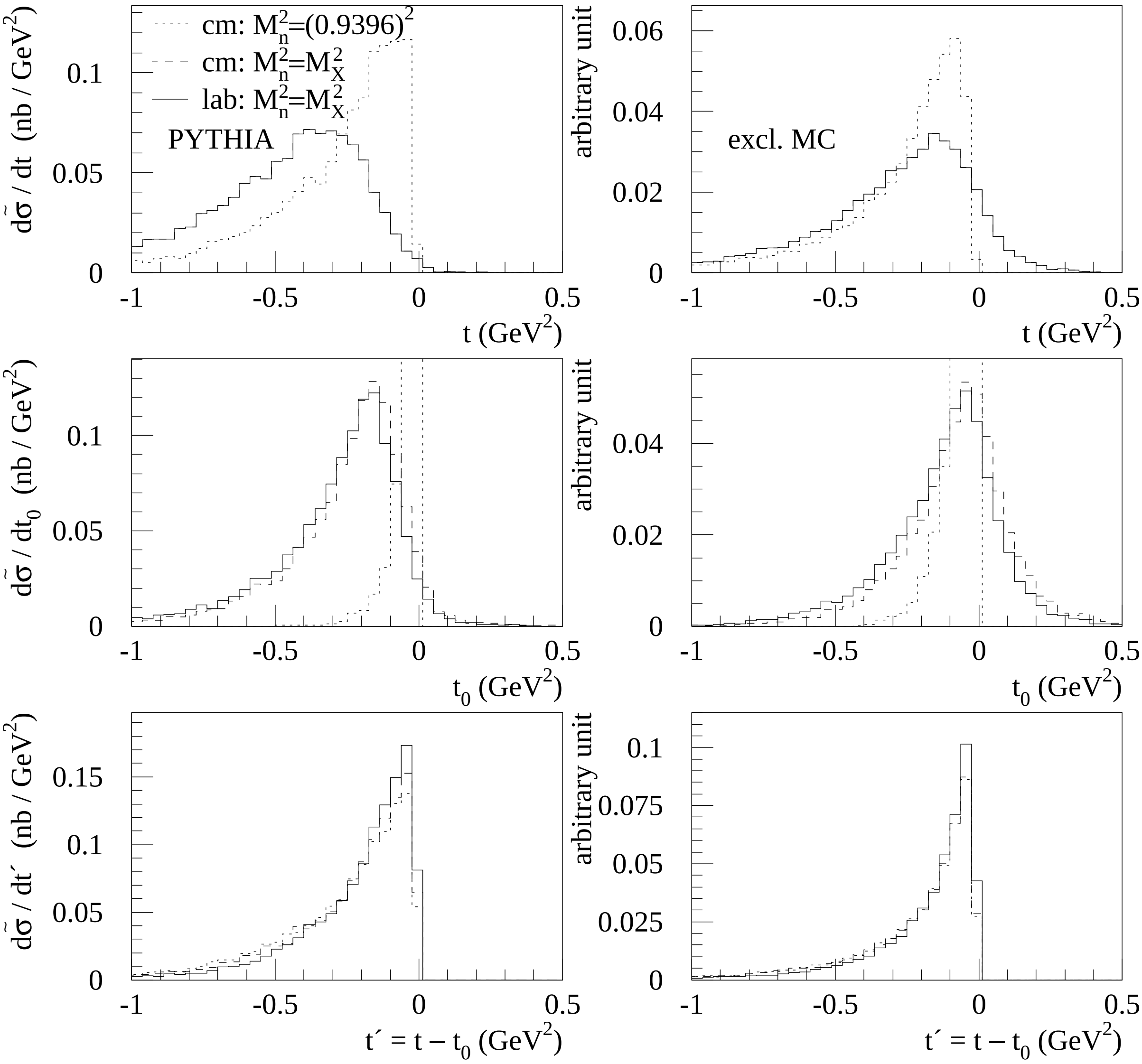

Figure D.1: Distributions of the t, t_0, and $t' = t - t_0$ values as computed in the *lab*-frame with the neutron mass $M_n = M_X$ (solid line), and in the *cm*-frame with $M_n = 0.9396\,\text{GeV}$ (dotted line) and $M_n = M_X$ (dashed line), where M_X is the missing neutron mass in the exclusive process $\gamma^* p \to n\pi^+$. The PYTHIA (left panel) and the exclusive MC (right panel) samples are selected with the final cuts (Table 6.5).

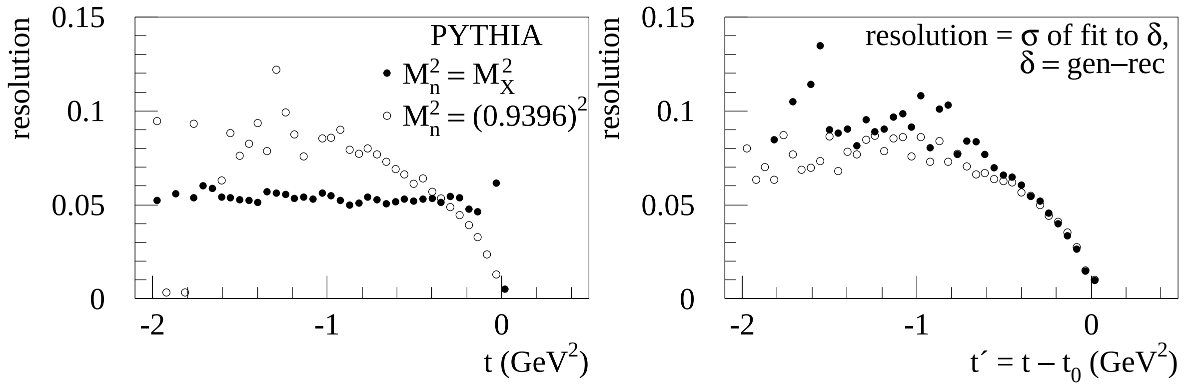

Figure D.2: Resolution of t and $t' = t - t_0$ as computed with $M_n = M_X$ (full points) and $M_n = 0.9396\,\text{GeV}$ (open points) in the *cm*-frame using the PYTHIA sample selected with the final cuts (Table 6.5).

Appendix E

Correlations of Kinematic Variables

The figures Fig. E.1 on the next page to Fig. E.10 on page 151 show the correlations of the 18 (= 16 + 2) kinematic variables $k = i, j$, where

$$i = \begin{array}{cccccccc} x, & y, & \nu, & Q^2, & W^2, & \theta_{\gamma^*}, & p_{\pi^+}, & P_{\pi^+\perp}, \\ M_X^2, & \theta_{\gamma^*\pi^+}, & \phi_{\pi^+}, & \phi_S, & \Theta_{\pi^+}, & \Phi_{\pi^+}, & t, & z, \end{array}$$

and

$$j = \quad p_{e^{+\prime}} + p_{\pi^+}, \quad t' = t - t_0,$$

with the variables i. These figures (one figure per page) are organised as follows:

x	vs. k	y	vs. k
ν	vs. k	Q^2	vs. k
W^2	vs. k	θ_{γ^*}	vs. k
p_{π^+}	vs. k	$P_{\pi^+\perp}$	vs. k

M_X^2	vs. k	$\theta_{\gamma^*\pi^+}$	vs. k
ϕ_{π^+}	vs. k	ϕ_S	vs. k
Θ_{π^+}	vs. k	Φ_{π^+}	vs. k
t	vs. k	z	vs. k

The kinematic variables

- x, y, ν, Q^2, W^2, p_{π^+}, M_X^2, t, z, and $\Theta_{e^{+\prime}}$ are defined in Table 3.1 on page 14
- ϕ_{π^+}, ϕ_S, $\theta_{\gamma^*\pi^+}$, and $P_{\pi^+\perp}$ are displayed in Fig. 3.1 on page 13, as well as l and q
- θ_{γ^*} is the angle between l and q
- Θ_{π^+} and Φ_{π^+}, and $\Theta_{e^{+\prime}}$ and $\Phi_{e^{+\prime}}$, are respectively the polar and azimuthal angles of the pion π^+ and of the scattered positron $e^{+\prime}$ relative to l
- $p_{e^{+\prime}}$ is the momentum of the scattered positron $e^{+\prime}$
- t' and t_0 are discussed in Appendix D
- $rapidity = \frac{1}{2} \log \frac{E_{\pi^+,cm} + \vec{p}_{\pi^+,cm} \cdot (\vec{q} + \vec{P})}{E_{\pi^+,cm} - \vec{p}_{\pi^+,cm} \cdot (\vec{q} + \vec{P})}$, $\quad x_F = 2 \frac{\vec{p}_{\pi^+,cm} \cdot (\vec{q} + \vec{P})}{\sqrt{W^2}}$

More figures showing the correlations for the full set of kinematic variables can be found in [46].

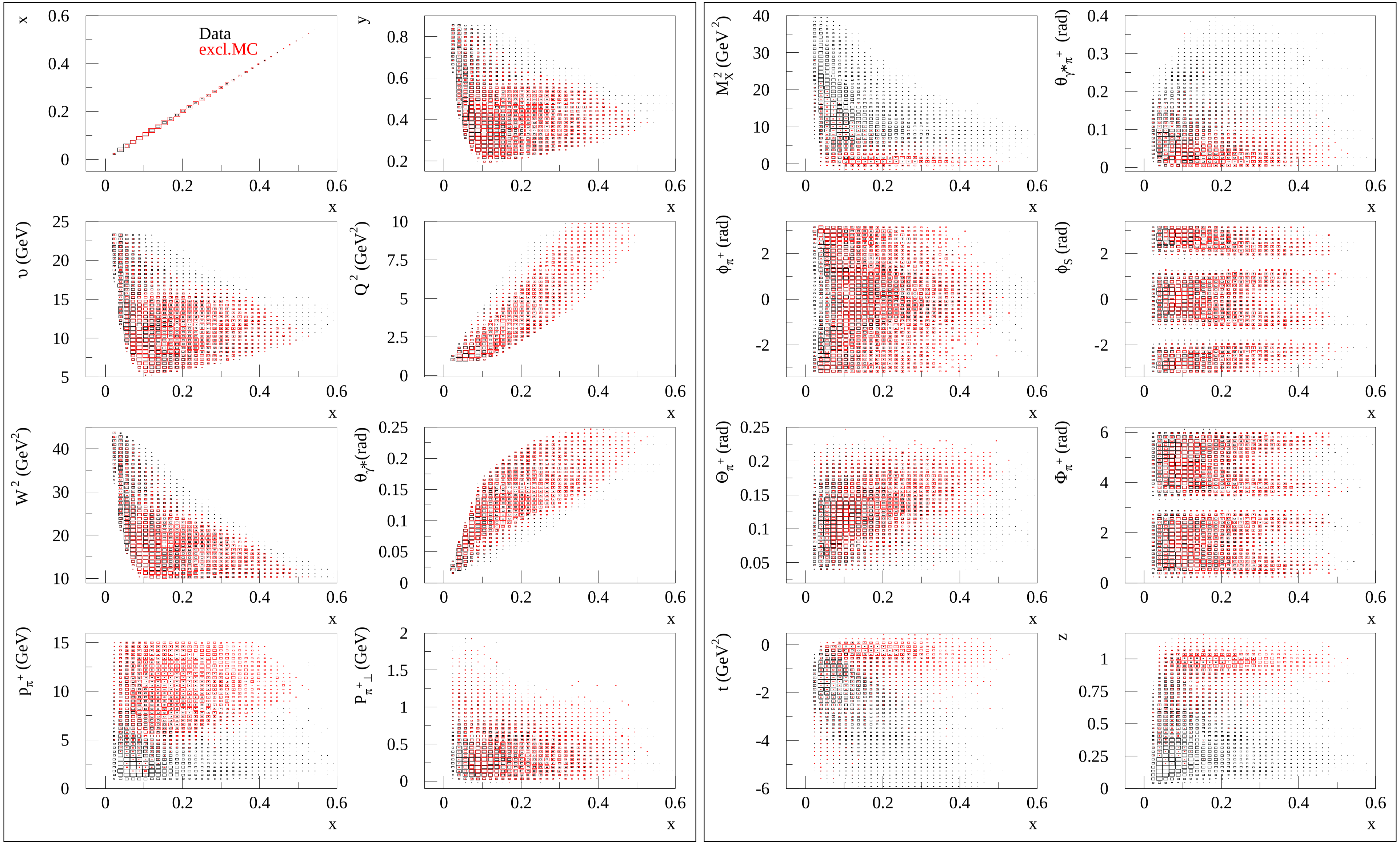

Figure E.1: Correlations of kinematic variables for $\boxed{x}$ for data (black) and exclusive MC (red) samples selected with the standard cuts (Table 6.2).

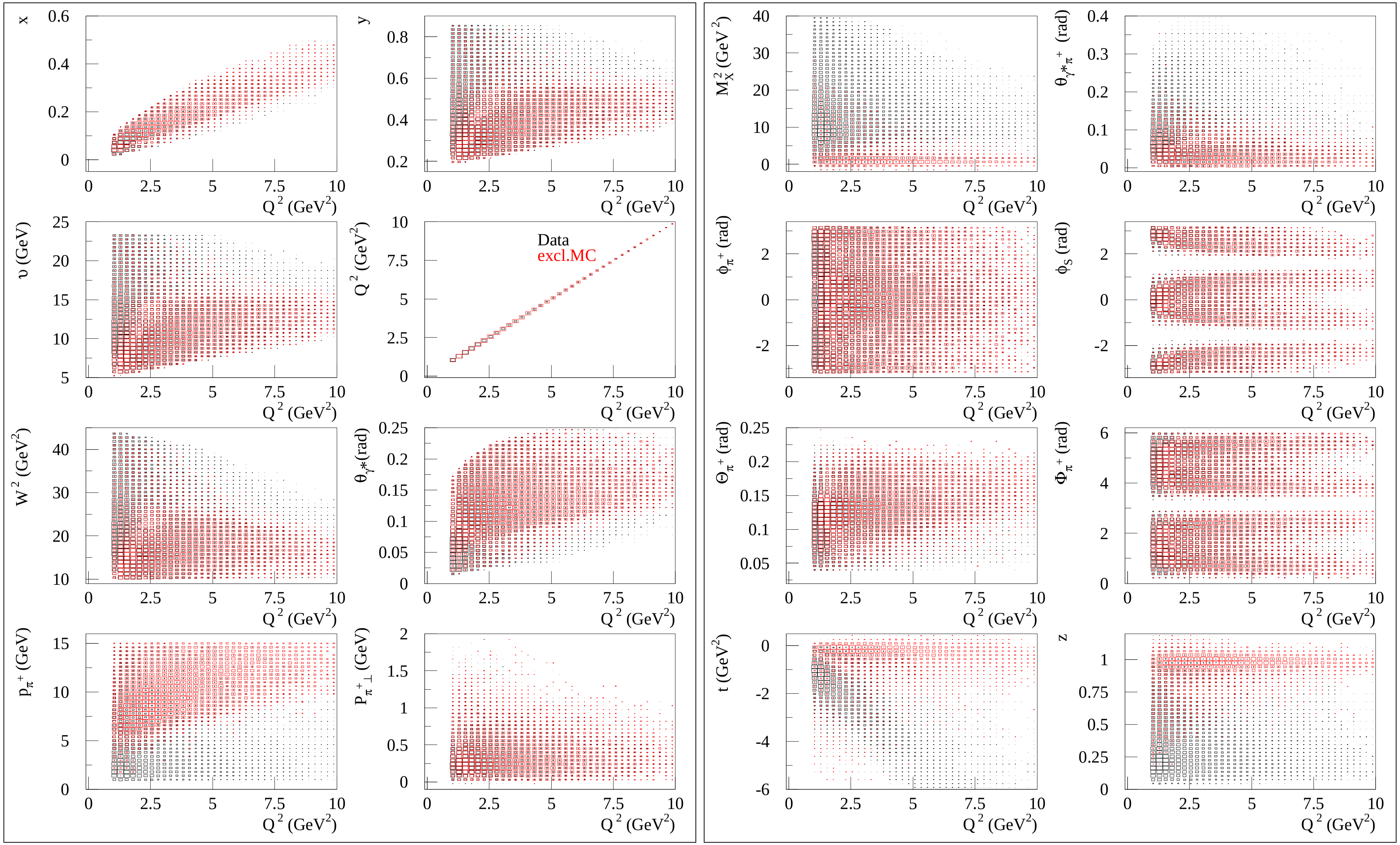

Figure E.2: Correlations of kinematic variables for $\boxed{Q^2}$ for data (black) and exclusive MC (red) samples selected with the standard cuts (Table 6.2).

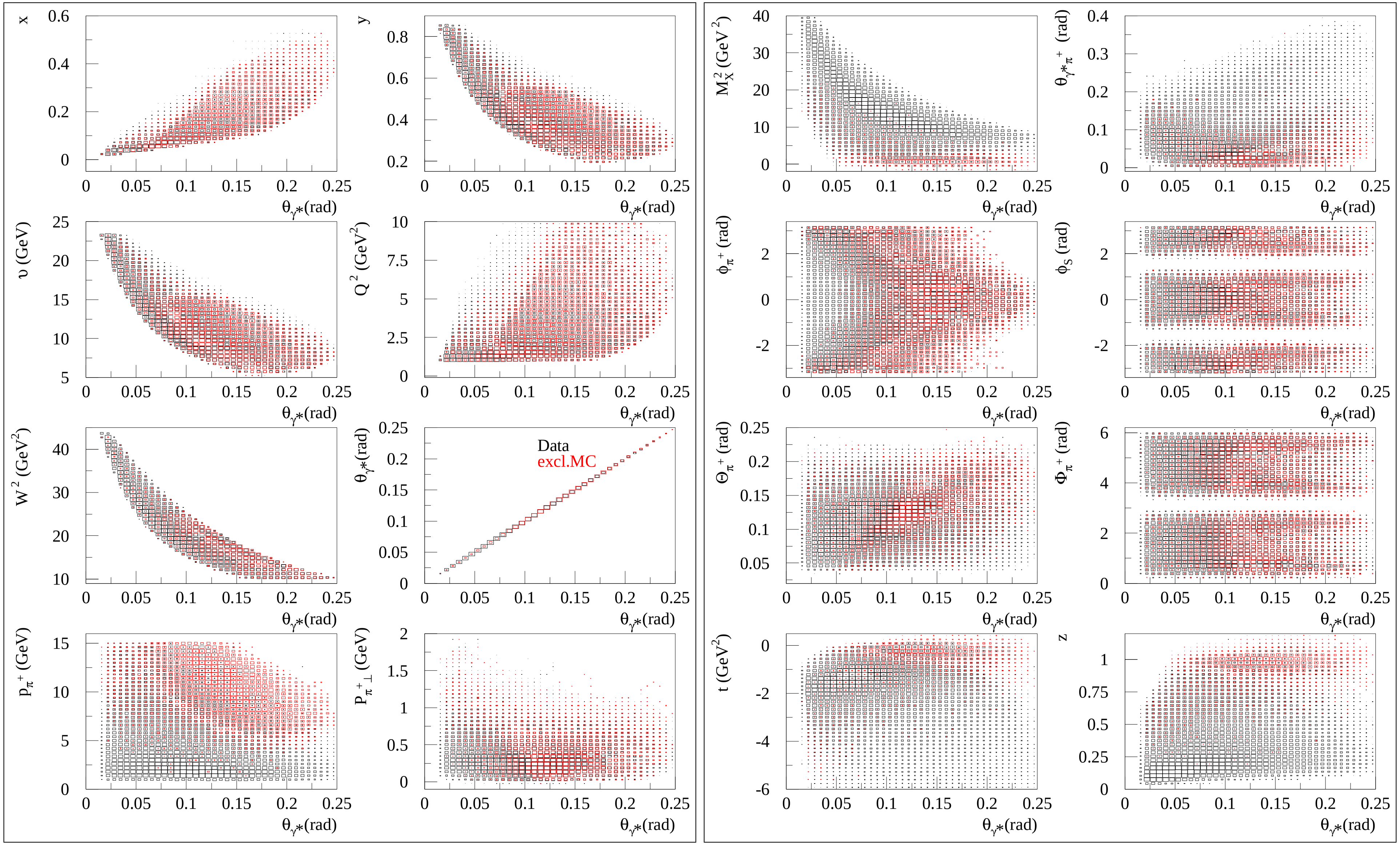

Figure E.3: Correlations of kinematic variables for $\boxed{\theta_{\gamma^*}}$ for data (black) and exclusive MC (red) samples selected with the standard cuts (Table 6.2).

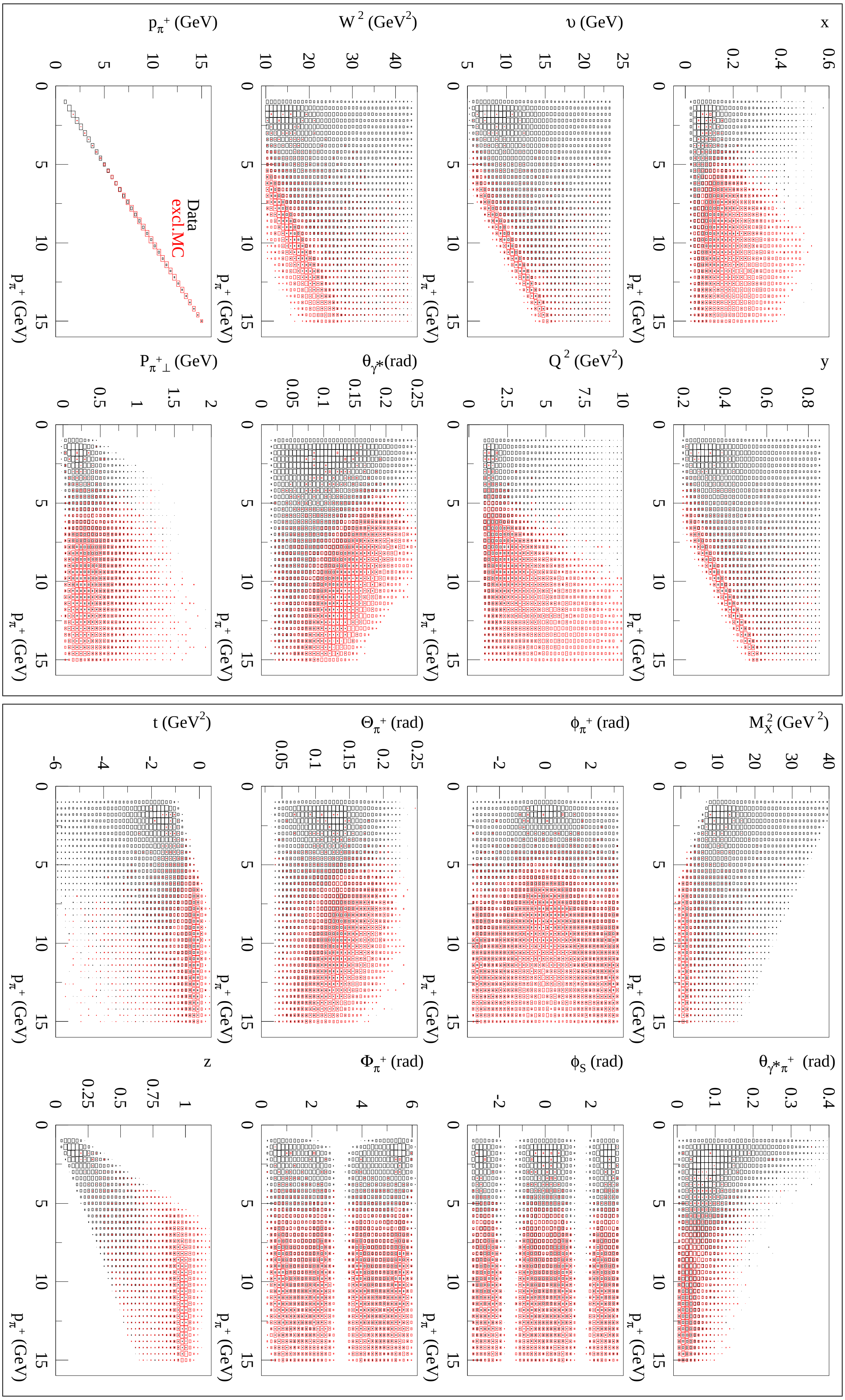

Figure E.4: Correlations of kinematic variables for $\boxed{p_{\pi^+}}$ for data (black) and exclusive MC (red) samples selected with the standard cuts (Table 6.2).

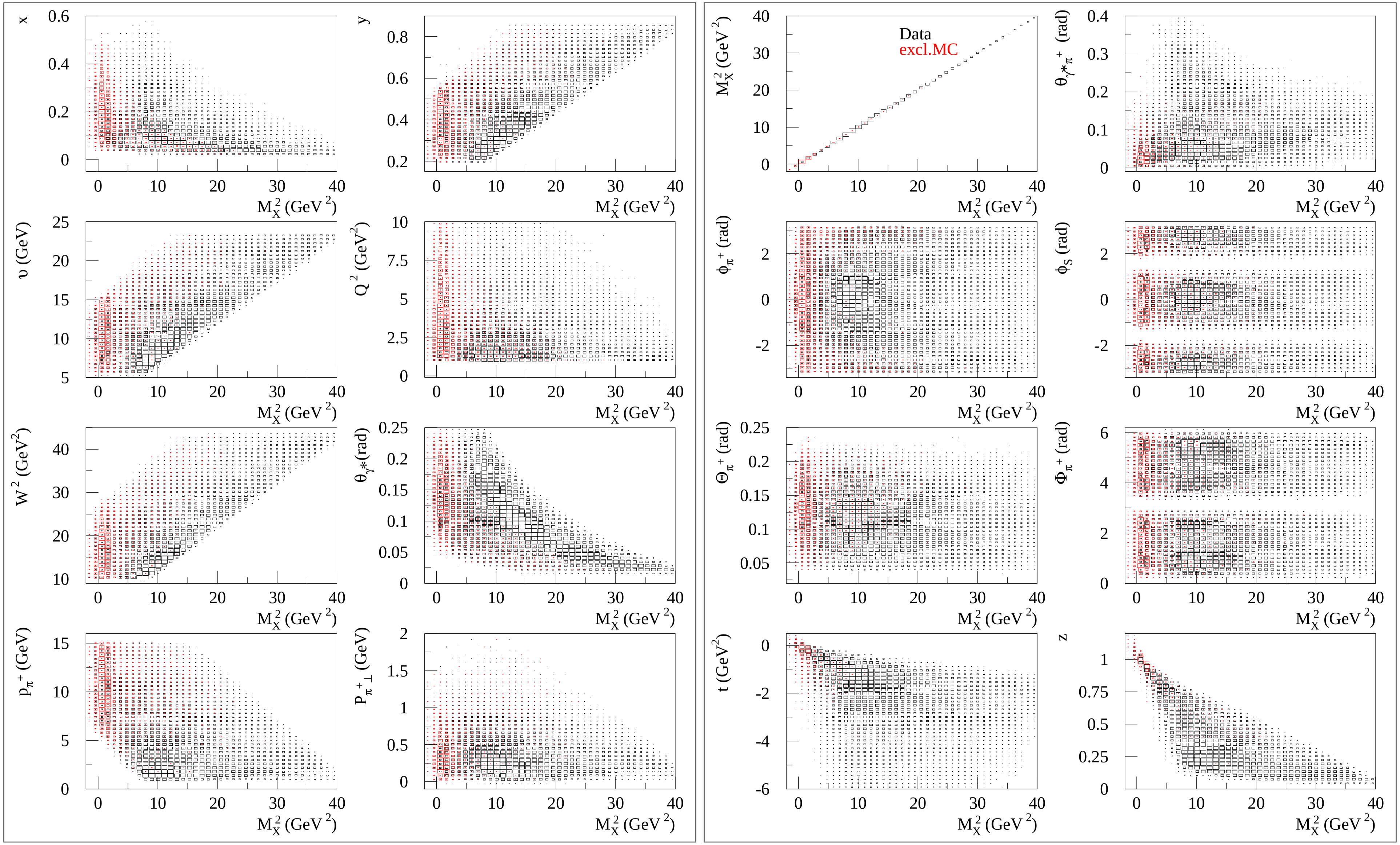

Figure E.5: Correlations of kinematic variables for $\boxed{M_X^2}$ for data (black) and exclusive MC (red) samples selected with the standard cuts (Table 6.2).

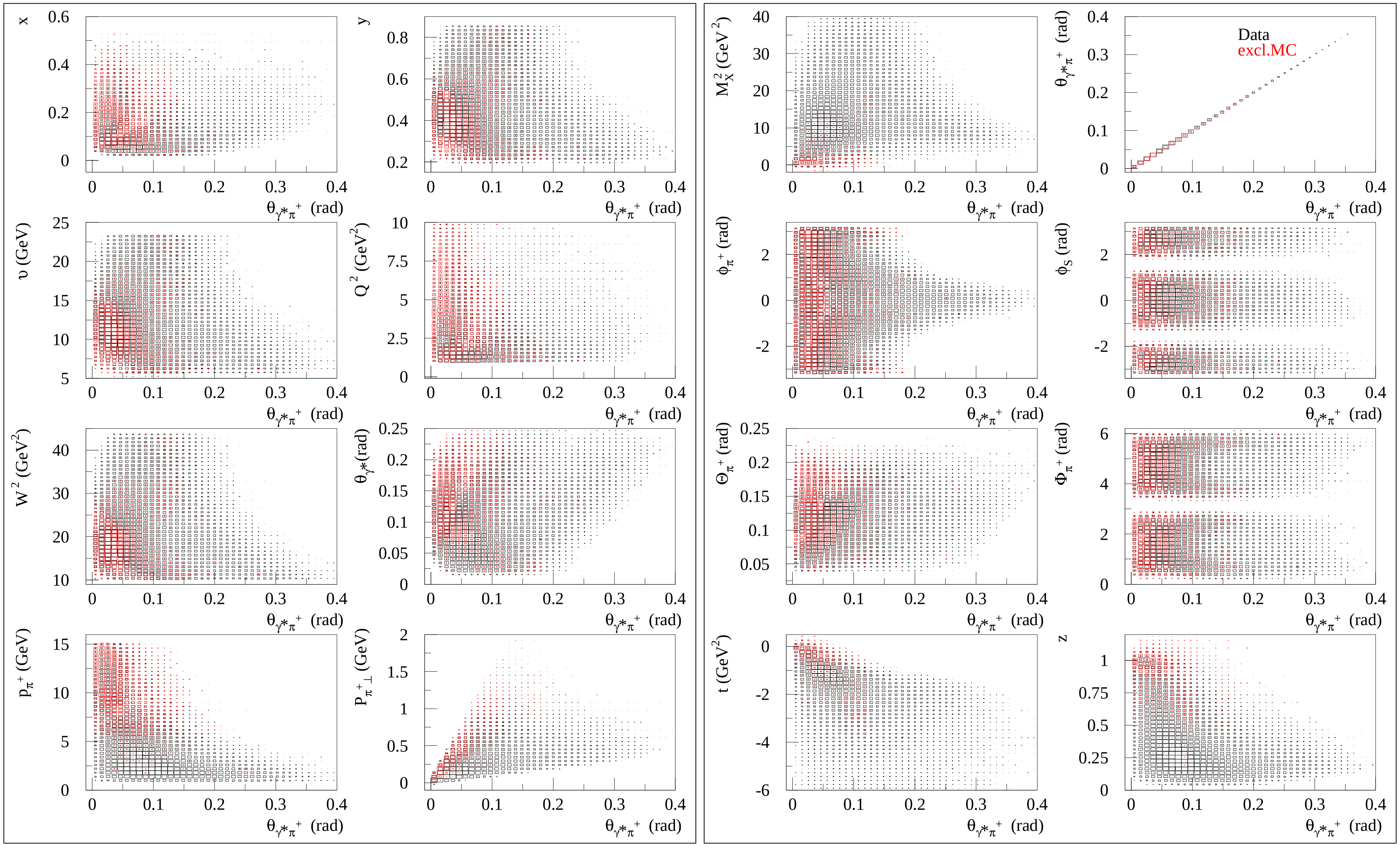

Figure E.6: Correlations of kinematic variables for $\boxed{\theta_{\gamma^*\pi^+}}$ for data (black) and exclusive MC (red) samples selected with the standard cuts (Table 6.2).

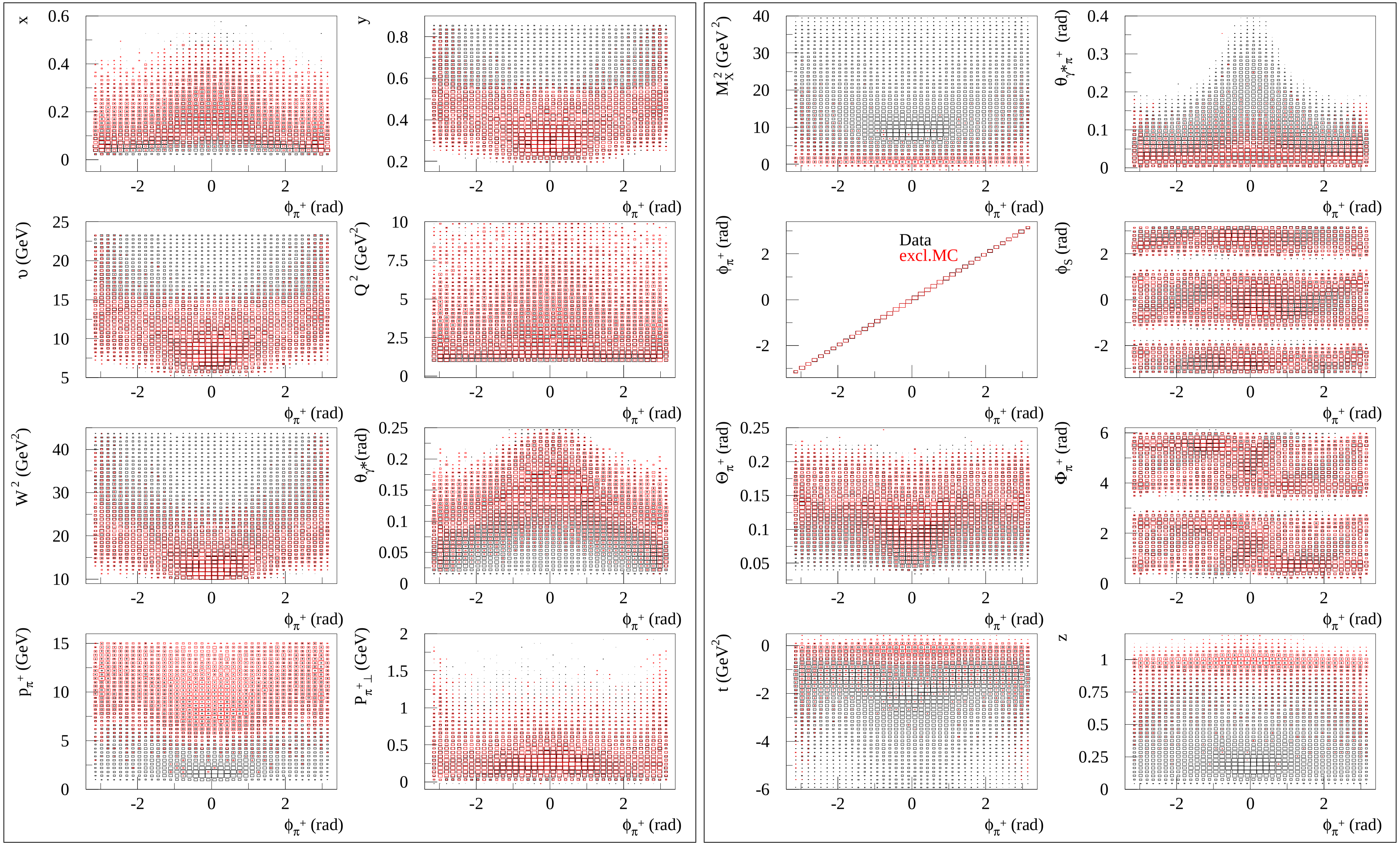

Figure E.7: Correlations of kinematic variables for $\boxed{\phi_{\pi+}}$ for data (black) and exclusive MC (red) samples selected with the standard cuts (Table 6.2).

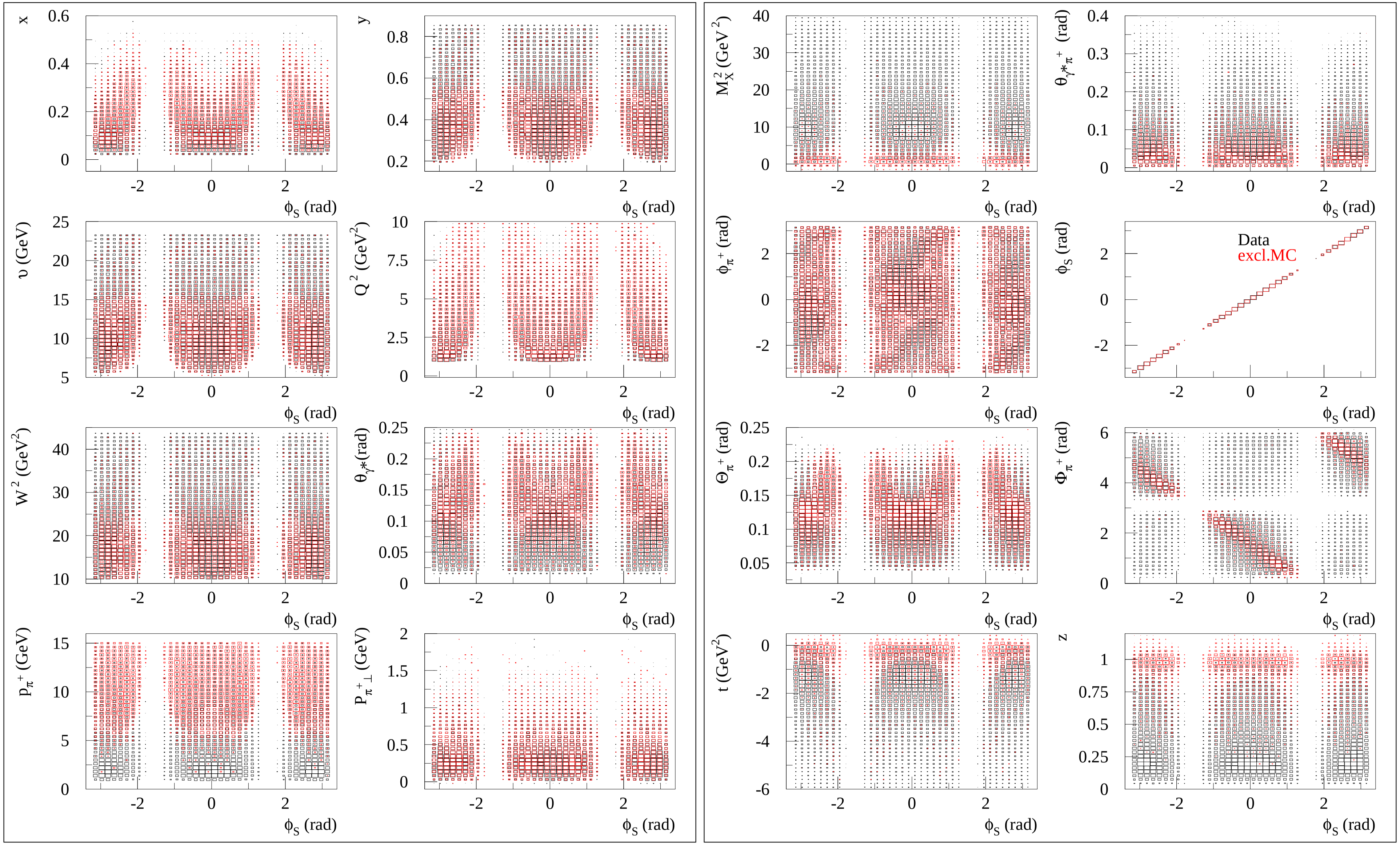

Figure E.8: Correlations of kinematic variables for $\boxed{\phi_S}$ for data (black) and exclusive MC (red) samples selected with the standard cuts (Table 6.2).

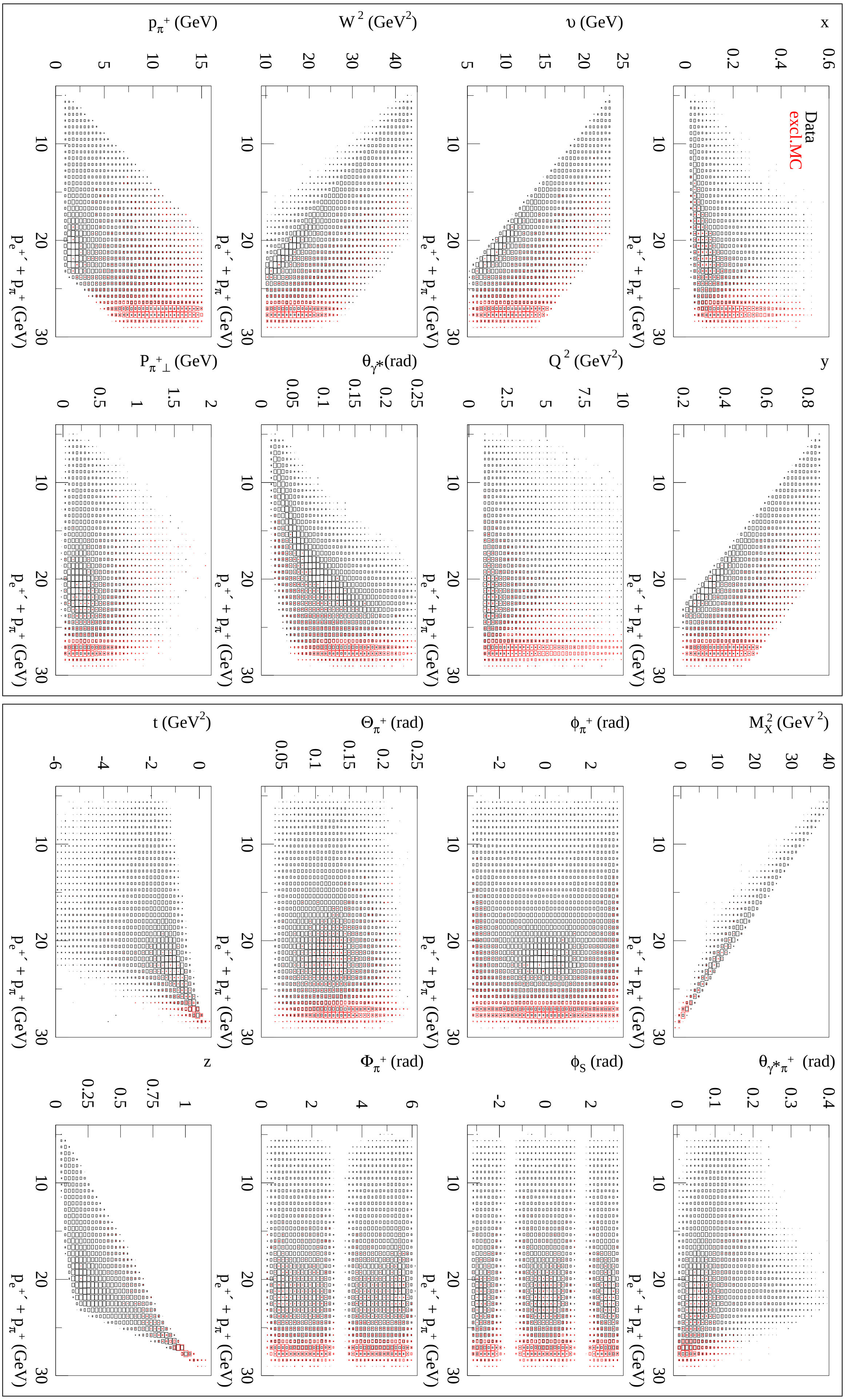

Figure E.9: Correlations of kinematic variables for $\boxed{p_{e^{+\prime}} + p_{\pi^+}}$ for data (black) and exclusive MC (red) samples selected with the standard cuts (Table 6.2).

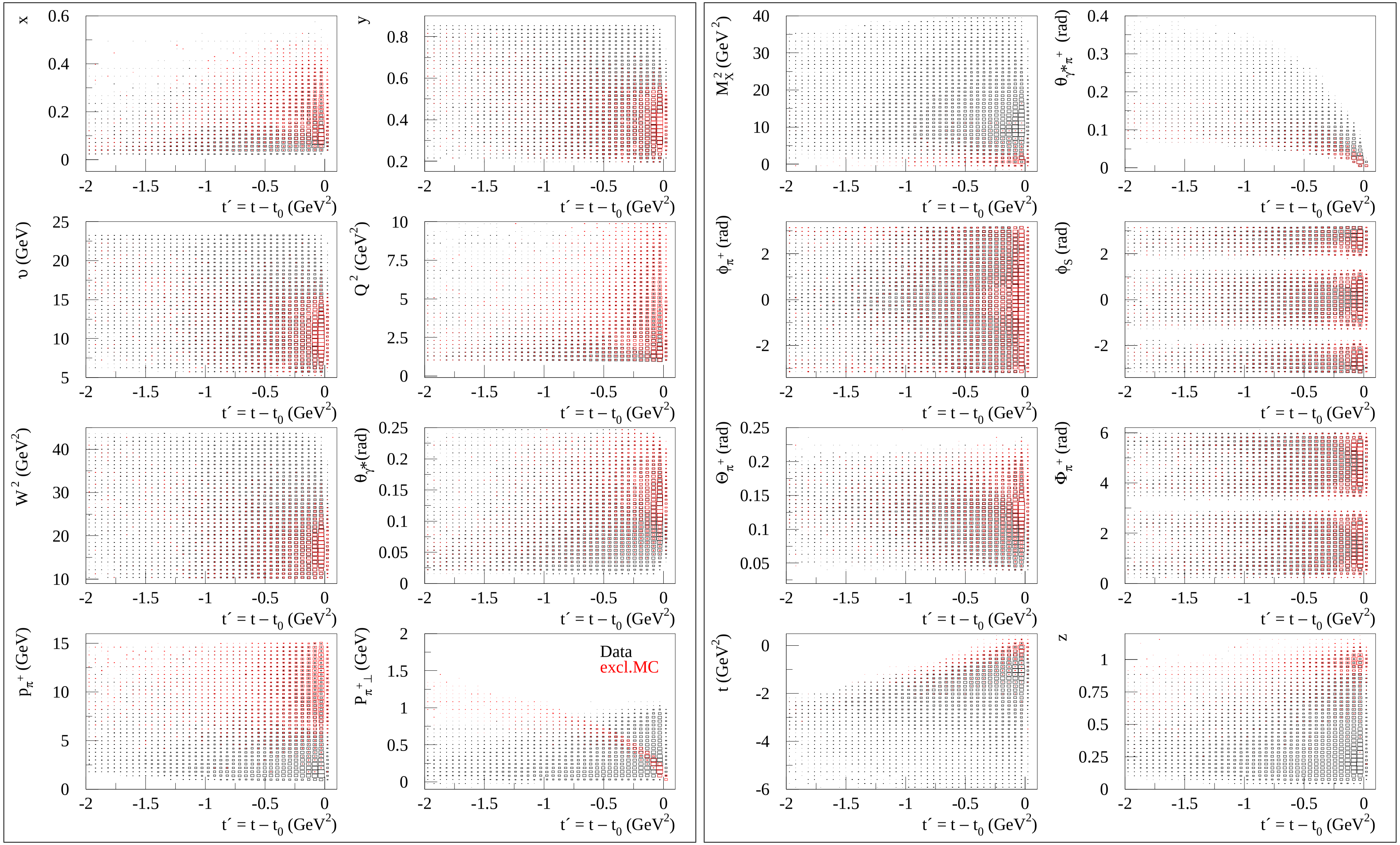

Figure E.10: Correlations of kinematic variables for $\boxed{t'}$ for data (black) and exclusive MC (red) samples selected with the standard cuts (Table 6.2).

Danksagung

First of all, I would like to thank my thesis advisor Dr. Wolf-Dieter Nowak for providing me the opportunity to participate in the HERMES experiment and for his continuous and extended support. His care in both setting the scope of my analysis and considering every step of its development have always made me feel on safe ground. I would also like to thank Prof. Hermann Kolanoski for taking over the role as my official advisor at the Humboldt-University in Berlin and for his valuable comments that have led to a substantial improvement of the manuscript.

I am deeply grateful to Cynthia Hadjidakis and Delia Hasch for sharing with me their knowledge and experience on all aspects of the exclusive analysis. I would not have been able to cope with the everyday challenges of my analysis work without their constant guidance, advice, and helpful criticism.

Many people have provided help at various stages of this analysis. I would like to thank Katerina Lipka and Elke-Caroline Aschenauer for their clear and straightforward help on setting up the analysis software. I am thankful to Ingrid-Maria Gregor, Gunar Schnell, and Delia Hasch for making the tedious phase of testing and debugging of the codes a rewarding and altogether joyful experience. I thank Elke-Caroline Aschenauer, Arne Vandenbroucke, Ulrike Elschenbroich, Armine Rostomyan, Zhenyu Ye, and Gunar Schnell for their contribution to the understanding of our data by sharing programs, plots, and results from their analyses. Special thanks go to Jeroen Dreschler for developing and giving us support for the UML fit used to extract our main results.

I thank Andy Miller, Elke-Caroline Aschenauer, Henk Blok, Stephen Rock, Frank Ellinghaus, Gunar Schnell, and all members of the subgroup meetings at which the status of this work has been regularly reported for fruitful discussions, questions, ideas, and interest in the analysis.

It is a pleasure to thank Markus Diehl for explanations regarding the theoretical description of our exclusive channel and Wolfgang Kugler for commenting on the theoretical part of the manuscript.

I enjoyed the busy times spent with the members of the silicon recoil detector group Arne Vandenbroucke, Mikhail Kopytin, Zhenyu Ye, Craig Shearer, James Stweart, Mathias Reinecke, Christian Vogel, Nils Pickert, Bernhard Krauß, and Friedrich Stinzing. I thank them for introducing me to detector related issues as well as to the physics of GPDs. Especially I would like to thank Ingrid-Maria Gregor for teaching me how to work with the hardware in the lab and in the testbeam. Gratitude also goes to Morgan Murray with whom I spent many days and nights working together in T22 during the testing phase of the silicon modules.

I am thankful for the friendly working atmosphere I experienced in Zeuthen in the company of my officemates Arne Vandenbroucke and Mikhail Kopytin, and our frequent guests Oxana Tarasova and Katerina Kuznetsova. Thanks to all the people with whom I enjoyed my time out of work in Hamburg: Ingrid-Maria Gregor, Caroline Riedl, Frank Ellinghaus, Elke-Caroline Aschenauer, James Stweart, Patricia Liebing, Benedikt Zihlmann, Morgan Murray, Hayg Guler, Dominik Gabbert, and many more who I forgot to mention.

Selbständigkeitserklärung

Hiermit erkläre ich, die Dissertation selbständig und nur unter Verwendung der angegebenen Hilfen und Hilfsmittel angefertigt zu haben.

Ich habe mich anderwärts nicht um einen Doktorgrad beworben und besitze einen entsprechenden Doktorgrad nicht.

Ich erkläre die Kenntnisnahme der dem Verfahren zugrunde liegenden Promotionsordnung der Mathematisch-Naturwissenschaftlichen Fakultät I der Humboldt-Universität zu Berlin.

Berlin, 21.08.2007
Ivana Hristova.

Bibliography

[1] EPIO — experimental physics input output package, user's guide. CERN Program Library Long Writeup I101, Application Software and Databases Group, Computing and Networks Division, December 1993.

[2] ADAMO — entity-relationship programming system, user's guide, version 3.3. CERN, ECP Division, Programming Techniques Group, January 1994.

[3] MINUIT — function minimization and error analysis, reference manual, version 94.1. CERN Program Library Long Writeup D506, Computing and Networks Division, March 1994.

[4] Hadronic physics from lattice QCD. In A. M. Green, editor, *International Review of Nuclear Physics Vol.9*. World Scientific, Singapore, 2004.

[5] A. Abragam and J. M. Winter. Proposal for a source of polarized protons. *Phys. Rev. Lett.*, **1**:374–375, 1958.

[6] A. Afanasev. Private communication to C. Hadjidakis and D. Hasch. HERMES Internal Release Report, April 2004.

[7] I. Akushevich, H. Boettcher, and D. Ryckbosch. RADGEN 1.0 Monte Carlo generator for radiative events in DIS on polarized and unpolarized targets, June 1999. arXiv:hep-ph/9906408v1.

[8] A. Bacchetta. *Probing the Transverse Spin of Quarks in Deep Inelastic Scattering.* PhD thesis, Vrije Universiteit Amsterdam, 2002. arXiv:hep-ph/0212025v1.

[9] A. Bacchetta, U. D'Alesio, M. Diehl, and C. A. Miller. Single-spin asymmetries: the Trento conventions. *Phys. Rev.*, **D70**:117504–1–4, 2004. arXiv:hep-ph/0410050v2.

[10] A. Belitsky and D. Müller. Hard exclusive meson production at next-to-leading order. *Phys. Lett.*, **B513**:349–360, 2001. arXiv:hep-ph/0105046v2.

[11] J. D Bjorken and E. A. Paschos. Inelastic electron-proton and γ-proton scattering and the structure of the nucleon. *Phys. Rev.*, **185**:1975–1982, 1969.

[12] F. Bloch. Nuclear induction. *Phys. Rev.*, **70**:460–474, 1946.

[13] F. Bloch and A. Siegert. Magnetic resonance for nonrotating fields. *Phys. Rev.*, **57**:522–527, 1940.

[14] S. J. Brodsky and G. P. Lepage. Exclusive processes in quantum chromodynamics. In A. H. Mueller, editor, *Perturbative Quantum Chromodynamics*, pages 93–240. World Scientific, Singapore, 1989.

[15] S. J. Brodsky, H.-Ch. Pauli, and S. S. Pinsky. Quantum chromodynamics and other field theories on the light cone. *Phys. Rep.*, **301**:299–486, 1998.

[16] R. Brun, R. Hagelberg, M. Hansroul, and J. Lassalle. GEANT: Simulation program for particle physics experiments. User guide and reference manual. CERN Report CERN-DD-78-2-REV, 1978.

[17] J. Buon and K. Steffen. HERA variable-energy "mini" spin rotator and head-on ep collision scheme with choice of electron helicity. *Nucl. Instrum. Meth.*, **A245**:248–261, 1986.

[18] C. Cohen-Tannoudji, B. Diu, and F. Laloë. *Quantenmechanik.* Walter de Gruyter, 1999.

[19] J. C. Collins, L. Frankfurt, and M. Strikman. Factorization for hard exclusive electroproduction of mesons in QCD. *Phys. Rev.*, **D56**:2982–3006, 1997. arXiv:hep-ph/9611433v4.

[20] J. C. Collins, D. E. Soper, and G. Sterman. Factorization of hard processes in QCD. In A. H. Mueller, editor, *Perturbative Quantum Chromodynamics*, pages 1–91. World Scientific, Singapore, 1989.

[21] D. Diakonov, V. Petrov, P. Pobylitsa, M. Polyakov, and C. Weiss. Nucleon parton distributions at low normalization point in the large N_c limit. *Nucl. Phys.*, **B480**:341–378, 1996. arXiv:hep-ph/9606314v1.

[22] D. I. Diakonov, V. Yu. Petrov, and P. V. Pobylitsa. A chiral theory of nucleons. *Nucl. Phys.*, **B306**:809–848, 1988. see also arXiv:hep-ph/9802298v1.

[23] M. Diehl. Generalized parton distributions. *Phys. Rep.*, **388**:41–277, 2003.

[24] M. Diehl. Private communication, December 2006.

[25] M. Diehl and W. Kugler. Next-to-leading order corrections in exclusive meson production. *Eur. Phys. J.*, **C52**:933–966, 2007. arXiv:0708.1121v1 [hep-ph].

[26] M. Diehl, W. Kugler, A. Schäfer, and C. Weiss. Exclusive channels in semi-inclusive production of pions and kaons. *Phys. Rev.*, **D72**:034034–1–24, 2005.

[27] M. Diehl and S. Sapeta. On the analysis of lepton scattering on longitudinally or transversely polarized protons. *Eur. Phys. J.*, **C41**:515–533, 2005. arXiv:hep-ph/0503023v1.

[28] P. A. M. Dirac. Forms of relativistic dynamics. *Rev. Mod. Phys.*, **21**:392–399, 1949.

[29] J. Dreschler. Private communication, July 2006.

[30] F. Ellinghaus. *Beam-Charge and Beam-Spin Azimuthal Asymmetries in Deeply-Virtual Compton Scattering.* PhD thesis, Humboldt-Universität Berlin, 2004. DESY-THESIS-2004-005.

[31] U. Elschenbroich. *Transverse Spin Structure of the Proton Studied in Semi-Inclusive DIS.* PhD thesis, Universiteit Gent, 2006. DESY-THESIS-2006-004.

[32] R. P. Feynman. Very high-energy collisions of hadrons. *Phys. Rev. Lett.*, **23**:1415–1417, 1969.

[33] L. L. Frankfurt, P. V. Pobylitsa, M. V. Polyakov, and M. Strikman. Hard exclusive pseudoscalar meson electroproduction and spin structure of the nucleon. *Phys. Rev.*, **D60**:014010–1–11, 1999. arXiv:hep-ph/9901429v1.

[34] L. L. Frankfurt, M. V. Polyakov, M. Strikman, and M. Vanderhaeghen. Hard exclusive electroproduction of decuplet baryons in the large N_c limit. *Phys. Rev. Lett.*, **84**:2589–2592, 2000. arXiv:hep-ph/9911381v1.

[35] C. Friberg and T. Sjöstrand. Jet production by virtual photons. *Eur. Phys. J.*, **C13**:151–174, 2000. arXiv:hep-ph/9907245v1.

[36] H Fritzsch and M. Gell-Mann. Current algebra: Quarks and what else? In J. D. Jaclson and A. Roberts, editors, *Proceedings of the XVI International Conference on High Energy Physics*. p.135, Volume 2. Chicago, 1972. arXiv:hep-ph/0208010v1.

[37] H. Fritzsch, M. Gell-Mann, and H. Leutwyler. Advantages of the color octet gluon picture. *Phys. Lett.*, **B47**:365–368, 1973.

[38] S. Fubini and G. Furlan. *Physics*, **1**:229, 1965.

[39] K. Goeke, M. V. Polyakov, and M. Vanderhaeghen. Hard exclusive reactions and the structure of hadrons. *Prog. Part. Nucl. Phys.*, **47**:401–515, 2001. arXiv:hep-ph/0106012v2.

[40] W. Greiner and A. Schäfer. *Quantum Chromodynamics*. Springer-Verlag, 1994.

[41] C. Hadjidakis and D. Hasch. Total cross section for hard exclusive pion production. HERMES Internal Release Report, April 2004.

[42] C. Hadjidakis and B. Krauß. gmc_exclpion – an event generator for exclusive pion production at HERMES, 2004.

[43] W. Haeberli. Sources of polarized ions. *Ann. Rev. Nucl. Sci.*, **17**:373–426, 1967.

[44] L. N. Hand. Experimental investigation of pion electroproduction. *Phys. Rev.*, **129**:1834–1846, 1963.

[45] A. Hillenbrand. *Measurement and Simulation of the Fragmentation Process at HERMES*. PhD thesis, Universität Erlangen–Nürnberg, 2005. DESY-THESIS-2005-035.

[46] I. Hristova. Methods for extraction and correction of the transverse target-spin asymmetry in exclusive production of single pions. HERMES Internal Note 07-014, August 2007.

[47] G. Ingelman, A. Edin, and J. Rathsman. LEPTO 6.5 – a Monte Carlo generator for deep inelastic lepton–nucleon scattering. *Comput. Phys. Commun.*, **101**:108–134, 1997. arXiv:hep-ph/9605286v1.

[48] R. Jakob. Transverse momenta in hard scattering processes, 2002. Postdoctoral Thesis, http://www.theorie.physik.uni-wuppertal.de/∼rainer/.

[49] P. Liebing. *Can the Gluon Polarisation in the Nucleon Be Extracted from HERMES data on single high-p_T Hadrons?* PhD thesis, Universität Hamburg, 2004. DESY-THESIS-2004-036.

[50] I. Mankiewicz, G. Piller, and A. Radyushkin. Hard exclusive electroproduction of pions. *Eur. Phys. J.*, **C10**:307–312, 1999. arXiv:hep-ph/9812467v1.

[51] F. Meißner. *Measurement of the J/psi Cross Section and Double-Spin Asymmetries in Vector Meson Production in Polarised Lepton-Nucleon Scattering at HERMES*. PhD thesis, Humboldt-Universität Berlin, 2000. DESY-THESIS-2000-014.

[52] M.V. Polyakov and S. Stratmann. Soft pion emission in hard exclusive pion production, September 2006. arXiv:hep-ph/0609045v1.

[53] A. V. Radyushkin. Symmetries and structure of skewed and double distributions. *Phys. Lett.*, **B449**:81–88, 1999.

[54] G. A. Schuler and T. Sjöstrand. Hadronic diffractive cross sections and the rise of the total cross section. *Phys. Rev.*, **D49**:2257–2267, 1994.

[55] T. Sjöstrand, P. Edén, C. Friberg, L. Lönnblad, G. Miu, S. Mrenna, and E. Norrbin. High-energy-physics event generation with PYTHIA 6.1. *Comput. Phys. Commun.*, **135**:238–259, 2001. arXiv:hep-ph/0010017v1.

[56] T. Sjöstrand, S. Mrenna, and P. Skands. PYTHIA 6.4 physics and manual. *J. High Energy Phys.*, **JHEP05**:1–574, 2006. arXiv:hep-ph/0603175v2.

[57] T. Sjöstrand and M. van Zijl. A multiple-interaction model for the event structure in hadron collisions. *Phys. Rev.*, **D36**:2019–2041, 1987.

[58] E. Steffens and W. Haeberli. Polarized gas targets. *Rep. Prog. Phys.*, **66**:1887–1935, 2003.

[59] P. Tait. *Beam-Induced Depolarisation at the HERMES Transversely Polarised Hydrogen Target.* PhD thesis, Universität Erlangen–Nürnberg, 2006.

[60] A. Airapetian *et al.* Single-spin azimuthal asymmetry in exclusive electroproduction of π^+ mesons. *Phys. Lett.*, **B535**:85–92, 2002. arXiv:hep-ex/0112022v4.

[61] A. Airapetian *et al.* The HERMES polarized hydrogen and deuterium gas target in the HERA electron storage ring. *Nucl. Instrum. Meth.*, **A540**:68–101, 2005. arXiv:physics/0408137v2.

[62] B. Clasie *et al.* Laser-driven target of high-density nuclear-polarized hydrogen gas. *Phys. Rev.*, **A73**:020703–1–4, 2006.

[63] C. Baumgarten *et al.* A gas analyzer for the internal polarized target of the HERMES experiment. *Nucl. Instrum. Meth.*, **A508**:268–275, 2003.

[64] D. P. Barber *et al.* The HERA polarimeter and the first observation of electron spin polarization at HERA. *Nucl. Instrum. Meth.*, **A329**:79–111, 1993.

[65] D. P. Barber *et al.* High spin polarisation at the HERA electron storage ring. *Nucl. Instrum. Meth.*, **A338**:166–184, 1994.

[66] D. P. Barber *et al.* The first achievement of longitudinal spin polarization in a high energy electron storage ring. *Phys. Lett.*, **B343**:436–443, 1995.

[67] K. Ackerstaff *et al.* The HERMES spectrometer. *Nucl. Instrum. Meth.*, **A417**:230–265, 1998. arXiv:hep-ex/9806008v1.

[68] M. Beckmann *et al.* The longitudinal polarimeter at HERA. *Nucl. Instrum. Meth.*, **A479**:334–348, 2002.

[69] N. Akopov *et al.* The HERMES dual-radiator ring imaging Cherenkov detector. *Nucl. Instrum. Meth.*, **A479**:511–530, 2002. arXiv:physics/0104033v1.

[70] S. Eidelman *et al.* Review of particle physics. *Phys. Lett.*, **B592**:1–1109, 2004.

[71] Th. Benisch *et al.* The luminosity monitor of the HERMES experiment at DESY. *Nucl. Instrum. Meth.*, **A471**:314–324, 2001.

[72] HERMES Collaboration. Cross section for hard exclusive electroproduction of π^+ mesons on a hydrogen target. To be published.

[73] M. Vanderhaeghen, P. A. M. Guichon, and M. Guidal. Deeply virtual electroproduction of photons and mesons on the nucleon: Leading order amplitudes and power corrections. *Phys. Rev.*, **D60**:094017–1–28, 1999. arXiv:hep-ph/9905372v1.

[74] G.-A. Voss and B. H. Wiik. The electron-proton collider HERA. *Ann. Rev. Nucl. Part. Sci.*, **44**:413–452, 1994.